Molecular diversity among adult hippocampal and entorhinal cells

Franjić, Daniel

UNIVERSITY OF ZAGREB
SCHOOL OF MEDICINE

Daniel Franjić

Molecular diversity among adult hippocampal and entorhinal cells

DISSERTATION

Zagreb, 2025

UNIVERSITY OF ZAGREB
SCHOOL OF MEDICINE

Daniel Franjić

Molecular diversity among adult hippocampal and entorhinal cells

DISSERTATION

Zagreb, 2025

Mentors:

Goran Sedmak, MD, PhD
Associate Professor of Neuroscience
University of Zagreb, School of Medicine

Nenad Šestan, MD, PhD
Harvey and Kate Cushing Professor of Neuroscience, and Professor of Comparative Medicine, of Genetics and of Psychiatry
Yale University, School of Medicine, New Haven, CT

Abbreviations

A1C	Primary auditory cortex
AD	Alzheimer's disease
ADAMTS12	ADAM Metallopeptidase With Thrombospondin Type 1 Motif 12
ADCYAP1	Adenylate Cyclase Activating Polypeptide 1
ADFP	Adipose Differentiation-Related Protein (ADFP) Pseudogene
ADRA1A	Adrenoceptor Alpha 1A
aEndo	Arterial endothelial cell
AMY	Amygdala
APBB1	Amyloid Beta Precursor Protein Binding Family B Member 1
APOE	Apolipoprotein E
APP	Amyloid Beta Precursor Protein
AQP4	Aquaporin 4
aSMC	Arterial smooth muscle cell
Astro	Astrocyte
Asym	Asymptomatic AD
BrdU	Bromodeoxyuridine
CA	Cornu Ammonis
CALB	Calbindin
CALNEXIN	Calnexin
CBC	Cerebellar cortex
CENPF	Centromere Protein F
CERAD	The Consortium to Establish a Registry for Alzheimer's Disease
CHRDL1	Chordin Like 1
CHRNA1	Cholinergic Receptor Nicotinic Alpha 1 Subun
COP	Committed oligodendrocyte precursor cell
CV	Central vein
CUX2	Cut Like Homeobox 2
cyc	Cycling
Cyhx	Cycloheximide
DCX	Doublecortin

DG	Dentate gyrus
dlPFC/DFC	Dorsolateral prefrontal cortex
DPYSL	Dihydropyrimidinase Like
DUSP14	Dual Specificity Phosphatase 14
EC	Entorhinal cortex
EGFP	Enhanced green fluorescent protein
EGR1	Early Growth Response 1
Endo	Endothelial cell
ER	Endoplasmoc reticulum
EvC	EvC Ciliary Complex Subunit
ExN	Excitatory neuron
F	Female
FN1	Fibronectin 1
GABA	Gamma-aminobutyric acid
GAD1	Glutamate Decarboxylase 1
GC	Granule cell
GCL	Granule cell layer
GFAP	Glial Fibrillary Acidic Protein
HICAP	Hilar commissural-associational pathway related cells
HIP	Hippocampal formation
HIPP	Hilar perforant path-associated cell
HSB	Homo sapiens brain
ICP	Intracardiac perfusion
IHC	Immunohistochemistry
IL	Immunolabeled
InN	Inhibitory neuron
IPC	Posterior inferior parietal cortex
IT	Intratelencephalic
ITC	Inferior temporal cortex
KEGG	Kyoto Encyclopedia of Genes and Genomes
LAMP5	Lysosomal Associated Membrane Protein Family Member 5
LC/MS-MS	Liquid Chromatography with tandem mass spectrometry

LD	Lipid droplet
LPAR1	Lysophosphatidic Acid Receptor 1
LRP1	LDL Receptor Related Protein 1
M	Male
M1C	Primary motor cortex
MA	Myelinated axon
Macro	Macrophage
MC	Mossy cell
MD	Mediodorsal nucleus of the thalamus
MEIS2	Meis Homeobox 2
METTL7B	Methyltransferase-like 7B
MFC	Medial prefrontal cortex
Micro	Microglia
MKI67	Marker Of Proliferation Ki-67
MTG	Middle temporal gyrus
MTL	Medial temporal lobe
Myelo	Myeloid cell
NADPH	Nicotinamide adenine dinucleotide phosphate
NAE1	NEDD8 Activating Enzyme E1 Subunit 1
NB	Neuroblast
NCBI	National Center for Biotechnology Information
NEUROD	Neuronal Differentiation
NIH	National Institute of Health
nIPC	Neural intermediate progenitor cells
NNC	Non-neuronal cell
NSC	Neural stem cells
OFC	Orbital prefrontal cortex
OLIG2	Oligodendrocyte Transcription Factor 2
Oligo	Oligodendrocyte
OPC	Oligodendrocyte progenitor cell
P2RX2	Purinergic Receptor P2X 2
PC	Pericyte

PCA	Principal component analysis
PDGFD	Platelet Derived Growth Factor D
PDGFRA	Platelet Derived Growth Factor Receptor Alpha
PDLIM5	PDZ And LIM Domain 5
PFA	Paraformaldehyde
PFC	Prefrontal cortex
PMI	Post-mortem interval
PROX1	Prospero Homeobox 1
PSA-NCAM	Polysialylated-neural cell adhesion molecule
PVALB	Parvalbumin
Pyr	Pyramidal
RELN	Reelin
RGL	Radial glial cell
RMB	Rhesus macaque brain
RNA	Ribonucleic acid
RNA-seq	Ribonucleic acid sequencing
ROBO1	Roundabout Guidance Receptor 1
RTN3	Reticulon 3
RTN4/NOGO	Reticulon 4
S1C	Primary sensory cortex
SAINT	Significance Analysis of INTeractome
SAM	S-Adenosyl methionine
SEMA3C	Semaphorin 3C
SGCZ	Sarcoglycan Zeta
SGZ	Subgranular zone
SHISAL2B	Shisa Like 2B
SLC17A7	Solute Carrier Family 17 Member 7
SNARE	Soluble N-ethylmaleimide-sensitive factor attachment protein receptor
SNN	Shared nearest neighbors
snRNA-seq	Single-nucleus RNA sequencing
SST	Somatostatin
ST8SIA2	ST8 Alpha-N-Acetyl-Neuraminide Alpha-2,8-Sialyltransferase 2

STC	Superior temporal cortex
STR	Striatum
Sub	Subiculum
T	T cell
THEMIS	Thymocyte Selection Associated
TLE4	TLE Family Member 4, Transcriptional Corepressor
TOP2A	DNA Topoisomerase II Alpha
tr	Technical replicate
UCSC	University of California, Santa Cruz
UMAP	Uniform Manifold Approximation and Projection
UMB	The University of Maryland Brain and Tissue Bank
UMI	Unique Molecular Identifier
V1C	Primary visual cortex
VAS	Vasculature
VFC	Ventrolateral prefrontal cortex
VIP	Vasoactive intestinal peptide
VLMC	Vascular and leptomeningeal cell
vSMC	Venous smooth muscle cell
WMA	World Medical Association
Y	Year

Table of Contents

1. Introduction

The hippocampal formation (HIP) and entorhinal cortex (EC) in the medial temporal lobe, further referred to in the text as the hippocampal system, are major components in memory formation and representation of space and time (1-3). The border between the hippocampal formation and the entorhinal cortex, the subicular complex, is also the transition between a three-layered archicortex and a six-layered neocortex, which contain structurally and functionally diverse circuits and cell types (1, 3-5). Another unique feature of this medial temporal system is persistent adult neurogenesis of excitatory granule neuron cells in the hippocampal dentate gyrus in many analyzed mammals (6), however, to what extent remains controversial.

1.1 Anatomy and localization of the hippocampal system

The hippocampal formation is one of the key structures of the limbic system – a network of cortical and subcortical structures important for emotional responses, learning, and memory (7-9). The hippocampal formation is a bilateral structure located deep within the medial part of the temporal lobe. It lies on the floor of the inferior (temporal) horn of the lateral ventricle, bordered laterally by the collateral eminence and medially by the fimbria and tela choroidea from which choroid plexus arises and covers most of its surface (1, 10-12). Dorsally, the hippocampal formation faces the roof of the inferior horn of the lateral ventricle, formed mainly by the tapetum of corpus callosum, the tail of the caudate nucleus, and the stria terminalis. Medially, it faces the transverse fissure, the lateral extension of the ambient cistern.

The hippocampal formation consists of three structures: the dentate gyrus, *cornu ammonis* (CA; i.e., hippocampus proper), and the subiculum (Figure 1.1) (11, 13). On gross dissection, the structures look like two "C" shapes interlocked together and resemble a seahorse. This resemblance inspired the term "hippocampus", derived from the Greek for "seahorse" (11). During development, the dentate gyrus and *cornu ammonis* roll up into the inferior horn of the lateral ventricle at the level of the hippocampal sulcus (14). On coronal sections, this area resembles ram's horns and is named *cornu ammonis* or "Ammon's horn" after the mythological Egyptian god with ram's head (1, 14). The *cornu ammonis* is a collection of sequential fields (CA4, CA3, CA2, CA1) with the CA4 field adjacent to the hilus of the dentate gyrus and the CA1 field bordering the subiculum. The hippocampal formation is continuous with dorsal aspects of the parahippocampal gyrus (i.e., perirhinal, entorhinal, and

parahippocampal cortices) which extends medially towards the midbrain and ends in a bulblike protrusion – the uncus (1, 10, 11, 15).

The surface of the hippocampal formation is covered by a thin layer of axons (the alveus) which continues medially as the fimbria on each side and joins together in the midline of the brain beneath the splenium of corpus callosum as the body of the fornix (1, 10-12). Some fibers cross medially and project to contralateral hippocampus (hippocampal commissure). The body of the fornix continues anteriorly and separates into right and left columns near the interventricular foramen of Monroe. The columns divide again near the anterior commissure into the anterior and posterior columns. The posterior columns of the fornix (postcommisural fornix) continue to the mamillary bodies and anterior nuclei of thalamus. The anterior columns (precommisural fornix) terminate at the septal nuclei of the basal forebrain and nucleus accumbens (10). The fornix is the main output of hippocampal information and also carries afferent fibers from septal and hypothalamic nuclei (10, 16).

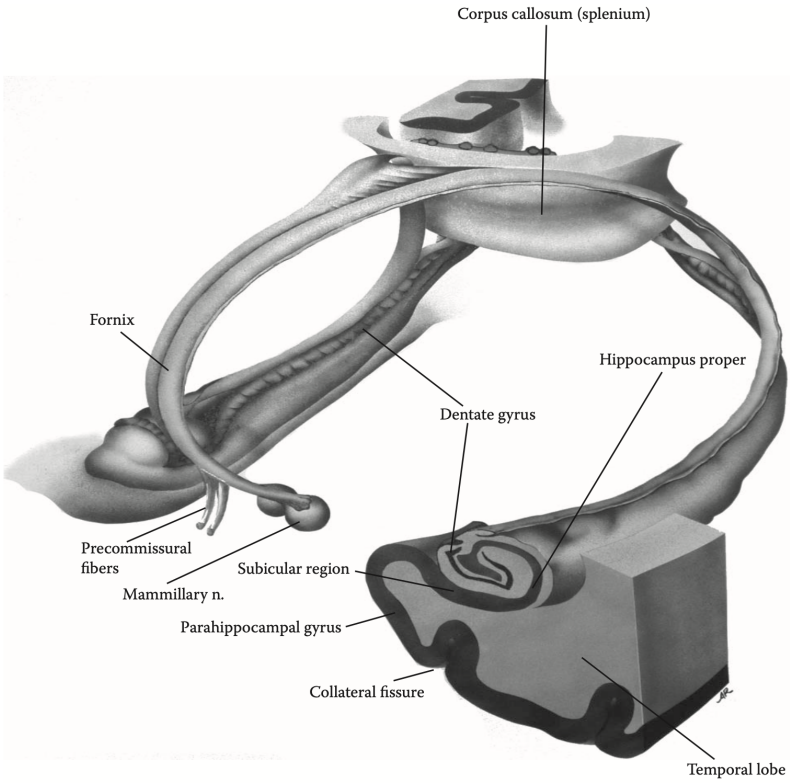

Figure 1. 1 Anatomy of the human hippocampal system
Source: Adapted from (11).

1.2 Cytoarchitecture of the hippocampal system

The hippocampal formation belongs to the phylogenetically older cortex, allocortex, that consists of three layers and can be subdivided into the archicortex (i.e., the dentate gyrus, *cornu ammonis*, subiculum) and the paleocortex (i.e., primary olfactory areas) (17, 18). The mesocortex represents a gradual transition from a three-layered allocortex to six-layered isocortex. It has three to six layers and is comprised if the periallocortex (i.e., presubiculum, parasubiculum, entorhinal and perirhinal cortices) and the proisocortex.

The dentate gyrus is a three-layered archicortical area (Figure 1.2). The outermost layer, named superficial molecular layer, is relatively cell free and contains the apical dendrites of granule cells and a variety of extrinsic terminals, predominantly from the perforate pathway (1, 19). It can be further subdivided into 3 bands in respect to the distribution of terminals (19). Although the layer is mostly cell-poor, at least two types of neurons can be found here: molecular layer perforant path-associated cells and GABAergic chandelier cells or axo-axonic cells (19-21).

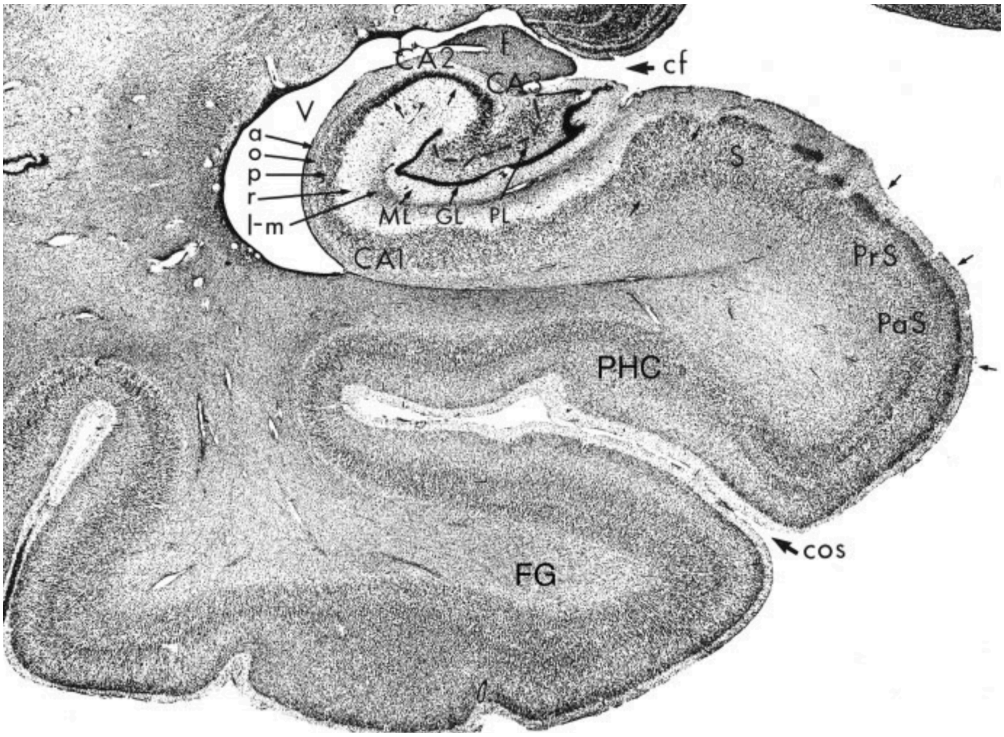

Figure 1.2 Nissl-stained coronal section through the human hippocampal system. CA, *Cornu Ammonis*; Layers of the dentate gyrus: ML, molecular layer; GL, granule cell layer; PL, polymorphic cell layer; Layers of the hippocampus (panel C): a, alveus; o, stratum oriens; p, pyramidal cell layer; r, stratum radiatum; l-m, stratum lacunosum- moleculare; S, Subiculum; PaS, Parasubiculum; PrS, Presubiculum PHC, parahippocampal cortex with entorhinal cortex; FG, Fusiform gyrus; cf, choroidal fissure; cos, collateral sulcus
Source: Adapted from (22).

Below the superficial molecular layer is the principal cell layer or the granule cell layer. Together, the two layers form “fascia dentata”, a U- or V- shaped structure that encloses the third dentate gyrus layer, the polymorphic cell layer. The two blades of the fascia dentata, the suprapyramidal and infrapyramidal blade, are oriented toward the CA fields and the hippocampal fissure, respectively, and are bridged together by the crest. The granule cell layer is comprised mostly of densely packed granule cells. These cells have large arborizations of spiny apical dendrites that extend through the molecular cell layer and end near the border with the hippocampal fissure. They give rise to the unmyelinated mossy fibers and synapse with the mossy cells in the polymorphic layer and pyramidal neurons in the CA3 field of the hippocampus (19, 23, 24). Pyramidal basket cells, a type of inhibitory interneurons, are typically found along the border between the granule cell layer and the polymorphic cell layer. These GABAergic cells extend a single nonspiny apical dendrite that arborizes in the molecular cell layer and have multiple basal dendrites that ramify and extend into the polymorphic cell layer. They synapse with granule cells and form a dense network of inhibitory connections (13, 19, 25, 26). Within the polymorphic layer, the most abundant neurons are triangular or multipolar shaped mossy cells with complex large spines on proximal dendrites named thorny excrescences. These excitatory cells innervate interneurons and have reciprocal connections with granule cells (19, 27). Furthermore, several types of fusiform cells in the polymorphic layer can be distinguished by the presence, shape and size of the spines, such as hilar perforant path-associated cell (HIPP) and hilar commissural-associational pathway related cells (HICAP) (19, 20, 28, 29). Presumably inhibitory, HIPP cells have abundant, branched out spines, give rise to axons to the outer two thirds of the molecular layer, and synapse with dendrites of granule cells. HICAP cells are multipolar or triangular shaped cells with aspiny dendrites and axons that extend through the granule cell layer and terminate in the inner third of the molecular layer. In addition, a number of other neurochemically distinct neurons can be distinguished in the dentate gyrus, such as complex spike cells and theta cells which excite with respect to the theta rhythm (30, 31).

The laminar organization of the *cornu ammonis* is more complex than in the dentate gyrus and is similar across all hippocampal fields but with some distinct differences (29). The pyramidal cell layer is the principal layer in all fields, however, the pyramidal cells in the CA3 and CA2 fields are larger in size and less densely packed than those in the CA1 field. They also show more heterogeneity in dendritic organization compared to the CA1 field (1, 32). The CA3 pyramidal cells receive input from the dentate gyrus granule cells via the mossy fibers. In the proximal portion of the CA3 field, the mossy fibers also terminate within and below the

pyramidal cell layer and we can distinguish three bundles: supra-, intra-, and infra- pyramidal bundle. Comparable to the CA3 field, the CA2 field contains large pyramidal cells that are not seen in the CA1 field but, similar to the CA1 field, they do not receive mossy fiber innervation (1). The CA1 field is characterized by smaller, more densely packed pyramidal cells and Schaffer collaterals from the CA3 field. It gives rise to topographically organized projection to the subiculum and to deep layers of the entorhinal cortex (1, 33). Superficial to the pyramidal cell layer is the stratum lucidum, a thin layer with the mossy fiber projections only seen in the CA3 field (33-36). Stratum radiatum lies directly above the stratum lucidum in the CA3 field and above the pyramidal cell layer in the CA2 and CA1 fields. It contains CA3 to CA3 associational connections and Schaffer collaterals travelling to the CA1 field. The most superficial hippocampal layer is the stratum lacunosum-moleculare with the entorhinal and thalamic afferents as well as a mixture of interneurons. Below the pyramidal cell layer is a cell-poor layer, the stratum oriens, with several types of interneurons and the basal dendrites of the pyramidal cells. Below the stratum oriens is a fiber-rich alveus carrying myelinated afferent and efferent fibers that eventually aggregate and form fimbria of the fornix (1).

The subiculum is an archicortical area adjacent to the CA1 field. The border between the two areas is marked by abrupt ending of the Schaffer collaterals (1, 37). The molecular layer of the subiculum is continuous with the stratum radiatum and stratum lacunosum-moleculare of the CA1 field and split into the deep and superficial portions that receive inputs from the CA1 field and the entorhinal cortex, respectively (1, 38). The principal cell layer is the pyramidal layer with large pyramidal neurons that extend dendrites into the molecular layer and the deeper parts of the pyramidal layer. At least two types of projection neurons can be distinguished based on their excitation characteristics and the neurochemical phenotype: regular spiking cells (NADPH-diaphorase/nitric oxide synthetase-positive) found superficially in the pyramidal layer and intrinsically bursting cells (somatostatin-positive) situated more in the deeper portions of the pyramidal layer (1, 37). The polymorphic cell layer lies deep to the pyramidal layer and is continuous with the stratum oriens of the CA1 field (38-40).

Presubiculum, parasubiculum, and the entorhinal cortex are mesocortical areas with progressively more complex laminar organization (1, 41-43). They mark a transition from a single neuronal layer in the allocortex, toward a progressively more complex laminar organization as seen in the neocortex. Although the layers in the periallocortex are labeled in the same way as in the neocortex (layers I-VI), they are not homologous (e.g., cell-free layer IV in the entorhinal cortex vs internal granular layer IV in the neocortex). The main characteristic of the periallocortical laminar organization is a cell free zone “lamina dissecans”

(layer IV) that splits the thickness of the cortex into roughly two equal parts and defines the external layers superficial to the lamina dissecans (lamina principalis externa, layers I-III) and internal layers beneath the lamina dissecans (lamina principalis interna, layers V-VI). In the presubiculum and parasubiculum, layer I is the molecular layer and contains mainly fibers of the perforant pathway. Layers II and III have no clear boundary between them and are comprised of pyramidal and other neurons that are larger in size and more densely packed in layer III than in layer II. Deep to the lamina dissecans are layers V and VI comprised of pyramidal and heterogenous mix of cells, respectively. Layers V and VI have ill-defined boundary and run continuously with deep layers of the entorhinal cortex.

Compared to the presubiculum and subiculum, the laminar organization of the entorhinal cortex is more defined and shows distinct alterations along the rostro-caudal and medio-lateral axis (1, 41-46). Thus, numerous approaches have been applied to subdivide the entorhinal cortex based on the cytoarchitectonic differences, ranging from two (medial and lateral) to 23 subdivisions (41). Using similar criteria as Amaral and colleagues (47) for the nonhuman primate entorhinal cortex, Insausti and colleagues (43) showed that the human entorhinal cortex can similarly be divided into eight subfields: olfactory subfield, lateral rostral subfield, rostral subfield, medial intermediate subfield, intermediate subfield, lateral caudal subfield, caudal subfield, and caudal limiting subfield. The molecular layer of the entorhinal cortex is mostly cell free and contains fibers of the perforant pathway (42). Layer II is comprised of pyramidal cells and large stellate cells clustered in cell islands that bulge out and form characteristic elevations of the cortical surface (i.e., entorhinal verrucae) (48). The verrucae are greatly present in the central part of the entorhinal cortex. Their number and the total area correlate with age and are greatly affected in neurodegenerative diseases, such as Alzheimer's disease, and their size corelates with pathological stage (42, 44, 48, 49). Rostrally, layer III pyramidal neurons are organized in cells clusters separated by cell-free areas though the distribution is more homogenous in the deep portion (42). Toward the caudal level, cells begin to show more radial, columnar organization as seen in the proisocortex. Layer IV (lamina dissecans) is most prominent at the caudal levels, while at other levels, it is invaded by cells from the surrounding areas and has incomplete appearance. Layer V is characterized by larger, darkly stained pyramidal cells that are more prominent in the central parts of the entorhinal cortex where it is also possible to distinguish three bands V_{a-c}. The border between layers V and VI is not always clear. Rostrally, the two layers are fused together while caudally the separation is more distinguishable. Layer VI is a heterogenous layer with cells of various shapes and sizes that rostrally invade the layer V and the subcortical white matter. Laterally,

the entorhinal cortex borders with proisocortex, an incomplete form of neocortex that retains some of the periallocortical characteristics and supports a subtle transition toward the neocortex (42).

1.3 Connectivity of the hippocampal system

The three major fiber bundles of the hippocampal system are the angular bundle, connecting the hippocampal formation with the entorhinal cortex; the fimbria-fornix pathway connecting the hippocampal formation with other cortical and subcortical structures (i.e., the basal forebrain, the hypothalamus, the brain stem); and the dorsal and ventral commissures connecting the contralateral hippocampal formations (1).

The entorhinal cortex is a major gateway between the unimodal and polymodal associational areas and the parahippocampal formation (Figure 1.3) (1). The majority of sensory information from various cortical areas (e.g., prefrontal, temporal, and parietal) is relayed to the entorhinal cortex via the perirhinal and parahippocampal cortices and most of the connection are reciprocal (50, 51). The entorhinal cortex projects to the hippocampal formation via the perforate pathway that originates in the superficial layers of the entorhinal cortex and terminates in all parts of the hippocampal formation (13, 52, 53). Entorhinal layer II neurons project to the to the dentate gyrus and the stratum lacunosum-moleculare of the CA3 field, whereas inputs to the CA1 field and the subiculum originate in layer III (the temporoammonic alvear pathway) (1). Compared to neocortical areas where interregional connections are vastly reciprocal, the majority of intrinsic hippocampal connections are unidirectional (1, 54). The trisynaptic loop of the hippocampus carries information from the entorhinal cortex to DG (first synapse) which processes the information and conveys to the CA3 subfield (second synapse) via the mossy fibers. In turn, the CA3 field projects to the CA1 field via “Shaffer collaterals” (third synapse) and the CA1 field via the subicular complex to the deep layers of the EC. Layers V and VI of the entorhinal cortex project back to various cortical and subcortical structures.

The dentate gyrus also receives minor afferents from the presubiculum and parasubiculum, the septal nuclei, the supramammillary area, and the brainstem areas such as the nucleus locus coeruleus, the raphe nuclei, and the ventral tegmental area (19, 55, 56). The subiculum has strong associational projections and is a major source of hippocampal subcortical projections to the diencephalon and the brain stem via the postcomissural fornix (1, 57, 58). To various degree, the subiculum projects to the prefrontal cortex, amygdala, septal nucleus, nucleus accumbens, the mammillary nuclei, and thalamus.

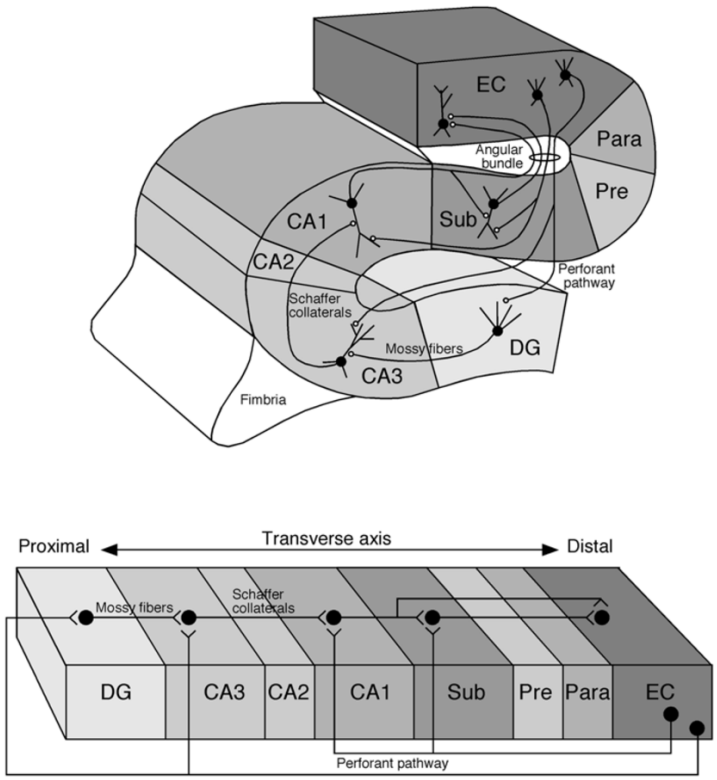

Figure 1. 3 Overview of the hippocampal circuitry. CA = Cornu Ammonis; Sub = subiculum; Para = parasubiculum; Pre = presubiculum; DG = dentate gyrus; EC = entorhinal cortex
Source: Adapted from (1).

1.4 Development of the hippocampal system

The human hippocampal system develops from the hippocampal primordium which undergoes a series of complex and tightly regulated events, including generation and migration of neuronal cells, organization of the axonal projections, synaptogenesis, and programmed cell death (59-62). As in the neocortex, the neuroepithelium located on the surface of the cerebral ventricles gives rise to progenitor cells that produce neuronal and glial precursors (59, 63-66). The newly generated neurons migrate to the surface along the migratory scaffolds in an inside-out fashion before reaching their final destination in the developing cortical plate. During the development, the hippocampal system undergoes progressive rotation with the CA lamina folding into the temporal lobe and forming the hippocampal fissure (67-69). The fissure partially closes as the dentate gyrus lamina rotates under the CA lamina creating an interlocked U-shaped appearance. In contrast to the neocortex, the hippocampal marginal zone is enlarged and rich in cortical and subcortical afferents that synapse with apical dendrites of the pyramidal cells (62). The cellular subtype specification of the newly generated neurons is determined at the time of asymmetrical division and influenced by molecular gradients. Doublecortin (*DCX*)

is an X-linked gene encoding a microtubule binding protein that is highly expressed in migrating neurons and required for proper lamination (70, 71). It has been widely used as a marker of neuroblasts and immature neurons (72-75). Mutations in *DCX* can disrupt neuronal migration and may lead to cognitive and neurological deficits, including lissencephaly in males and double cortex syndrome in females.

1.5 Evolutionary aspects of the hippocampal system

The hippocampal region shows remarkable anatomical and functional homology across species (76-79). The comparative evidence shows that hippocampal homologues are present across vertebrate lineages and share common developmental origin (i.e., dorsomedial pallium) and similar topographic position with respect to the lateral ventricle (77, 79-84). Prominent connections with other cortical regions and evidence of synaptic plasticity suggest that the hippocampal homologues across vertebrates may serve as a site of integration for processed information (13, 76, 77, 79, 85-87). However, despite these similarities, the morphology and cytoarchitectonic landscape exhibit significant differences and do not directly mirror the same subdivisions across vertebrate lineages. Reptiles and mammals, and to less extent birds, are the only vertebrates with clear laminar organization of the cerebral cortex. Compared to mammals, the three-layered reptilian cortex is simpler and can be divided into the medial, dorsal, and lateral segments (77, 88-90). Although it is unclear whether hippocampal homologues exist across all vertebrates, it is thought that the medial and dorsomedial areas of the medial reptilian cortex are homologues to the mammalian dentate gyrus and the hippocampus proper, respectively, and have reciprocal connections with other cortical regions (85, 91, 92).

The cytoarchitectonic differentiation of the allocortex and neocortex occurred early across evolutionary time (78, 80, 91). The six-layered neocortex (isocortex) only appeared as mammals emerged, but it expanded at an exponential rate in some groups, such as Cetartiodactyla and Catarrhini, in parallel with the addition of new functional areas and circuits (93, 94). While the mammalian neocortex underwent extensive changes, the laminar organization of the mammalian allocortex resembles more of a three-layered reptilian cortex, rather than a six-layered mammalian neocortex. Nonetheless, certain evolutionary innovations, such as convolution of the dentate gyrus and its characteristic C- or V-shape that encompasses the hilus, are present in all mammals (except cetaceans) and not seen in reptiles (88, 89 , 95). Similar to phylogenetically older vertebrates, the mammalian allocortex retained a single principal cell layer comprised mainly of excitatory, glutaminergic neurons that share reciprocal connections with the neighboring interneurons and is hypothesized that these excitatory cells

resemble those of the deep layers of the mammalian neocortex (96-99). Compared to rodents, the medial temporal lobe and circuits are greatly expanded in humans and non-human primates and have undergone extensive changes across evolutionary time (6, 95, 100-104). These differences increase along the long axis, from the proximal dentate gyrus toward the distal subiculum, as well as across the mammalian taxon, from rodents to non-human primates to humans. In humans and non-human primates, the longitudinal aspects of the hippocampal system have shifted down the septotemporal axis and the entire hippocampal system is enclosed within the medial temporal lobe (46, 85, 95). The cytoarchitectural characteristics, such as prominent CA2 field of the hippocampal formation and clear border between the CA1 field and the subiculum are more prominent in primates compared to smaller-brained mammals (85). The most striking differences, however, are within the primate entorhinal and neighboring cortical areas which exhibit more complex laminar organization (e.g., clear distinction of layers V and VI) and stronger unimodal and multimodal interconnections (1, 42, 45). In comparison, the macaque entorhinal cortex receives more than two thirds of the neocortical inputs via the perihippocampal and parahippocampal cortices, whereas in rodents this accounts for less than one fourth of the information. Although some of these differences can be accounted by vast direct inputs from the olfactory bulb in rodents, it appears that the hippocampal system in the larger-brain mammals receives more processed information (85, 104, 105). In addition, the complexity is also reflected on a grosser scale, with the rodent entorhinal cortex typically divided into two parts (i.e., the medial and lateral area), and the primate and human entorhinal cortices into 7 and 8 segments, respectively (41, 43, 47).

Interestingly, despite massive differences in size (i.e., the volume the hippocampus is estimated to be about 10 larger in non-human primates compared to rodents and about 100 times larger in humans compared to rodents), the basic circuitry motifs appear to be evolutionarily conserved across the mammalian lineage (1). To what degree human-specific evolutionary changes drive regional features of hippocampal cell types or have functional and disease-related implications remains unknown and necessitates further study of the human hippocampal system.

1.6 Adult neurogenesis in the dentate gyrus

Key features of the hippocampal system may also exhibit substantial differences between species or across subregions or cell types. One such distinctive feature seen in many mammals (except cetaceans) is persistent adult neurogenesis of the granule cells in the dentate gyrus (6). The subgranular zone of the dentate gyrus and the subventricular zone of

the lateral ventricle are considered two main neurogenic areas in the adult mammalian brain. The newly generated cells in the subgranular zone of the dentate gyrus migrate to the granule cell layer and become granule cells (106, 107). Behavioral studies suggest that the generation of new granule cells and their integration in the dentate gyrus is critical for cognitive processes, such as pattern separation and memory formation, and can make up as much as ten percent of the overall granule cell population (108, 109). Pattern separation refers to the process of encoding distinct representations of similar experiences and can be enhanced or impaired by the rate of neurogenesis, suggesting a regenerative potential (6, 106, 109-112). Although neurogenesis of granule cells in the adult dentate gyrus has been best described in rodents, there is also evidence indicating the continuation of neurogenesis in non-human primates, including rhesus macaque, though with considerably lower frequency (113-118). However, whether persistent neurogenesis occurs in the adult human dentate gyrus and its relevance have not been fully resolved. Over the past several decades, multiple attempts and different approaches have been made in an effort to answer that question. While some studies have reported proliferation of neuronal progenitors with the aid of ^{14}C (119) or thymidine analogs, such as bromodeoxyuridine (BrdU) (120), other have reported the presence of cells expressing doublecortin (DCX), a marker of neuroblast cells and immature neurons, as a reliable indicator of adult neurogenesis in the dentate gyrus (72, 73, 75, 121). Consistent with these observations, RNA sequencing of human hippocampal tissue detected *DCX* gene expression throughout the adulthood, though at significantly lower levels than in the developing human or adult non-human primate hippocampus (103, 122, 123). Conversely, many studies have challenged the notion of persistent adult human neurogenesis after unsuccessful attempts to identify neural progenitors or DCX-expressing cells in adult or aging human hippocampus (124-127). Nonetheless, a recent study taking advantage of single cell RNA sequencing delineated the granule cell differentiation trajectory, progressing from the radial glia-like cells, to proliferating neuronal intermediate progenitor cells (nIPCs), to neuroblasts, to immature and mature granule cells, and provided insights into the associated gene expression heterogeneity in mouse developing and adult dentate gyrus (128). Given the potential of this approach, several proposals have been made to apply this technique to the human dentate gyrus to help resolve the controversy (129-133).

1.7 Role of the hippocampal system in memory formation, consolidation, and retrieval

Although there are still controversies in certain aspects of memory acquisition and processing, it is generally accepted that the medial temporal lobe, often referred to as the medial temporal lobe memory system, is critical for the formation, consolidation, and retrieval of declarative or explicit memory, one of the two main types of long-term memory (29, 134-136). Declarative memory refers to conscious recollection of information about facts (semantic) or events (episodic). In contrast to this, implicit or nondeclarative memory is not consciously recalled and is expressed through performance. It allows us to execute certain tasks (e.g., riding a bike, playing a guitar) or primes us to react in a certain way based on prior experiences without being aware of how the past experiences influenced us. Other examples of implicit memory are certain types of classical conditioning (e.g., emotional responses, reflexes involving skeletal musculature) and simple forms of non-associative learning (i.e., habituation, sensitization). Implicit memory is thought to be independent of the medial temporal lobe and processed in other regions of the brain (Figure 1.4).

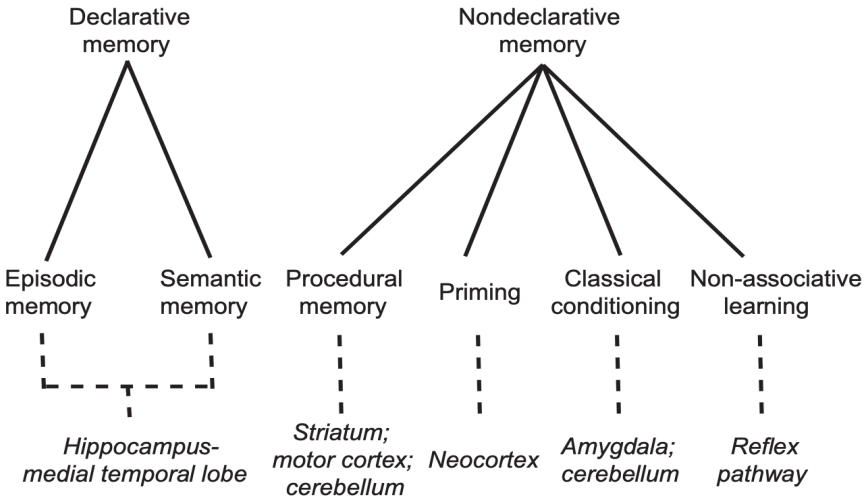

Figure 1.4 Classification of memory and associated brain areas
Source: Adapted from (1).

The areas of the MTL involved in declarative memory are the hippocampal formation (i.e., CA fields, dentate gyrus, subiculum), and the adjacent perirhinal, entorhinal, and parahippocampal cortices that comprise most of the parahippocampal gyrus (137, 138). The entorhinal cortex receives the unimodal and polymodal cortical inputs via the adjacent perirhinal and parahippocampal cortices and converges the information to the hippocampal

formation where it's processed in a series of mostly unidirectional connections and relayed back to the neocortex (1, 137). To what degree individual components of the MTL contribute to memory processing and whether there are functional dichotomies remains elusive (Figure 1.5).

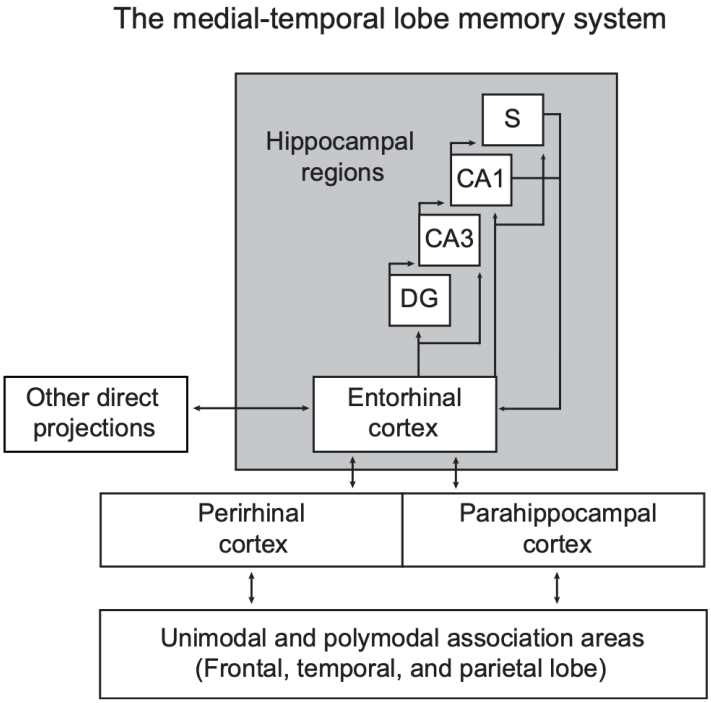

Figure 1.5 Medial temporal lobe memory system
Components of the medial temporal lobe memory system with arrows representing unidirectional or bidirectional flow of information. DG = dentate gyrus; CA = Cornu Ammonis; S = subiculum
Source: Adapted from (1).

The critical role of MTL in memory formation was first described in 1950s with notably the most famous case of patient H.M. who underwent bilateral medial temporal lobe resections in an effort to relieve seizures due to intractable epilepsy (139, 140). Following the surgery, the patient showed profound deficits to acquire long-term memory for new facts or events ("anterograde amnesia") as well as loss of memory preceding several years to surgery ("retrograde amnesia"). His early memories and other types of nondeclarative memory were intact. There was no impairment in personality or general intelligence. Consistent with this, similar deficits were seen in other amnesia patients whenever bilateral lesions extended far enough posteriorly to damage the hippocampal formation and parahippocampal gyrus (140, 141). Likewise, isolated lesions to other areas of MTL, such as amygdala and uncus, did not lead to memory impairment. Injury to MTL produces a temporally graded retrograde amnesia in which memories that have occurred shortly before the injury are more affected than the ones

from the remote past (135, 140). This supports the concept of memory consolidation over time and that the role of the MTL in declarative memory is transient in nature. It is thought that the MTL is only initially required for memory processing and as time passes by memory is consolidated and stored elsewhere, presumably the neocortex. The MTL is not involved in implicit memory nor immediate ("working") memory (142, 143).

1.8 Role of the hippocampal system in representation of space and time

The hippocampal system is essential for establishing cognitive maps, a neural representation of the spatial environment (144-148). This is orchestrated through an interplay of various cell types from all parts of the hippocampal system and several cortical area (147, 149). Place cells are found throughout the hippocampal formation and fire when animal is at a particular location in an environment, known as "place field" (145, 146, 150). Different place cells correspond to different place fields and each environment is represented by a unique combination of place cells that fire correspondingly, enabling encoding and retrieval of maps of different environments. Remapping occurs once an animal encounters a new environment or when landmarks or certain objects change and alter the familiar environment (151). Place fields are organized without apparent topography, however, the size of the field increases from dorsal to ventral hippocampus (149, 151-153). In addition, the firing pattern of place cells can be influenced by visual landmarks and various cues such as, vestibular or olfactory stimuli.

Grid cells are predominantly located in the medial entorhinal cortex (149, 151). They fire in a pattern of repeating triangles (hexagons) spaced throughout the environment and contribute to distance processing (147, 154). Head direction cells are found throughout the limbic system and to lesser degree in the striatum (155, 156). They fire in relation to the position of the head in the horizontal plane of the environment and provide sense of direction (147, 155). Head direction cells are predominately influenced by visual landmarks that are stably represented over time. Border (boundary) cells of the entorhinal cortex and the subiculum discharge when animal is close to a border of the current environment and help establish metric relationships between the place fields and fixed landmarks (148, 149, 157, 158). In addition to spatial processing, certain cells can change their firing rate as a function of time, encoding temporal component of the experiences (148, 159). Collectively, this complex interaction of heterogenous cells throughout the hippocampal system and beyond provides framework for an internal navigational system and presumably adds spatial and temporal context to memories.

1.9 Susceptibility to disease

Certain cell types and circuits in the hippocampal system have been shown to be selectively vulnerable in normal aging (102) and clinical conditions, such as hypoxia-ischemia, intractable temporal lobe epilepsy, and Alzheimer's disease (AD) (102, 160, 161).

AD, which is defined by extracellular aggregation of amyloid-beta (Aβ) peptides in senile plaques and intracellular aggregates of hyperphosphorylated tau protein (neurofibrillary tangles), is a prominent example of selective vulnerability accompanied by neuronal and synaptic loss which progresses in a stereotypical manner (162-169). Pathology is first observed in the allocortex and limbic areas, with the most vulnerable being the mesial temporal cortical regions critical for learning and memory (i.e., entorhinal cortex and hippocampal CA1 field) (170). Pathology then spreads in an anatomically defined pattern to the association areas of the neocortex, whereas the primary motor (M1C), somatosensory sensory (S1C), and visual (V1C) areas are virtually unaffected in the early stages of the disease (171-173). Moreover, within the affected cortical regions, cortico-cortical projection (pyramidal) neurons are selectively vulnerable (102, 171, 172). In contrast, subcerebral projection neurons in the neocortical layer 5B, such as Betz and Meynert neurons in M1C and V1C (102, 171), respectively, as well as the hippocampal dentate granule cells and CA2-4 neurons (174-178) are more resilient. There is also evidence to suggest that AD could have distinct manifestation in humans or primates. Brain regions and circuits affected in AD are greatly expanded in humans and non-human primates (171, 179). Aged macaques and great apes also exhibit AD-like signs of amyloid and tau pathology (180-184). However, the molecular mechanisms controlling Aβ production and providing resilience to AD in a cell type and human/primate-specific manner remain elusive.

2. Hypothesis

There is a significant diversity in the transcriptomic profile of cells in different subregions of the hippocampal-entorhinal system.

3. General and specific aims

3.1 General aim

To survey the transcriptomic diversity and functional specification of the mesial temporal cortex and gain insights into neuronal and non-neuronal populations within this system.

3.2 Specific aims

1. To reveal organizational principles underlying the specialization and function of the mammalian cerebral cortex and refine our understanding of the evolution of allo-, meso-, and neo-cortex.
2. To describe previously uncharacterized cell populations in the hippocampal-entorhinal system.
3. To analyze cells expressing DCX, a marker for immature neurons that is associated with neurogenesis, and determine the degree of neurogenesis in the adult human hippocampus.

4. Materials and methods

4.1 Tissue Sampling

4.1.1 Human, rhesus macaque and pig postmortem tissue

Human samples were obtained from the collections of the Sestan and Rakic laboratories and from Javier DeFelipe's collection in the Instituto Cajal in Madrid (Spain). Rhesus macaque and pig brain specimens were obtained from the tissue collection of the Sestan and Rakic laboratories. All clinical histories, tissue specimens, and histological sections were evaluated to assess for signs of disease, injury, and gross anatomical and histological alterations.

Fresh tissue specimens for histology were fixed with 4% paraformaldehyde/PBS followed by 30% sucrose/PBS. No obvious signs of neuropathological alterations were observed in any of the human, macaque or pig specimens analyzed in this study. The postmortem interval (PMI) was defined as hours between time of death and time when tissue samples were fresh frozen or started to undergo fixation process.

Frozen archival tissue human specimens were used for snRNA-seq. No obvious signs of neuropathological alterations were observed in any of the specimens considered and analyzed in this study. For all other specimens, regions of interest were sampled from frozen tissue slabs or whole specimens stored at -80 ºC. To ensure consistency between specimens, all dissections from the same species were performed by the same person. Frozen tissue slabs were kept on a chilled aluminum plate during dissections. EC and four hippocampal subregions (DG, CA 2-4, CA1, and Sub) were microdissected as previously reported (122) from fresh frozen post-mortem human brains previously cut into 1-cm thick serial, coronal sections, and snap frozen in isopentane (J. T. Baker).

All human (*Homo sapiens*) brain specimens used for snRNA-seq transcriptome and DCX immunostaining (Table 4.1 and 5.3) were de-identified and collected from clinically unremarkable donors and one case that died in status epilepticus. Tissue was collected following the guidelines provided by the Yale Human Investigation Committee (HIC) for the Sestan and Rakic collection or by the European Union for DeFelipe's samples from Spain. Tissue was collected and handled in accordance with ethical guidelines and regulations for the research use of human brain tissue set forth by the NIH (http://bioethics.od.nih.gov/humantissue.html) and the WMA Declaration of Helsinki (http://www.wma.net/en/30publications/10policies/b3/index.html). Appropriate informed

consent was obtained and all available non-identifying information was recorded for each specimen.

The brain tissue samples of Alzheimer disease were sourced from 4 biobanks, with Braak stage II-VI and/or CERAD confirmed neuropathologic diagnosis and the PMI span 8-28 hours (Table 4.2).

All studies using non-human primates and pigs were carried out in accordance with a protocol approved by Yale University's Committee on Animal Research and NIH guidelines. Rhesus macaque (*Macaca mulatta*) brain samples were collected postmortem from 7 adult specimens (Tables 4.1, 5.2, 5.3). Pig brain samples were collected postmortem from 10 young adult specimens (Tables 4.1, 5.2, 5.3).

Table 4.1 Human, macaque and pig specimens used for snRNA-seq

Case	Source	Species	Age (Y)	Sex	# tr	# RGL	# nIPC	# NB	Cause of death	PMI
HSB 628	Yale	Human	50	F	1	0	1	0	Respiratory insufficiency and/or myocardial infarction	19.0 h
HSB 231	Yale	Human	79	F	1	0	0	0	Myocardial infarction	9.0 h
HSB 237	Yale	Human	51	M	1	0	0	0	Myocardial infarction	10.0 h
HSB 179	UMB #5244	Human	48	M	7	0	0	1	Atherosclerotic cardiovascular disease	17.0 h
HSB 181	UMB #5273	Human	44	M	7	0	0	0	Atherosclerotic cardiovascular disease	21.0 h
HSB 282	Yale	Human	48	M	8	0	0	0	Cardiovascular disease, end stage renal failure	18.0 h
RMB1	Yale	Rhesus	9.89	F	1	1	0	12	Euthanasia	≤ 1.0 h
RMB2	Yale	Rhesus	8.56	F	1	0	22	308	Euthanasia	≤ 1.0 h
RMB3	Yale	Rhesus	14.2	F	2	6	1	80	Euthanasia	≤ 1.0 h
p41	Yale	Pig	0.25	F	1	3	0	675	Euthanasia	30 mins, used for cross-species integration
p42	Yale	Pig	0.25	F	1	3	1	525	Euthanasia	30 mins, used for cross-species integration
p43	Yale	Pig	0.25	F	1	2	3	406	Euthanasia	30 mins, used for cross-species integration
p38	Yale	Pig	0.25	F	1	0	0	309	Euthanasia	1 h, used for Figure 5.17C
p39	Yale	Pig	0.25	F	1	0	0	286	Euthanasia	1 h, used for Figure 5.17C
p40	Yale	Pig	0.25	F	1	2	2	861	Euthanasia	1 h, used for Figure 5.17C
p26	Yale	Pig	0.25	F	1	0	2	444	Euthanasia	7 h, used for Figure 5.17C
p32	Yale	Pig	0.25	F	1	2	2	426	Euthanasia	7 h, used for Figure 5.17C
p33	Yale	Pig	0.25	F	1	0	0	340	Euthanasia	7 h, used for Figure 5.17C

Source: Table adapted from (185).

Table 4.2 Human AD tissues used for METTL7B immunostaining

Our ID	Source	Source ID	Age	Sex	PMI	Diag-nosis	Neuropathology
HSB 347	Harvard NIH Biobank	AN 02690	62	M	26.1	CTL	Neurofibrillary degeneration, Braak stage I; Arteriosclerosis
HSB 348	Harvard NIH Biobank	AN 04073	61	F	24.9	CTL	Neurofibrillary degeneration, Braak stage I; Arteriosclerosis
HSB 351	Harvard NIH Biobank	AN 07194	76	F	8.1	CTL	Neurofibrillary degeneration, Braak late stage I; Remote probable tentorial notching of ventral uncus
HSB 180	Yale	HSB 180	42	M	15.0	CTL	No significant abnormalities
HSB 698	Yale	HSB 698	38	M	19.0	CTL	No significant abnormalities
HSB 699	Yale	HSB 699	74	F	2.0	CTL	No significant abnormalities
HSB 355	HBSFRC /UCLA	HSB #3893	79	M	10.0	AD	Alzheimer disease (CERAD)
HSB 410	Miami Brain Bank	HBJV_ 16_HIP P_001	79	M	13.1	AD	Alzheimer disease, Braak stage I-II
HSB 408	Miami Brain Bank	HBJG_ 16_HIP P_001	79	M	9.1	AD	Alzheimer disease, Braak stage VI
HSB 354	HBSFRC /UCLA	HSB 3946	71	M	28.0	AD	Alzheimer disease (CERAD), Braak stage II-III
HSB 409	Miami Brain Bank	HBFF_ 16_HIP P_002	85	M	17.6	AD	Alzheimer disease, Braak stage III

HSB 356	HBSFRC /UCLA	HSB #3829	72	M	15.1	AD	Alzheimer disease (CERAD); No evidence of Lewy body disease
HSB 554	UMB	UMB 5525	89	F	8.0	AD	Alzheimer disease
HSB 358	HBSFRC /UCLA	HSB #3734	76	M	10.8	AD	Alzheimer disease (CERAD); No evidence of Pick disease
HSB 357	HBSFRC /UCLA	HSB #3804	66	M	22.0	AD	Alzheimer disease, (CERAD); Braak stage V; Strokes; Head Injuries; Dementia
HSB 346	Harvard NIH Biobank	AN 00571	62	M	24.06	AD	Alzheimer disease, early Braak stage VI, with amyloidangiopathy; Minor cerebrovascular disease with atherosclerosis and a minute microinfarcts
HSB 349	Harvard NIH Biobank	AN 06938	62	F	13.17	AD	Alzheimer disease, early Braak stage VI, with amyloidangiopathy; Arteriosclerosis
HSB 350	Harvard NIH Biobank	AN 07004	62	M	25.33	AD	Alzheimer disease, Braak stage VI, with amyloid angiopathy; Atherosclerosis and Arteriosclerosis; Moderate autolysis
HSB 352	Harvard NIH Biobank	AN 12317	76	F	21.93	AD	Alzheimer disease Braak stage VI, with amyloid angiopathy; Athero- and arterio-sclerosis
HSB 353	Harvard NIH Biobank	AN 13901	61	M	21.42	AD	Alzheimer disease Braak stage VI.; Difuse Lewy body disease, limbic stage; Arteriosclerosis, mild

Source: Table adapted from (185).

4.1.2 Anatomical definition of sampled subregions of the hippocampal formation and entorhinal cortex

The dentate gyrus (DG) was sampled from the posterior part of the anterior third of the hippocampal formation. It included all three layers: molecular, granular, and polymorphic. The deeper part of the hilus of the DG was dissected as part of the proximal portion (nearer DG) of the CA2-4 region.

Cornu Ammonis (CA) 2-4 region was sampled after DG was dissected and contained the remaining hilus containing CA4 and the proximal hippocampal fields CA3 and CA2 (until approximately the CA1 region), including all three layers: molecular, pyramidal and stratum oriens.

CA1 region (Sommer's sector) was sampled from approximately the border of CA2 to the subiculum, comprising the most distal (from the DG) portion of Cornu Ammonis. The border between CA1 and CA2 is difficult to reliably identify and thus small pieces of the neighboring CA2 and, vice versa, could have been occasionally present in the samples.

The subiculum (Sub) is part of the subicular complex (subiculum, presubiculum and parasubiculum) located between the hippocampus and EC. Our sample was taken adjacent to CA1, corresponding to the subiculum, and was composed of the molecular, pyramidal and polymorphic layers and the superficial region of underlying white matter.

The entorhinal cortex (EC) spreads over both the gyrus ambiens and a considerable part of the parahippocampal gyrus. The EC samples were collected from the middle portion of the parahippocampal gyrus of the same tissue slab used to dissect the subregions of the hippocampal formation, corresponding to the proper entorhinal subregion and Brodmann area 28. The EC was also defined by presence of numerous wart-like elevations (verrucae hippocampi) on the surface of the gyrus. Samples contained all cortical layers and the superficial region of underlying white matter.

4.1.3 Brain cell nuclei isolation

The brain cell nuclei were isolated according to our previous protocol (123, 186) with some modifications. Hippocampal regions (DG, CA1, CA2-4, Sub) and adjacent entorhinal cortex were dissected from six frozen adult human brains (Table 4.1). In order to avoid experimental bias and evenly dissociate the tissue for cell nuclei isolation, whole tissue was finely pulverized to powder in liquid nitrogen with mortar and pestle (Coorstek #60316, #60317). All buffers were ice cold and all reagents used for consequent nuclear isolation were molecular biology grade unless stated otherwise. 5 - 10 mg of pulverized tissue was added into

5 ml of ice-cold lysis buffer consisting of 320 mM sucrose (Sigma #S0389), 5 mM CaCl2 (Sigma #21115), 3 mM Mg(Ace)2 (Sigma #63052), 10mM Tris-HCl (pH 8) (AmericanBio #AB14043), protease inhibitors w/o EDTA (Roche #11836170001), 0.1 mM EDTA (AmericanBio #AB00502), RNAse inhibitor (80U/ml) (Roche #03335402001), 1mM DTT (Sigma #43186), and 0.1% TX-100 (v/v) (Sigma#T8787). DTT, RNAse Protector, protease inhibitors, and TX-100 were added immediately before use. The suspension was transferred to Dounce tissue grinder (15ml volume, Wheaton #357544; autoclaved, RNAse free, ice-cold) and homogenized with loose and tight pestles, 30 cycles each, with constant pressure and without introduction of air. The homogenate was strained through 40 um tube top cell strainer (Corning #352340) which was pre-wetted with 1ml wash buffer: (250 mM sucrose (Sigma #S0389), 25 mM KCl (Sigma #60142), 5mM MgCl2 (Sigma #M1028), 20mM Tris-HCl (pH 7.5) (AmericanBio #AB14043; Sigma #T2413), protease inhibitors w/o EDTA (Roche #11836170001), RNAse inhibitor (80U/ml) (Roche #03335402001), 1mM DTT (Sigma #43186)). Additional 4 ml of wash buffer was added to wash the strainer. Final 10 ml of solution was mixed with 10 ml of 50% Optiprep (Axis-Shield# 1114542) solution (50% iodixanol (v/v), 250 mM sucrose (Sigma #S0389), 25 mM KCl (Sigma #60142), 5mM MgCl2 (Sigma #M1028), 20mM Tris-HCl (pH 7.5) (AmericanBio #AB14043; Sigma #T2413), protease inhibitors w/o EDTA (Roche #11836170001), RNAse inhibitor (80U/ml) (Roche #03335402001), 1mM DTT (Sigma #43186)) by inverting the tube 10x and carefully pipetted into 2 centrifuge tubes (Corning #430791). The tubes were centrifuged at 1000g, for 30 min at 4 ˚C on centrifuge (Eppendorf #5804R) and rotor (Eppendorf #S-4-72). Upon end of centrifugation, the supernatant was carefully and completely removed and total of 5 ml of resuspension buffer (250 mM sucrose (Sigma #S0389), 25 mM KCl (Sigma #60142), 5mM MgCl2 (Sigma #M1028), 20mM Tris-HCl (pH 7.5) (AmericanBio #AB14043; Sigma #T2413), protease inhibitors w/o EDTA (Roche #11836170001), RNAse inhibitor (80U/ml) (Roche #03335402001), 1mM DTT (Sigma #43186)) was added carefully on the pellets in tubes and centrifuged at 1000g, for 10 min at 4 ˚C on the same centrifuge and rotor. Supernatants were then carefully and completely removed, pellets were gently dissolved by adding 100 ul of resuspension buffer (see above) and pipetting 30x with 1ml pipette tip, pooled and filtered through 35 um tube top cell strainer (Corning #352340). Finally, nuclei were counted on hemocytometer and diluted to 1 million/ml with sample-run buffer: 0.1% BSA (Gemini Bio-Products #700-106P), RNAse inhibitor (80U/ml) (Roche#03335402001), 1mM DTT (Sigma #43186) in DPBS (Gibco #14190). Some DG nuclei samples (HSB179, HSB181, HSB282 and RMB3, Table 4.1) were fixed with methanol (American Bio AB#09110). At the

end of nuclei isolation, four volumes of methanol (–20 °C) were added dropwise, while mixing the nuclei suspension (final concentration: 80% methanol). The methanol-fixed nuclei were kept on ice for 15 min and then stored at –80 °C. For rehydration nuclei were placed on ice, centrifuged on the same centrifuge and rotor as above - at 3000g, 10 min at 4 ˚C, resuspended in modified sample-run buffer (1% BSA), centrifuged at 1000g, for 10 min at 4 ˚C, resuspended in sample-run buffer, and prepared for 10x Genomics assay as indicated above.

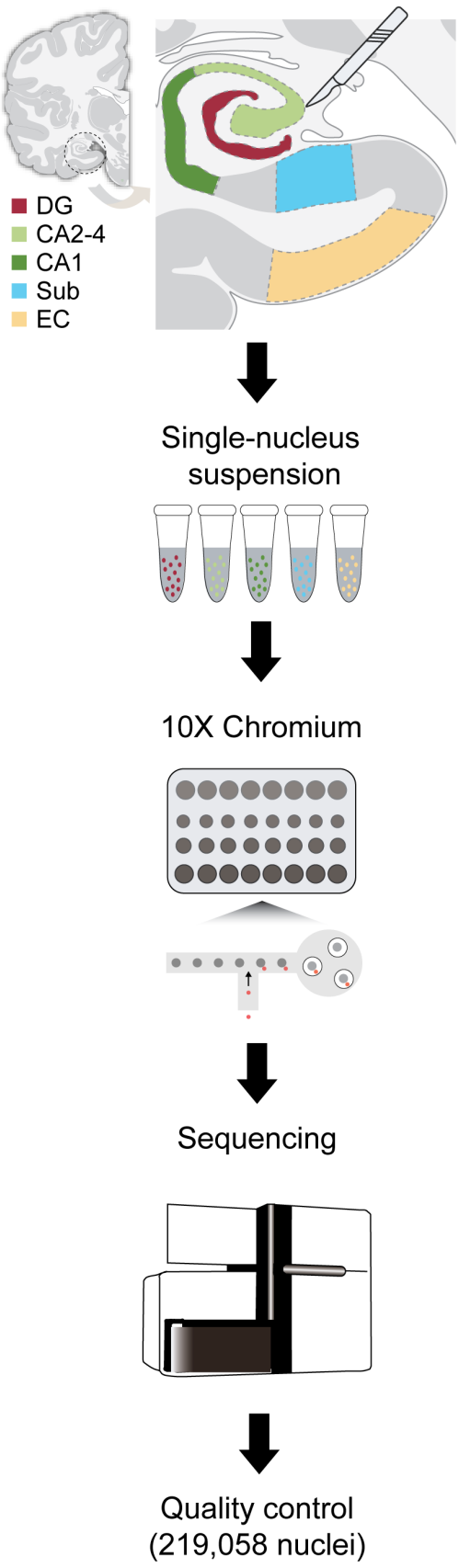

Figure 4.1 Schematic of the analytic workflow
Source: Adapted from (185).

4.2 Histological Analysis

4.2.1 *In situ* hybridization

Human brain tissue samples were fixed in 4% PFA overnight at 4 °C and sectioned at 30 μm using a Leica VT1000 S vibratome. The RNA probes complementary to human *METTL7B* cDNA (NM_152637.2) were labeled with digoxigenin-UTP (Roche). After acetylation, sections were hybridized with the probes at 63 °C for 16 hours. Following hybridization, the riboprobes were immunolabeled with anti-digoxigenin-AP conjugate and the signal was developed with NBT/BCIP overnight in dark.

4.2.2 Immunolabeling and histology

For METTL7B immunohistochemistry (IHC), tissue sections were pretreated with antigen retrieval with citrate buffer pH 6 at 95C for 20 mins, incubated with anti-Mettl7b antibody raised in rabbit (Atlas antibodies HPA038644; RRID:AB_2676130; 1:500) followed by ImmPRES Excel Amplified HRP Polymer Staining Kit (Anti-Rabbit IgG, MP-7601-15, Vector Laboratories) per manufacturer's protocol and using standard biotinylated secondary antibodies followed by Vectastain ABC-AP kit (AK-5000, Vector Labs) and developed with ImmPACT-DAB (SK-4105, Vector labs). For mouse α-β-galactosidase (*lacZ*) stain, tissue sections were blocked with blocking solution (5% normal donkey serum, 1% BSA, 0.1% glycine, 0.1% lysine, and 0.3% Triton X-100 in PBS) for 1 hour and incubated with primary antibodies and biotinylated secondary antibodies. The signal was amplified with Vectastain ABC-AP kit and developed with Vector Blue AP kit (SL-5300, Vector Labs) per manufacturer's protocol. DCX IHC was performed with anti-DCX antibodies raised in guinea pig (EMD Millipore AB2253; RRID:AB_1586992; 1:4000) and antibodies raised in mouse (Santa Cruz sc-271390; RRID:AB_10610966; 1:500). Immunohistochemistry for GAD1 was performed with anti-GAD1 antibody raised in goat (R&D AF2086; RRID:AB_2107724; 1:200) and for PSA-NCAM with antibodies raised in mouse (5A5-s Hybridoma Bank; RRID:AB_528392; 1:500). All antibodies were incubated in 3% normal donkey serum, 0.25% Triton X-100 in PBS). Antigen retrieval (20 mins in citrate buffer pH 6 at 95C) was required for optimal results with DCX and GAD1 antibodies, but not in IHC for PSA-NCAM, as it precludes it to work. Chromogenic antibody detection was achieved with biotinylated secondary antibodies, followed by ABC-AP kit and ImmPACT-DAB as described for Mettl7b. DCX controls were performed in the same way, except the primary antibody was omitted. For colocalization of DCX and GAD1, anti-guinea pig biotinylated secondary antibodies followed

by Streptavidin conjugated (Jackson Immunoresearch) antibodies were used for DCX and anti-goat secondary antibodies (Jackson Immunoresearch) for GAD1. DAPI was used for nuclear staining. All histology samples were imaged on Aperio ScanScope system, Leica microscope, Zeiss Axio Observer with an Apotome 2 system or on a Zeiss LSM 510 confocal microscope. Cell culture samples were fixed with ice-cold 4% paraformaldehyde (PFA) for 10 minutes at room temperature, blocked for 30 minutes at RT with blocking solution (5% normal donkey serum, 1% BSA, 0.1% glycine, 0.1% lysine, and 0.3% saponin in PBS), incubated with primary and appropriate Alexa Flour-conjugated secondary antibodies, and imaged on Zeiss LSM 510 confocal microscope.

4.2.3 IHC labeling for electron microscopy

Rhesus macaque brain (N=3) was fixed with intracardial perfusion of 4% paraformaldehyde and 0.05% glutaraldehyde mixture. Postmortem human brain (N=3) was fixed with immersion in same fixative. For antigen retrieval, vibratome 40-mm-thick slices from the hippocampus and entorhinal cortex were immersed in citrate buffer pH6 at 60ºC during 20 min. Then, slices were blocked in 5% bovine albumin and incubated in rabbit METTL7B (1:500) polyclonal antibodies overnight at room temperature. For immunoperoxidase labeling, the slices were immersed in solution of biotinylated goat anti-rabbit antibodies (Jackson Immunoresearch Inc., West Grove, PA; 1:300) and developed by the Elite ABC kit (Vector Laboratories, Burlingame, CA) with Ni-intensified 3,3'-diaminobenzidine-4HCl as a chromogen and post-fixed with 1% OsO_4. For immunogold labeling, after primary antibodies, slices were blocked in the mixture of 0.8% bovine albumin and 0.1% cold water fish skin gelatin (Aurion, Wageningen, The Netherlands). Then, slices were incubated with goat anti-rabbit IgGs conjugated with 1-nm gold particles (1:80) overnight at 4ºC with subsequent silver intensification in R-Gent SE-LM kit (all from Aurion) and post-fixed with 0.5% OsO_4. Slices were dehydrated and embedded in Durcupan (ACM; Fluka, Buchs, Switzerland) on microscope slides. For electron microscopic investigations, fragments from identified hippocampal zones were re-embedded into Durcupan blocks and cut by Leica UC7 ultramicrotome into 60-nm-thick sections. Ultrathin sections were collected on one-slot grids covered with Butvar B-98 films (EMS, Hatfield, PA), stained with lead citrate, and evaluated in Talos L120C electron microscope.

4.3 RNA / DNA Expression Analysis

4.3.1 Single nucleus microfluidic capture and cDNA synthesis

The nuclei samples were placed on ice and taken either to Yale Center for Genome Analysis core facility or processed in the laboratory within 15 minutes for snRNA-seq with targeted nuclei recovery of 10000 nuclei, respectively, on microfluidic Chromium System (10x Genomics) by following the manufacturer's protocol (10x Genomics, CG000183_Rev_A), with Chromium Single Cell 3′ GEM, Library & Gel Bead Kit v3, (10x Genomics #PN-1000075) and Chromium Single Cell B Chip Kit (10x Genomics #PN-1000074), Chromium i7 Multiplex Kit (10x Genomics #PN-120262) on Chromium Controller (10x Genomics). Due to limitations imposed by source RNA quantity, cDNA from nuclei was amplified for 14 cycles.

4.3.2 Single nucleus RNA-seq library preparation

Post cDNA amplification cleanup and construction of sample-indexed libraries and their amplification followed manufacturer's directions (10x Genomics, CG000183_Rev_A), with the amplification step directly dependent on the quantity of input cDNA.

4.3.3 Sequencing of libraries

In order to reach sequencing depth of 20000 raw reads per nucleus, single nucleus libraries were run using paired end sequencing with single indexing on the HiSeq 4000 platform (Illumina) by following manufacturer's instructions (Illumina; 10x Genomics, CG000183_Rev_A). To avoid lane bias, multiple uniquely indexed samples were mixed and distributed over several lanes.

4.3.4 Single nuclei expression quantification and quality control

We quantified the expression levels of genes in each potential nucleus represented by a cellular barcode using the 10X Genomics CellRanger pipeline (version 3.0.2). For the human samples, reads were mapped to human reference genome GRCh38 (Ensembl release 98) and quantified in units of Unique Molecular Identifiers (UMIs) based on the combined exon-intron human annotation. Same strategies were applied to macaque and pig except that genome assembly Mmul10 and susScr11 was used for rhesus macaque and pig, respectively. Associated NCBI RefSeq gene annotations of pig and rhesus macaque were downloaded from UCSC genome browser. We took advantage of the enhanced cell-calling methodology in CellRanger to distinguish true cells from damaged or empty droplets. Specifically, RNA content

distribution of each barcode was compared to the background concentration which was generalized from extremely low RNA-containing barcodes, and was subsequently classified as damaged if comparable profiles were seen. To further rule out low-quality cells, we excluded nuclei with mitochondrial content greater than 10%. This loose criterion was set as we aimed to incorporate certain cell types into analyses such as endothelial cells which were shown to be prone to high mitochondrial content (187). Additional filtering procedure was performed after clustering and low-dimensional embedding (see below) to eliminate cell clusters collectively displaying elevated mitochondrial and ribosomal gene expression and showing no signals of reasonable cell types.

4.3.5 Plasmids

For expression of *METTL7B*, full length cDNA (NM_152637.2) was inserted into pCAGIG (a gift from Connie Cepko, Addgene #11159) (188). For lentiviral generation, pFUGW (a gift from David Baltimore, Addgene #14883) (189) was digested with PacI, 3' overhangs removed with Klenow (NEB) to form blunt ends, and additionally digested with BsrGI to release hUBC promoter and EGFP. The CAG-IRES-EGFP was removed from pCAGIG and ligated into pFUGW. For protein pulldown experiments, BirA-HA and HaloTag constructs were PCR-amplified from pcDNA3.1-MCS-BirA(R118G)-HA (a gift from Kyle Roux, Addgene #36047) (190) and pHTC-CMVneo-HaloTag (G7711, Promega), respectively, and ligated into pFUGW-CAG.

4.3.6 Lentiviral purification and generation of stable cell lines

Ten 15-cm dishes of sub-confluent Lenti-X 293T cells (Clontech) were used for each purification. pFUGW-CAG specific plasmids (BirA, METTL7B-BirA, HaloTag, METTL7B-HaloTag) along with pMD2.G, pRSVrev and pMDLg/pRRE (a gift from Didier Trono, Addgene #12259, #12253, #12251) (191) were transfected at 1:1:1:1 molar ratio using PolyJet (SignaGen). Cell culture media containing lentiviral particles (LVP) was collected at 48- and 60-hours post-transfection and filtered through 0.2 μm filter to remove cellular debris. Filtered supernatants were centrifuged at 100,000g for 2 hours. One milliliter of PBS was laid over LVP pellet and left overnight at 4 °C. Next day, resuspended pellets were centrifuged through 30% sucrose gradient to further purify the virus. Lentiviral titers were determined by transducing Lenti-X 293T cells and calculating titer from FACS data between 1-10% infection rate using formula: Titer (IU/ml) = (# cells seeded x dilution factor x % GFP-positive cells) / (volume of virus solution added).

For pulldown experiments, 50,000 ReNcell CX (EMD Millipore) cells were plated on a laminin coated 24-well plate in triplicate wells. Cells were transduced with lentiviral particles at MOI of 10 in a 150 μL of cell culture media supplemented with 10 μg/mL of protamine sulfate (#02194729, MP Biomedicals) and saved as ReN-CAG-BirA, ReN-CAG-METTL7B-BirA, ReN-CAG-HaloTag, and ReN-CAG-METTL7B-HaloTag stable cell lines.

4.3.7 RNA isolation and digital droplet PCR

Total RNA was extracted from human and mouse brain tissue samples, or cultured cells, using RNAeasy Plus Mini Kit (#74134, Qiagen) per manufacturer's protocol. RNA concentrations and quality were determined using R6K ScreenTape (#5067-5576, Agilent) and TapeStation analyzer (Agilent). cDNA was synthesized from 1 μg of total RNA using SuperScript III First-Strand Synthesis kit (#18080051, Invitrogen) and random primers. Digital droplet PCR was performed using QX200 Droplet Digital PCR (Bio-Rad) and data was normalized to *TBP* expression. PCR amplification was performed using primer sets and probes listed in Table 4.4.

4.4 Proteomic Analysis

4.4.1 Affinity capture of proteins

For BioID and HaloTag experiments, two million cells (ReN-CAG-BirA, ReN-CAG-METTL7B-Bira, ReN-CAG-HaloTag, ReN-CAG-METTL7B-HaloTag) were plated on four laminin coated 10-cm dishes. BioID pulldown was performed per protocol (192). At near confluency, cell culture media was supplemented with 50 μM biotin (B4639, Sigma-Aldrich). The next day, cells were rinsed twice with PBS, detached with Accutase (Millipore) for 10 minutes at 37 °C, centrifuged at 200 g for 3 minutes, rinsed with PBS, and centrifuged again. Bead-protein conjugates were resuspended in 50 mM ammonium bicarbonate. HaloTag pulldown was performed per manufacturer's protocol (G6500, Promega). Proteins were eluted by resuspending HaloTag resin in 50 μL of 8 M urea prepared in 50 mM ammonium bicarbonate and shaking for 30 minutes at room temperature. Ten percent fractions of BioID and HaloTag eluates were saved for immunoblot and silver stain analysis.

4.4.2 Mass spectrometry and proteomic data analysis

BioID and HaloTag tryptic digestion was performed using the optimized method from the original published method (193). Proteins were reduced by adding 2 μl of 0.5M Tris (2-carboxyethyl) phosphine (TCEP) at 30 °C for 60 min. The reaction was cooled to room temperature (RT) and proteins were alkylated in the dark for 30 min by adding 4 μl of 0.5M Iodoacetamide. Sample volume was adjusted by adding 350 μl of 50 mM Ammonium Bicarbonate to dilute the 8M urea to 1M before trypsin digestion. Mass spectrometry grade trypsin (Promega) was added for overnight digestion at 30°C using Eppendorf Thermomixer at 700 rpm. Formic acid was added to the peptide solution (to 2%), followed by desalting by C18 TopTip (TT10C18.96, PolyLC) and finally dried on a SpeedVac. Tryptic peptides were resuspended in 100 μl of 2% Acetonitrile in 0.1% formic acid. Ten microliters of total tryptic peptides were used in triplicate runs for the 1D LC-MS/MS analysis, consisting of an EASY-nLC 1000 HPLC Acclaim PepMap peptide trap with a 25 cm- 2μm Easy-Spray C18 column, Easy Spray Source, and a Q Exactive Plus mass spectrometer (all from Thermo Fisher Scientific). A 230-min gradient consisting of 5–16%B (100% acetonitrile) in 140 min, 16-28% in 70 min, 28-38% in 10 min, 38-85% in 10 min was used to separate the peptides. The total LC time was 250 min. The Q Exactive Plus was set to scan precursors at 70,000 resolution followed by data-dependent MS/MS at 17,500 resolution of the top 12 precursors.

4.4.3 Immunoblotting and silver stain

Tissue sample preparation: Tissue was lysed in PBS with 0.01% Tween-20 and protease inhibitor cocktail (P-2714, Sigma-Aldrich), and sonicated in two sessions (30 pulses at an output level of 3 using a Microson Ultrasonic Cell Disruptor [Misonix]) with 1-minute rest on ice between sessions. Samples were centrifuged at 14 000 g for 10 minutes at 4 °C. Total protein concentrations were measured by the Bradford assay (#23246, Pierce).

Immunoblotting: Samples were mixed with NuPAGE LDS Loading Buffer (NP0007) supplemented with 50 mM DTT, incubated at 72 °C for 10 minutes, and loaded on 4-12% Bis-Tris gel (NP0321, Thermo Fisher Scientific). Proteins were transferred to a 0.2 μm PVDF membrane (#162-0218, Bio-Rad), blocked with 5% non-fat milk or BSA in 1% TBST buffer, and blotted with appropriate primary and secondary HRP-conjugated antibodies. The signal was developed with SuperSignal West Pico Plus Chemiluminescent Substrate (#34577, Pierce) and visualized on G:BOX Chemi XRQ (Syngene) system.

Silver stain: 5% of HaloTag eluates were prepared as above and electrophoresed on 4-12% Bis-Tris gel. Gel was processed using Silver Stain for Mass Spectrometry kit per manufacturer's instructions (#24600, Pierce).

4.4.4 SAM assay

Custom made recombinant METTL7B was expressed in *E. Coli* ArcticExpress and purified from inclusion bodies by GenScript. Recombinant RTN3, RTN4, LRP1, and APP peptide were purchased directly from vendors. SAMfluoro Methyltransferase Assay (786-431, G-Biosciences) was performed per manufacturer's instructions using ~2 μg of METTL7B and ~1 μg of substrate protein. Recombinant proteins were incubated with or without METTL7B in triplicate wells. Assay was performed at 37 °C and resorufin fluorescence was measured on GloMax Multi Detection System (Promega) plate reader with an excitation wavelength of 530-540 nm and an emission wavelength of 585-595 nm.

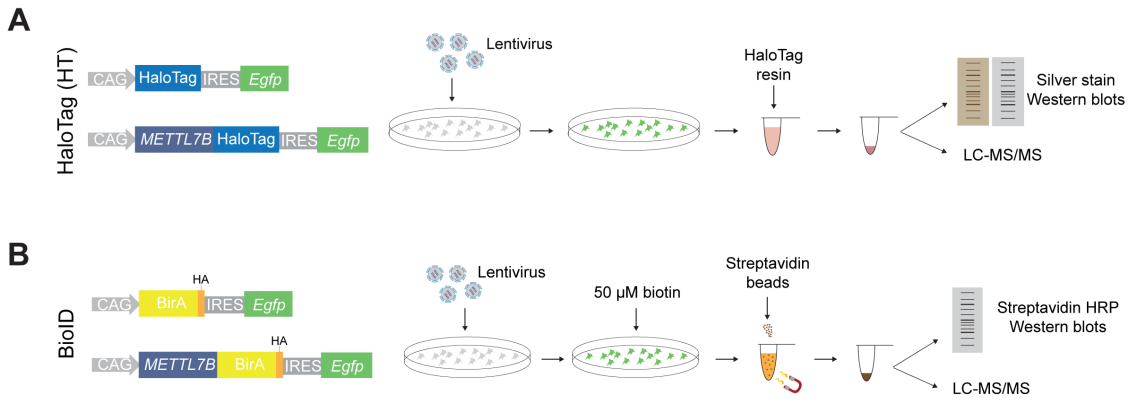

Figure 4.2 Schematic of pulldown design.
(A) Schematic of HaloTag pulldown experimental design.
(B) Schematic of BioID pulldown experimental design.

4.5 Animal Models

4.5.1 Generation of knockout mice and tissue processing

All experiments with mice were performed in accordance with a protocol approved by Yale University's Committee on Animal Research. Targeted embryonic stem (ES) cells (Mettl7b$^{tm1(KOMP)Vlcg}$) were obtained from Knockout Mouse Project (KOMP) repository. Chimeric mice were generated by blastocyst injection of ES cells at Yale Genome Editing Center (YGEC). Mice were bred for germline transmission to generate gene knockout mice. Genotyping was performed using the TUF/TUR primer set (145 bp) for the wild-type allele and the NeoFwd/SD primer set (351 bp) for the *Mettl7b* deletion allele.

Both wild type and *Mettl7b* mutant mice were reared in group housing in a 12h light:12h dark cycle and provided food and water ad libitum with veterinary care provided by Yale Animal Resource Center. Only mice in good, healthy condition, as approved by Yale Animal Resource Center, were used for breeding and experimentation. Multiple breeding pairs were maintained and siblings were never mated to increase genetic diversity, and prevent unintended selection for features that could affect results. Both sexes were used and randomly assigned for all experiments. Adult mice were anesthetized and intracardially perfused with ice-cold PBS and 4% PFA. All mouse brain tissue specimens were fixed by immersion in 4% PFA overnight at 4 °C and sectioned at 50 μm using a vibratome (Leica).

4.6 Statistical Analysis

4.6.1 Normalization, dimensionality reduction and clustering

We normalized the raw UMI counts using the 'NormalizeData' function in the R package Seurat with the scaling factor equal to 10,000 (194). To position all nuclei in a two-dimensional representation reflecting their transcriptomic similarities (Figure 5.1), the top 2,000 highly variable genes were obtained by the Seurat function 'FindVariableFeatures' with the default variance stabilizing process. We further integrated nuclei from a given species on the basis of the summarized anchor features via the function 'IntegrateData' and embedded ensuing nuclei in the PCA dimensions followed by Uniform Manifold Approximation and Projection (UMAP) visualization (195, 196). To cluster nuclei according to their nearest transcriptomic neighbors, we searched for shared nearest neighbors (SNN) in the PCA space with the neighbor number being 25 and optimized the graph modularity using the Seurat function 'FindClusters'. In general, we performed an iterative removal-clustering approach to remove nuclei with high mitochondrial or ribosomal contents and without clear cluster-related markers followed by re-clustering of the remaining nuclei. Moreover, cells and clusters co-expressing combinatory of major cell-type (ExN, InN, Astro, OPC, Oligo, immune and Vas) signatures were manually marked as doublets and excluded from the downstream analytical flow. Lastly, we re-embedded cell types of interest (i.e., ExN, InN and NNC) in the PCA space and re-clustered them using the same procedure as mentioned above, as this would offer finer details into the cell types we sought to probe into.

4.6.2 Tree construction

To explore the taxonomic relationships among all cell subtypes, we constructed a hierarchical tree by first averaging the gene expression levels across cells of the same subtype. The derived expression was standardized to mean of zero and variance of one within each subtype across the anchor genes selected in the previous integration step. Following this step, we calculated the Euclidean distances between pairwise subtypes, and clustered these subtypes in a structured tree (Figure 5.3) by the 'hclust' function in R with the method set to 'ward.D2'.

4.6.3 Relative cell cluster contribution from subregions and donors

Because of the absolute ratio of donors or subregions in each cluster can be biased by the differences of sample size as well as the subregions dissected in each donor, we used relative ratio instead to measure the contribution of donors or subregions to cells clusters.

Specifically, we calculated the absolute ratio of a given cluster in each donor or subregion and divided this ratio by the sum of ratios across all subregions or donors. Results are visualized in Figure 5.3.

4.6.4 Global across-dataset comparison

We performed global comparisons with two previous human HIP single nuclei RNA-seq datasets (197, 198). We calculated the average log-transformed expression of the highly variable genes across all clusters and then performed Pearson correlation to demonstrate the subtype-subtype similarity across datasets, which were further displayed in gradient heat maps (Figures 5.6 and 5.7). Because the annotated neural stem cell cluster in the pioneer HIP data actually represents an ependymal cell cluster (126), we updated the cluster label accordingly.

4.6.5 Classification of cell subtypes in human

We grouped cell clusters with strong signals of *SLC17A7* expression into ExN. Furthermore, we categorized them into different subtypes through marker gene expression and comparisons with published datasets (Figures 5.6 and 5.7) (197-202). Specifically, granule cells were characterized by the predominant composition of DG nuclei and prominent expression of *PROX1*. Mossy cells were described by the principal origin from DG and exclusive expression of *ADCYAP1*. We initially identified three granule cell subtypes characterized by the high expression of *SGCZ*, *PDLIM5* and *EGR1*, respectively. Given that the *EGR1*-expressing subtype is solely contributed by one donor, which are most likely caused by batch effects rather than true biological variations, it was merged to the most similar cluster, *SGCZ*-expressing subtype. ExN from CA fields were arranged mainly according to subfields: CA3 pyramidal neurons (co-expression of *CFAP299* and *SYN3*), CA2 pyramidal neurons (co-expression of *CFAP299* and *HGF*), dorsal CA1 pyramidal neurons (co-expression of *GRIK1* and *GRM3*), and ventral CA1 pyramidal neurons (co-expression of *ACVR1C* and *SYT13*). For the Sub ExN, we categorized them into three subtypes: one distal (away from CA1) (*FN1*+) subtype and two proximal ones (*ROBO1*+). Of note, the spatial registrations of CA and Sub cell subtypes were achieved on the basis of previous transcriptomic studies of hippocampal pyramidal neurons (199, 201, 202). With regards to entorhinal ExN, we classified them by two means. First, we aligned them with ExN from single nucleus data of human MTG using the same procedure as described above. Second, we examined the subtype-specific marker genes in both our ExN and related literature reports. Specifically, two layer 2 subtypes were classified as *RELN*+ and one as *CALB1*+ (45). Other upper-layer subtypes were depicted based on marker

gene expression of *LAMA3*, *PDGFD*, *IL1RAPL2*, and *PCP4* (203-205). The middle-to-deep layer subtypes were delineated by the specific gene expression of *RORB*, *THEMIS*, *ADRA1A*, and *TLE4*.

Cell clusters showing high *GAD1* expression were then assigned as InN. InN clusters were first classified to major groups based on the expression of three canonical function markers (*PVALB*, *SST*, *VIP*) as well as *LAMP5*, a marker mostly representing a group of neurogliaform InN and recently being adopted as a major InN marker (206, 207). For a given cluster expressing two markers simultaneously (e.g., InN *LAMP5 NMBR* cluster expresses both *SST* and *LAMP5*), it was assigned to the same major group of the neighboring cluster in the hierarchical tree. Additionally, we used *LHX6* (a medial ganglionic eminence marker) and *NR2F2* (a caudal ganglionic eminence marker) to classify the rest of the InN clusters which do not express these markers. Finally, each InN cluster was named after the combination of major group marker (eg. *SST*, *VIP*) and one top subtype marker (eg. *ANO2*). Apart from these InN clusters, we also identified a *MEIS2*-expressing InN cluster corresponding to the white-matter residing InN type described before (206, 208) and a neuron cluster co-clustered with InN showing strong signals of *RELN*, *NDNF,* highly indicative of Cajal Retzius cells.

The remaining nuclei were collectively referred to as NNC. We classified these nuclei into four big groups based on marker gene expression of *SOX10* (oligodendrocyte lineage-related cells), *AQP4* (astrocytes), *PTPRC* (immune cells) and *RGS5* (endothelial cells) (Figure 5.12). The first group was further subdivided by the expression of *PDGFRA* (oligodendrocyte precursor cells, OPCs), *GPR17* (committed oligodendrocyte precursor cells, COPs), and *MOBP* (oligodendrocytes). We additionally grouped OPCs and oligodendrocytes into specific subtypes according to the high expression of specific genes: *EGR1* and *GRIA4* for OPCs; *CPXM2*, *SLC5A11*, *LINC01098* and *LAMA2* for oligodendrocytes. For astrocyte subtype specification, we classified them by the laminar distribution: *GFAP*+ ones located in deep layers and *CHRDL1*+ ones in upper layers (209). Regarding immune cells, we used marker genes *C1QB*, *F13A1*, *LYZ* and *SKAP1* to deconstruct them into microglia, macrophages, myeloid cells and T cells, respectively. Microglia were further subdivided via specific gene expression of *P2RY12* and *CD83*. In terms of vasculature lineage, we employed combinational expression of genes to sort them into arterial endothelial cells (*DKK2*+), endothelial cells (*CLDN5*+ and *VWF*+), pericytes (*CLDN5*+ and *ABCC9*+), venous smooth muscle cells (*ABCC9*+ and *P2RY14*+), arterial smooth muscle cells (*ACTA2*+ and *TAGLN*+) and vascular and leptomeningeal cells (*COL1A2*+ and *COL1A1*+) (210).

Most of clusters identified are shared across donors while certain exhibited minimal or even no representation in some of the donors (Figure 5.2). Among those disproportionally distributed clusters, two clusters, CR *RELN NDNF* and InN *SST NPY*, only account for 0.01%-0.02% of the cell population and were more prone to show disproportional distribution. Another interneuron subtype "InN *PVALB PLCL1*", which exhibits certain level of depletion in HIP as compared to EC (Figure 5.3), is also absent in a donor where only DG region was dissected. All the EC ExN subtypes were exclusively contributed by EC and were missing in the donors where only DG regions were dissected. Additionally, we observed one cluster "T *SKAP1 CD247*" absent in one donor, probably reflecting variations of immune response across donors.

Table 4.3 Cell type classification

Cell type	Genes	References
Excitatory neurons (ExN)	***SLC17A7***	(45, 185, 197-205)
Granule cells (GC)	*PROX1* Subtypes (*SGCZ, PDLIM5 and EGR1*)	
Mossy cells	*ADCYAP1*	
CA3	*CFAP299* and *SYN3*	
CA2	*CFAP299* and *HGF*	
CA1	Dorsal *(GRIK1* and *GRM3)* Ventral *(ACVR1C* and *SYT13)*	
Subiculum	Distal (*FN1*) Proximal (*ROBO1*)	
Entorhinal	Layer II (*RELN, CALB1*) Upper non-layer II (*LAMA3, PDGFD, IL1RAPL2,* and *PCP4*) Middle-to-deep (*RORB, THEMIS, ADRA1A, and TLE4*)	
Inhibitory neurons (InN)	***GAD1, PVALB, SST, VIP***	(185, 197-202, 206-208)
Medial ganglionic eminence	*LHX6*	
Caudal ganglionic eminence	*NR2F2*	
White-matter	*MEIS2*	
Cajal Retzius cells	*RELN, NDNF*	
Non-neuronal cells (NNC)		(185, 197-202, 209, 210)
Oligodendrocyte lineage-related cells	*SOX10*	
Oligodendrocyte precursor cells (OPCs)	*PDGFRA, EGR1 and GRIA4*	
Committed oligodendrocyte precursor cells (COPs)	*GPR17, CPXM2, SLC5A11, LINC01098 and LAMA2*	
Astrocytes	*AQP4* Upper layers (*CHRDL1*) *Deep layers (GFAP)*	

Non-neuronal cells (NNC) continued…		
Oligodendrocytes	*MOBP*	(185, 197-202, 209, 210)
Immune cells	*PTPRC*	
Microglia	*C1QB, P2RY12* and *CD83*	
Macrophages	*F13A1*	
Myeloid cells	*LYZ*	
T cells	*SKAP1*	
Endothelial cells	*RGS5, CLDN5* and *VWF*	
Arterial endothelial cells	*DKK2*	
Pericytes	*CLDN5* and *ABCC9*	
Venous smooth muscle cells	*ABCC9* and *P2RY14*	
Arterial smooth muscle cells	*ACTA2* and *TAGLN*	
Vascular and leptomeningeal cells	*COL1A2* and *COL1A1*	

4.6.6 Classification of cell types in pig and rhesus macaque

The cell identity classification of pig and macaque were carried out using the same procedures as described above with a few exceptions. The annotation of nIPC and neuroblast was based on two criteria, expression of canonical cell type markers (nIPC: *MKI67*, *CENPF*, *TOP2A*; neuroblast: *DCX*, *CALB2*, *PROX1*) and clustering with mouse progenitors and neuroblast cells when integrated with mouse data. Due to the scarcity of RGL cells in pig and rhesus and their transcriptomic similarity to astrocytes, we classified those pig and macaque cells co-clustered with mouse RGL cluster as RGL cells. In total, we identified 8 and 7 RGL cells in pig (30 minutes PMI) and macaque, respectively.

4.6.7 Classification of cell types in fetal human hippocampus

Fetal human hippocampus cells (211) were further subclustered using the same procedure described above to separate granule cell and pyramidal neuron differentiation lineages. Neural intermediate progenitor cells (nIPCs) were classified as $SOX2^{+}EOMES^{+}NEUROG1^{+}$ and radial glia cells were annotated as $SOX2^{+}PAX6^{+}VIM^{high}OLIG2^{low}EOMES^{-}$. Neuroblast cells were identified via the combinatory expression of *DCX* and *NHLH1*. Separation of DG versus non-DG ExN lineage was based on the expression of *MEIS2* (non-DG lineage) and *PROX1* (DG lineage).

4.6.8 Integrate dentate gyrus data across species and developmental stages

We used the same Seurat integration pipelines to integrate the DG data from mouse (128), pig, rhesus macaque and human. Young adult mouse data referred to P120-P132 period of the dataset C in the original data and juvenile mouse data (P12-P35) referred to the dataset A (128). Importantly, variable features were first selected via the Seurat function 'FindVariableFeatures' with the default variance stabilizing process for each sample and the union of highly variable genes were set as the anchor features for data integration. To more rigorously identify putative human nIPCs and neuroblasts, we applied pairwise integration between human and each of other species using both Seurat (212) and Harmony (213) harnessing the union of highly variable genes of each species pair. Here, for simplicity, we only used pig hippocampus data at 30 minutes postmortem interval for the four-species integration (Figures 5.9 and 5.11). Same integration pipelines were applied for the integration including human doublets (Figure 5.15B-C) as well as the integration between fetal and adult human data (Figures 5.15 and 5.16).

4.6.9 RNA velocity analysis for mouse, pig, rhesus macaque and human

We first applied velocyto (214) to count the abundances of un-spliced and spliced transcripts using the bam output of CellRanger in pig, rhesus macaque and human. With regard to the mouse data (128), because of the incompatibility of public sequencing files with Cellranger input, we reperformed the read alignment and UMI counting using STARsolo (215), a tool performing similar preprocessing analysis to CellRanger, and passed the bam files to velocyto package. We then applied scVelo (216) to find variable genes, calculated RNA velocities via dynamical models and visualized the velocities on the UMAP embeddings where four species were integrated together using the Seurat pipelines described above (Figure 5.9B).

4.6.10 Comparison of subtype markers across species and developmental stages

Subtype marker gene calculation was performed separately in each dataset using "FindMarkers" function in Seurat. We used the following strategy to minimize the marker set size bias and extrapolate the subtype similarity. Specifically, for each cluster, we checked the percentage of the top 75 markers (ranked by average fold changes) of species A present in species B markers and the percentage calculated in the reverse direction, which were then averaged to indicate the subtype similarity of the cluster between species A and B (Figure 5.8C).

To get cell-type specific markers that are only enriched in a given cell type, we further retained marker genes with fold changes of expression ratio no less than 1.2 and adjusted p value (Bonferroni correction) no more than 0.01. The top 20 specific markers of each subtype were then visualized in dot plots (Figure 5.10). As there are insufficient RGL cells in pig and rhesus and limited nIPCs in pig, these clusters were not included in the marker analysis.

4.6.11 Expression profiling of *DCX* across species and regions

In order to compare the *DCX* expression across species, we down-sampled all the datasets to a comparable level. Specifically, we calculated the median of the total UMIs of the granule cell subtype in each species and computed a scaling factor using dataset with the lowest depth. We reasoned that granule cell cluster is the best anchor given that it presents in all species with high abundance and it is a crucial part of the granule cell lineage. Then, the UMIs of each cell were subsampled to the level equal to multiplying the original library size by the scaling factor and the generated down-sampled datasets were used for the comparative analysis

including DCX expression (Figures 5.18A and 5.19A and Table 5.1) and enrichment analysis (Figure 5.19B).

4.6.12 Enrichment of neurogenic marker sets in *DCX*-expressing cells

To test whether *DCX*-expressing cells show enriched expression of these neuroblast markers, we compared the area under the curve (AUC) scores of these marker sets (217) in *DCX*-expressing and *DCX*-negative cells using Wilcoxon rank sum test (one-tailed test, Figure 5.19B). Gene expression ranking was first performed in each cell followed by calculation of the enrichment of the given marker set using AUC scores. Because expression ranking rather than expression level was used, the calculation was less vulnerable to expression units. We also used the down-sampled datasets to further minimize sequencing depth bias. We removed *DCX* gene from each of these marker sets prior to AUC score calculation as the presence of *DCX* in these markers could increase the AUC scores for *DCX*-expressing cells and bias the analysis.

4.6.13 Reanalysis of data from Ayhan et al., 2021

We extracted the relevant cell types from a previous adult human hippocampus snRNA-seq data(198), which includes all the neurons, astrocytes and oligodendrocytes. Then we used the same Seurat integration pipeline described above to integrate the data from multiple batches and visualized the cell on the UMAP layout (Figure 6.1). We were not able to access the cell annotations for the original Gra.Neu.5 cluster, but we found a group of granule cells corresponding to that cluster clearly marked by *LPAR1*, a marker used to label cluster Gra.Neu.5. Since we observed strong expression of all the top oligodendrocyte markers (calculated by FindMarkers function in Seurat) in this cluster (one representative marker is shown in Figure 6.1), we then used AUCell (217) to calculate the AUROC scores of oligodendrocyte markers to test their enrichment in this cluster. Doublet scores were calculated using Scrublet package (218).

4.6.14 Cell subtype comparisons among HIP, EC, MTG and dlPFC

To explore the transcriptomic divergence across HIP, EC, MTG and dlPFC for all cell subtypes, we constructed a network demonstrating the relationships among the subtypes in the four brain regions based on the extent of overlap of their specific marker genes. In detail, in each region we first determined the marker genes of each subtype using the 'FindAllMarkers' function in Seurat. Subsequently, we generated a similarity matrix representing the overlap between marker genes of pairwise subtypes across all regions, followed by the visualization of

this matrix in the form of a network via the R package 'igraph' through the force-directed graphopt algorithm (Figures 5.23B, 5.29B and 5.32B). Especially, for ExN types we displayed their connections in a between-region manner (HIP and EC, EC and MTG, and MTG and dlPFC). To further examine the cell subtype connections across different regions, in each brain region we focused on marker genes detected in at least one subtype and assessed their expression across all subtypes of remaining brain regions visualized in heat maps (Figure 5.25). Additionally, given the upper- and deep-layer marker genes identified in MTG, we calculated the percentages of genes in each subtype of each region where expression was greater than the expression constraint of 40% quantile across all expression values (Figure 5.26A). Furthermore, we evaluated the expression of marker genes from intratelencephalic/intracerebral (IT) neurons and non-IT neurons of MTG in all subtypes of the four regions through first averaging the expression of each gene across cells of the same subtype and then displaying the average values across IT markers/Non-IT markers in scatter plots (Figure 5.26B).

4.6.15 Identifying genes specific to ExN of different regions

In order to identify a list of genes that exhibit enriched expression to a specific region, we first calculated the expression ratio of all the genes across all the ExN subtypes. Stringent criteria were applied to minimize the influence of technical differences across datasets. Specifically, we required the gene to have a maximum expression ratio of 0.3 across all the ExN subtypes in that region and have a minimum of fold change of 2.2 compared to the expression ratios in other regions. We also filtered genes that were prominently expressed in other regions. The region-specific genes were visualized in Figure 5.27 and the hippocampus ExN-specific genes were passed to the below analysis to survey their temporal specificity.

4.6.16 Temporal specificity of the HIP ExN-specific genes in bulk tissue transcriptomic datasets

Gene expression analysis was performed on the PsychENCODE RNA-seq datasets (200). Time periods 3-15 were collapsed into three time groups: prenatal (periods 3-7), early postnatal (periods 8-12), and adult (periods 13-14). We used limma (219) to run a regression that included the time group and brain region, as well as the region-group interactions, as factors. Genes were then ranked by the region-group coefficient differences between HIP and the maximum of other regions (Figure 5.28).

4.6.17 Exclusive markers of cluster InN *SST ADAMTS12*

To find hippocampus-specific transcriptome features in the cluster InN *SST ADAMTS12*, we first sought to confirm the enrichment of this cluster in hippocampus by integrating InN from HIP, EC, MTG and dlPFC using the 'RunHarmony' function in the Harmony R package (Figure 5.28) (213). Following the integration, we identified a set of markers exclusively expressed in this cluster as compared to other interneuron clusters in hippocampus and SST-expressing interneuron clusters in MTG or dlPFC. To do so, we first calculated the markers of InN *SST ADAMTS12* in the hippocampal dataset using "FindMarkers" function in Seurat and removed those identified as marker genes in *SST* subtypes in MTG and dlPFC.

4.6.18 Protein identification and data analysis

The LC-MS/MS raw data of two technical replicates was combined and submitted to Sorcerer Enterprise v.3.5 release (Sage-N Research Inc.) with SEQUEST algorithm as the search program for peptide/protein identification. SEQUEST was set up to search the target-decoy UniProt Human Reviewed (v. March 2015) protein fasta database using trypsin for the enzyme and with the allowance of up to 2 missed cleavages, semi tryptic search, fixed modification of 57 Da for cysteines to account for carboxyamidomethylation and precursor mass tolerance of 50 ppm. Differential search included 226 Da on lysine for biotinylation (BioID samples), 16 Da for methionine oxidation, and 14, 28 and 42 Da on lysine for mono-, di- and tri- methylayion. The search results were viewed, sorted, filtered, and statically analyzed by using comprehensive proteomics data analysis software, Peptide/Protein prophet v.4.02 (ISB) (220). The minimum trans-proteomic pipeline (TPP) probability score for proteins was set to 0.9 to assure very low error (less than FDR 2%) with good sensitivity. The differential spectral count analysis was done by QTools, an open source SBP in-house developed tool for automated differential peptide/protein spectral count analysis (221) and the protein prophet peptide report was utilized to report biotinylated peptides. The LC-MS/MS raw data were also submitted to Integrated Proteomics Pipelines (IP2) Version IP2 v.3 (Integrated Proteomics Applications, Inc.) with ProLuCID algorithm as the search program (222) for peptide/protein identification. ProLuCID search parameters were set up to search the UniProt Human Reviewed (v. March 2015) protein fasta database including reversed protein sequences using trypsin for enzyme with the allowance of up to 2 missed cleavages, semi tryptic search,

fixed modification of 57 Da for cysteines to account for carboxyamidomethylation and precursor mass tolerance of 50 ppm. Differential search included 226 Da on lysine for biotinylation (for BioID samples), 16 Da for methionine oxidation, and 14, 28 and 42 Da on lysine for mono-, di- and tri- methylayion. The search results were viewed, sorted, filtered, and statically analyzed by using DTASelect for proteins to have protein FDR rate of less than 2.5% (223). Differential label-free proteomics data analysis was done by IP2-Census, Protein Identification STAT COMPARE (224) using two technical replicates. This result was a label-free quantification analysis, of duplicate technical data for each sample; using spectral count analysis with t-test and Gene Ontology analysis (225).

4.6.19 Identification of true pulldown proteins based on mass spectrometry spectral counting data

We discriminated true prey-bait interactions from false interactions in the Halotag and BioID pulldowns by using Significance Analysis of INTeractome (SAINT) method (226, 227). Briefly, the SAINT method utilizes MS/MS spectral counting data and models true and false prey-bait interactions as separate Poisson distributions to obtain the probability of a *true* protein-protein interaction based on Bayesian statistical inference. The estimated probability provides a quantitative measure of the confidence of prey-bait interactions such that false interactions can be filtered out in a statistically controlled manner. Upon applying the SAINT method to MS/MS spectral count data available from each pulldown experiment system, we identified 275 (out of 3 cases and 3 controls) and 1795 (3 cases and 3 controls) proteins as true METTL7B interactors from Halotag and BioID pulldowns, respectively, at Bayesian False Discovery Rate (BFDR) of 5%.

4.6.20 Subcellular localization of METTL7B

To characterize subcellular localization of the true METTL7B interactors, we performed fold-enrichment test for major subcellular compartments cataloged in the Human Protein Atlas database (228) and mammalian lipid droplet proteomes (229). Human Protein Atlas provides genome-wide analysis of major subcellular localization information of human proteins based on immunofluorescent stained cells. It consists of 20 main subcellular compartments and 10,003 proteins (www.proteinatlas.org). To make the fold-enrichment test comparable across Human Protein Atlas and the mammalian lipid droplet proteome datasets, we merged the mammalian lipid droplet protein list to Human Protein Atlas dataset as a separate subcellular localization category and used the entire Human Protein Atlas subcellular

localization records uniformly as a null (background) set. We found that 73.8% (203/275) and 77.7% (1384/1795) of true METTL7B interactors from HaloTag and BioID pulldown experiments had matching HGNC gene symbols in Human Protein Atlas. Of the 152 mammalian cytoplasmic lipid proteins (229), 80 proteins had matching HGNC gene symbols in the Human Protein Atlas. Twenty-three (HaloTag) and 37 (BioID) true METTL7B interactors were identified to be among 80 lipid droplet proteins in the Human Protein Atlas database.

4.6.21 Validation of pulldown experiments

We evaluated the performance of SAINT method by benchmarking the true METTL7B interactors against non-redundant physical BioGRID protein-protein interaction network (230). We computed the significance of interactions between proteins from the true METTL7B interactor set and the rest of the proteins (background set) in the protein-protein interaction (PPI) network by using binomial proportions test Z-score as follows (231):

$$Z = \frac{p_1/N_1 - p_2/N_2}{\sqrt{p(1-p)\cdot(1/N_1 + 1/N_2)}} \quad \text{(Eq. 1)}$$

where

p_1 : number of true METTL7B interactors among the adjacent PPI network neighbors of a given protein,

p_2 : number of all the adjacent PPI network neighbors of a given protein,

N_1 : number of the true METTL7B interactors present in the PPI network,

N_2 : number of the all PPI network proteins, and

$p = (p1 + p2)/(N1 + N2)$.

The Z-score thus provides an approximate quantitative measure of how significantly a given protein in the PPI network interacts with the true METTL7B interactors in the immediate neighborhood of the protein-protein interaction network compared to the background proteins in the protein-protein interaction network. We found that the true METTL7B interactors tend to interact much more significantly to each other than to the rest of proteins in the protein-protein interaction network (Wilcoxon rank sum test p-value < 2e-16, data not shown). This indicates that the true METTL7B interactors are significantly clustered and proximal to each other in the protein-protein interaction network as expected.

4.6.22 KEGG pathway enrichment analysis

Towards the assessment of KEGG pathway enrichment, only these 110 high-confidence METTL7B interacting proteins reported by both strategies, were submitted to the online software, i.e., DAVID Bioinformatics Resources 6.8 (232), with the selection of "Homo sapiens" as species background and "KEGG_PATHWAY" as the targeted functional term.

4.6.23 snRNA-seq profiling of human Alzheimer's disease brain middle temporal gyrus

To understand the cellular heterogeneity and disease-associated cellular changes in human AD brain, we performed unbiased massively parallel snRNA-seq with post-mortem frozen human brain tissues of middle temporal gyrus (MTG), a brain cortical region strongly affected by AD. The collection and characteristics of the AD and neurologically intact control brain samples has been described previously (233, 234). From 12 individuals with and without AD, we isolated brain nuclei by sucrose gradient ultracentrifugation, generated single nucleus libraries with 10x Chromium platform (10x Genomics), and sequenced on NovaSeq S4 sequencer (Illumina). We integrated snRNA-seq data of human brains from these 12 individuals of both AD (Braak Stage V/VI, n = 6) and age-matched normal controls (Ctrl, Braak Stage I/II, n = 6) by single nucleus analysis using Seurat (212). After quality control filtering, we profiled and analyzed 64,845 single nucleus transcriptomes, clustered all the cells jointly across the 12 donors that include 6 females and 6 males, and identified and annotated the major cell types of the human brain by interrogating the expression patterns of known gene markers, including neurons (*GRIN1*), excitatory neurons (ExN, *SLC17A7*), inhibitory neurons (InN, *GAD1*), astrocytes (Astro, *AQP4*), microglia (Micro, *ITGAM*), oligodendrocytes (Oligo, *MBP*), oligodendrocyte precursor cells (OPC, *PDGFRA*), and endothelial cells (Endo, *CLDN5*). Full analysis and data will be reported elsewhere (Zhang and Strittmatter, unpublished communication).

4.6.24 Quantification and statistical analysis

Differential gene expression tests, as well as the differential enrichment test of neuroblast markers, were carried out using the *wilcox.test* function implemented in R. This method does not require the assumption of normal distribution, which is appropriate for single cell data, that there is no consensus distribution model established. The related results are shown in Figures 5.10, 5.19B, 5.23B, 5.32A, 5.13, and 5.17B. The regression of gene

expression with factors including time group, brain region, as well as the region-group interactions, were performed via the R package limma (219). The results are shown in Figure 5.29A. The differential test of *METTL7B* expression in AD brains versus control brains was performed using two-tailed Fisher's exact test (Fig. 5.48B-C)

In the proteomic data analysis, we identified true pulldown proteins via Significance Analysis of INTeractome (SAINT) (235), and benchmarked its acquisition using binomial proportions test detailed in a previous study (231). Gene ontology enrichment tests were performed using an online software, DAVID Bioinformatics Resources (232).

Additional statistical tests were applied to test the significance of signal differences in certain biochemical assays using the following methods: differential gene expression tests in ddPCR were carried out using one-way ANOVA with post-hoc Dunnett's adjustment (Figure 5.37C, E); the signal differences in the SAM methyltransferase assay were tested using two-tailed t-test (Figure 5.46F).

4.6.25 Data and code availability

- Supplement of (185) contains transcriptome analysis and proteomic data with analysis. RNA-seq data is deposited at http://www.psychencode.org/, https://biccn.org/data and NCBI dbGAP Accession phs000755.v2.p1. The data can also be interactively visualized at: https://sestanlab.shinyapps.io/hippocampus/.
- All scripts are available at Github repository https://github.com/sestanlab/Hippocampus.

Table 4.4 Reagents and resources

REAGENT or RESOURCE	SOURCE	IDENTIFIER
Antibodies		
a-Streptavidin-Cy3 (1:1000)	BioLegend	Cat#405215
a-Streptavidin-HRP, high sensitivity (1:40,000)	Pierce	Cat#21130
Chicken a-ADFP (1:1000)	Abcam	Cat#ab37516; RRID:AB_722641
Chicken a-BirA (1:1000)	Abcam	Cat#ab14002; RRID:AB_300830
Donkey a-Goat	Jackson ImmunoResearch	Cat#705-225-147; RRID:AB_2307341
Donkey a-Guinea pig IgG (H+L), biotin	Jackson ImmunoResearch	Cat#706-065-148; RRID:AB_2340451
Donkey a-Mouse, Alexa Fluor 555	Invitrogen	Cat#A-31570; RRID:AB_2536180
Donkey a-Rabbit IgG (H+L), biotin	Jackson ImmunoResearch	Cat#711-065-152; RRID:AB_2340593
Donkey a-Rabbit IgG, Alexa Fluor 488	Invitrogen	Cat#A-21206; RRID:AB_2535792
Donkey streptavidin conjugated	Jackson ImmunoResearch	Cat#016-160-084; RRID:AB_2337244
Goat a-Chicken IgY H&L (HRP)	Abcam	Cat#ab97150 RRID:AB_10679811
Goat a-Chicken IgY, Alexa Fluor 647	Invitrogen	Cat#A-21449; RRID:AB_2535866
Goat a-GAD1 (1:200)	R&D	Cat#AF2086; RRID:AB_2107724
Goat a-Rabbit IgG H&L (HRP)	Abcam	Cat#ab97080; RRID:AB_10679808
Guinea pig a-DCX (1:4000)	EMD Millipore	Cat#AB2253; RRID:AB_1586992
Mouse a-DCX (1:500)	Santa Cruz	Cat#sc-271390; RRID:AB_10610966
Mouse a-PSA-NCAM (1:500)	DBSH	Cat#5A5-s; RRID:AB_528392
Mouse a-CALNEXIN (1:50)	Santa Cruz	Cat#sc-23954; RRID:AB_626783

Mouse a-GAPDH (1:2500)	Invitrogen	Cat#MA5-15738-HRP; RRID:AB_2537659
Mouse a-HaloTag (1:1000)	Promega	Cat#G9211; RRID:AB_2688011
Rabbit a-APP (Y188) (1:200 IF, 1:10,000 WB)	Abcam	Cat#ab32136; RRID:AB_2289606
Rabbit a-b-galactosidase (1:500)	Invitrogen	Cat#A-11132; RRID:AB_22153
Rabbit a-CALNEXIN (1:1000)	Cell Signaling	Cat#2679; RRID:AB_2228381
Rabbit a-Lactate Dehydrogenase (1:5000)	Abcam	Cat#ab52488; RRID:AB_2134961
Rabbit a-LRP1 (1:200 IF, 1:1000 WB)	Abcam	Cat#ab92544; RRID:AB_2234877
Rabbit a-METTL7B (1:500 IHC, 1:1000 WB)	Atlas Antibodies	Cat#HPA038644; RRID:AB_2676130
Rabbit a-RTN3 (1:50 IF, 1:1000 WB)	Protein Tech	Cat# 12055-2-AP; RRID:AB_2301357
Rabbit a-RTN4 (NOGO A+B) (1:200 IF, 1:2000 WB)	Abcam	Cat#ab47085; RRID:AB_881718
Vectastain ABC-AP kit	Vector Labs	Cat#AK-5000
Vector Blue AP kit	Vector Labs	Cat#SL-5300
Vectastain Elite ABC-HRP kit	Vector Labs	Cat#PK-6100
CFWS Gelatin	Aurion	Cat#900.033
ImmPRES Excel Amplified HRP Polymer Staining Kit	Vector Labs	Cat#MP-7601-15
R-Gent SE-LM	Aurion	Cat#500.011
Goat-anti-Rabbit IgG (H&L) (gold particles conjugated)	Aurion	Cat#806.011
Durcupan™ ACM	Sigma	Cat#44610
Anti-Digoxigenin-AP, Fab fragments	Roche	Cat#11093274910

Chemicals, peptides, and recombinant proteins		
APP (peptide)	rPeptide	Cat#A-1203-1
LRP1	Abnova	Cat#H00004035-G01
METTL7B (24-244 aa)	GenScript	This paper
RTN3	Antibodies-Online	Cat#ABIN3111137
RTN4	Sino Biological	Cat#13030-H09E
Digoxigenin-UTP	Roche	Cat#11209256910
BsrGI	New England BioLabs	Cat#R0575L
PacI	New England BioLabs	Cat#R0547L
Klenow	New England BioLabs	Cat#M0210M
Trypsin Gold, Mass Spectrometry Grade	Promega	Cat#V5280
PolyJet	SignaGen	Cat#SL100688
Protamine sulfate	MP Biomedicals	Cat#02194729
NBT/BCIP Stock Solution	Roche	Cat# 11681451001
Protector RNase Inhibitor	Roche	Cat#03335402001
cOmplete™, EDTA-free Protease Inhibitor Cocktail	Roche	Cat#11836170001
Optiprep	Axis-Shield	Cat#1114542
Bovine Serum Albumin (BSA), Fraction V— Molecular Biology Grade	Gemini Bio-Products	Cat#700-106P
Critical commercial assays		
Chromium Single Cell 3′ GEM, Library & Gel Bead Kit v3	10x Genomics	Cat#PN-1000075
TMRDirect (1:1000)	Promega	Cat#G2991
HaloTag	Promega	Cat#G6500
C18 TopTip	PolyLC	Cat#TT10C18.96

Chromium Single Cell B Chip Kit	10x Genomics	Cat#PN-1000074
Chromium i7 Multiplex Kit (10x Genomics #PN-120262)	10x Genomics	Cat#PN-120262
Deposited data		
Human adult hippocampus snRNA-seq	This paper	dbGAP Accession phs000755.v2.p1
GRCh38 (Ensembl release 98)	Ensembl, GENCODE	https://www.gencodegenes.org/human/#
Mmul10	UCSC, RefSeq	https://hgdownload.soe.ucsc.edu/goldenPath/rheMac10/bigZips/
susScr11	UCSC, RefSeq	https://hgdownload.soe.ucsc.edu/goldenPath/susScr11/bigZips/
PsychENCODE RNA-seq data	Li et al., 2018	http://www.development.psychencode.org/
Developmental human brain exon array data	Kang et al., 2011	https://hbatlas.org/
Human, chimpanzee and macaque RNA-seq data	Zhu et al., 2018	https://evolution.psychencode.org/
Mammalian brain development RNA-seq data	Cardoso-Moreira et al., 2019	https://apps.kaessmannlab.org/evodevoapp/
Human fetal hippocampus scRNA-seq data	Zhong et al., 2020	GSE131258
Mouse adult hippocampus scRNA-seq data	Hochgerner et al., 2018	GSE95753
Human hippocampus DroNc-seq data	Habib et al., 2017	https://portals.broadinstitute.org/single_cell
Axis-specific human hippocampus snRNA-seq data	Ayhan et al., 2021	https://cells.ucsc.edu/?ds=human-hippo-axis
snRNA-seq data of human Alzheimer's disease brain middle temporal gyrus	NCBI GEO	N/A

snRNA-seq data of human Alzheimer's disease brain prefrontal cortex	Mathys et al., 2019	https://www.synapse.org/#!Synapse:syn18485175
Bulk tissue RNA-seq data of Alzheimer's disease brains	Swarup Lab	http://swaruplab.bio.uci.edu:3838/bulkRNA/
Experimental models: Cell lines		
Targeted embryonic stem (ES) cells Mettl7b$^{tm1(KOMP)Vlcg}$	Knockout Mouse Project (KOMP) repository	https://www.komp.org/redirect.html
ReN-CAG-BirA	This paper	N/A
ReN-CAG-METTL7B-BirA	This paper	N/A
ReN-CAG-HaloTag	This paper	N/A
ReN-CAG-METTL7B-HaloTag	This paper	N/A
Lenti-X 293T cells	Clontech	Cat#632180
ReNcell CX	EMD Millipore	Cat#SCC007 RRID:CVCL_E922
Experimental models: Organisms/strains		
Mettl7b$^{tm1(KOMP)Vlcg}$ Chimeric Mice	Yale Genome Editing Center	https://medicine.yale.edu/compmed/ags/
Oligonucleotides		
Primers for genotyping Mettl7b$^{tm1(KOMP)Vlcg}$ Chimeric Mice	KOMP	**TUF:** 5'-TGCCTCTGCT GACGGTTG-3'; **TUR:** 5'-TCCTCCACACC ATGATAACTTC-3'; **NeoFwd:** 5'-TCATTCTCAGT ATTGTTTTGCC-3'; **SD:** 5'-GGGCCACAT GGTGTAGTTTC-3'
Digital droplet PCR	This paper	Human METTL7B IDT (Hs.Pt.58.39517850)

Digital droplet PCR	This paper	Human TBP IDT (Hs.PT.58v.39858774)
Digital droplet PCR	This paper	Mouse Mettl7b-fwd 5'-GGTCAGGTAAAGCATGAGAGAG-3'
Digital droplet PCR	This paper	Mouse Mettl7b-probe 5'-/56-FAM/CGCTGCAG/ZEN/GGTGAT CATTCATCA/3IABkFQ/-3'
Digital droplet PCR	This paper	Mouse Mettl7b-rev 5'-CAGGGCTTAG CAGTGTAGTTT-3'
Digital droplet PCR	This paper	Mouse Tbp IDT (Mm.PT.39a.22214839)
Recombinant DNA		
METTL7B, cDNA (NM_152637.2)	This paper	Integrated DNA Technologies
pHTC-CMVneo-HaloTag	Promega	Cat#G7711
pMD2.G	Dull et al., 1998	Addgene #12259
pRSVrev	Dull et al., 1998	Addgene #12253
pMDLg/pRRE	Dull et al., 1998	Addgene #12251
pDTET-METTL7B	This paper	N/A
hPKG promoter (M60581.1)	This paper	Integrated DNA Technologies
pCAGIG	Matsuda and Cepko, 2004	Addgene #11159
pFUGW	Lois et al., 2002	Addgene #14883
pcDNA3.1-MCS-BirA(R118G)-HA	Roux et al., 2012	Addgene #36047
pCW57.1	David Root	Addgene #41393
Software and algorithms		
CellRanger v3.0.2	10x Genomics	https://support.10xgenomics.com/single-cell-gene-expression/software/downloads/latest

R version 3.6.1	R project	https://www.r-project.org/
Seurat v3	Stuart et al., 2019	https://satijalab.org/seurat/index.html
Harmony	Korsunsky et al., 2019	https://github.com/immunogenomics/harmony
scrublet	Wolock et al., 2019	https://github.com/swolock/scrublet
AUCell	Aibar et al., 2017	https://github.com/aertslab/AUCell
UMAP	Becht et al., 2018	https://github.com/lmcinnes/umap
limma	Smyth et al., 2005	https://bioconductor.org/packages/release/bioc/html/limma.html
scVelo	Bergen et al., 2020	https://scvelo.readthedocs.io/
velocyto	La Manno et al., 2018	http://velocyto.org/velocyto.py/index.html#
STARsolo	Dobin et al., 2013	https://github.com/alexdobin/STAR/blob/master/docs/STARsolo.md
Shiny	Rstudio	https://www.shinyapps.io/
SEQUEST	Sage-N Research Inc.	http://proteomicsresource.washington.edu/protocols06/sequest.php
Peptide/Protein prophet v.4.02	Nesvizhskii et al., 2003	http://proteinprophet.sourceforge.net/index.html
QTools	Brill et al., 2009	N/A
ProLuCID	Xu et al., 2006	https://www.manula.com/manuals/ip2/ip2/1/en/topic/7-1-prolucid-search-engine
DTASelect	Tabb et al., 2002	https://www.scripps.edu/cravatt/protomap/dtaselect_instructions.html
Census	Park et al., 2008	http://fields.scripps.edu/yates/wp/?page_id=824
Ontologizer	Robinson et al., 2004	http://ontologizer.de/

SAINT	Choi et al., 2011; Teo et al., 2014	http://saint-apms.sourceforge.net/Main.html
DAVID	Huang et al., 2009	https://david.ncifcrf.gov/
Other		
UC7 ultramicrotome	Leica	N/A
Talos L120C TEM	Thermo Fisher Scientific	N/A
EASY-nLC 1000 Liquid Chromatograph	Thermo Fisher Scientific	Cat#LC120
Acclaim™ PepMap™ 100 C18 HPLC Columns	Thermo Fisher Scientific	Cat#164941
Exactive™ Plus Orbitrap Mass Spectrometer	Thermo Fisher Scientific	Cat#IQLAAEGAAPFALGMBCA

Source: Table adapted from (185).

5. Results

Better molecular understanding of the taxonomic diversity of cells in the human hippocampal region would likely provide new critical insights into their heterogeneity, regional and evolutionary divergence, neurogenic capacity, and variable susceptibility to disease. Transcriptomic profiling by single-nucleus RNA-sequencing (snRNA-seq) has enabled molecular characterization of cell types in the adult postmortem human brain (187, 197, 200, 207, 236-240), including innovative profiling of the hippocampus and entorhinal cortex (197, 198, 241, 242). To gain a more systematic and in-depth molecular view of the cellular composition of the hippocampal system, we performed high-coverage snRNA-seq on five anatomically defined hippocampal subregions from postmortem adult human brains. To assess species differences in neurogenesis and cell-types, we also profiled DG cell populations in adult rhesus macaques (*Macaca mulatta*), hippocampal fields from young-adult pigs (*Sus scrofa*), and made cross-comparisons with parallel samples from young-adult mice (*Mus musculus*) (128). Integrated analysis revealed a greatly diverse set of neuronal and non-neuronal cell types, whereas the subsequent histological, proteomic, and biochemical analyses revealed new molecular insights into cellular heterogeneity, adult neurogenic capacity, and important implications for human brain function, evolution, and disease.

This resource is available at https://sestanlab.shinyapps.io/hippocampus/.

5.1 Transcriptomic diversity of cells in the hippocampal system

We profiled five subregions of the human hippocampal system (DG, CA2-4, CA1, subiculum, EC) by using single-nucleus RNA sequencing (snRNA-seq) (Figure 4.1). Samples were dissected from fresh-frozen postmortem brains of clinically and histopathologically unremarkable adult donors of both sexes (4 males and 2 females), spanning ages 44 to 79 (Table 4.1). The average post-mortem interval of samples was 15.6 ± 2.0 h (Table 4.1). After quality control filtering, snRNA-seq yielded 219,058 single-nucleus profiles from all five regions (Figures 4.1, 5.1 and 5.2A–C) which based on marker gene expression corresponded to 69,461 neurons (35.7% ± 4.1%) and 149,597 (64.3% ± 4.1%) non-neuronal cells (NNCs) (Figures 5.1 and 5.2D). Within the neuronal population, we identified 55,888 (77.8% ± 2.8% of all neurons) glutamatergic excitatory neurons (ExN) and 13,542 (22.1% ± 2.8%) GABAergic inhibitory neurons (InN). The ExN to InN ratios differed across the regions (Figure 5.2C).

Iterative clustering revealed 69 transcriptomically unique cell clusters or presumable cell types across all individuals (Figure 5.1). Cell clusters were categorized by their gene

expression patterns and assigned identities corresponding to their predicted cell type, which encompassed 25 excitatory neuron subtypes, 23 inhibitory neuron subtypes, a Cajal Retzius-like cell type, and 20 non-neural cell subtypes (Figures 5.3, 5.4, and 5.5). Identified cell subtypes correlated with those previously described in bulk tissue snRNA seq experiments (Figures 5.6 and 5.7) (197, 198).

Reflecting the dramatic differences in the cytoarchitectonic organization within the hippocampal formation and the entorhinal cortex, we found a highly diverse set of excitatory neurons across all subregions (Figures 5.3, 5.4, and 5.5). Moreover, several of the broad classifications of neurons identified could be further discriminated on the basis of their molecular signatures indicating intraregional heterogeneity. For example, we found in DG two distinct subpopulations of granule cells that express *PROX1*. These subpopulations are distinguished by their expression of *PDLIM5* and *SGCZ*, respectively (Figure 5.5). Similarly, we found diversity among excitatory neurons in CA1 and CA2-4 (Figures 5.3 and 5.5). Within the subiculum, we observed two proximal subtypes close to CA1 expressing *ROBO1* and a distal subtype expressing *FN1*, matching previous literature (199). Excitatory neurons of EC clustered based on laminar positioning and we identified multiple subtypes in layer 2/3 expressing *CUX2* and *RELN* and layers V and VI expressing deep layer markers, such as *TLE4*, *ADRA1A*, and *THEMIS*.

In contrast, transcriptomic diversity of interneurons and non-neuronal cells was more evenly distributed across all regions (Figure 5.3). We found all major subtypes of interneurons (expressing *SST*, *PVALB*, *VIP*, or *LAMP5*) and identified several non-neuronal cell subtypes, including astrocytes, oligodendrocyte precursor cells, oligodendrocytes, microglia, and vasculature cells.

These results provide further insights into transcriptomic diversity of neuronal and non-neuronal populations of the hippocampal system and describe previously uncharacterized cell populations, enabling further exploration of basic principles of this system (4, 5, 104).

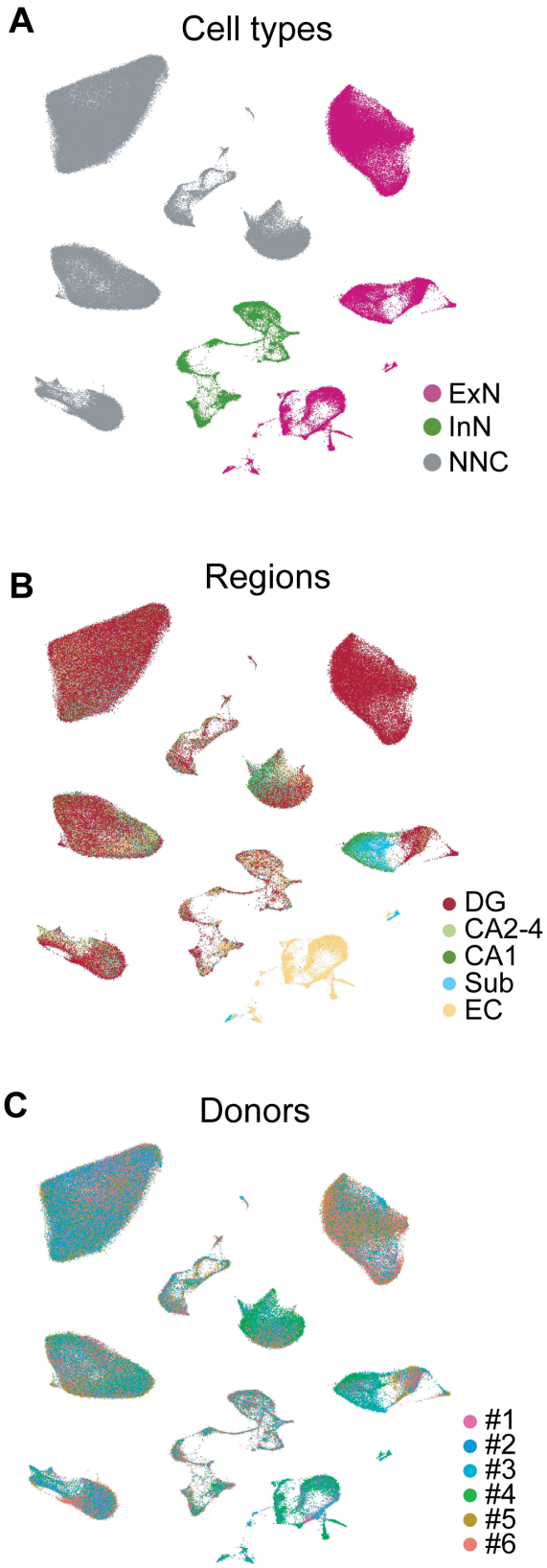

Figure 5.1 UMAP visualization of all nuclei, colored by major cell types (A), subregions (B), and donors (C). ExN = excitatory neuron; InN = inhibitory neuron; NNC = non-neuronal cell; DG = dentate gyrus; CA = Cornu Ammonis; Sub = subiculum; EC = entorhinal cortex
Source: Adapted from (185).

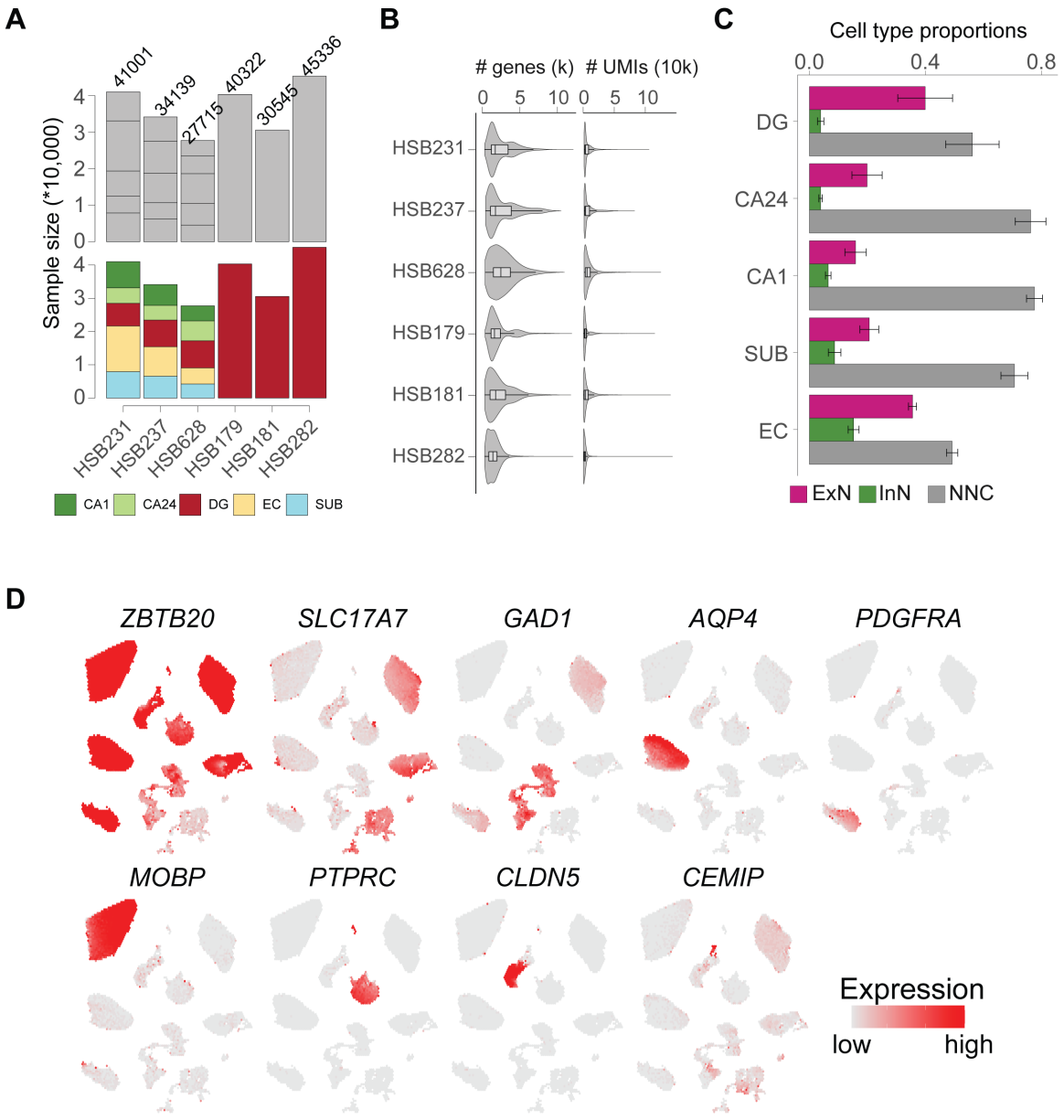

Figure 5.2 Overview of data quality and preprocessing.
(A) Bar plot showing the number of cells in each donor (x-axis) with segments representing technical replicates (upper panel) and colors denoting subregions (bottom panel). **(B)** Violin plot showing the distribution of the number of UMIs and genes detected across donors. **(C)** Cell type proportions across regions with error bars representing standard error of mean. Although the overall percentages match the expected ratio of 3 to 1 ExN to InN (207, 243), we found substantial variations in those proportions between different regions.
(D) UMAP layout visualizing the expression of major cell type markers.
ExN = excitatory neuron; InN = inhibitory neuron; NNC = non-neuronal cell; DG = dentate gyrus; CA = Cornu Ammonis; Sub = subiculum; EC = entorhinal cortex
Source: Adapted from (185).

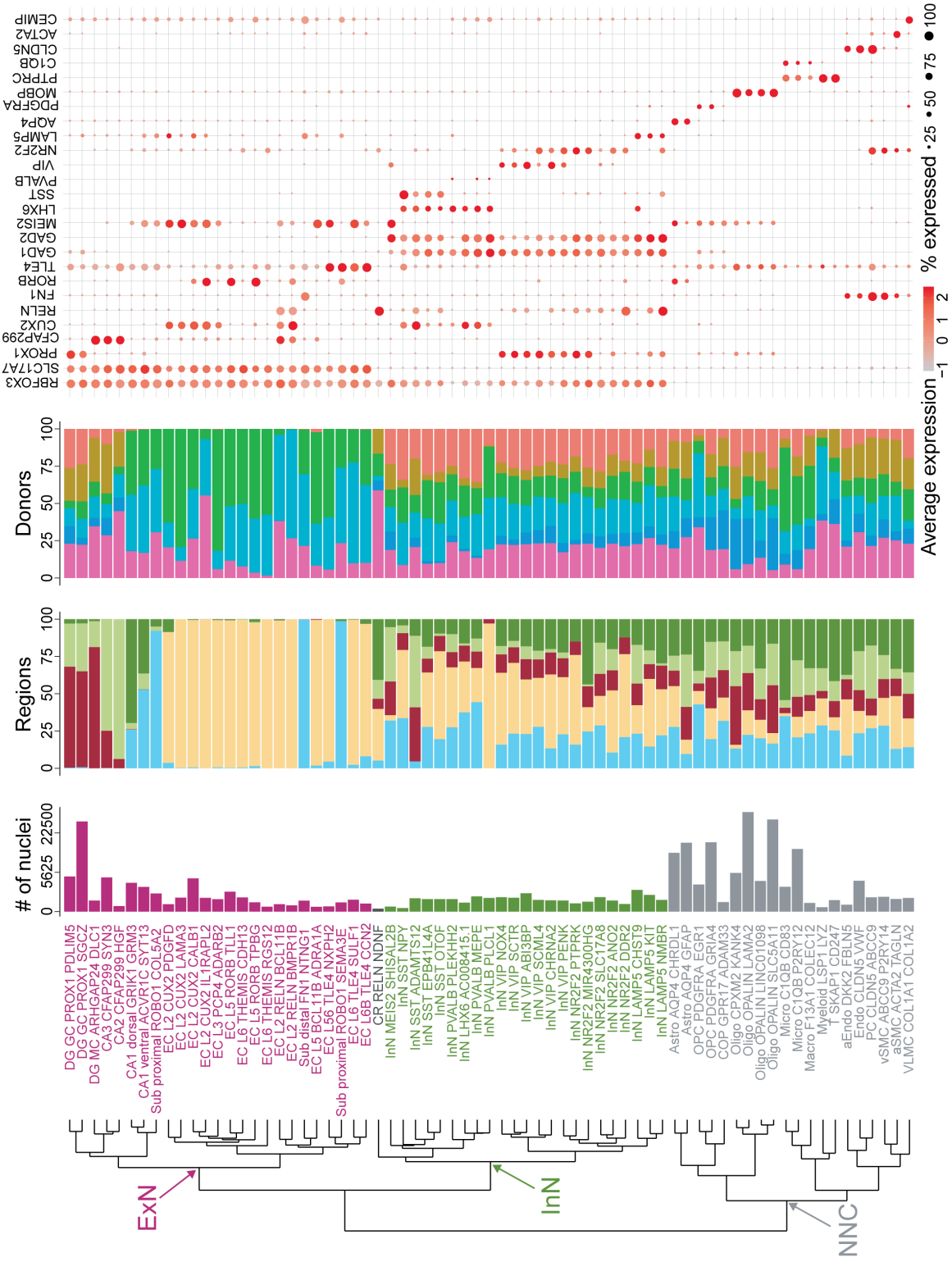

Figure 5.3 Dendrogram depicting the hierarchical taxonomy across all cell subtypes. Bar plots show the number of nuclei, relative subregional and donor contributions. Dot plot shows the expression of marker genes. ExN = excitatory neuron; InN = inhibitory neuron; NNC = non-neuronal cell; DG = dentate gyrus; CA = Cornu Ammonis; Sub = subiculum; EC = entorhinal cortex
Source: Adapted from (185).

Figure 5.4 Violin plots displaying the distribution of the number of UMIs and genes across cell subtypes with box plots showing the median, 25th quantiles and 75th quantiles. ExN = excitatory neuron; InN = inhibitory neuron; NNC = non-neuronal cell; DG = dentate gyrus; CA = Cornu Ammonis; Sub = subiculum; EC = entorhinal cortex; UMI = Unique Molecular Identifier
Source: Adapted from (185).

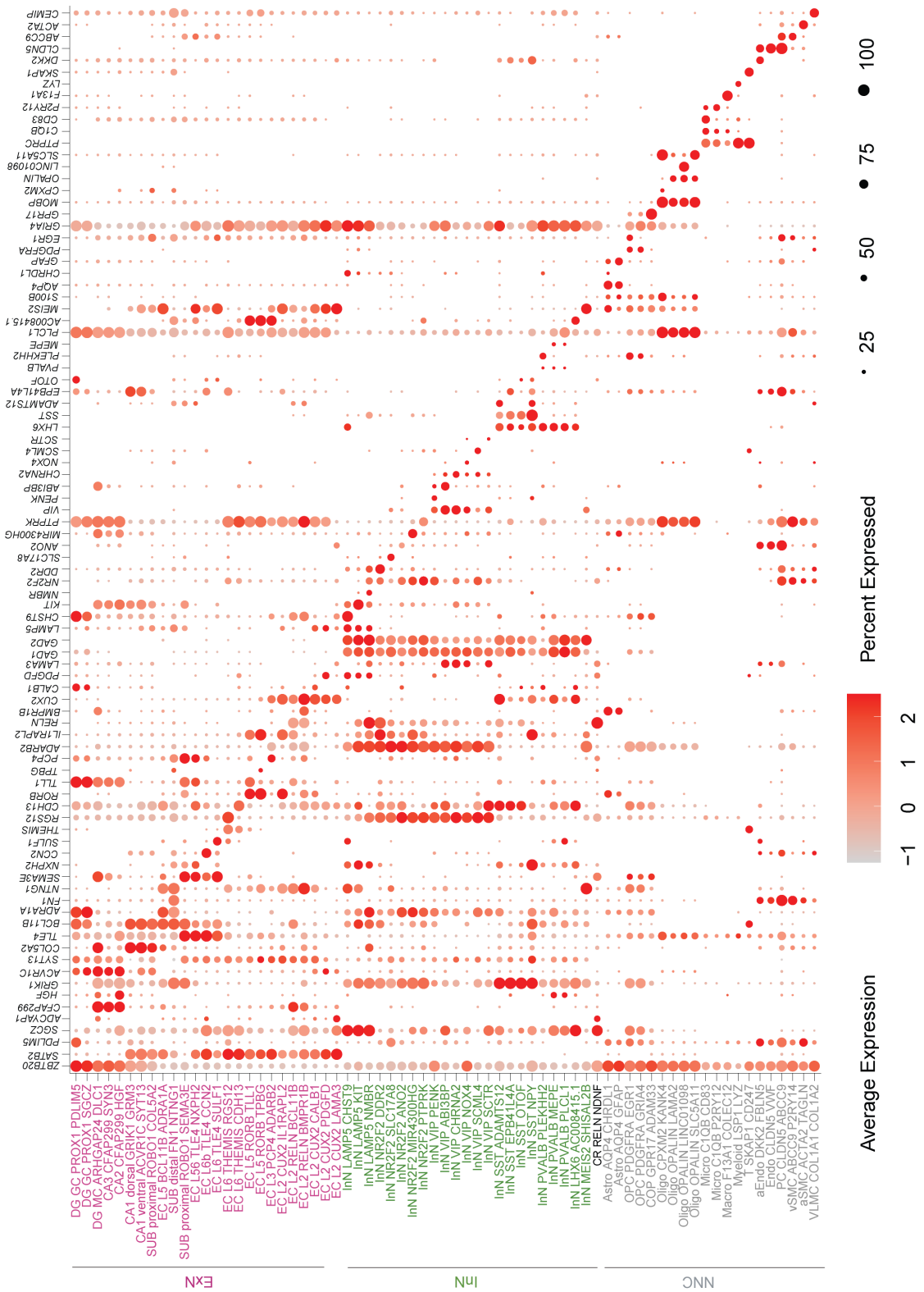

Figure 5.5 Dot plots showing the subtype markers. ExN = excitatory neuron; InN = inhibitory neuron; NNC = non-neuronal cell; DG = dentate gyrus; CA = Cornu Ammonis; Sub = subiculum; EC = entorhinal cortex; Astro = astrocyte; OPC = oligodendrocyte progenitor cell; COP = committed oligodendrocyte precursor cell; Oligo = oligodendrocyte; Micro = microglia; Macro = macrophage; aEndo = arterial endothelial cell; Endo = endothelial cell; PC = pericyte; vSMC = venous smooth muscle cell; aSMC = arterial smooth muscle cell; VLMC = vascular and leptomeningeal cell
Source: Adapted from (185).

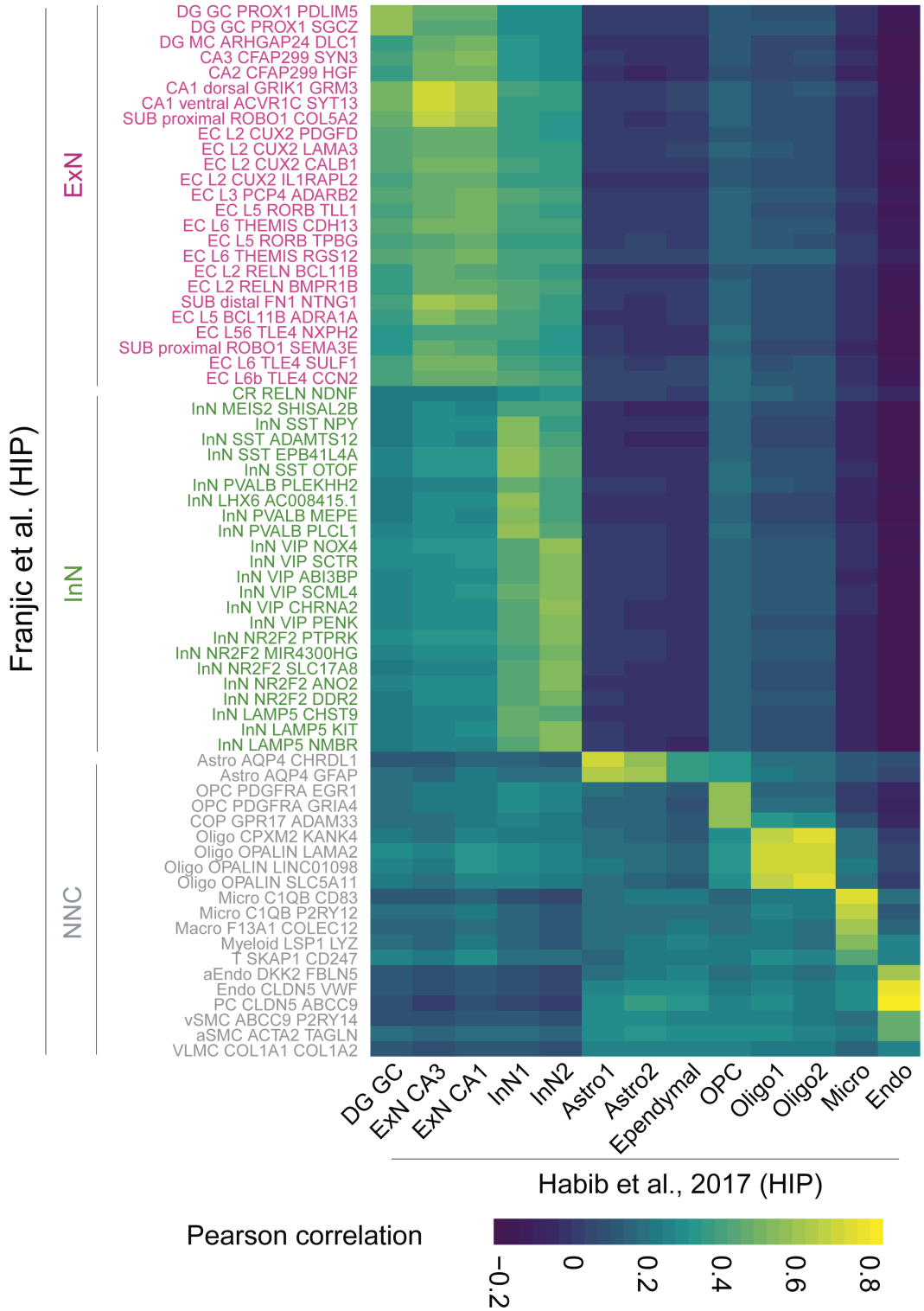

Figure 5.6 Cell types defined in this dataset (y axis) matched to those previously defined in a published hippocampus dataset (197) (x axis), where subregions were not selectively dissected. ExN = excitatory neuron; InN = inhibitory neuron; NNC = non-neuronal cell; DG = dentate gyrus; CA = Cornu Ammonis; Sub = subiculum; EC = entorhinal cortex; Astro = astrocyte; OPC = oligodendrocyte progenitor cell; COP = committed oligodendrocyte precursor cell; Oligo = oligodendrocyte; Micro = microglia; Macro = macrophage; aEndo = arterial endothelial cell; Endo = endothelial cell; PC = pericyte; vSMC = venous smooth muscle cell; aSMC = arterial smooth muscle cell; VLMC = vascular and leptomeningeal cell Source: Adapted from (185).

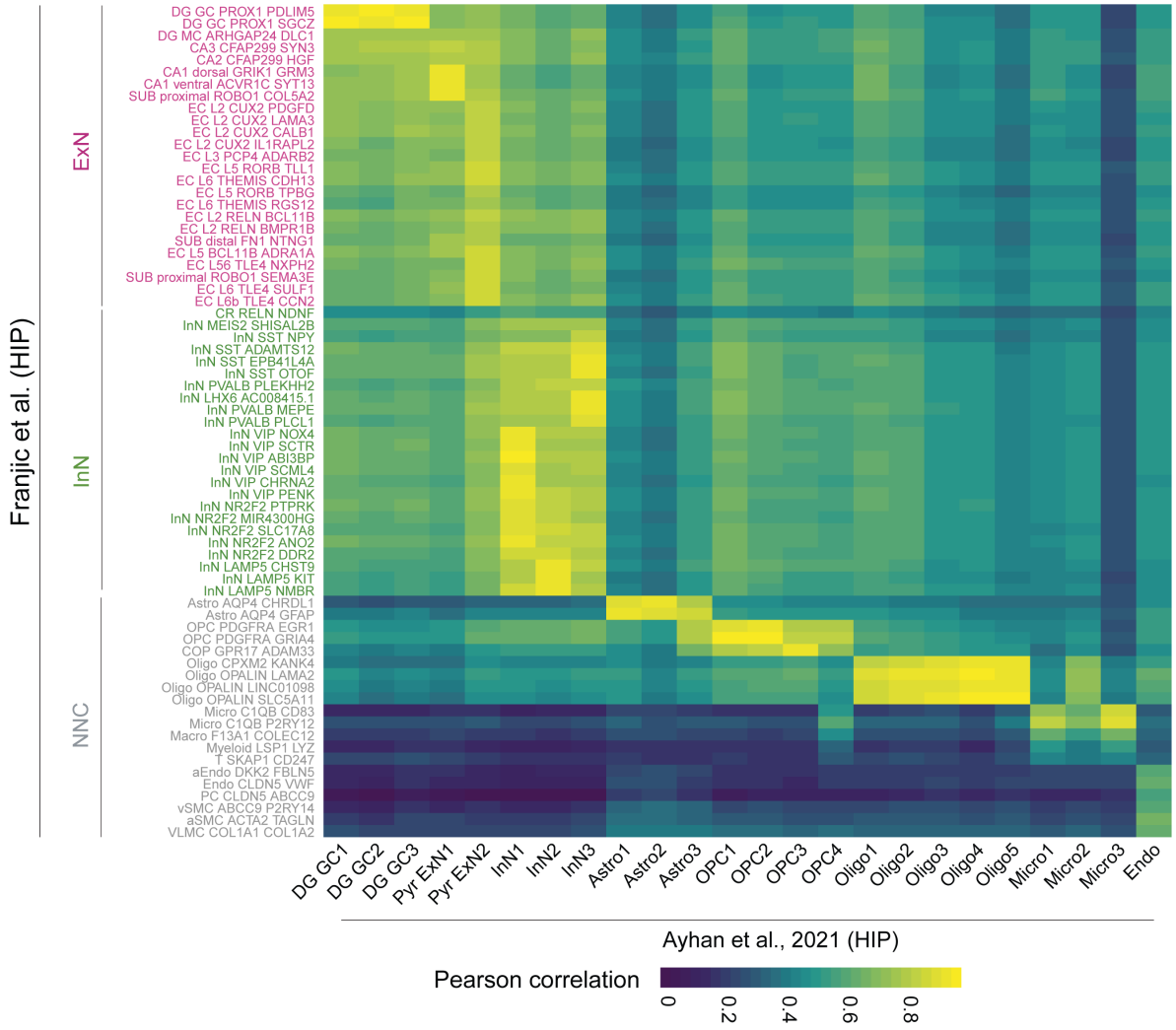

Figure 5.7 Same as in Figure 5.6 but showing the comparison with the recently published hippocampus data (198). ExN = excitatory neuron; InN = inhibitory neuron; NNC = non-neuronal cell; DG = dentate gyrus; CA = Cornu Ammonis; Sub = subiculum; EC = entorhinal cortex; Astro = astrocyte; OPC = oligodendrocyte progenitor cell; COP = committed oligodendrocyte precursor cell; Oligo = oligodendrocyte; Micro = microglia; Macro = macrophage; aEndo = arterial endothelial cell; Endo = endothelial cell; PC = pericyte; vSMC = venous smooth muscle cell; aSMC = arterial smooth muscle cell; VLMC = vascular and leptomeningeal cell
Source: Adapted from (185).

5.2 Integrated cross-species transcriptomic comparison of neurogenic capacity of the adult hippocampal system

In light of the reported scarcity of human adult neurogenesis suggested by several studies (Table 5.1), we isolated a total of 139,187 DG nuclei from 6 adult human donors (Figure 5.8A, Table 5.1, Materials and methods). The samples were processed in 1-8 technical replicates. In addition, we generated complementary snRNA-seq data from adult rhesus macaques and young adult pigs (Table 4.1), all serving as references for significant neurogenesis (6), and then integrated our DG datasets with published single cell RNA-seq data from adult mouse DG (128) to evaluate for *DCX* expression and the presence of DG progenitor and neuroblast cells. Different from traditional approaches which mostly rely on profiling the expression of one or two markers, the integrative analysis harnessed the whole transcriptome and more importantly, it could borrow information across species and unveil rare signals that are often masked in a given species when analyzed separately. While cell types can be broadly matched across the four species, homologs of mouse neuronal intermediate progenitor cells and neuroblasts were only found in pig and macaque, but not in humans, despite processing 25 times more cells in humans and successfully identifying *DCX* transcripts in all human DG samples processed for snRNA-seq (Figures 5.8A and 5.9A). The integration was also sensitive enough to identify the cycling population of oligodendrocyte progenitor cells (cyc OPCs), which were close to nIPC domain but marked by oligodendrocyte progenitor signatures including *PDGFRA* and *OLIG2* (Figures 5.8B-C and 5.9A). We also noticed that mouse radial glia-like (RGL) cells co-cluster with astrocytes, consistent with the observation that RGL and astrocytes exhibit expression similarities (128, 244, 245). To gain a better resolution of granule cell lineage and its variations across species, we re-integrated the data with only the granule cell lineage and astrocytes, which validated the alignment and revealed a more distinct path from nIPC to neuroblast to granule cell in mouse, pig and macaque, but not in human (Figure 5.9B). Such trajectory variations among species were further recapitulated via RNA velocity (Figure 5.9B), which infers cell differentiation trajectory through splicing kinetics (216). Although single nucleus transcriptome captures fewer splicing events compared to single cell transcriptome**,** such ability to recover splicing dynamics is in line with previous studies in other systems (246, 247).

We further recapitulated the species variations of the trajectory using two independent methods, Seurat and Harmony (212, 213), and performed pairwise integration of human cells with macaque, pig, young adult mouse and juvenile mouse (128), the latter exhibiting similar

neurogenic signatures but more abundant neurogenesis activity than young adult mouse. Together with the four-species integration, we found a total of 20 cells in humans residing in the proximity of homolog progenitors and neuroblast cells (Figures 5.10 and 5.11).

Although the integration highlighted all nIPCs and neuroblasts as a domain bridging RGL cells and granule cells, assignment to this domain does not necessarily indicate neurogenic identity, and multiple factors contribute to the misplacement, such as low cell quality and alterations between species. Indeed, we spotted sporadic astrocytes and granule cells intermingled with nIPCs and neuroblast cells (Figure 5.9). To delineate both shared and divergent signatures shaping granule cell differentiation across species, especially in human, we compared the subtype marker genes in other species. The comparison revealed a relative higher similarity in nIPC as compared to neuroblast (Figure 5.12), probably attributed to the common burst of cell cycle genes during the proliferation of progenitors (e.g., *TOP2A*, *CENPF* and *MKI67*) (red gene labels, Figures 5.10 and 5.13). The neuroblast markers shared in more than two species included the widely used neuroblast markers *DCX* and *CALB2* as well as *ST8SIA2* (red gene labels, Figure 5.13), a gene encoding a polysialyltransferase that polysialylates *NCAM* to *PSA-NCAM* (248), another putative marker of immature neurons and neuroblasts (127). There were also three key regulators (*DPYSL3*, *DPYSL5* and *SEMA3C*) (red gene labels, Figure 5.13) of semaphorin signaling, a pathway critical for neuron growth and polarity formation (249). Nevertheless, not all of those conserved markers exhibited similar expression patterns in human, and some showed very high expression in mature granule cells (e.g., *SEMA3C* and *DPYSL5*) (Figure 5.13). Moreover, multiple markers showed divergent patterns among surveyed species, including two neurogenesis modulators *NEUROD4* and *DUSP14* (blue gene labels, Figure 5.10) (250, 251). Such species-related discrepancies suggest that transcriptomic neurogenic signatures are not faithfully preserved across species, and accordingly, caution is advised when determining cell identity.

We performed comprehensive profiling of these markers along with other established proliferative (252) and neuroblast markers (128). Although we identified 20 adult human cells aligned with nIPC or neuroblasts from reference neurogenesis data, they overall displayed very low expression of the majority of the markers and the expression of the rest of the markers was similar to background granule cells (Figure 5.10).

We identified one cell with high expression of neuroblast markers *PROX1*, *DCX*, *CALB2*, *NEUROD6*, and *DPYSL3* (blue arrow, Figure 5.10), and another co-expressing *PROX1* and nIPC markers, such as *TOP2A*, *CENPF* and *MKI67*, suggestive of progenitor

identity (red arrow, Figure 5.10). To see if there are more human cells expressing similar neurogenic features, we unbiasedly searched for cells co-expressing the species-conserved neurogenic markers that mark these two cells. However, we could only find one additional *PROX1*-expressing granule cell co-expressing the 3 putative neuroblast markers (*DCX*, *CALB2* and *DPYSL3*) in humans (Figures 5.13 and 5.14A). Nevertheless, this gene profile lacks specificity, as similar profile is particularly evident in human interneurons.

As neuroblasts continue to mature, they may display a mix of traits from both progenitor and mature granule cells, resembling the features observed in doublets. This led us to re-integrate previously excluded doublets into our integrative analysis of human and mouse dataset. We found only several human cells aligned with the mouse neuroblast subtype on the UMAP and they mostly resembled mature neuron, glia, or neuron/glia doublets, rather than neurogenic cells (Figure 5.14B-C). Since it is possible that neuroblast cells from prenatal and adult stages share certain similarities (128), we compared adult and fetal human DG data (211) but have not observed a clear trajectory from nIPC to neuroblast to granule cell in adult human DG (Figures 5.15 and 5.16). Only 4 adult cells aligned with fetal progenitors and neuroblasts (Figure 5.15). Nevertheless, they did not express fetal human nIPC or neuroblast markers, nor did they express canonical markers including *MKI67*, *DCX* and *CALB2* (Figure 5.16), suggesting they were not *bona fide* progenitors or neuroblasts. Taken together, through comprehensive data integration across species and developmental stages, we found strong evidence supporting adult neurogenesis in mice, pigs, and macaques; however, this was not evident in humans. We found only one potential neuronal progenitor cell and one neuroblast out of 139,187 DG cells (0.0007% for each cell) and 32,067 granule cells (0.003% for each cell). This is drastically lower than previously reported estimates from studies evaluating DCX protein expression and ^{14}C incorporation, which have indicated a range of 28 to 1,218 neuroblasts for a sample size similar to ours (see Table 5.1 with estimated prevalence of adult neurogenesis in humans).

Table 5.1 Quantitative data on neurogenic rates estimated by DCX immunostaining and ^{14}C incorporation in mouse, macaque and human DG from the literature

Species	Reference	Method	Detection rate (among GC cells)	Expected number neuroblasts in our human data (32,067 granule cells)
Mouse 2 m.o. (young adult)	Ben-Abdallah et al., 2010[a]	DCX IL	3.4% DCX+ cells	1090
Mouse 4 m.o. (young adult)	Ben-Abdallah et al., 2010[b]	DCX IL	1.24% DCX+ cells	398
Mouse 9 m.o. (adult)	Ben-Abdallah et al., 2010[c]	DCX IL	0.24% DCX+ cells	77
Rhesus (adult)	Ngwenya et al., 2015[d]	DCX IL	0.05% DCX+ cells	16
Rhesus (adult)	Perera et al., 2011[e]	DCX IL	0.03% DCX+ cells	10
Human (adult)	Boldrini et al., 2018[f]	DCX IL	0.09% DCX+ cells	28
Human (adult)	Tobin et al., 2019[g]	DCX IL	1.1% DCX+ cells	346
Human (adult)	Moreno-Jimenez et al., 2019[h]	DCX IL	3.8% DCX+ cells	1218
Human (adult)	Spalding et al., 2013[i]	^{14}C incorporation	0.84% immature granule cells	269

[a] Ben-Abdallah and colleagues (253) reported 14947 DCX+ cells out of 440K GCs in mice 2 m.o., representing 3.4% of the total.

[b] Ben-Abdallah and colleagues (253) reported 6202 DCX+ cells out of 500K GCs in mice 4 m.o., representing 1.24% of the total.

[c] Ben-Abdallah and colleagues (253) reported 1342 DCX+ cells out of 550K GCs in mice 9 m.o., representing 0.24% of the total.

[d] Ngwenya and colleagues (117) showed DCX+ cells in a graph (Figure 2), that can be estimated to an average of 3521 DCX+ cells/DG, or 0.05% of the 7.2M of GC cells in the macaque DG (114).

[e] Perera and colleagues (254) in Figure 3 show (estimated) average of 260 DCX+ cells/mm3 in SGZ. Assuming SGZ volume about 8.68 mm^3 (255) gives a total of 2256 or 0.03% of the total 7.2M (114). Perera et al., 2011 (254) showed density of DCX+ cells/mm3 in a graph (Figure 3) that can be estimated to an average 260 DCX+ cells/mm3 of SGZ. They do not report volume of the SGZ but they estimate the volume of GCL as 1.8 mm3. If we assume similar volume for GCL and SGZ, we get (260X1.8) 468 DCX+ cells or 0.0065%. However, 1.8 mm3 seems too small volume, and (255) reported that GCL volume was 8.68 mm3. With that estimate, we obtain (260X8.68) 2256 DCX+ cells/DG, or 0.03% DCX+ cells in the DG.

[f] Boldrini and colleagues (73) reported 10K to 15K DCX+ cells in GCL, their data showing an average of 10345 out of 12M GCL cells, representing 0.086%.

[g] Tobin and colleagues (75) estimated 162,047 DCX+ cells in the DG that means 1.1% DCX+ cells out of 15M GCs (256-258).

[h] Moreno-Jimenez and colleagues (121) Figure 1 show an average of about 32,000 DCX+/mm3 from a total of about 840,000 neu/mm3 in the DG, representing 3.8%.

[i] Spalding et al., 2013 (119) estimated 700 newly generated granule cells a day. Data from macaque indicates that expression of DCX, and therefore maturation of newly generated cells in the macaque dentate gyrus last for about 6 months or more (115). Assuming similar timing of maturation in the human dentate gyrus, the number of neuroblasts and immature cells present at any timepoint would be 126,000 (700×180), that means 0.84% out of 15M GCs.

Source: Table adapted from (185).

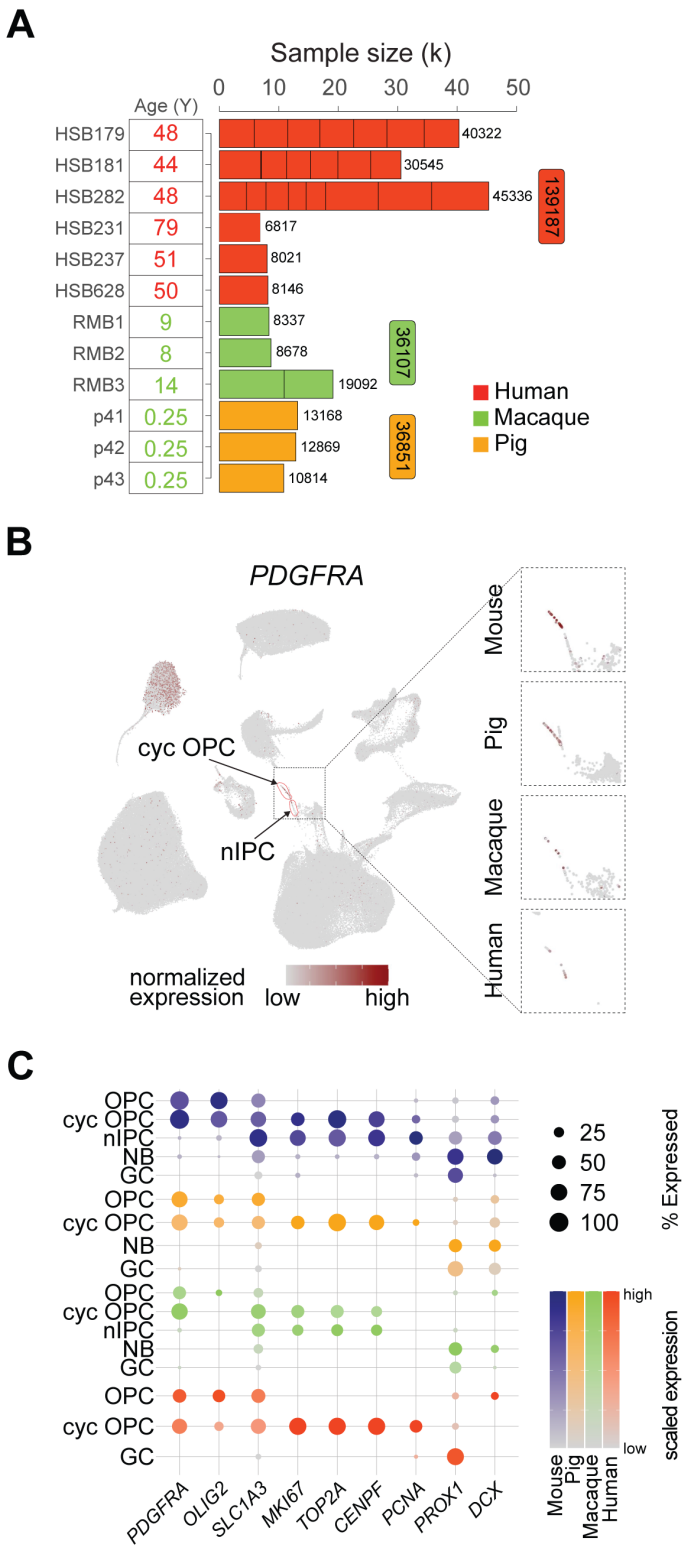

Figure 5.8 (A) Donor ages and sample sizes. Donors are shown on the y-axis and technical replicates are represented by bar segments. **(B)** The integration was sensitive enough to identify the cycling oligodendrocyte precursor cells (cyc OPCs), which were close to nIPC domain but marked by an oligodendrocyte precursor marker *PDGFRA*. **(C)** Expression of selective OPC, cell cycle markers, as well as *DCX* and *PROX1*, in the granule cell lineage and OPC cells. OPC = oligodendrocyte progenitor cell; nIPC = neural intermediate progenitor cells; NB = neuroblast; GC = granule cell
Source: Adapted from (185).

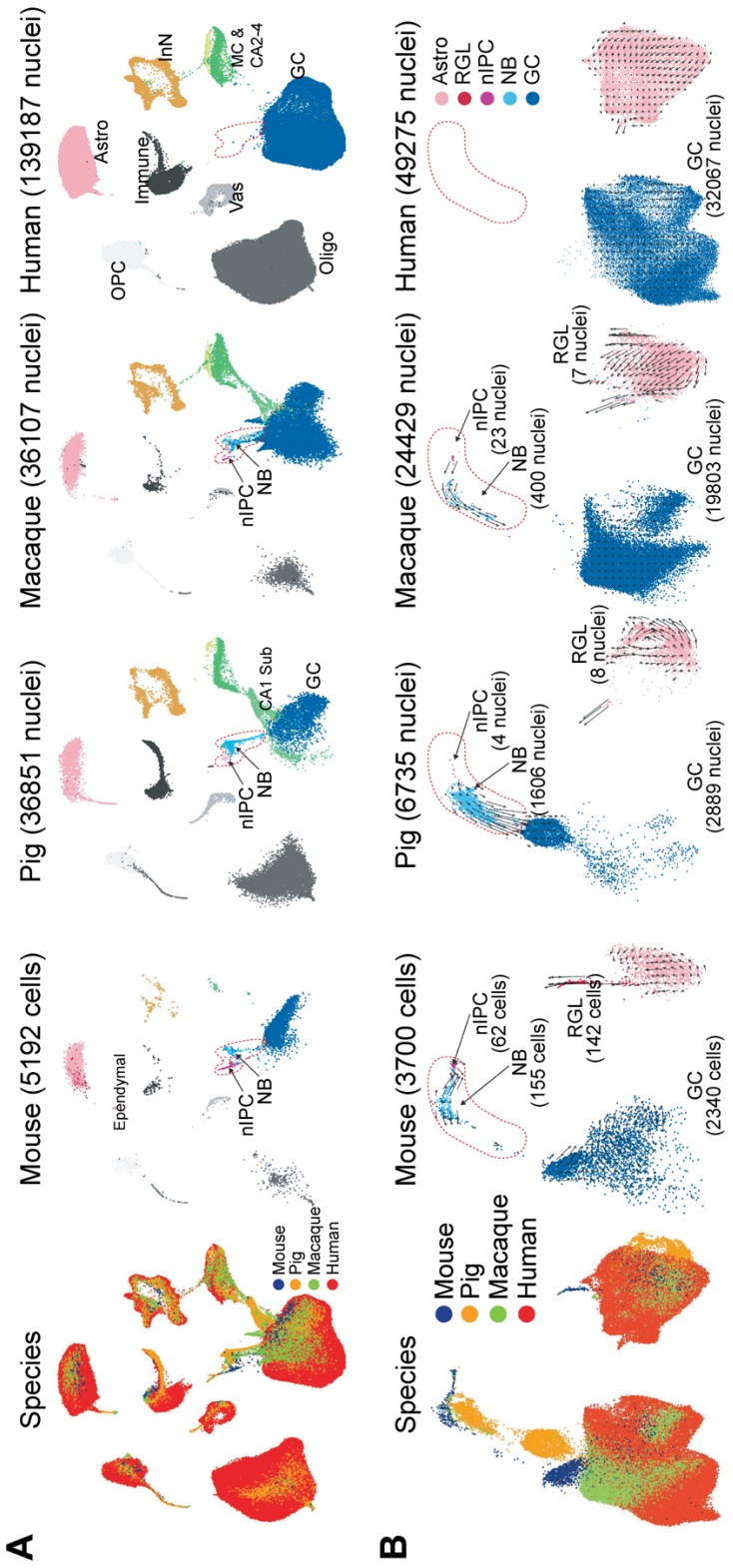

Figure 5.9 Seurat integration of all DG cells **(A)** or only astrocytes and the granule cell lineage **(B)** across species. In B, arrows indicate the direction and speed (arrow length) of the RNA velocity. InN = Inhibitory neuron; nIPC = Neural intermediate progenitor cells; NB = neuroblast; GC = granule cell; CA = Cornu Ammonis; Sub = subiculum; OPC = oligodendrocyte progenitor cell; Oligo = oligodendrocyte; Astro = astrocyte; Vas = vasculature; MC = mossy cell; RGL = radial glial cell; Source: Adapted from (185).

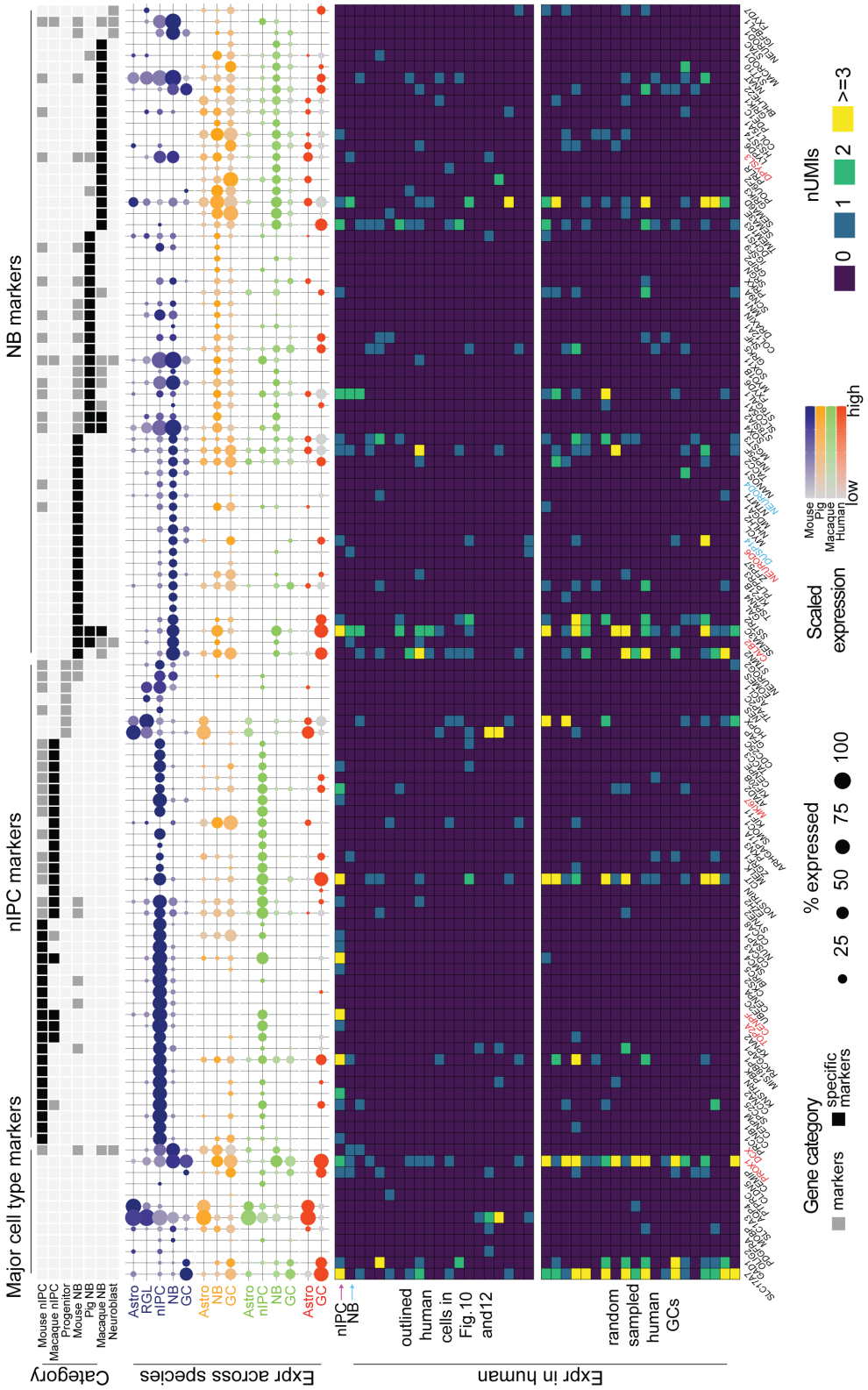

Figure 5.10 Expression of cluster markers across species. The categories "proliferative" and "neuroblast" were manually annotated (128, 252). Middle: Dot plot depicting the expression of the markers with dots colored by species. Bottom: Marker expression in the 20 human cells residing in the nIPC and neuroblast domain as well as the randomly sampled human granule cells. The first two rows highlighted by arrows represent the two putative human neurogenic cells. nIPC = neural intermediate progenitor cells; NB = neuroblast; GC = granule cell; Astro = astrocyte
Source: Adapted from (185).

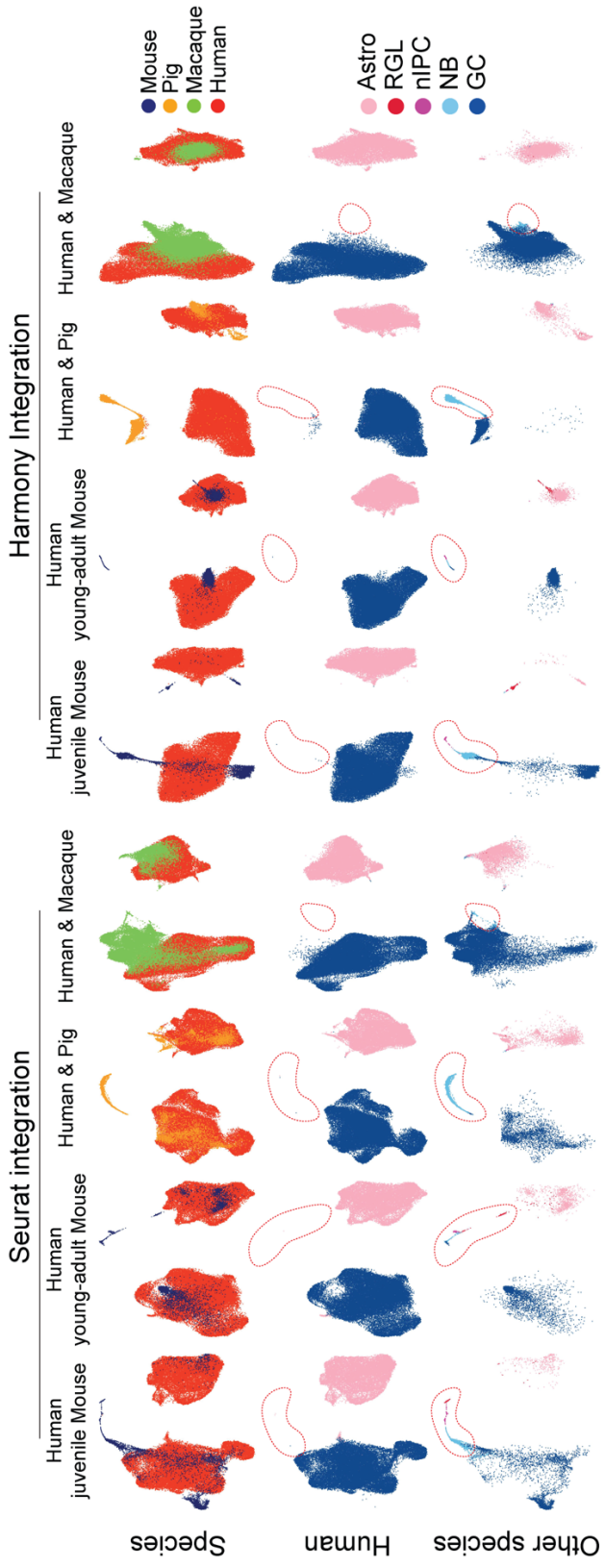

Figure 5.11 Pair-wise integration of astrocytes and granule cell lineage between human and each of the other species using Seurat (left) and Harmony (right). The nIPC and neuroblast domains are outlined. nIPC = neural intermediate progenitor cells; NB = neuroblast; GC = granule cell; Astro = astrocyte; RGL = radial glial cell

Source: Adapted from (185).

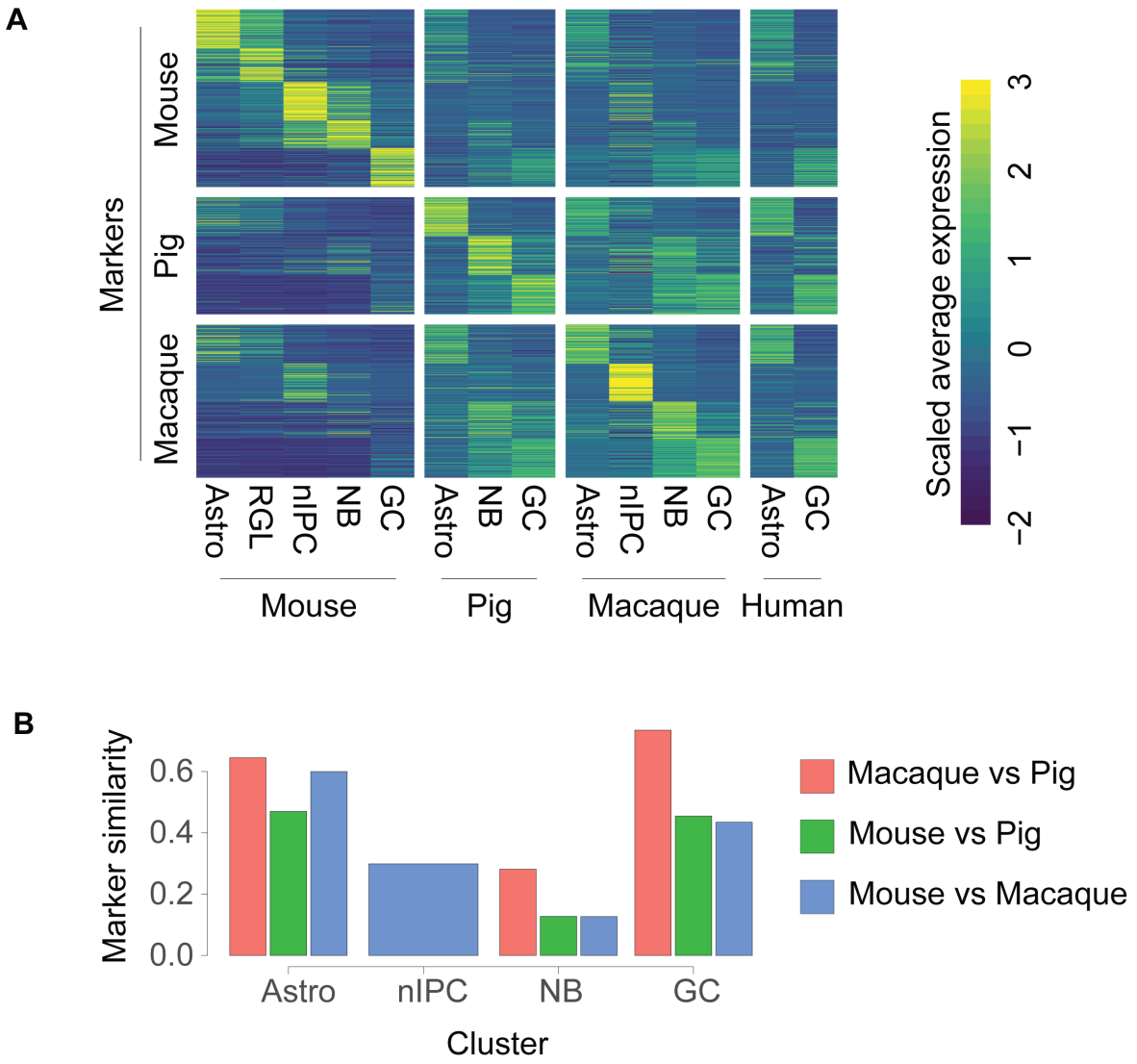

Figure 5.12 (A) Scaled average expression of markers across species with rows representing genes and columns denoting cell types. **(B)** Similarity of cluster markers measured by the proportion of shared markers. nIPC = neural intermediate progenitor cells; NB = neuroblast; GC = granule cell; Astro = astrocyte

Source: Adapted from (185).

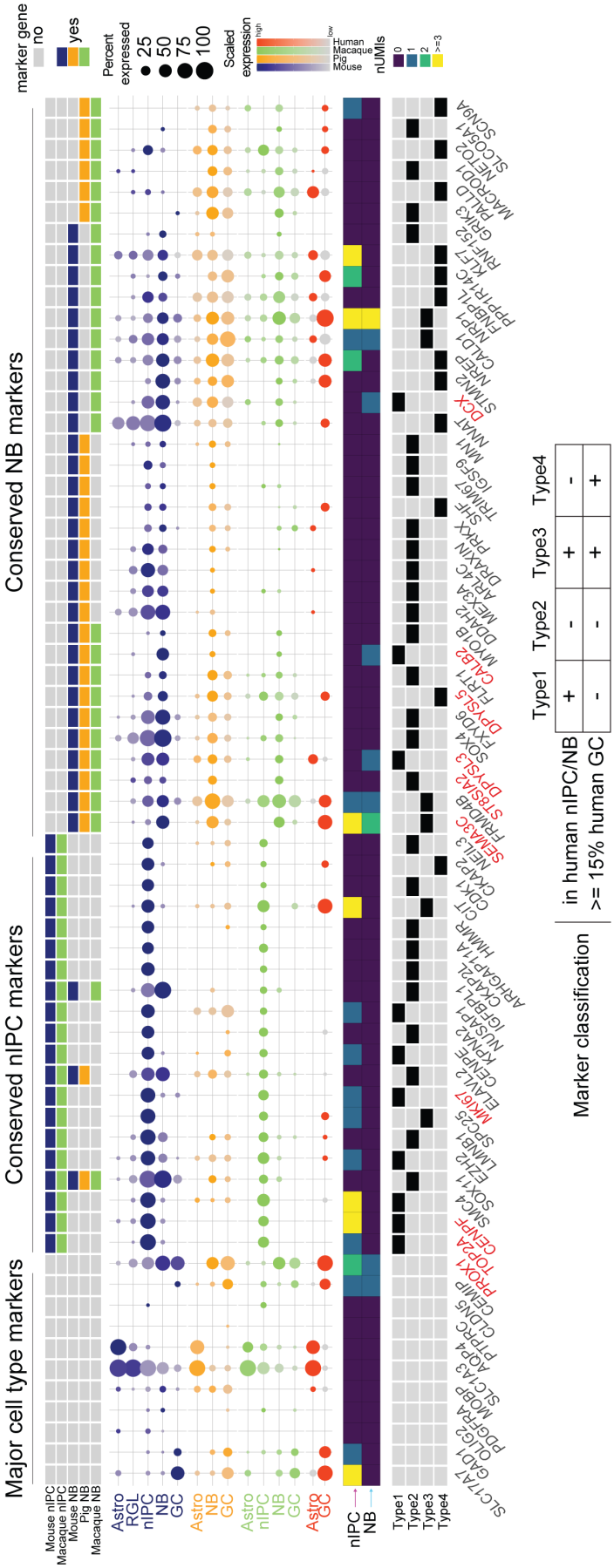

Figure 5.13 Expression of species-conserved nIPC and neuroblast markers. Top panel: marker categories. Middle dot plot: expression of the conserved markers across species. Middle heatmap: expression of the markers in the human nIPC and neuroblast. Bottom panel: classification of the markers based on their expression in human neurogenic cells and background granule cells. nIPC = neural intermediate progenitor cells; NB = neuroblast; GC = granule cell; Astro = astrocyte
Source: Adapted from (185).

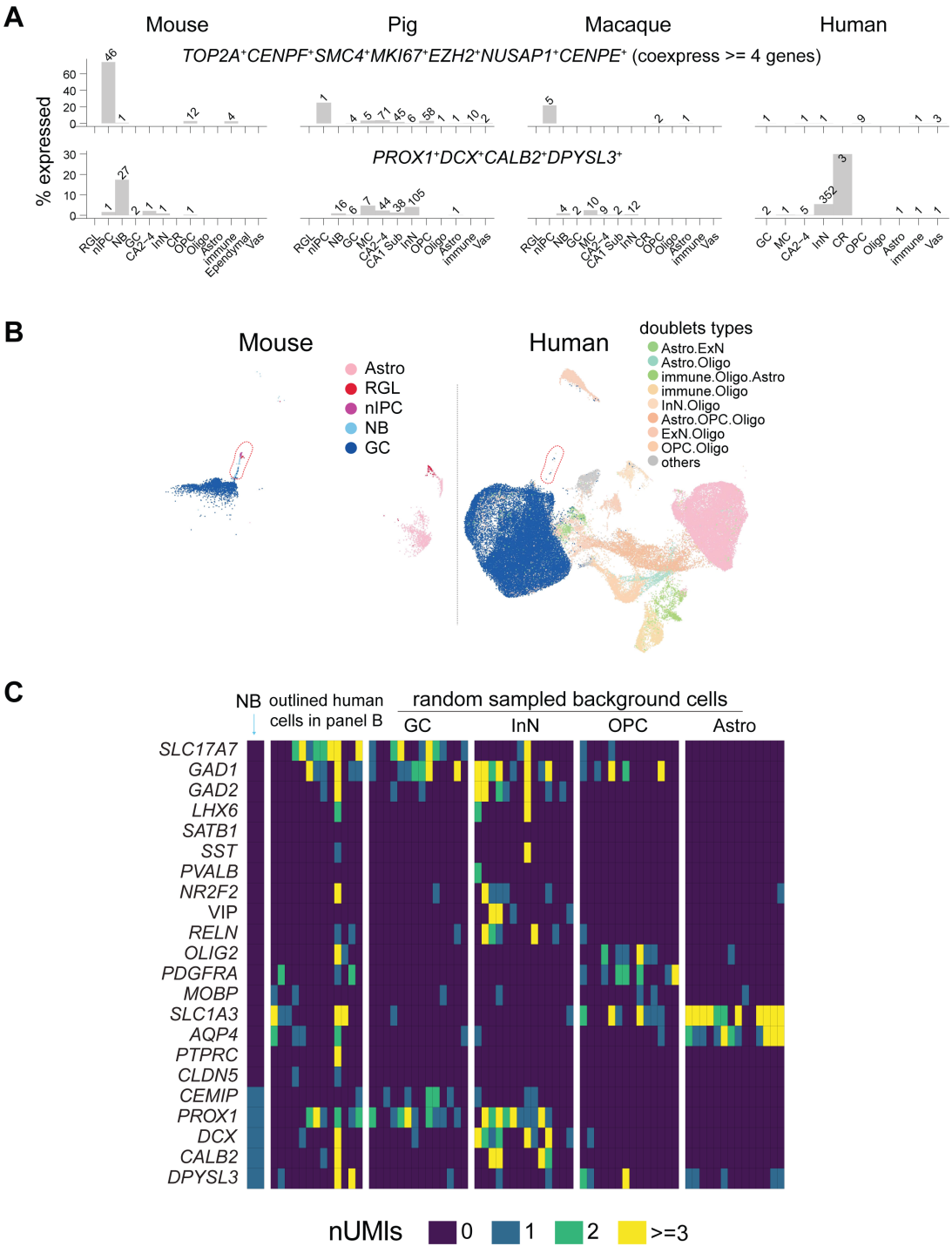

Figure 5.14 (A) Co-expression of type 1 markers identified in panel G across species. **(B)** Integration of human and mouse astrocytes and the granule cell lineage along with previously removed human DG doublets. **(C)** Expression of major cell type markers and several key neuroblast markers in the human cells outlined in panel B as well as some randomly sampled cells from other cell types. The human neuroblast cell was put on the left for reference. nIPC = neural intermediate progenitor cells; NB = neuroblast; GC = granule cell; Astro = astrocyte; Oligo = oligodendrocyte; RGL = radial glial cell; ExN = excitatory neuron; InN = inhibitory neuron

Source: Adapted from (185).

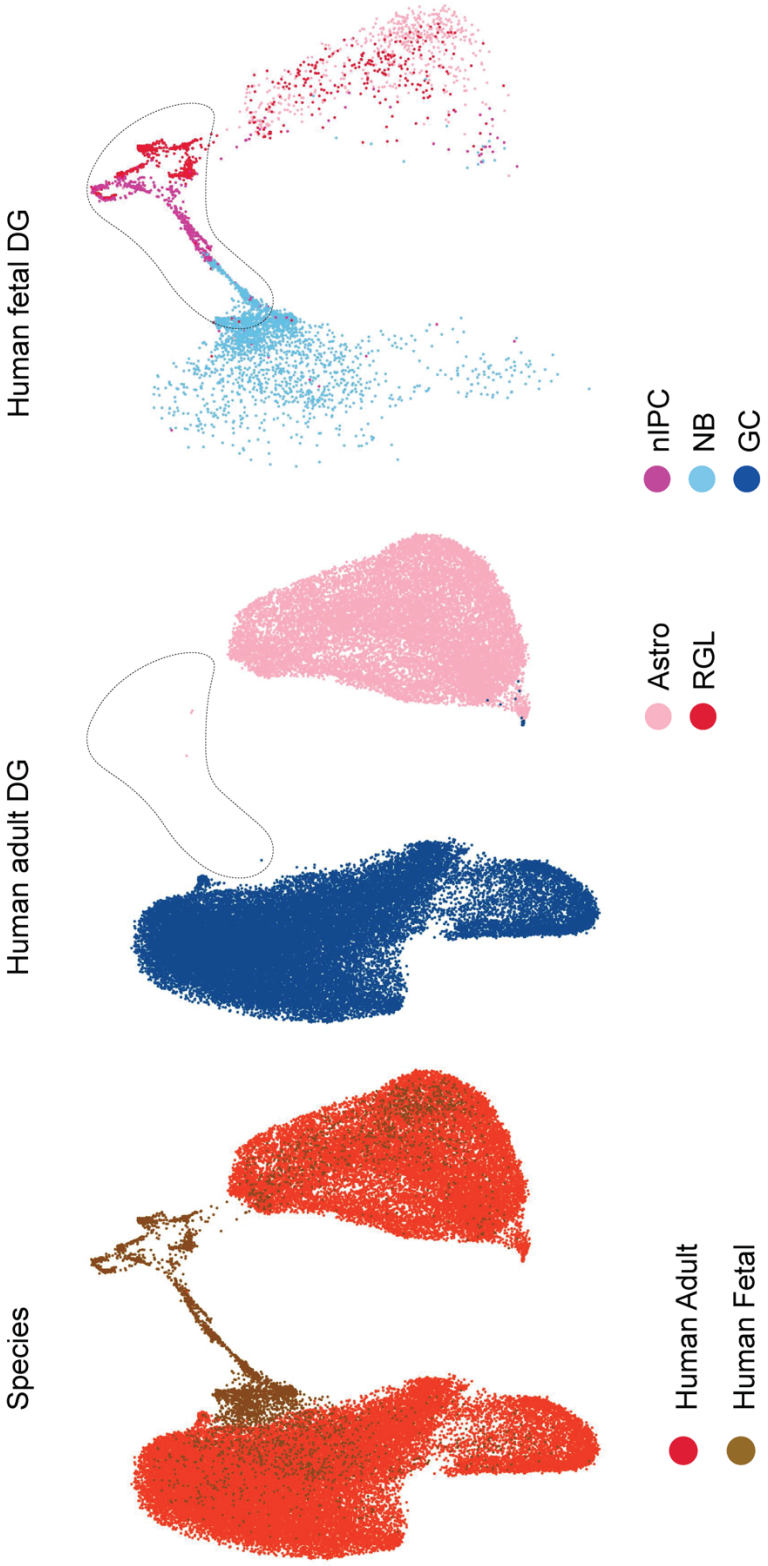

Figure 5.15 Integration of adult human DG data and fetal human DG data (211). nIPC = neural intermediate progenitor cells; NB = neuroblast; GC = granule cell; Astro = astrocyte; RGL = radial glial cell
Source: Adapted from (185).

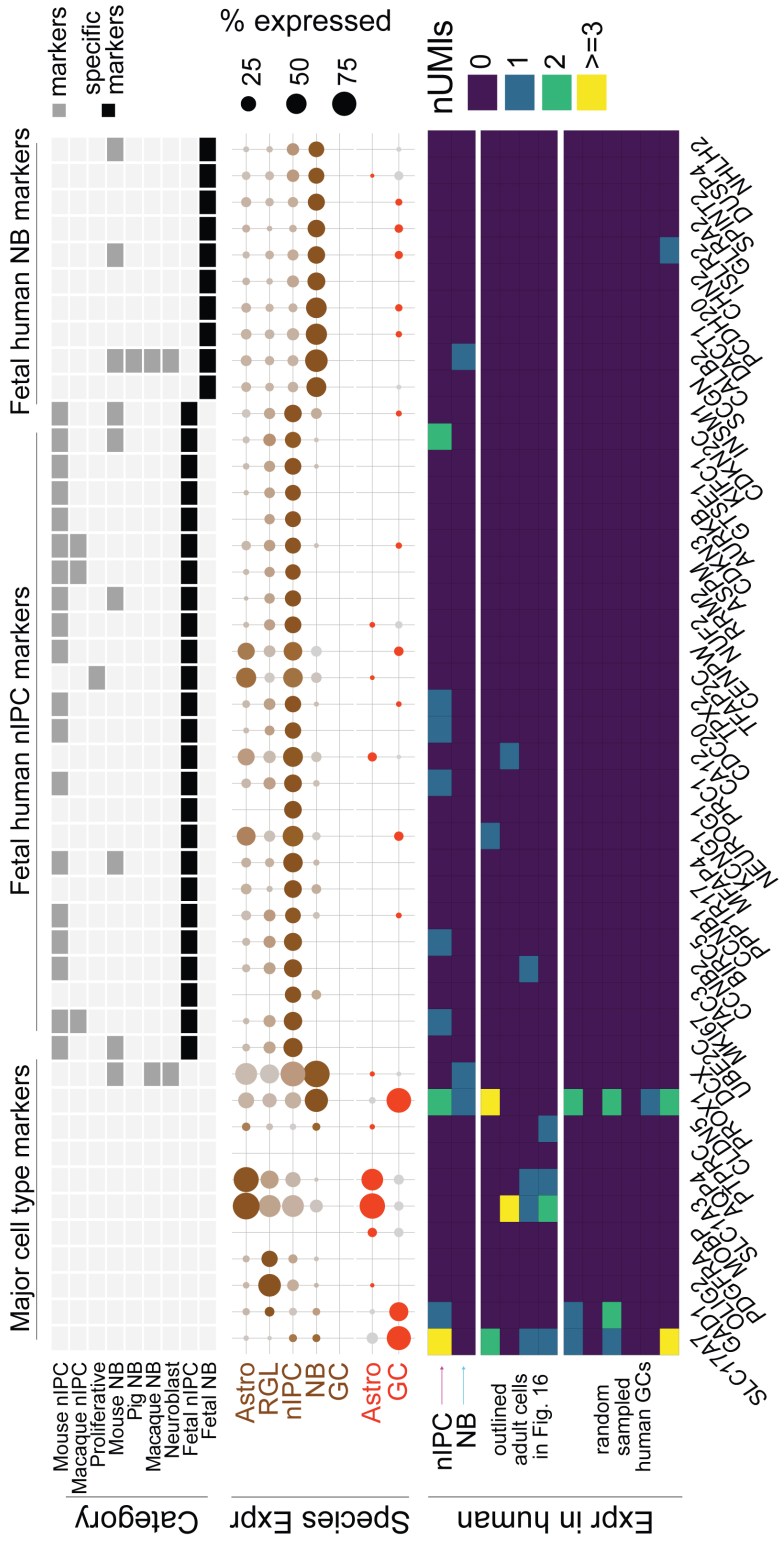

Figure 5.16 Top panel: categories of fetal human markers. Middle panel: expression of these markers in fetal and adult humans. Bottom heatmap: expression of the markers in human with the identified human nIPC and neuroblast arranged on the top for positive controls. nIPC = neural intermediate progenitor cells; NB = neuroblast; GC = granule cell; Astro = astrocyte; RGL = radial glial cell
Source: Adapted from (185).

5.3 Evaluation of *DCX* as a marker of adult neurogenesis in human hippocampus

We next sought to profile *DCX* expression across species given that *DCX* has been the widely adopted marker of neuroblasts and immature neurons in both fetal and adult neurogenesis (72-75). In addition, bulk tissue transcriptome data shows that *DCX* is expressed in the adult human HIP, however, at strikingly lower levels than in the adult rhesus macaque HIP or during early developmental stages (Fig. 5.18A) (103, 122, 123).

In order to compare the *DCX* expression in the same scale, we down-sampled the datasets to the same sequencing depth prior to the comparative analysis (see Materials and methods). We found *DCX* was highly expressed in mouse neuroblasts and, to a lower degree, in pig and macaque neuroblasts (Figure 5.18). Overall, there was scarce expression of *DCX* (at least one UMI) in adult human GCs (110/32,067 cells or 0.34%) compared to other species (mouse: 75/2,340 cells or 3.21%; pig: 430/2,889 cells or 14.88%; rhesus macaque: 609/19,803 cells or 3.08%) (Figure 5.18; Table 5.2). Given that some cell type markers may show background expression (Figure 5.2D), we compared gene expression levels across datasets to filter the potential background (at least 2 UMIs). In the adult human, only 0.01% of granule cells (4 cells) expressed at least 2 *DCX* UMIs (Table 5.2), a ratio much lower in humans than other species (mouse, 12/2,340 cells or 0.51%; pig, 57/2,889 cells or 1.97%; rhesus macaque 39/19,803 or 0.2%). Nevertheless, obvious *DCX* expression, both in terms of ratio and level, was detected in human non-granule neurons where 466 out of 32,067 interneurons or 7.28% expressed at least 2 *DCX* UMIs (Figure 5.18; Table 5.2) suggesting that the scarcity of *DCX* in human granule cells can be attributed to low expression rather than low detection. Moreover, this indicates that the longer PMI of our human samples (Table 4.1) is not a limiting factor for the detection of *DCX* transcripts. To further investigate this, we evaluated the pig DG with 30 minutes, 1 hour, and 7 hours PMI using snRNA-seq, and detected similar *DCX* expression and presence of neural progenitors and neuroblasts (Figure 5.17C). Overall, *DCX* expression in cell populations other than neuroblasts and granule cells was found across all species but it was more similar in the pig, rhesus macaque, and human compared to mouse (Figure 5.19A). These finding suggest that relying solely on *DCX* expression may be insufficient to characterize adult neurogenesis.

To further test whether *DCX* can highlight neuroblasts in granule cell lineage of human, we checked the enrichment of all the neurogenic markers in *DCX*-expressing cells versus *DCX*-negative cells. However, all four set of neuroblast markers were only enriched in *DCX*-expressing cells in mouse, pig, and macaque, but not in human (Figure 5.19B),

similar to findings prior to down-sampling (Figure 5.17B). With such conserved enrichment pattern among mouse, pig and macaque we reasoned that this method is sensitive enough to detect potential neuroblasts despite any species differences. The fact that human *DCX*-expressing cells are not enriched in neuroblast markers further confirms the scarcity of adult neurogenesis in human DG and suggests that, similar to other mature neurons, mature GCs express *DCX* to some extent.

We next investigated the DCX protein patterns using immunohistochemistry with two different antibodies. We immunolabeled hippocampus of adult mouse, pig, rhesus macaque, and human. Mice and macaque exhibited numerous DCX immunolabeled (DCX-IL) cells in the DG, with both immature and mature granule cell morphology (Figure 5.20A), as has been extensively reported (117, 254). Pig showed a more immature, less consolidated granule cell layer and very numerous cells immunolabeled for DCX in the subgranular zone (SGZ) but also in the hilus, as expected by the young age and the relatively protracted DG development in pigs, as previously described (259). In humans, we evaluated 10 cases that included amygdala and the hippocampus or EC. The amygdala served as a positive control since abundant DCX-IL cells could be detected with both antibodies in the paralaminar nucleus (260). We used several protocols of antigen retrieval, including one used by Moreno-Jimenez and colleagues (121) detailed in the publication from Flor-Garcia and colleagues (261), with similar results. We detected abundant DCX-IL cells in the amygdala of all 10 samples with strong labeling in the soma and processes. We found sporadic DCX immunoreactive cells in the EC and the adjacent perirhinal cortex and even more infrequent DCX-IL cells in the subiculum and CA fields of some cases (Table 5.3). We only found some cells in the DG faintly immunolabeled by DCX, located mainly near and, occasionally, within the granule cell layer, typically in the molecular layer or in the hilus and SGZ regions (Figure 5.20A, 5.21A-D, and 5.22A-E). Interestingly, their morphology and localization resembled GABAergic interneurons more than immature granule cells and some of them stained faintly with interneuron marker GAD1 (Figures 5.20B and 5.22D–F), which is consistent with our snRNA-seq data. In addition, we observed similar faint staining of cells in other regions, including pyramidal cells, which potentially could be due to a background staining (Figures 5.21A-D). The PMI of our human samples did not seem to a limiting factor in detecting DCX since we identified DCX-IL cells in the amygdala, the EC, and the adjacent perirhinal cortex with PMIs up to 24 hours. Similarly, immunohistochemistry for DCX in the pig DG with 15 and 24 hours PMI and rhesus macaques with 16 hours PMI

(Figure 5.21F-I; Table 5.3) showed that the number of DCX-IL cells was reduced (Figures 5.20A and 5.21F-I) but the detection of DCX was still possible.

Next, we performed immunostaining against PSA-NCAM, another common marker of neuroblasts and immature neurons in the mouse dentate gyrus (127, 262). As previously reported in the human, we found numerous cells immunoreactive to PSA-NCAM in the hippocampus, and especially in the hilar and DG area, whose morphology resembles GABAergic interneurons (Figure 5.21E) (127, 244) and corroborates the cell-type distribution seen with DCX. We did not colocalize those markers due to technical incompatibility of PSA-NCAM immunolabeling and antigen retrieval required for anti-DCX antibodies.

Taken together, our comprehensive snRNA-seq analysis and DCX immunolabeling demonstrated strong evidence of adult neurogenesis in mouse, pig, and rhesus macaque, while this was not evident in the human.

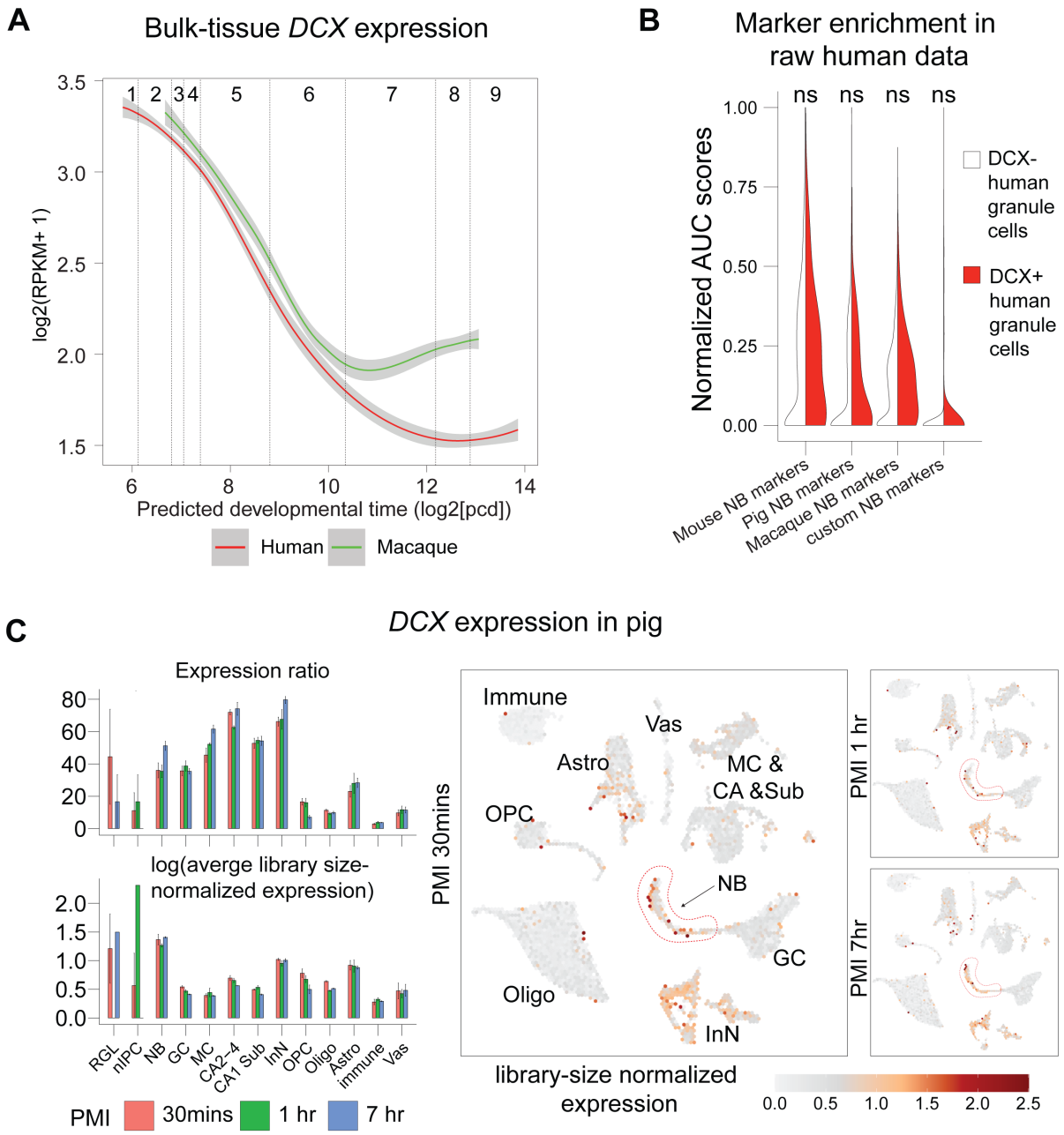

Figure 5.17 Cross-species comparison of the DCX expression.
(A) Line plots visualizing the expression pattern of DCX along the predicted developmental time (123, 200). Dashed lines represent the segregation of nine developmental stages described previously (200). **(B)** Enrichment of different sets of neuroblast markers in DCX+ compared to DCX- cells in the raw human data prior to down-sampling. Significance was tested using one-tailed Wilcoxon rank sum test (ns: not significant). **(C)** Left: Expression ratio and library size normalized expression of DCX in pig hippocampus at 30 mins, 1 hour and 7 hours postmortem interval (PMI). Right: UMAP showing normalized expression of DCX in pig hippocampus across postmortem intervals. nIPC = neural intermediate progenitor cells; NB = neuroblast; GC = granule cell; RGL = radial glial cell; CA = Cornu Ammonis; Sub = subiculum; OPC = oligodendrocyte progenitor cell; Oligo = oligodendrocyte; Astro = astrocyte; Vas = vasculature; MC = mossy cell;
Source: Adapted from (185).

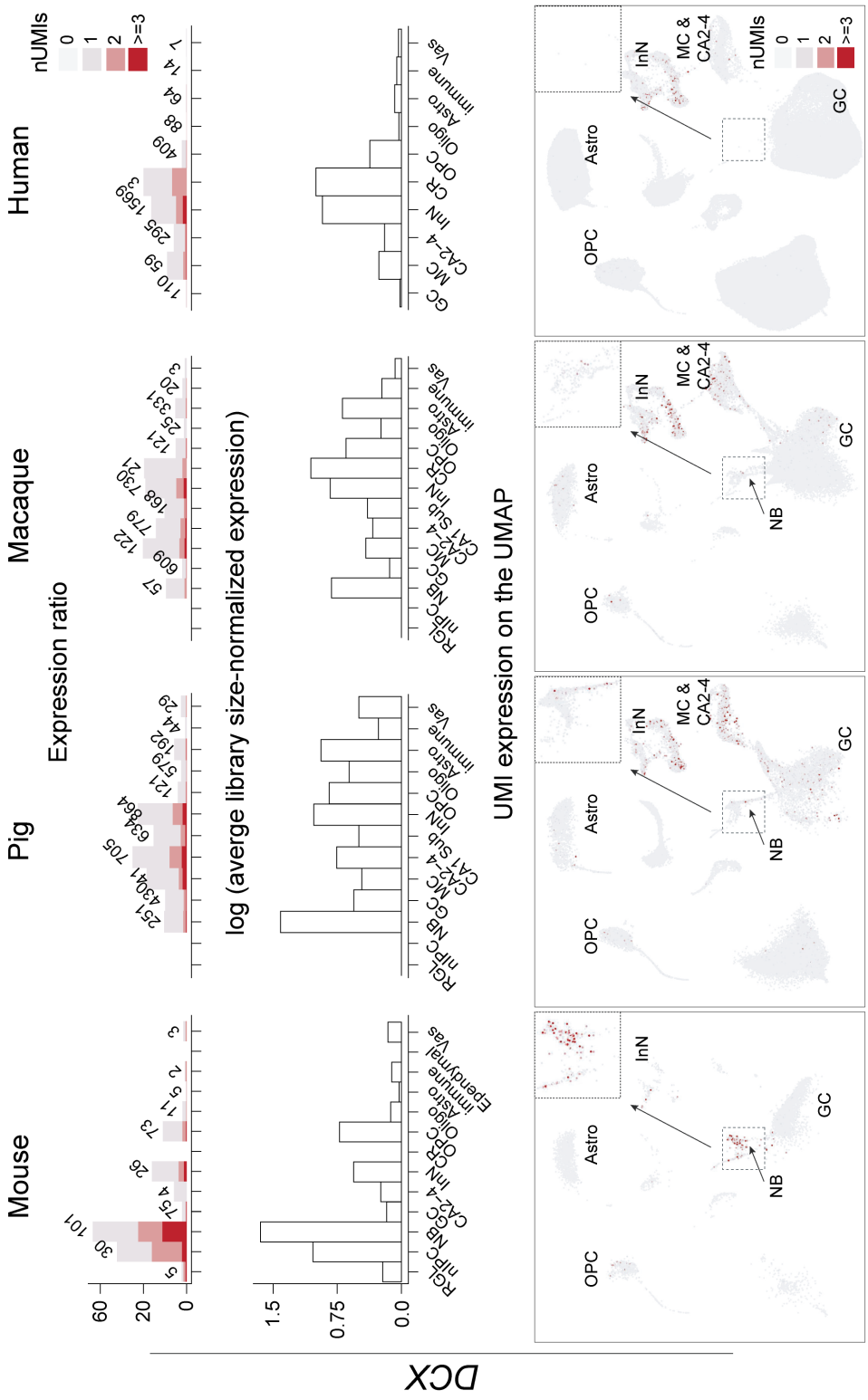

Figure 5.18 Hippocampal DCX expression across species. Top: The number (text label) and percentage (y axis) of cells expressing *DCX*. Middle: Average library size-normalized expression of *DCX*. Bottom: *DCX* expression on UMAP with insets highlighting the neuroblast domain. nIPC = neural intermediate progenitor cells; NB = neuroblast; GC = granule cell; RGL = radial glial cell; CA = Cornu Ammonis; Sub = subiculum; OPC = oligodendrocyte progenitor cell; Oligo = oligodendrocyte; Astro = Astrocyte; Vas = vasculature; MC = mossy cell; InN = inhibitory neuron

Source: Adapted from (185).

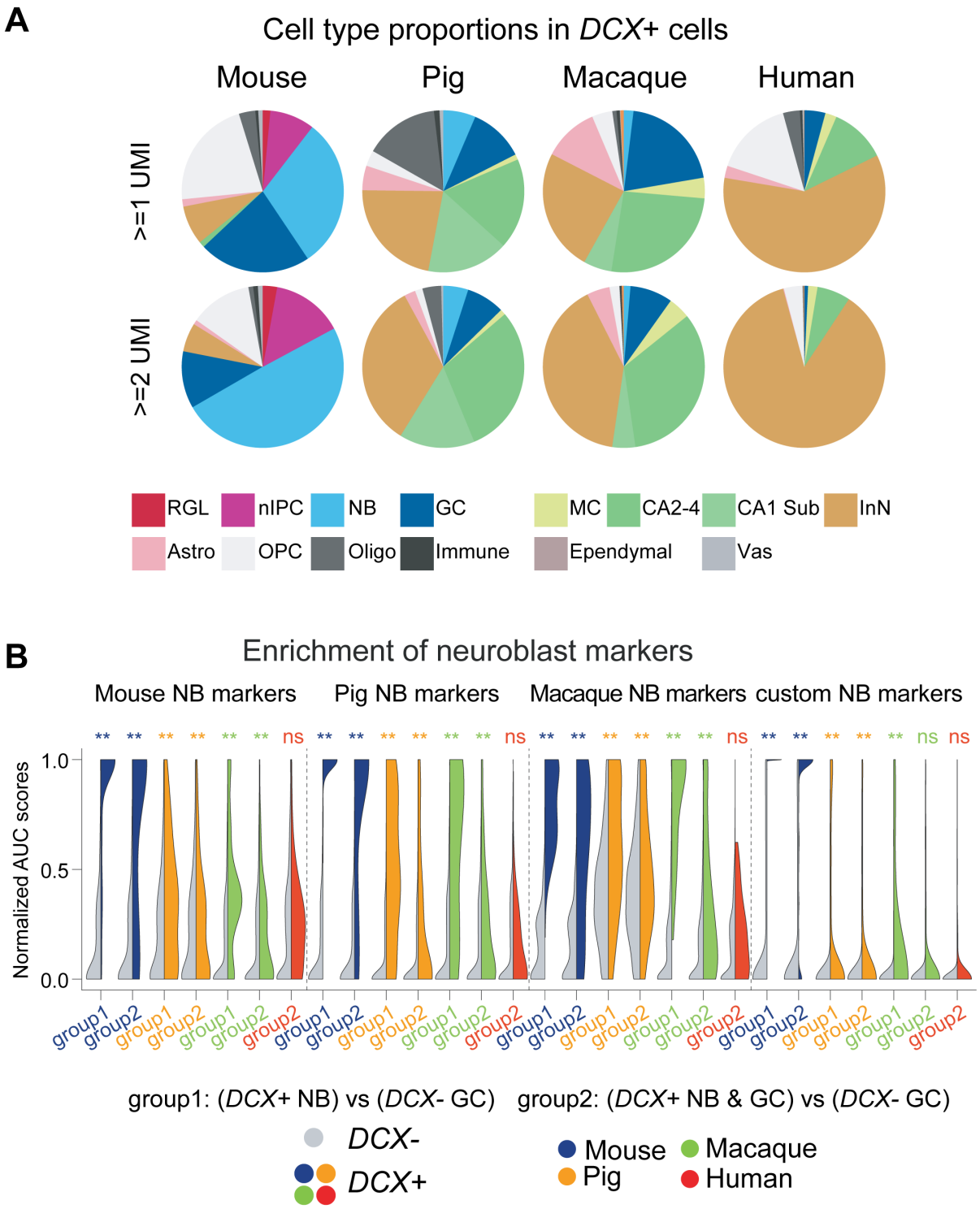

Figure 5.19 (A), Cell type proportions of *DCX*-expressing cells across species. **(B)**, Enrichment of different set of neuroblast markers in *DCX*+ compared to *DCX*- cells. Significance was tested using one-tailed Wilcoxon rank sum test (**: $p < 0.01$, ns: not significant). nIPC = neural intermediate progenitor cells; NB = neuroblast; GC = granule cell; RGL = radial glial cell; CA = Cornu Ammonis; Sub = subiculum; OPC = Oligodendrocyte progenitor cell; Oligo = oligodendrocyte; astro = Astrocyte; Vas = vasculature; MC = mossy cell; InN = inhibitory neuron
Source: Adapted from (185).

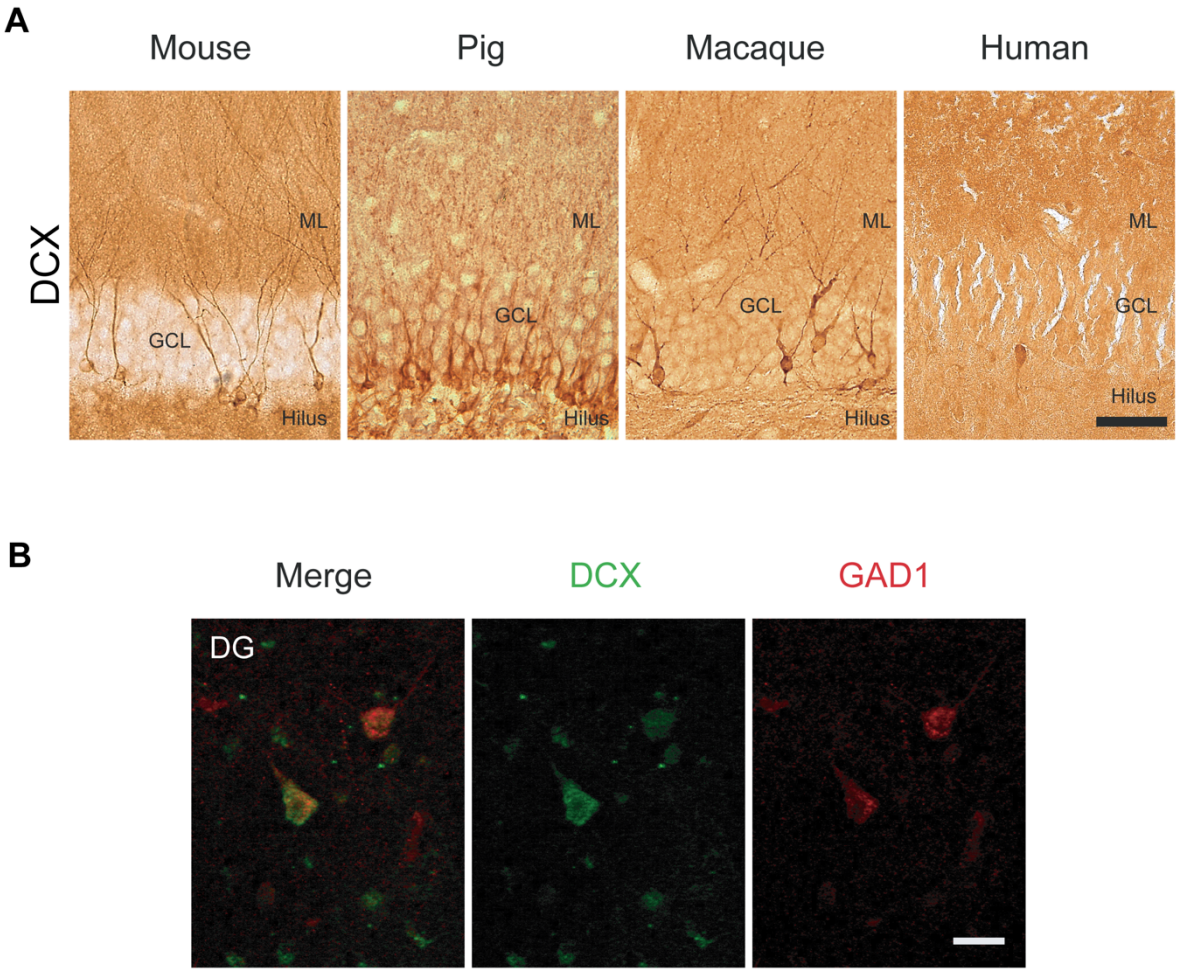

Figure 5.20 (A), Images of the mouse, pig, macaque and human DG immunolabeled against DCX. Scale bar represents 50 µm in mouse, pig and macaque and 75 µm in human. **(B),** Colocalization of DCX and GAD1 in cells with InN morphology in the molecular layer of the human DG. Scale bar is 30 µm. GCL = granular cell layer; ML = molecular layer.
Source: Adapted from (185).

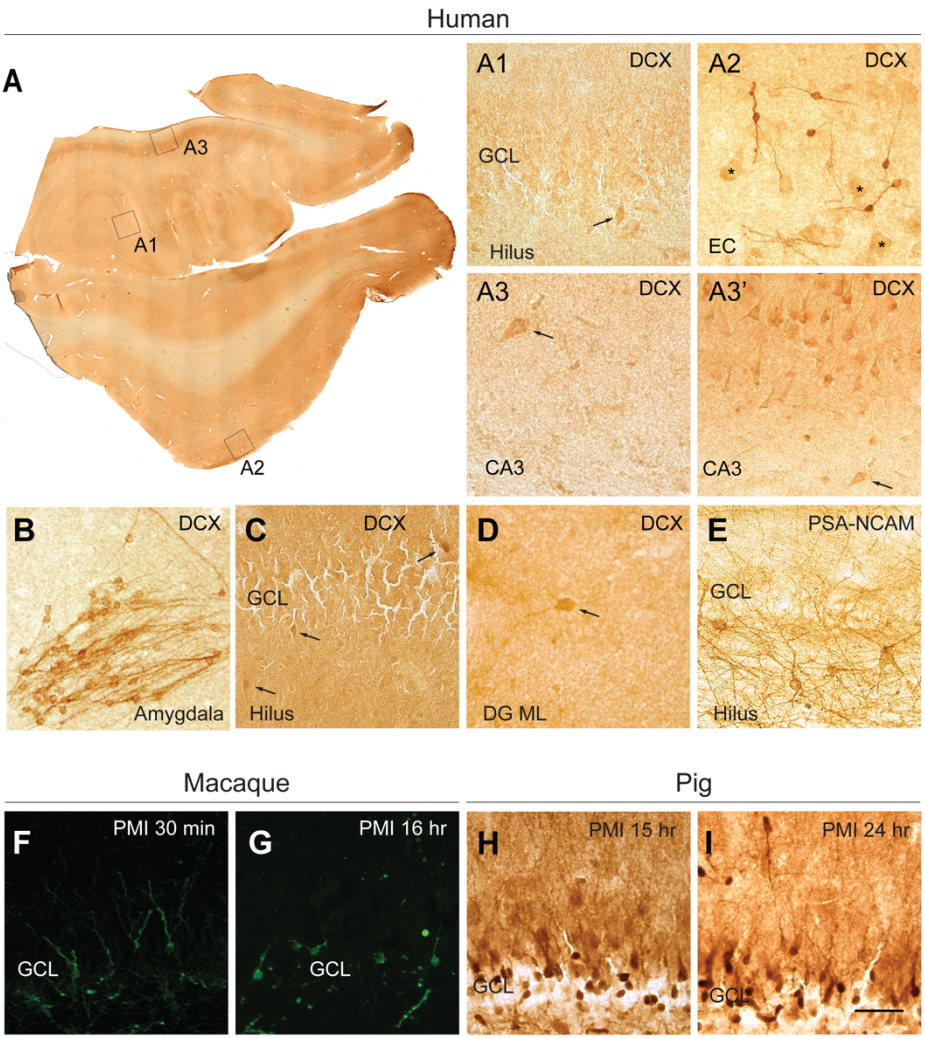

Figure 5.21 (A) Panoramic view of the human hippocampus immunolabeled for DCX (DCX-IL) indicating the location of panels A1-A3. A1, DCX-IL dentate gyrus illustrating the lightly labeled cells (arrow) occasionally found around the granule cell layer (GCL). A2, high magnification of the EC layer 2 showing cells clearly immunolabeled by DCX; ghostly, lightly stained cells with pyramidal morphology are marked with asterisks. A3, Lightly DCX-IL cell (arrow) in the stratum oriens of CA3. A3', Same cell (arrow) in the context of other lightly labeled cells in CA3, suggesting possible background staining. **(B)** DCX-IL reveals numerous clearly immunoreactive cells in the human amygdala. **(C-D)** examples of lightly DCX labeled cells typically located in the hilus, putative SGZ and molecular layer of the DG (arrows). **(E)** PSA-NCAM in the human hippocampus labels numerous cells, especially in the hilus of the DG, revealing lack of specificity to label neuroblasts or immature neurons. **(F-I)** Effects of PMI on DCX immunolabeling. F, G, DCX-IL cells in the GCL of rhesus macaque after 30 minutes and 16 hours PMI. H, I, DCX-IL cells in the GCL of domestic pig after 15 and 24 hours PMI. Reduced number of DCX-IL cells and increase in dendritic varicosities were observed with increased PMIs, but a sizeable number of cells could be detected. Pig showed occasional cells labeled in the molecular layer and a more immature, less consolidated granule cell layer and numerous cells immunolabeled for DCX in the subgranular zone (SGZ) but also in the hilus, as expected by the young age and the relatively protracted DG development in pigs, as previously described (259). DG = dentate gyrus; ML = molecular layer; CA = Cornu Ammonis; GCL = granule cell layer; EC = entorhinal cortex Scale bar represents 2.2 mm in A, 500 µm in A1, 40 µm in A2, 330 µm in A3, 70 µm in A3', 450 µm in B, 800 µm in C, 45 µm in D, 80 µm in E, 50 µm in F and G, 35 µm in H, 50 µm in I.
Source: Adapted from (185).

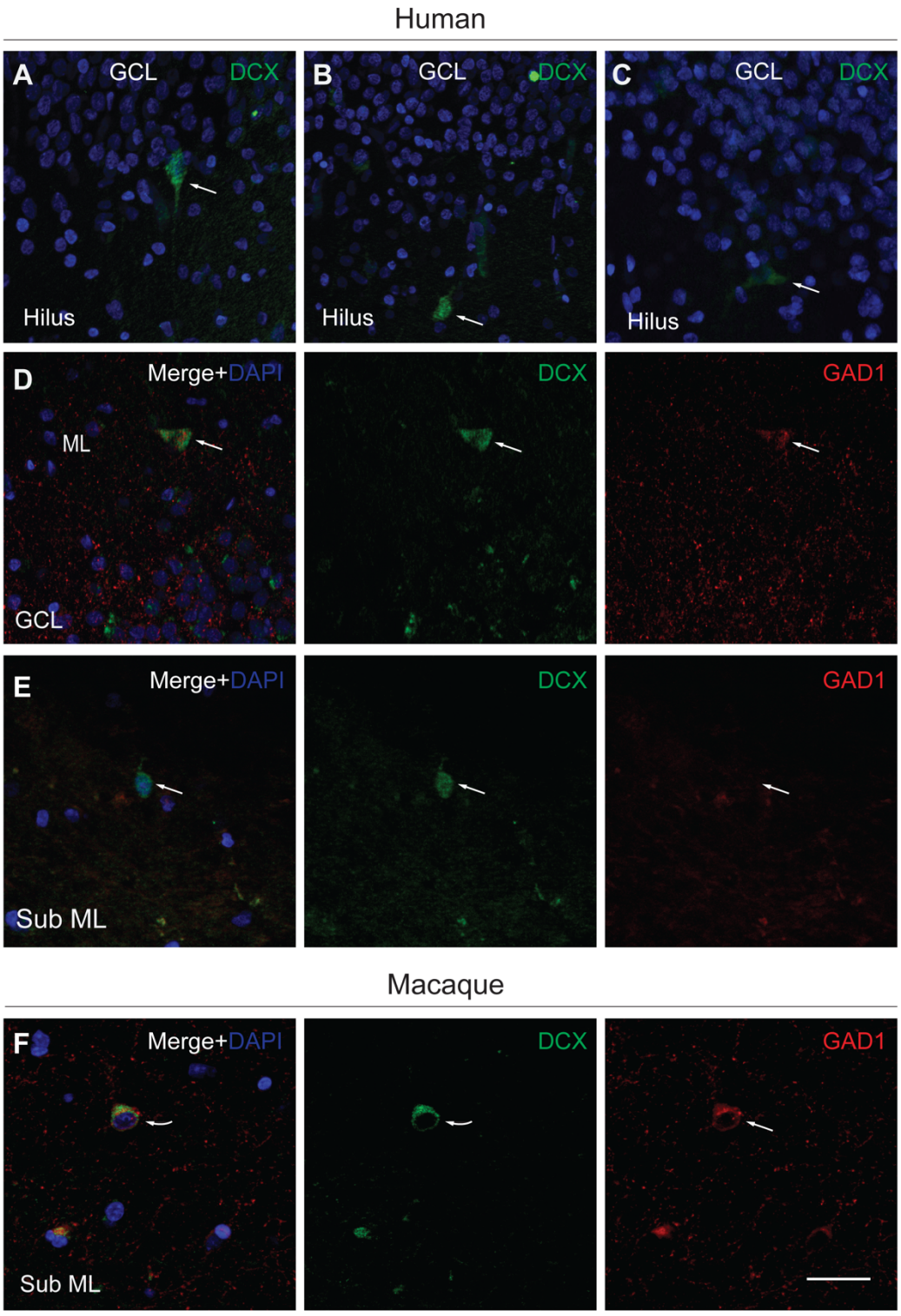

Figure 5.22 (A-B) Examples of DCX-IL in the GCL and hilar region of the human. **(D-F)** Immunofluorescence labeling of DCX and GAD1 in the hippocampus of human (D, E) and rhesus macaque (F). Notice colocalization of DCX and GAD1 in one cell (arrow) located in the molecular layer (ML) of the DG of the human (D) and in one cell (arrow) in the molecular layer of the subiculum (Sub ML) of the rhesus (F). Panel E illustrates a DCX-IL cell located in the Sub ML in the human immunonegative for GAD1. GCL = granule cell layer. Scale bar represents 40 µm in A, 50 µm in B, 35 µm in C, D, 25 µm in E and 30 µm in F.
Source: Adapted from (185).

Table 5.2 *DCX* expression in transcriptome data

		Species						
	Cell type	**Mouse (Juvenile), Hochgerner et al., 2018**	**Mouse (Young adult), Hochgerner et al., 2018**	**Pig (Young adult, 30min PMI), Present study**	**Pig (Young adult, 1hr PMI), Present study**	**Pig (Young adult, 7hr PMI), Present study**	**Rhesus (Adult), Present study**	**Human (Adult), Present study**
Cluster size and proportion	**GC**, n	3045	2340	2889	2411	3393	19803	32067
	RGL, n (%)	165 (5.42)	142 (6.07)	8 (0.28)	2 (0.08)	2 (0.06)	7 (0.04)	0 (0)
	nIPC, n (%)	88 (2.89)	62 (2.65)	4 (0.14)	2 (0.08)	4 (0.12)	23 (0.12)	1 (0.003)
	NB, n (%)	874 (28.7)	155 (6.62)	1606 (55.59)	1456 (60.39)	1210 (35.66)	400 (2.02)	1 (0.003)
	Astro, n	335	1143	2229	4182	4157	4196	17208
	InN, n	99	108	2553	1862	1141	2554	6397
≥ 1 UMI DCX+	**GC**, n (%)	159 (5.22)	75 (3.21)	430 (14.88)	314 (13.02)	416 (12.26)	609 (3.08)	110 (0.34)
	RGL, n (%)	1 (0.61)	5 (3.52)	0 (0)	0 (0)	0 (0)	0 (0)	0 (0)
	nIPC, n (%)	5 (5.68)	30 (48.38)	0 (0)	0 (0)	0 (0)	0 (0)	0 (0)
	NB, n (%)	230 (26.31)	101 (65.16)	251 (15.63)	185 (12.7)	230 (19.01)	57 (14.25)	0 (0)
	Astro n (%)	1 (0.3)	5 (0.44)	192 (8.61)	427 (10.22)	407 (9.79)	331 (7.89)	64 (0.38)
	InN, n (%)	15 (15.15)	26 (24.08)	864 (33.84)	652 (35.02)	498 (43.65)	730 (28.58)	1569 (24.52)
≥ 2 UMI DCX+	**GC**, n (%)	10 (0.33)	12 (0.51)	57 (1.97)	37 (1.53)	45 (1.33)	39 (0.2)	4 (0.01)
	RGL, n (%)	0 (0)	3 (2.11)	0 (0)	0 (0)	0 (0)	0 (0)	0 (0)
	nIPC, n (%)	0 (0)	15 (24.19)	0 (0)	0 (0)	0 (0)	0 (0)	0 (0)
	NB, n (%)	75 (8.58)	52 (33.55)	37 (2.3)	28 (1.92)	39 (3.22)	6 (1.5)	0 (0)
	Astro, n (%)	0 (0)	1 (0.09)	17 (0.76)	55 (1.32)	47 (1.13)	21 (0.5)	1 (0.01)
	InN, n (%)	1 (1.01)	6 (5.56)	247 (9.67)	194 (10.42)	179 (15.69)	184 (7.2)	466 (7.28)

The calculation is based on the down-sampling data across species. "n" represents the number of cells and "%" indicates the percentage among the GCs.

Source: Table adapted from (185).

Table 5.3: DCX immunostaining samples

Case	Species	Age (years)	Sex	PMI (h)	Fixation methods	DCX+ cells in DG	DCX+ cells in EC	DCX+ cells in Amygdala
H180	Human	42	Male	15	4% PFA (i)	0 (caudal level)	+	+
Hu19202	Human	78	Female	24	4% PFA (i)	(+)	+	+++
M1	Human	23	Male	3	4% PFA (i)	0	+	+++
M7	Human	49	Male	2.5	4% PFA (i)	(+)	0	+++
M8	Human	69	Male	3	4% PFA (i)	(+)	NA	+++
MSE	Human	NA	NA	NA	4% PFA (i)	0	0	+++
Hu2615	Human	46	Female	14	10% formaline (i)	(+)	+	++
Hu2616	Human	62	Female	22	10% formaline (i)	0	0	++
Hu2617	Human	33	Female	16	10% formaline (i)	0	++	++
Hu2691	Human	48	Female	16	10% formaline (i)	0	0	++
SS1	Pig	0.33	Female	0.5	4% PFA (i)	+++	NA	NA
SS2	Pig	0.33	Female	0.5	4% PFA (i)	+++	NA	NA
SS3	Pig	0.33	Female	0.5	4% PFA (i)	+++	NA	NA
SS4	Pig	0.33	Female	15	4% PFA (i)	+++	NA	NA
SS5	Pig	0.33	Female	15	4% PFA (i)	+++	NA	NA
SS6	Pig	0.33	Female	15	4% PFA (i)	+++	NA	NA
SS7	Pig	0.33	Female	24	4% PFA (i)	+++	NA	NA
SS8	Pig	0.33	Female	24	4% PFA (i)	+++	NA	NA
SS9	Pig	0.33	Female	24	4% PFA (i)	+++	NA	NA
RM1	Rhesus	8.1	Female	0	ICP and 4% PFA (i)	+++	+++	NA
RM2	Rhesus	8.3	Male	0	ICP and 4% PFA (i)	+++	+++	NA
RM3	Rhesus	15.3	Female	0.5	4% PFA (i)	+++	+++	NA
RM4	Rhesus	8.6	Female	16	4% PFA/10% formaline (i)	+	NA	NA
Mouse	Mouse	0.33	Female	0	ICP and 4% PFA (i)	+++	0	0

0: no DCX+ cells; (+): rare lightly immunolabeled DCX+ cells detected; +: rare moderately immunolabeled DCX+ cells detected; ++: often moderately and strongly immunolabeled DCX+ cells; +++: numerous moderately and strongly immunolabeled DCX+ cells; NA: not available; PFA: paraformaldehyde; ICP: Intracardiac perfusion; (i): immersion

Source: Table adapted from (185).

5.4 Taxonomic correlation among neural cells in the allocortex, mesocortex, and neocortex

To reveal the organizational principles across different cortices and the cell type alterations from allo- to neo-cortex, we compared cell profiles among subregions of the hippocampal system, and as well with those from the human middle temporal gyrus (MTG) (207) and the dorsolateral prefrontal cortex (dlPFC/DFC) (200) using previously published snRNA-seq datasets. Within the hippocampal system, we observed an evident differentiation between excitatory neurons of the hippocampal formation and those of entorhinal cortex (Figure 5.23A), as well as those of MTG and dlPFC (Figure 5.23B). As expected, given its laminar structure more close to neocortical areas, ExN of the EC showed more similarity with those of MTG and dlPFC. Likewise, we observed transcriptomic similarities between ExN in all neocortical layers in MTG and dlPFC (Figure 5.23B). Overall, we identified 15 region-specific ExN subtypes. These include three in the DG, two in CA2–CA4, two in CA1, two in Sub, five in the EC, and one in the dlPFC (Figure 5.23B).

We examined the extent of transcriptome similarities of excitatory neuron subtypes across regions and revealed a gradual transition from the hippocampal formation, EC, to the neocortex at the single cell level (Figure 5.24). Specifically, we found that the excitatory neurons of hippocampal formation were more similar to deep-layer neurons in EC (Figure 5.24). Consistent with this, the molecular markers for deep layers of the neocortex exhibited convergently higher expression in each subtype of the hippocampus as compared to upper-layer ones (Figure 5.25 and 5.26A). In addition, the intratelencephalic (IT) projection neurons exhibited lower expression of canonical markers in each of the hippocampal subtypes compared to other populations existing in neocortex (Figure 5.26B) which is in line with the previous finding showing lack of commissural connections of hippocampal formation (263). However, we did find one subtype of granule cells in the dentate gyrus that showed transcriptomic similarities with one upper-layer ExN subtype in the EC (Figure 5.24), potentially mirroring the parallels observed between the HIP and neocortex in mice (264). In EC, the specification of upper layers arose, with some of the upper-layer subtypes being molecularly close to neocortical upper layers (e.g. layer II *CUX2* and *CALB1*/*PDGFD*+ subtypes), however, not all the upper-layer neuron types in EC were faithfully recapitulated by the neocortex (Figures 5.23B and 5.24)For instance, two *RELN*-expressing layer II subtypes, in keeping with the previous analysis of reelin-expressing cells in EC upper layers (45), were detected in the EC but did not closely align with any ExN subtype identified in MTG or dlPFC. In addition, several upper-layer subtypes had mixed gene expression patterns characteristic of

both deep and upper layers (Figures 5.23B, 5.24, and 5.27). Ultimately, clear upper and deep distinction was observed in the neocortex (Figures 5.24, and 5.27).

Next, we identified several region-specific genes within the HIP, including *CHRNA1*, *METTL7B*, and *P2RX2* (Figure 5.27), and complemented this with analysis of their temporal expression. We found genes with clear up- and downregulation over developmental and aging periods suggesting their potentially important role in the hippocampal specification (Figure 5.28).

In contrast to our observations related to excitatory neurons, inhibitory interneurons did not demonstrate a clear transition between the allo-, meso-, and neo-cortex. We found only two HIP inhibitory neuronal populations (InN *MEIS2 SHISAL2B* and InN *SST ADAMTS12*) that did not clearly match any InN subtypes in the EC and neocortex (Figure 5.29A-B and 5.30). InN *MEIS2 SHISAL2B* refers to an interneuron subtype residing in the white matter and variations of the cell population could stem from the dissection differences (206, 208). InN *SST ADAMTS12* had high expression of two EvC ciliary complex genes, *EVC* and *EVC2* (Figure 5.31), associated with sonic hedgehog signaling in hippocampus (265-267). Finally, non-neuronal cell types were the most transcriptomically conserved populations across the allo-, meso-, and neocortex. We observed significant similarity in each NNC subtype across all regions (Figure 5.32A-B). We identified two astrocyte subtypes, Astro *AQP4 GFAP* and Astro *AQP4 CHRDL1*, which correspond to interlaminar astrocytes at layer 1 and protoplasmic astrocytes at layer 2 to 6, respectively, in all the 4 regions (Figure 5.33), suggesting that astrocyte lamination may not have emerged with a six-layered neocortex in mammals but may be an evolutionary conserved characteristic (207, 268).

Taken together, these results suggest that the excitatory neurons account for the most significant differences across the allo-, meso-, and neo-cortex. This includes a higher occurrence of IT projection neurons in the neocortex in contrast to the allocortex.

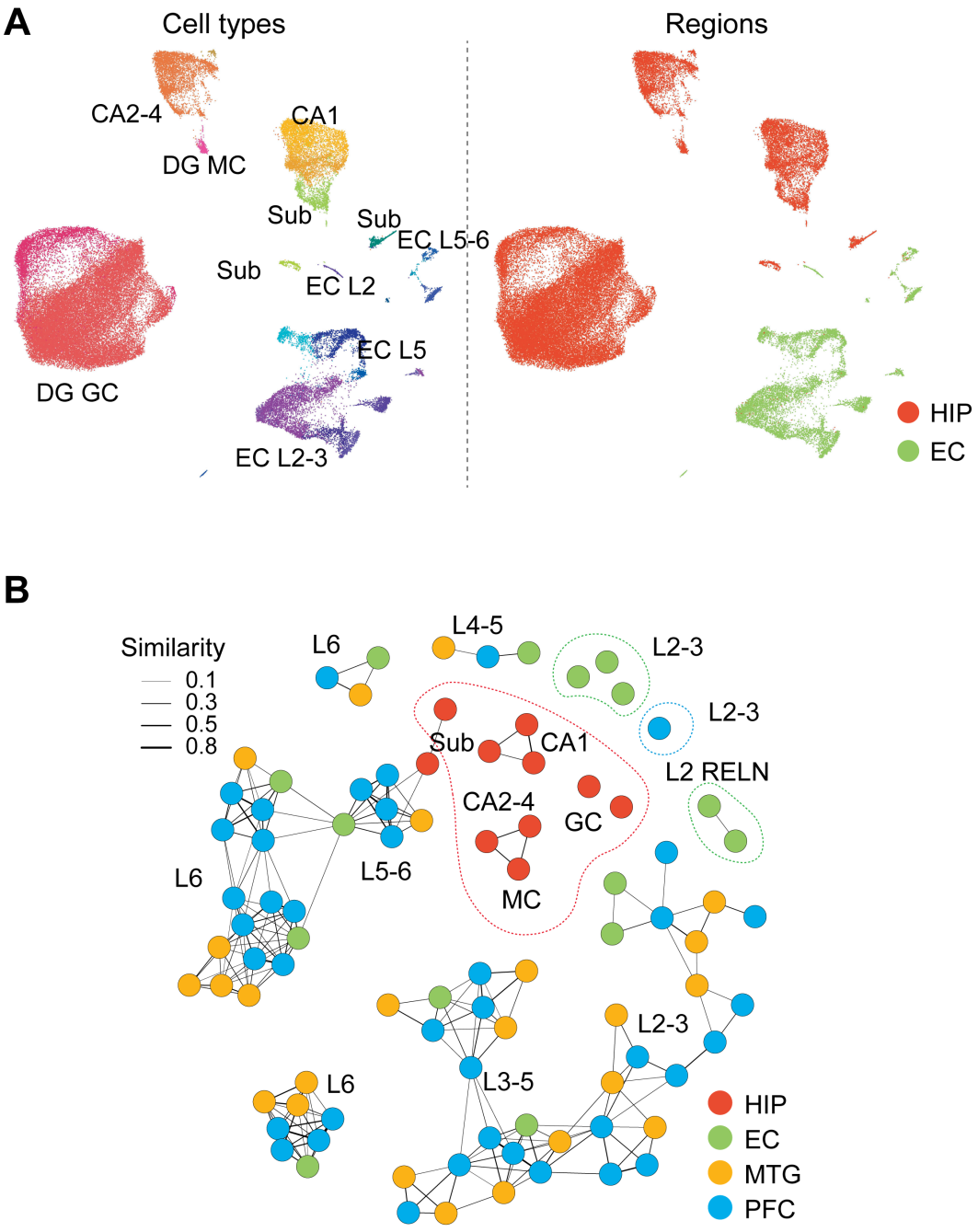

Figure 5.23 Transcriptomic similarities and differences of hippocampal, entorhinal and neocortical cell types. **(A)**, Left: UMAP showing all ExN nuclei colored by subtypes (left) or regions (right). **(B)**, Network demonstrating the extent of transcriptome similarities among ExN subtypes of HIP, EC, MTG (207) and dlPFC (200). Dots represent the subtypes within each brain region and the widths of lines represent the strength of similarity. Subtypes with regional-specificity were outlined in corresponding colors. DG = dentate gyrus; GC = Granule cell; CA = Cornu Ammonis; Sub = subiculum; MC = mossy cell; EC = entorhinal cortex; HIP = hippocampal formation; MTG = middle temporal gyrus; PFC = prefrontal cortex

Source: Adapted from (185).

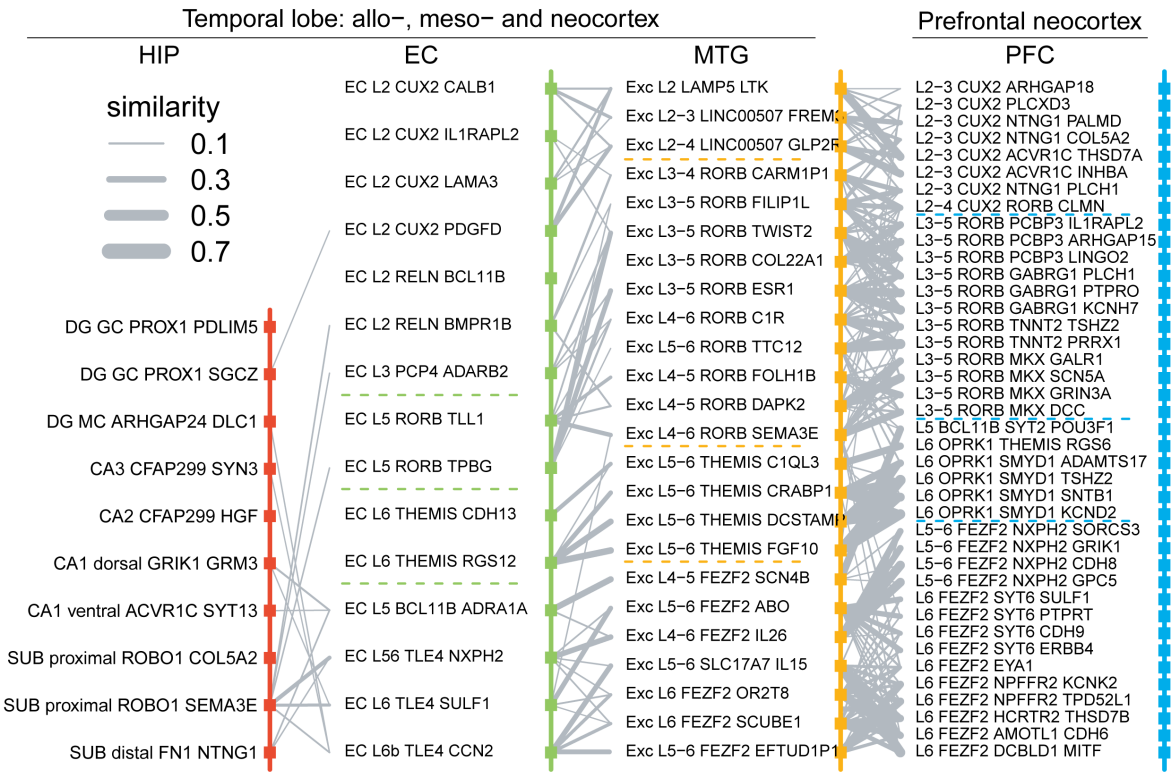

Figure 5.24 Transcriptomic relations across subtypes of pairwise regions organized according to layer distributions. Broad layer distinction was marked by dotted lines. DG = dentate gyrus; GC = granule cell; CA = Cornu Ammonis; Sub = subiculum; MC = mossy cell; EC = entorhinal cortex
Source: Adapted from (185).

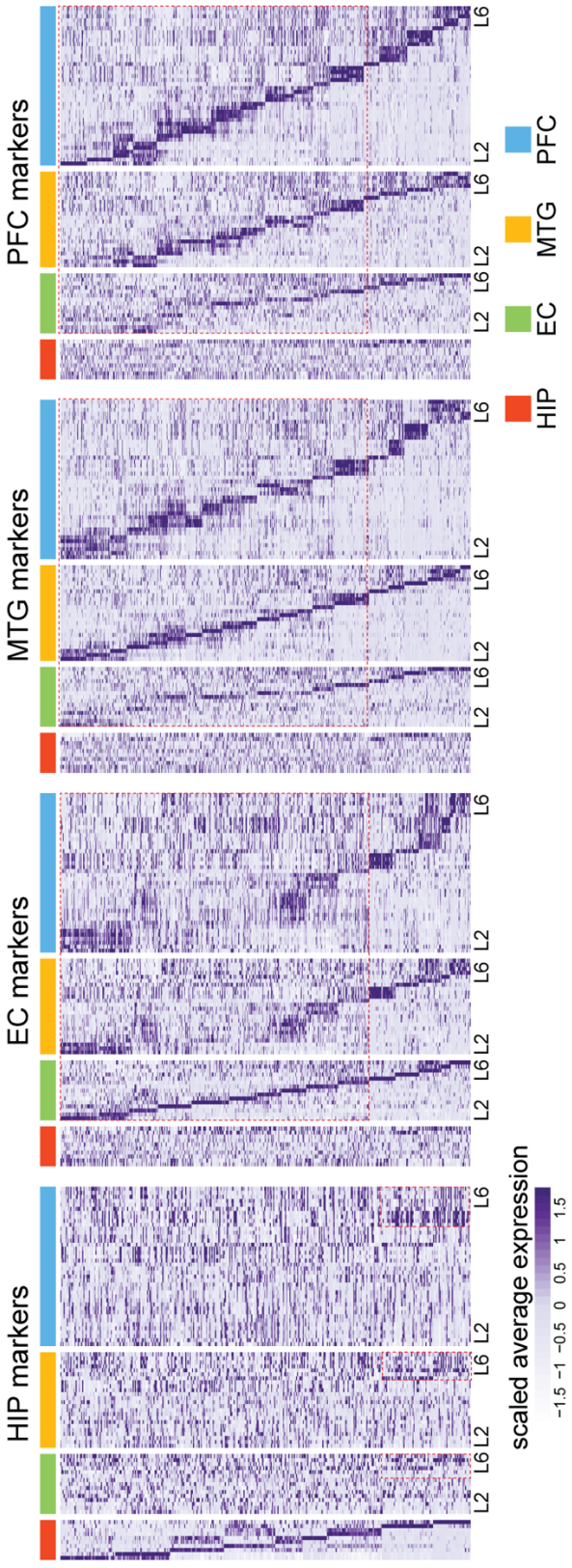

Figure 5.25 Heatmap depicting the expression of marker genes from a certain region (rows) across subtypes (columns) of all the four regions: HIP, EC, MTG and PFC. The relative expression enrichment of hippocampal marker genes in deep layers of EC, MTG and PFC, and the upper layer divergence between the EC and neocortex are outlined. HIP = hippocampal formation; EC = entorhinal cortex; MTG = middle temporal gyrus; PFC = prefrontal cortex

Source: Adapted from (185).

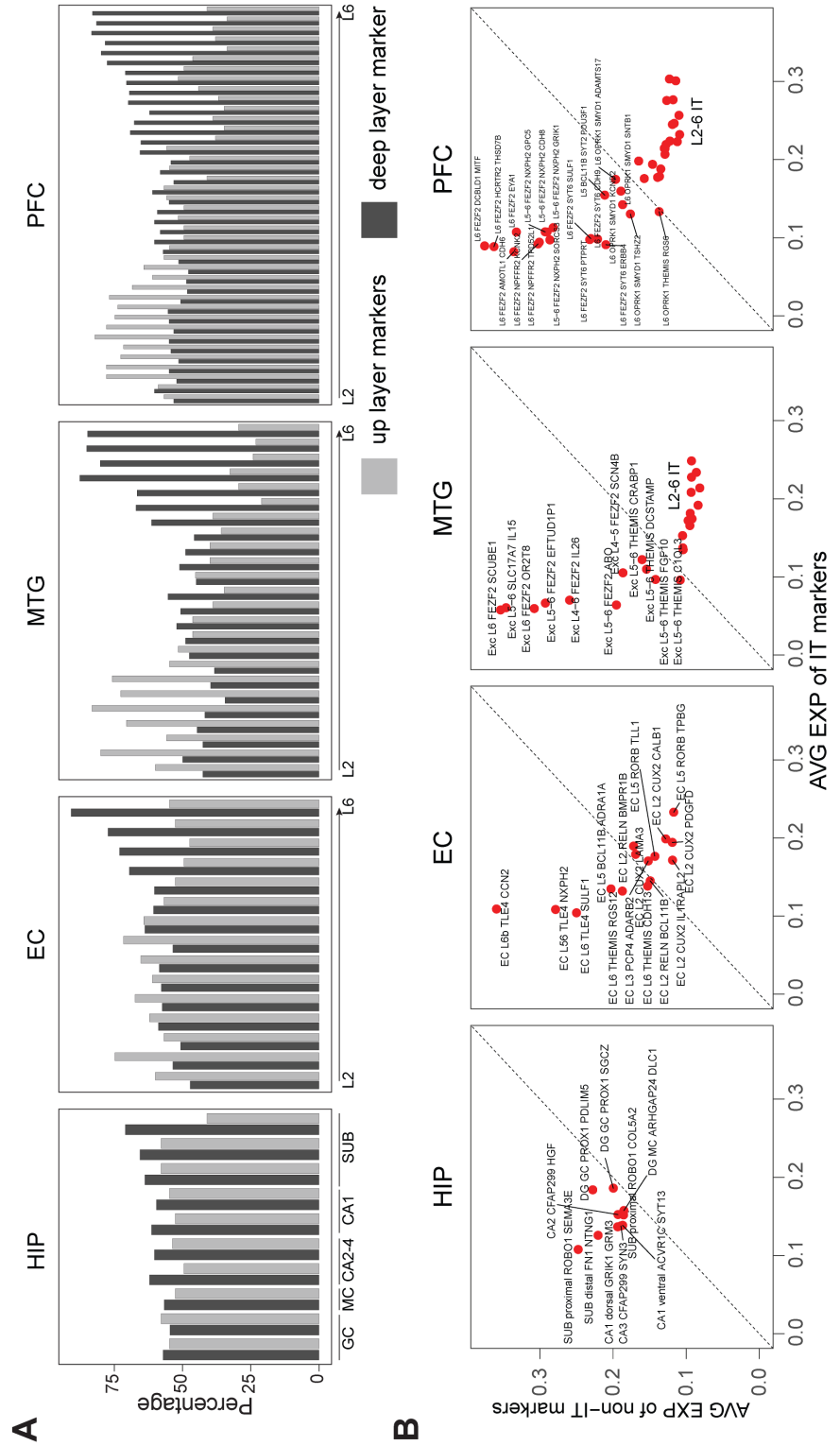

Figure 5.26 (A) Bar plots denoting the percentages of neocortical upper- (light grey) and deep- (black) layer marker genes that were expressed in each subtype of HIP, EC, MTG, and PFC. **(B)** Scatter plots showing the average expression of intratelencephalic (IT) neuron markers (x axis) versus that of non-IT markers (y axis) in each subtype of HIP, EC, MTG and PFC. HIP = hippocampal formation; EC = entorhinal cortex; MTG = middle temporal gyrus; PFC = prefrontal cortex
Source: Adapted from (185).

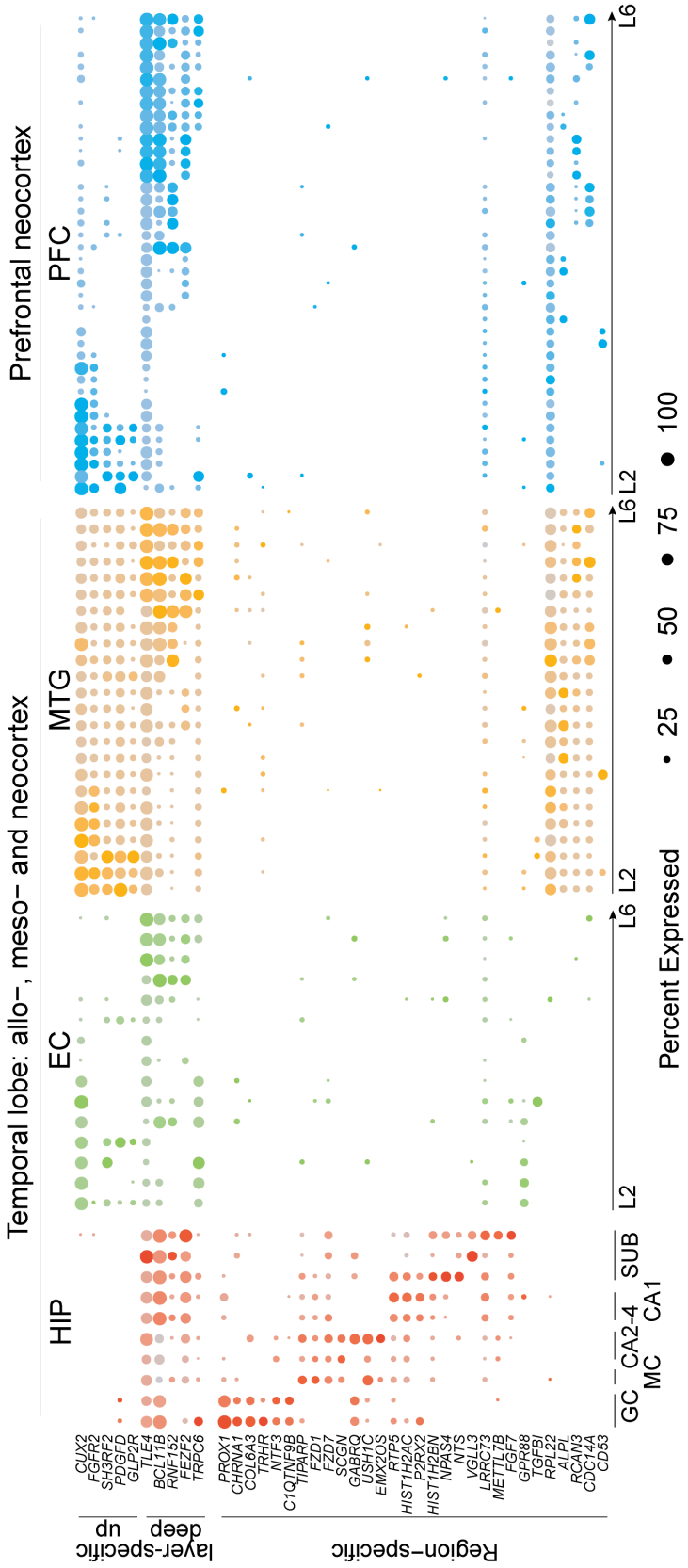

Figure 5.27 Expression of neocortical upper-layer and deep-layer markers, as well as region-specific genes. HIP = hippocampal formation; EC = entorhinal cortex; MTG = middle temporal gyrus; PFC = prefrontal cortex; GC = granule cell; CA = Cornu Ammonis; Sub = subiculum; MC = mossy cell
Source: Adapted from (185).

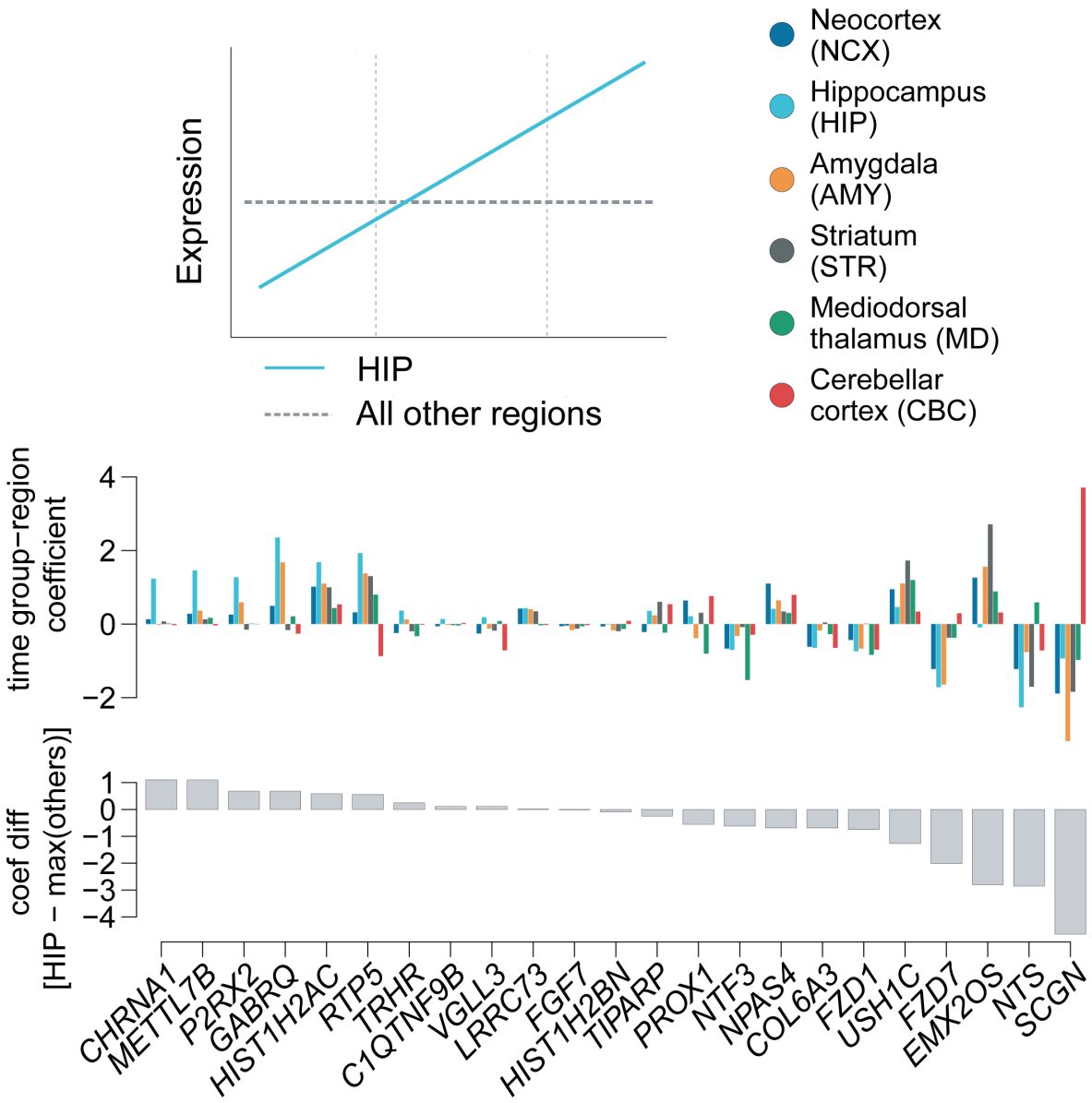

Figure 5.28 Rank of the hippocampus-specific genes based on their temporal specificity in adult hippocampus using PsychENCODE data (200). Top: Coefficients of time group-region with large positive values indicating upregulation along development (illustrated in the diagram). Bottom: Differences of the time group-region coefficients between HIP and the maximum of other regions. Source: Adapted from (185).

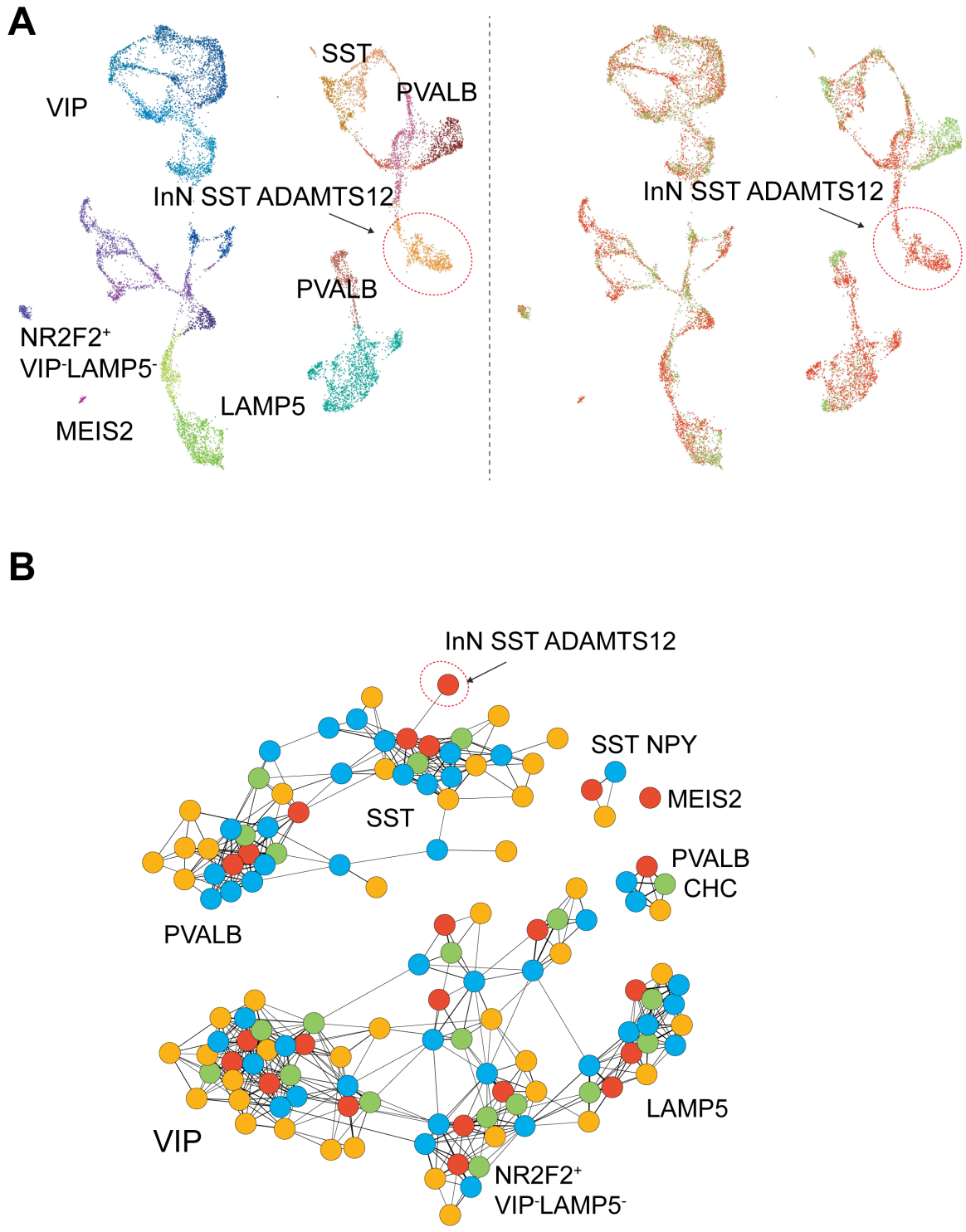

Figure 5.29 Transcriptomic similarities and differences of hippocampal, entorhinal and neocortical cell types. **(A)**, Left: UMAP showing all InN nuclei colored by subtypes (left) or regions (right). **(B)**, Network demonstrating the extent of transcriptome similarities among InN subtypes of HIP, EC, MTG (207) and dlPFC (200). Dots represent the subtypes within each brain region and the widths of lines represent the strength of similarity. Subtypes with regional-specificity were outlined in corresponding colors. InN = inhibitory neuron
Source: Adapted from (185).

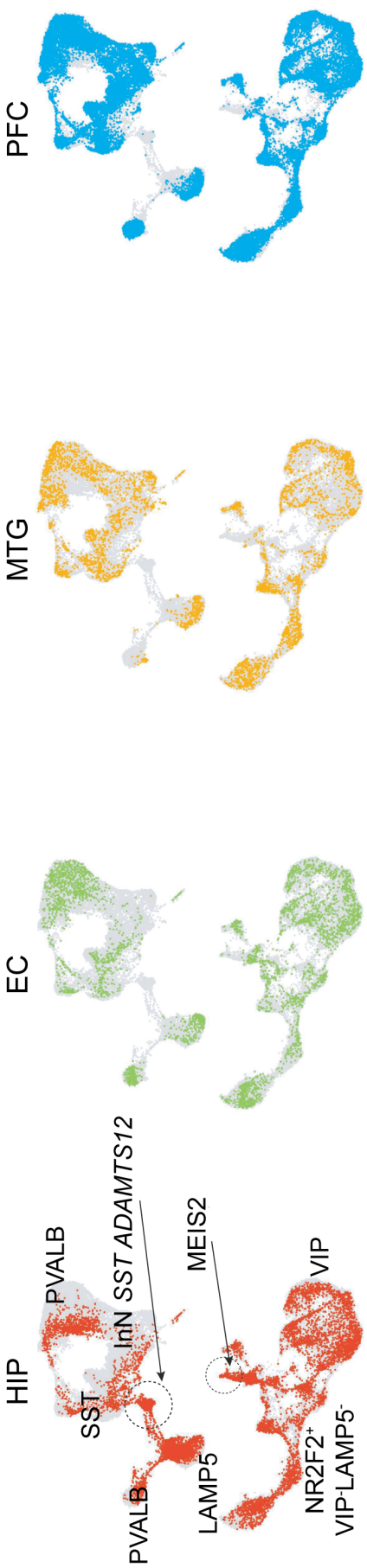

Figure 5.30 Integration of InN from 4 regions. Grey dots denote cells from other regions. HIP = hippocampal formation; EC = entorhinal cortex; MTG = middle temporal gyrus; PFC = prefrontal cortex
Source: Adapted from (185).

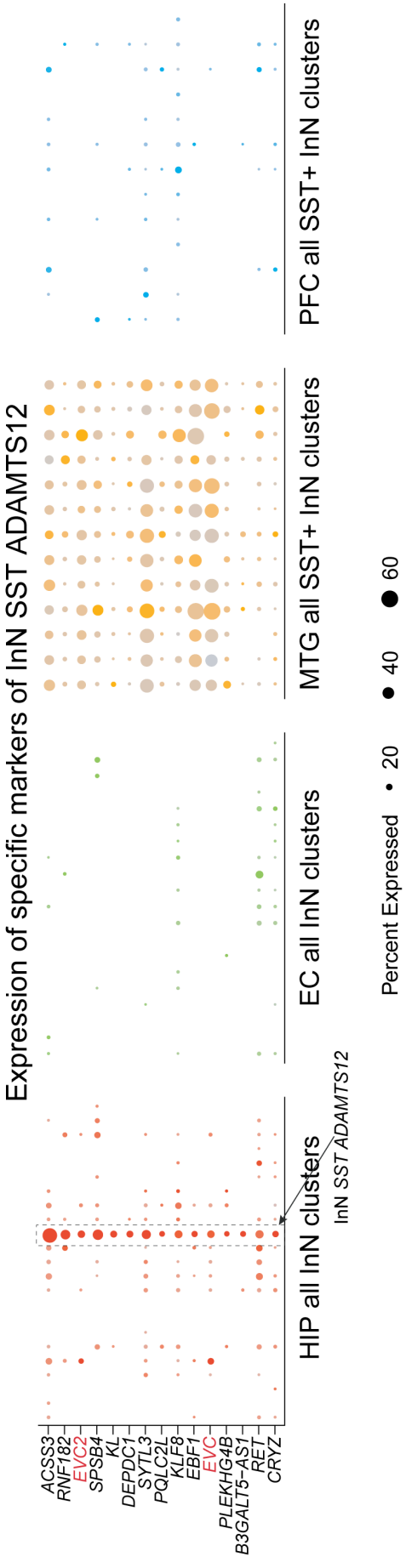

Figure 5.31 Expression of the exclusive markers (rows) of the cluster 'InN SST *ADAMTS12'* across all InN subtypes (columns) in HIP and EC, and all SST+ InN subtypes (columns) in MTG and dlPFC. HIP = hippocampal formation; EC = entorhinal cortex; MTG = middle temporal gyrus; PFC = prefrontal cortex
Source: Adapted from (185).

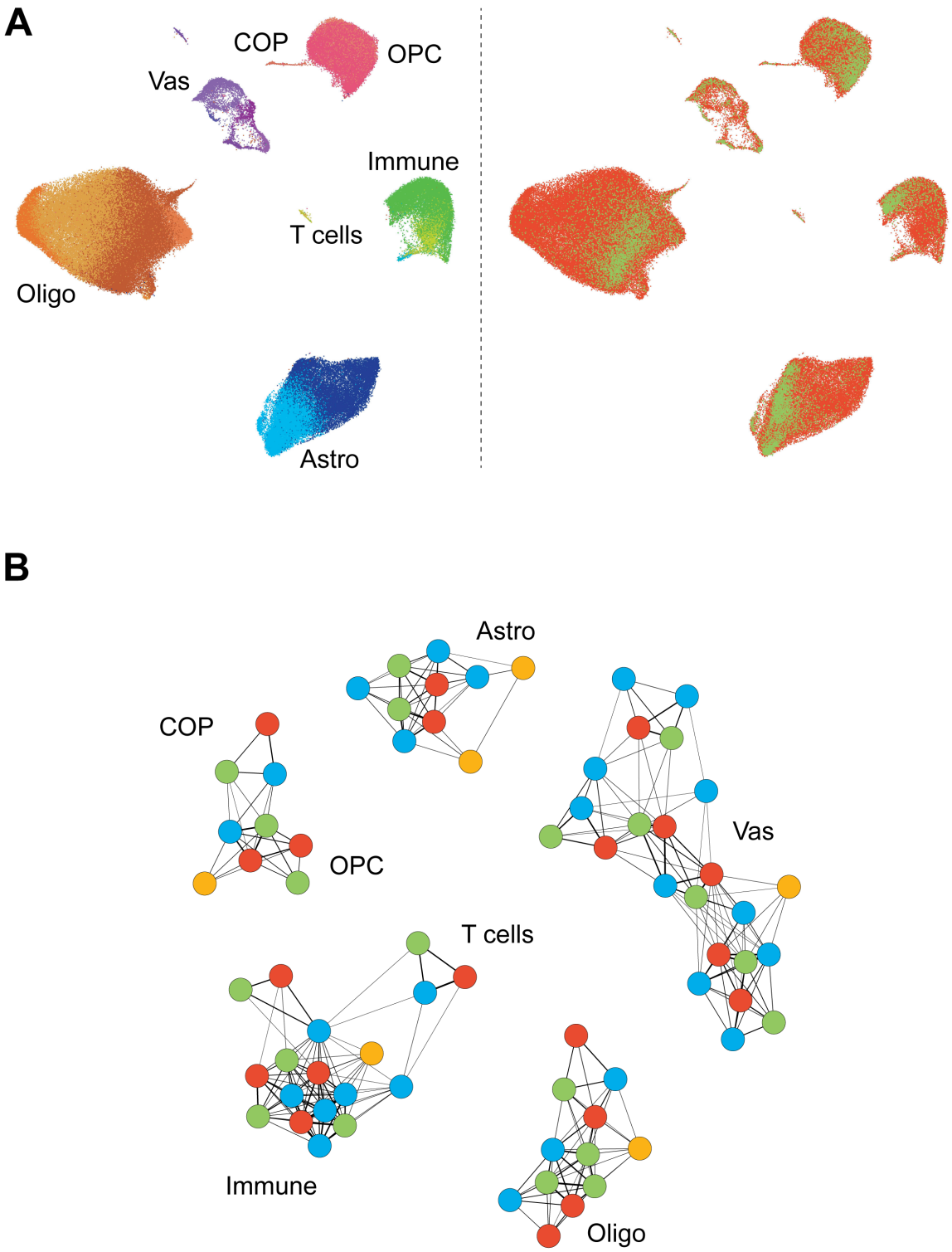

Figure 5.32 Transcriptomic similarities and differences of hippocampal, entorhinal and neocortical cell types. **(A)**, Left: UMAP showing all NNC nuclei colored by subtypes (left) or regions (right). **(B)**, Network demonstrating the extent of transcriptome similarities among NNC subtypes of HIP, EC, MTG (207) and dlPFC (200). Dots represent the subtypes within each brain region and the widths of lines represent the strength of similarity. Subtypes with regional-specificity were outlined in corresponding colors. NNC = non-neuronal cell; Astro = astrocyte; Oligo = oligodendrocyte; OPC = oligodendrocyte progenitor cell; COP = committed oligodendrocyte precursor cell; Vas = vasculature
Source: Adapted from (185).

# nuclei	Astro AQP4 GFAP	Astro AQP4 CHRDL1
DG	11787	5421
CA2-4	2044	573
CA1	1712	1733
Sub	690	1960
EC	1023	2851

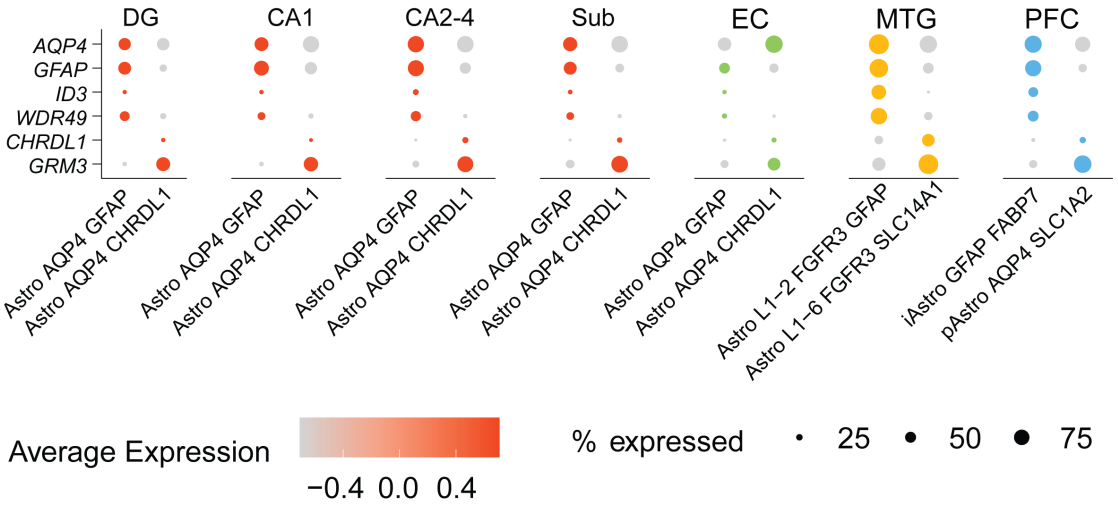

Figure 5.33 Left panel: table summarizing the number of cells of each astrocyte subtype across all subregions. Dot plots visualizing the expression of general astrocyte marker (*AQP4*), interlaminar (*GFAP*, *ID3*, *WDR49*) and protoplasmic astrocyte markers (*CHRDL1*, *GRM3*) across all the regions surveyed. DG = dentate gyrus; CA = Cornu Ammonis; Sub = subiculum; EC = entorhinal cortex; MTG = middle temporal gyrus; PFC = prefrontal cortex
Source: Adapted from (185).

5.5 Cell-type-specific and temporal expression of *METTL7B* across species

By intersecting transcriptomic datasets with cellular, regional, and temporal resolution, we identified *CHRNA1* and *METTL7B* as two genes with remarkable enrichment in adult hippocampal ExN (Figure 5.28). Genes that exhibit such specific expression profiles may underlie unique biology of that cell type or region. We used this rationale as our motivation to explore how these genes play a role in hippocampal physiological function and potentially related pathology. Because *CHRNA1* belongs to the nicotinic acetylcholine receptors family which has been extensively investigated in the context of AD (269, 270), we focused on elucidating some foundational biology of *METTL7B* since it has not been studied in the context of the vertebrate brain. *METTL7B* is predominantly expressed in the liver and encodes a membrane protein associated with the endoplasmic reticulum (ER) and lipid droplets (LD) (228). By amino acid sequence homology, *METTL7B* is predicted to belong to the methyltransferase superfamily, a large family of proteins that use S-adenosyl-L-methionine (SAM) as the methyl donor in methylation reactions (271, 272).

We first investigated the expression patters of *METTL7B* across species using snRNA-seq and found that *METTL7B* is expressed in the human and rhesus macaque brain and not detected in the pig or mouse brain (Figure 5.34). In humans, we found moderate expression in astrocytes and the highest expression in ExN, with highest levels in the DG, followed by CA2-4, and subiculum (Figure 5.34). Immunolabeling of the human HIP confirmed that the highest *METTL7B* signal intensity was in DG granule neurons and pyramidal neurons in CA2, with lesser expression in CA3-4 subfields and Sub, as well as astrocytes, and almost no expression in CA1 and non-pyramidal subicular layers (Figure 5.35). The staining patterns observed in rhesus macaques closely resemble those of humans, with robust immunolabeling for METTL7B in hippocampal DG, CA2 and subicular pyramidal neurons (Figure 5.36). While its expression was found in the same homolog cell types in rhesus macaque, the relative enrichment of expression exhibited distinct patterns with astrocytes.

Though we found significant HIP enrichment of METTL7B, we also observed minimal expression in human MTG (Figure 5.27), prompting us to investigate 11 areas of the adult human neocortex. We found the highest expression in M1C and S1C (Figure 5.37A). On immunolabeling, we observed high levels in the large pyramidal neurons of layer 5B (Figure 5.38), such as Betz and Meynert cells in M1C and V1C, respectively. Interestingly, these specific areas, layers, and cell subtypes are typically affected by AD-related pathology at later stages of the disease (170, 171, 174-178, 273, 274). We observed similar findings in rhesus

macaque with limited METTL7B expression in the upper layers (L2-4), layer 5A, and CA1 neurons (Figure 5.36). On immunoelectron microscopy, we detected METTL7B in neurons and astrocytes in the adult human and rhesus macaque hippocampus and confirmed previous reports that METTL7B colocalizes with the endoplasmic reticulum and lipid droplets (Figure 5.39A-B).

We also validated our snRNA-seq results, showing that *METTL7B* is enriched in the adult human hippocampus (Figure 5.37B-D). We then expanded our analysis to other primates and analyzed *METTL7B* expression in the same 16 homologous regions in the human, chimpanzee, and rhesus macaque brain using previously published datasets (103, 123). We found similar *METTL7B* expression patterns in human and chimpanzee (Figure 5.40A). However, *METTL7B* was more broadly expressed throughout the brain in rhesus macaques, possibly related to the increased levels detected in astrocytes (Figure 5.34 and 5.36). Next, we analyzed this expression profile in the mouse brain and using RNA and antibody-based analyses determined that in contrast to primates, the brain regions we sampled in mice do not express *Mettl7b* (Figure 5.37E-F). Using a knock-in *lacZ* reporter mouse line, we confirmed that while the liver expresses high levels of *Mettl7b*, it is not detected in the brain (Figure 5.41). We expanded our analysis of *METTL7B* homologs across species at different developmental stages using previously published datasets and found enrichment in the human and macaque brain, but not in the mouse, rat, rabbit, and opossum brain (Figure 5.40B) (103, 123, 275).

These results suggest that *METTL7B* expression and its potential role in the hippocampal physiological function may be primate specific.

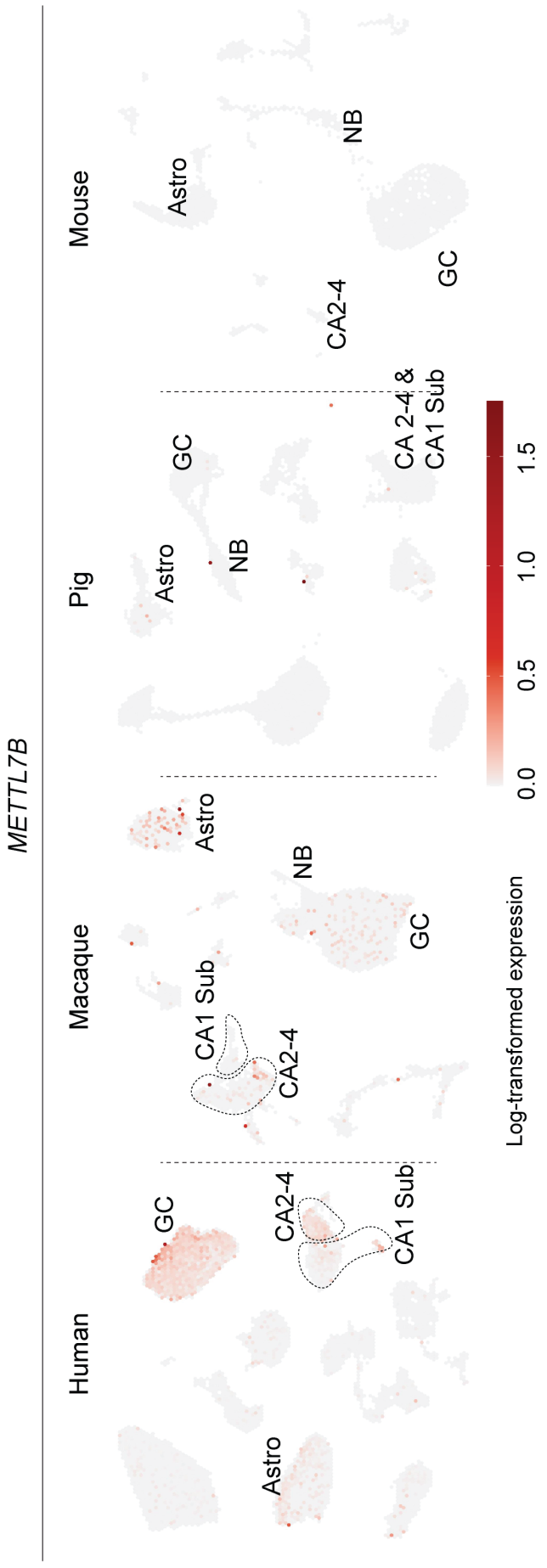

Figure 5.34 *METTL7B* expression in adult human HIP-EC, macaque DG, pig HIP and mouse DG. GC = granule cell; CA = Cornu Ammonis; Sub = subiculum; EC = entorhinal cortex; Astro = astrocyte; NB = neuroblast
Source: Adapted from (185).

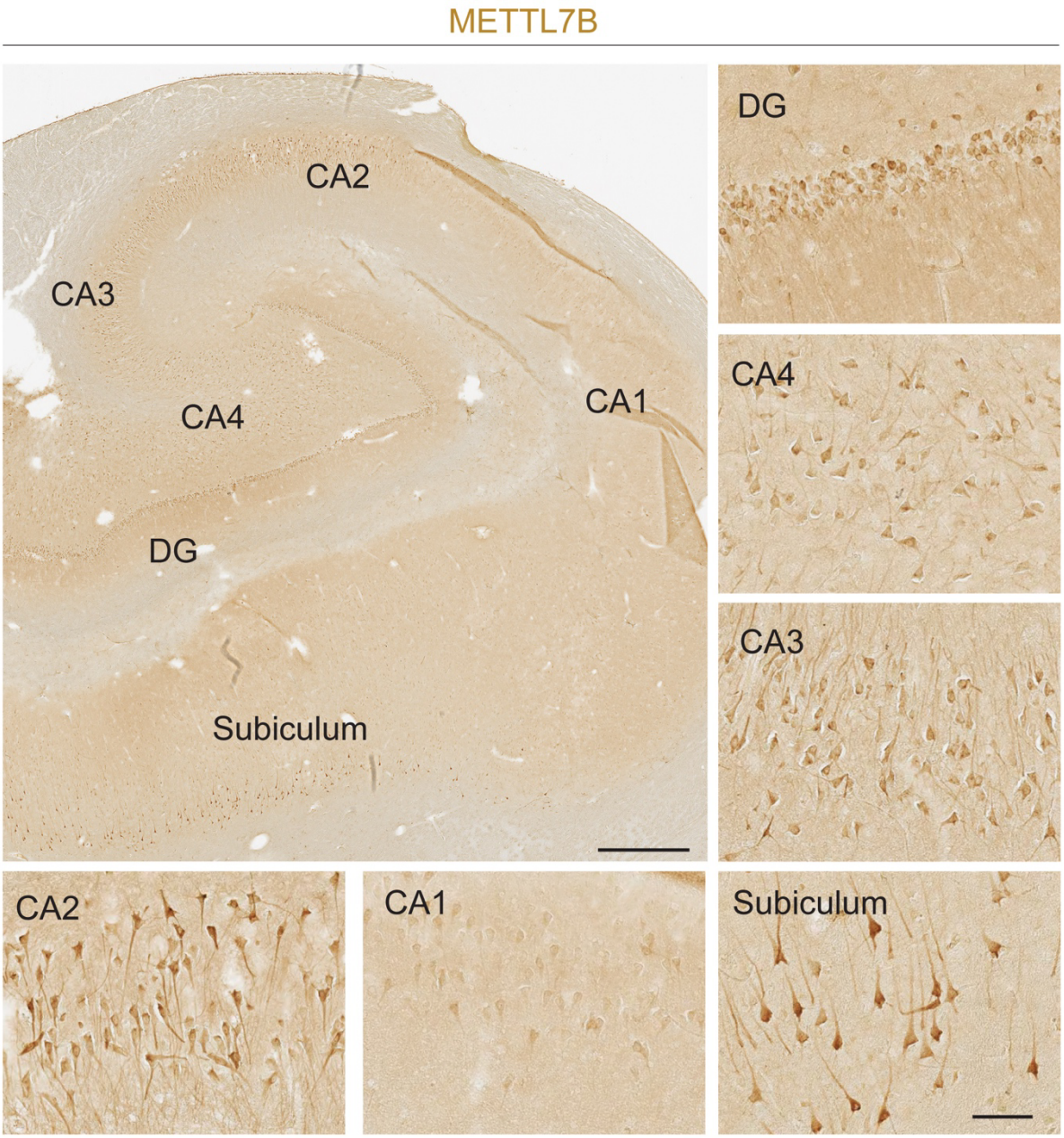

Figure 5.35 METTL7B immunostaining of adult human hippocampus. Scale bars = 1 mm; insets = 100 µm; immunofluorescence = 10 µm. DG = dentate gyrus; CA = Cornu Ammonis; Sub = subiculum; Source: Adapted from (185).

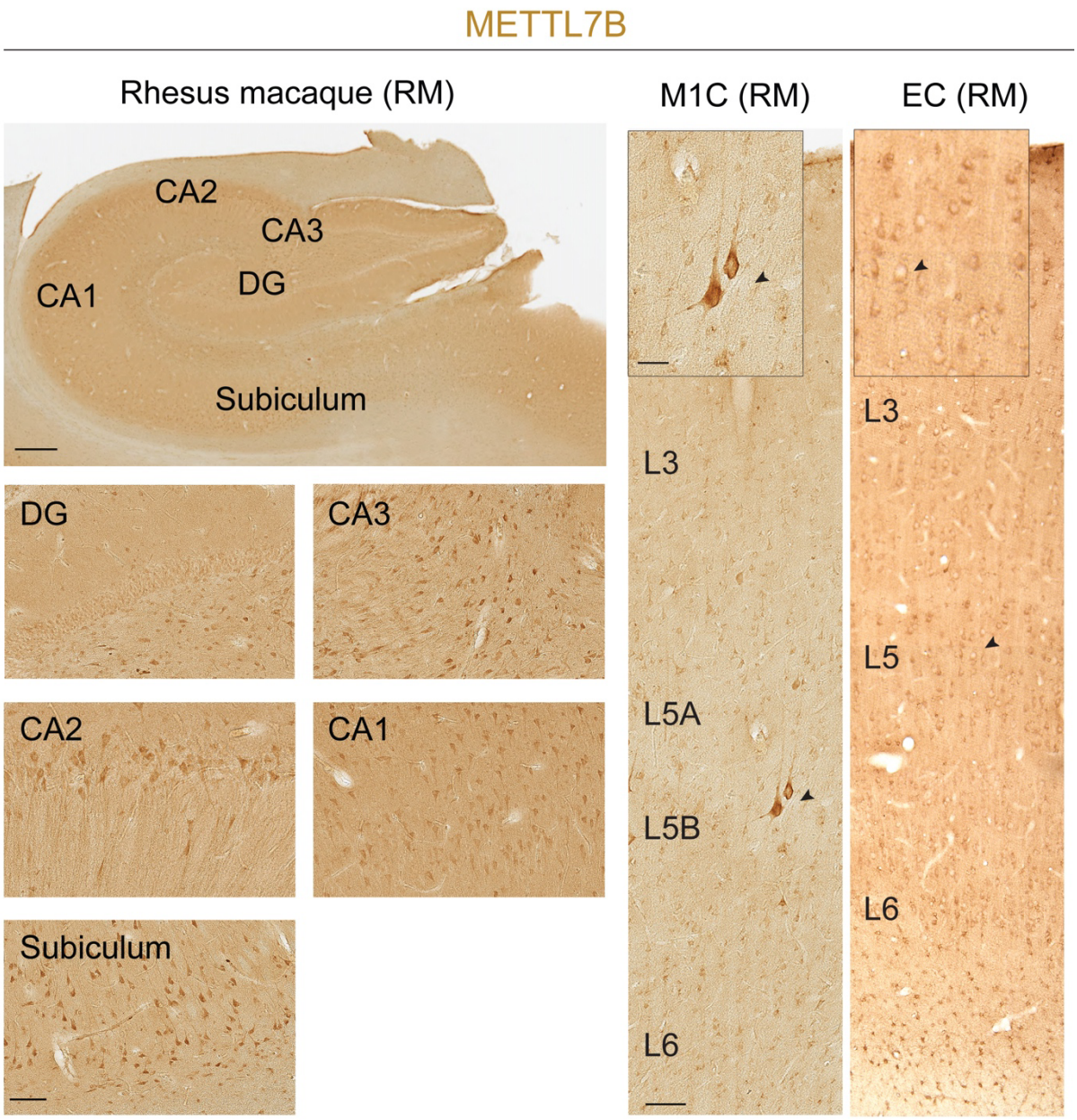

Figure 5.36 METTL7B immunolabeling of hippocampus, Betz cells, and pyramidal neurons in rhesus macaque brain. DG = dentate gyrus; CA = Cornu Ammonis; Sub = subiculum. M1C = primary motor cortex; EC = entorhinal cortex. Scale bars = 100 µm; inset = 50 µm.
Source: Adapted from (185).

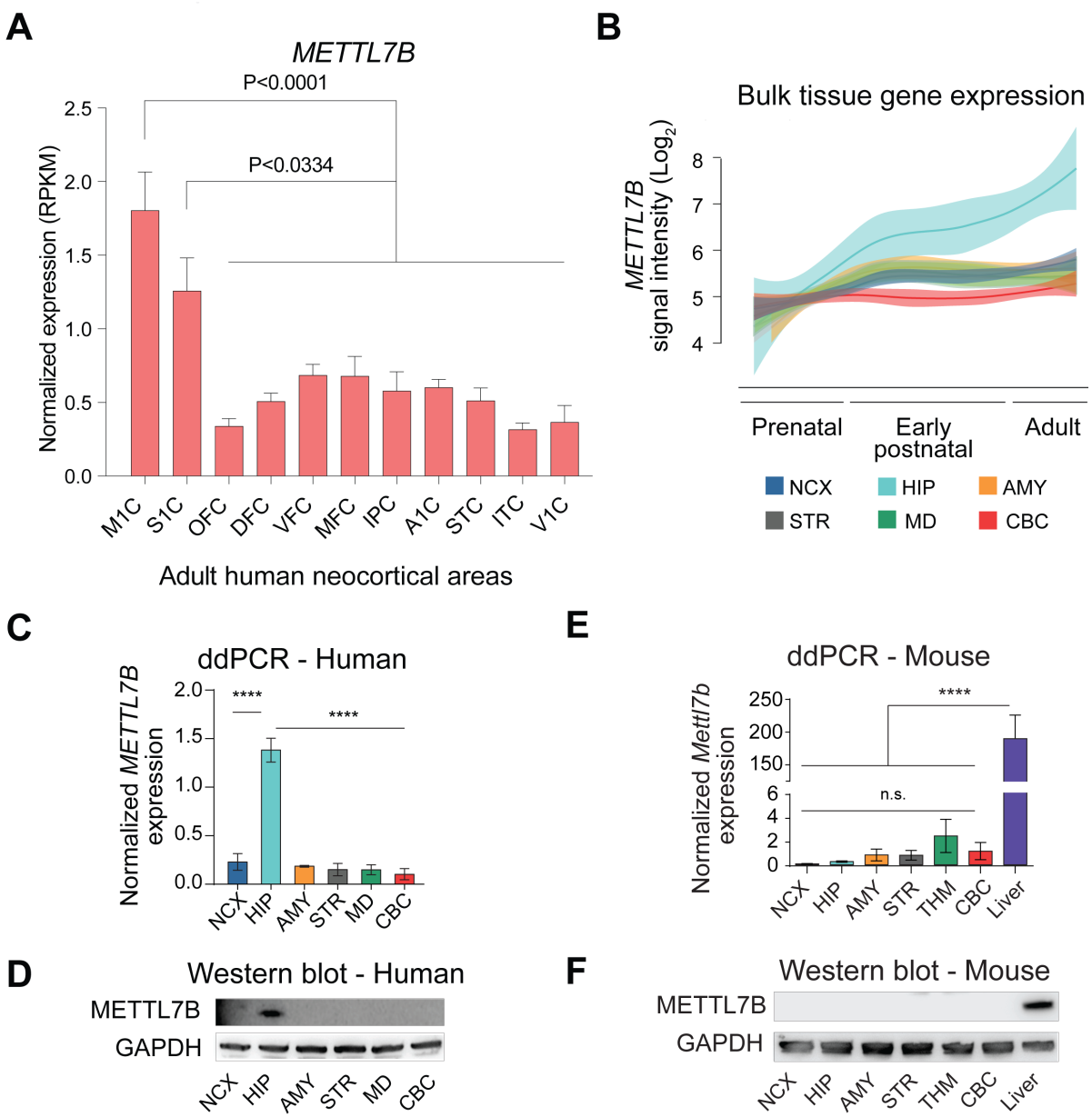

Figure 5.37 *METTL7B* expression pattern in human and mouse tissues

(A) RNA-seq expression of *METTL7B* in human neocortex. One-way ANOVA with post- hoc Dunnett's adjustment, all groups N=6, except MFC N=5. Data are means ± SEM.

(B), Expression of *METTL7B* showing temporal specificity in adult human hippocampus (122).

(C-D), Droplet digital PCR and immunoblot validation in six regions of adult human brain. One-way ANOVA with post-hoc Dunnett's adjustment (****P<0.0001), N=3 per group.

(E-F), Same as C-D using mouse tissues, including liver as a positive control. M1C = primary motor cortex; S1C = primary sensory cortex; OFC = orbital prefrontal cortex; DFC = dorsolateral prefrontal cortex; VFC = ventrolateral prefrontal cortex; MFC = medial prefrontal cortex; IPC = posterior inferior parietal cortex; A1C = primary auditory cortex; STC = superior temporal cortex; ITC = inferior temporal cortex; V1C = primary visual cortex; AMY = amygdala; NCX = neocortex; HIP = hippocampal formation; STR = striatum; MD = mediodorsal nucleus of the thalamus; CBC = cerebellar cortex

Source: Adapted from (185).

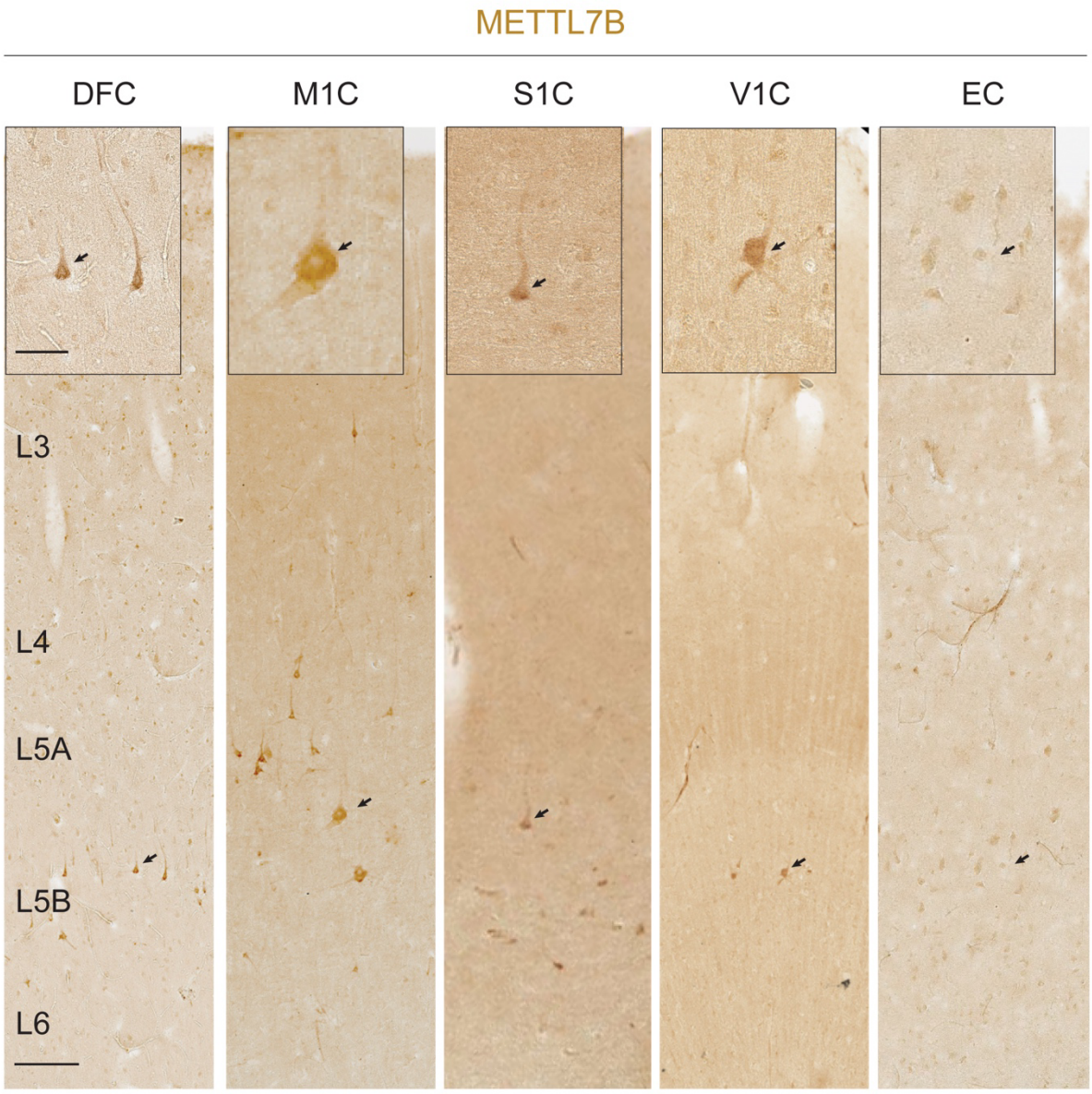

Figure 5.38 Prominent immunolabeling of layer 5B (L5B) pyramidal neurons (arrowheads), including Betz and Meynert cells in M1C and V1C, respectively. DFC = dorsolateral prefrontal cortex; M1C = primary motor cortex; S1C = primary sensory cortex; V1C = primary visual cortex; EC = entorhinal cortex. Scale bars = 150 µm; insets = 50 µm
Source: Adapted from (185).

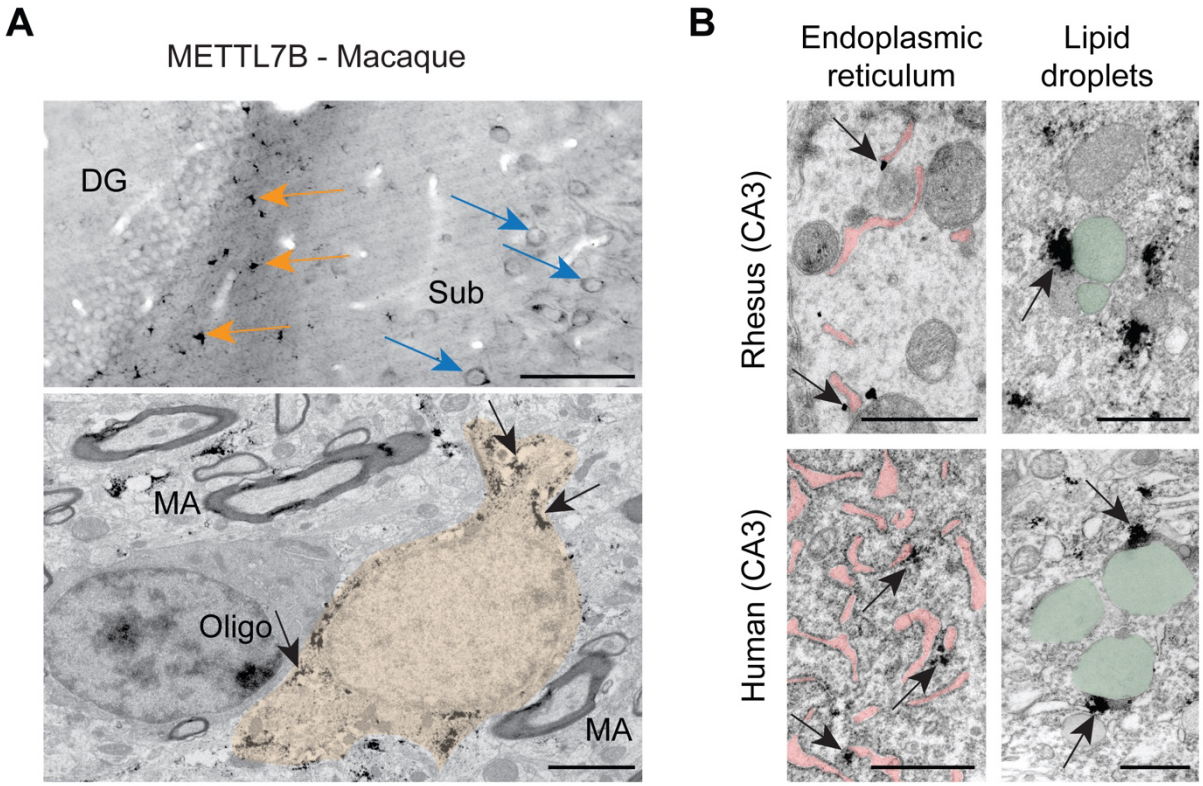

Figure 5.39 Immunoelectron microscopy of METTL7B
(A), Upper panel: Numerous METTL7B immunopositive astrocytes (orange arrows) and neurons (blue arrows). Bottom panel: Immunoelectron microscopy of astrocytes (orange; pointed with arrows). Scale bar is 100 µm (upper) and 2 µm (bottom). MA, myelinated axon. **(B)**, Immunoelectron microscopy CA3 hippocampal pyramidal neurons in rhesus macaque and human. Notice METTL7B labeling (arrows) on the outer surface of ER cisterns (pink) and in contact with LDs (green). Scale bar is 1µm for each panel. DG = dentate Gyrus; Sub = subiculum; Oligo = oligodendrocyte; MA, myelinated axon; CA = Cornu Ammonis
Source: Adapted from (185).

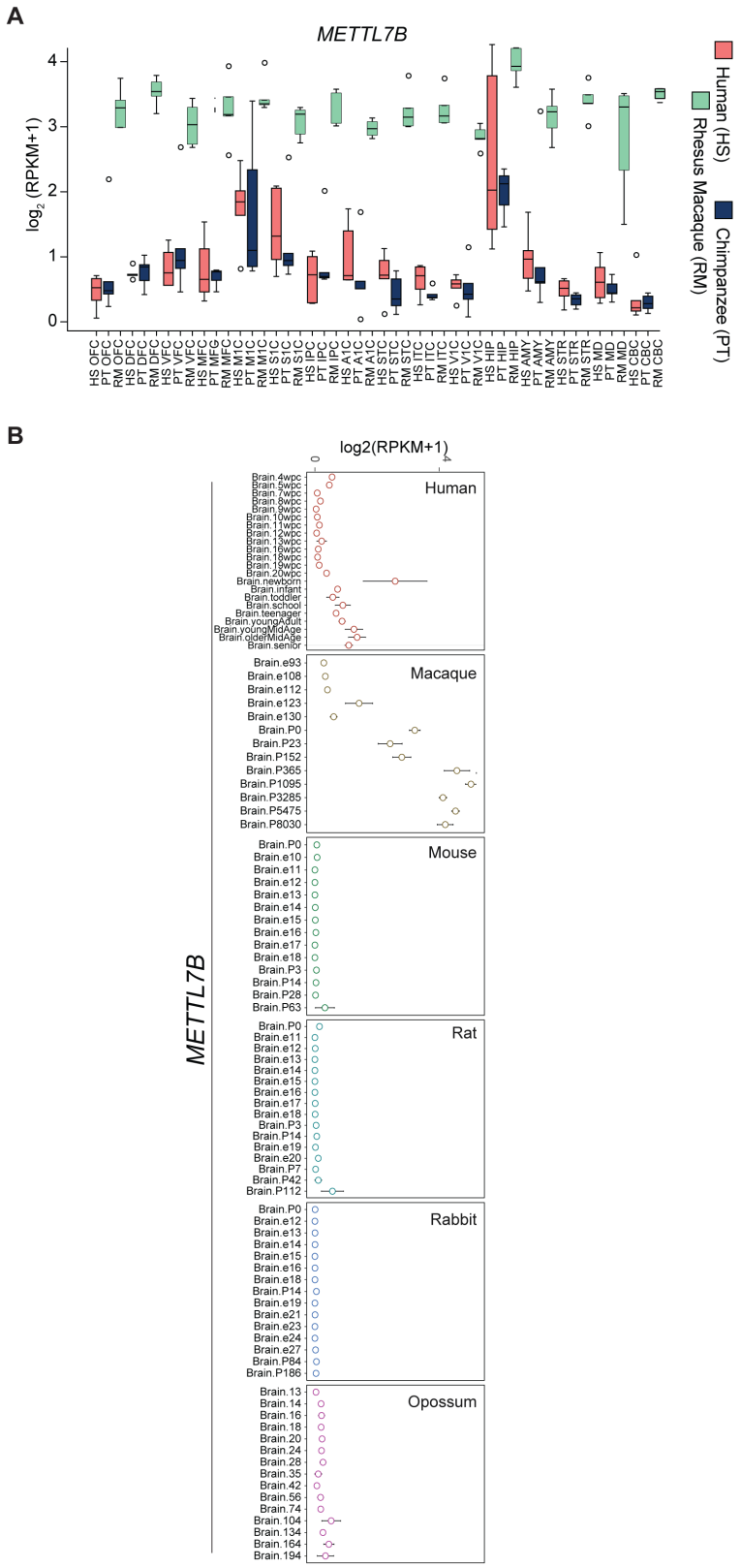

Figure 5.40 RNA-seq expression of *METTL7B* homologs. **(A)** RNA-seq expression of *METTL7B* homologs in human, chimpanzee, and rhesus macaque brain regions (103). **(B)** RNA-seq expression of *METTL7B* in the brain (forebrain/cerebrum) of multiple species at different developmental stages. Expression data was obtained from Cardoso-Moreira et al. 2019.
Source: Adapted from (185).

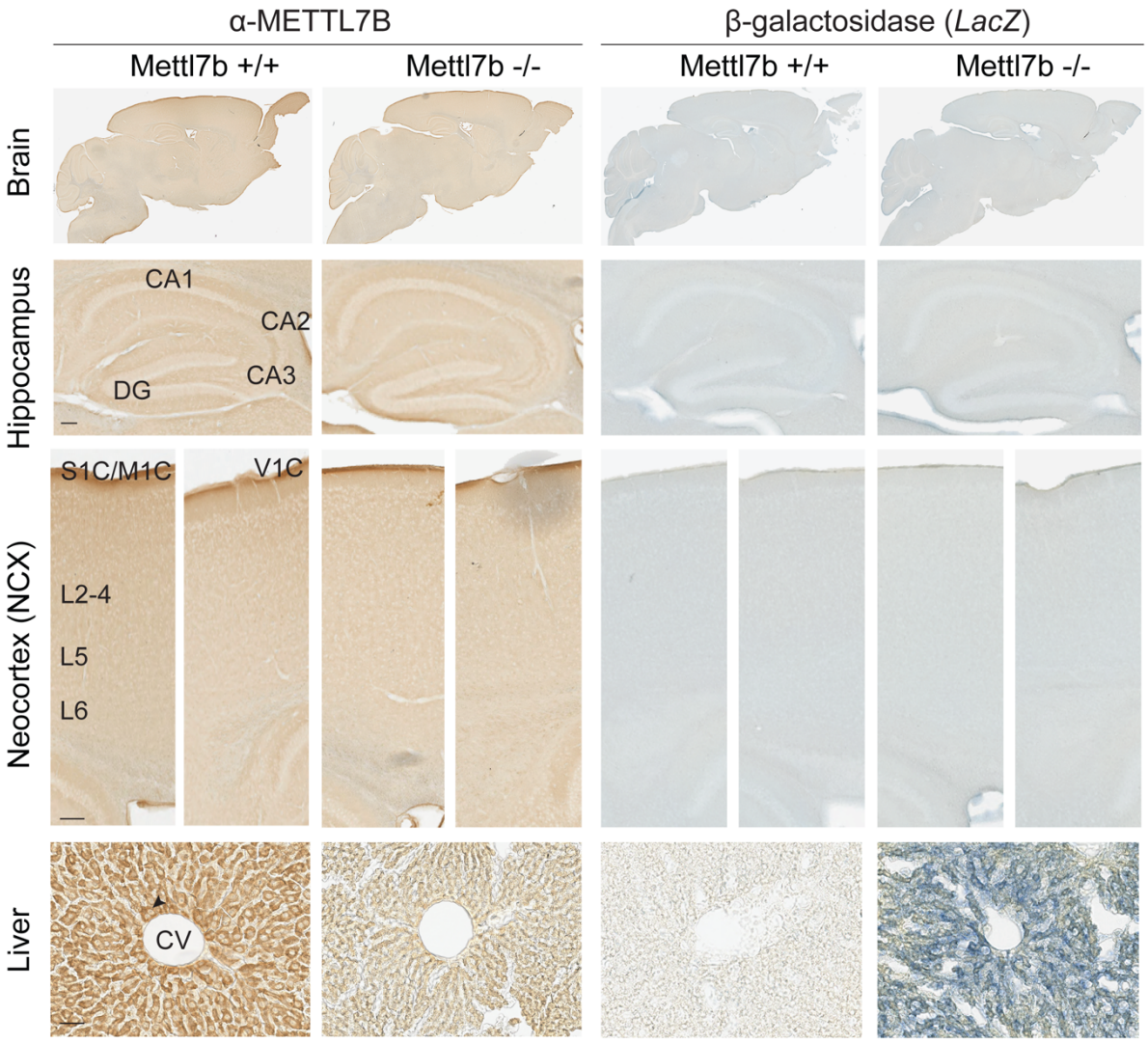

Figure 5.41 Immunostaining reveals Mettl7b protein and lacZ expression in liver. No expression observed in adult mouse brain. Scale bars: brain = 100 µm; liver = 50 µm. CV = central vein; DG = dentate Gyrus; CA = Cornu Ammonis; M1C = primary motor cortex; S1C = primary sensory cortex; V1C = primary visual cortex
Source: Adapted from (185).

5.6 Functional characterization of METTL7B

The proteins with which METTL7B interacts are unknown. As these interacting proteins are putative methylation targets, identifying them would provide insight into METTL7B function. We therefore performed unbiased proteomic analysis using two different approaches to find METTL7B interacting partners.

The first approach relied on tandem affinity pull-down using HaloTag fusion protein technology known to have low non-specific binding (276). This method promotes retrieval of entire protein complexes and allows stringent washing steps to reduce background. Using lentiviral vectors, we created stable cell lines of human cortical neural progenitors (ReNcell CX, EMD Millipore) expressing EGFP and either HaloTag or METTL7B-HaloTag fusion protein (Figure 4.2A). Captured proteins were processed for LC/MS-MS analysis and directly visualized by silver stain (Figure 5.42A). Direct fluorescent labeling of HaloTag protein with TMRDirect in cell culture showed high degree of overlap of METTL7B-HaloTag fusion protein with ER (CALNEXIN) and lipid droplet (ADFP) markers, consistent with our, and from others, earlier observation about intracellular localization of METTL7B (Figure 5.42B) (271). Using computational method Significance Analysis of INTeractome (SAINT) (235), we identified 275 true METTL7B interactors (Figure 5.43A, see also Supplementary tables S4-5 from (185)). To characterize the subcellular localization of the METTL7B interactors, we performed fold-enrichment analysis for major sub-cellular compartments cataloged in the Human Protein Atlas database and published datasets for mammalian cytoplasmic lipid droplets proteomes (229). We found that METTL7B interactors showed significant enrichment in ER- and LD-associated proteins (Figure 5.43B). Similarly, to understand which molecular processes are associated with METTL7B interactors, we performed KEGG pathway enrichment analysis which showed the most substantial enrichment in proteasome, protein processing in the ER, oxidative phosphorylation, and three neurodegenerative diseases, including AD (Figure 5.43C).

We next employed a parallel method using BioID technology, better suited to identify weak or transient interactions (Figure 4.2B) (190). BioID utilizes a mutated biotin ligase (BirA) that biotinylates proteins in the vicinity of a protein of interest. Similar to HaloTag, we observed that the putative METTL7B interactors intersected with markers of the endoplasmic reticulum and lipid droplets (Figure 5.44A-B). We identified 1794 METTL7B interactors that also showed significant enrichment in ER- and LD-associated proteins (Figure 5.45A-B, Supplementary tables S4-5 from (185)). KEGG pathway enrichment analysis showed the

highest enrichment for endocytosis, SNARE interactions in vesicular transport, and protein processing in ER (Figure 5.45C).

We then overlapped the two datasets and found 110 METTL7B interactors of the highest confidence present in both pull-downs (Figure 5.46A). These proteins showed enrichment in protein processing in ER (Figure 5.46B) and many of them overlapped with Alzheimer's Disease KEGG pathway (Figure 5.46C), including amyloid precursor protein (APP), inhibition of γ-secretase (RTN3 and RTN4/NOGO), and amyloid binding (NAE1, LRP1, APBB1). Within our snRNA-seq dataset, we found that genes encoding many of these proteins were co-expressed with *METTL7B* across various hippocampal populations (Figure 5.47). We confirmed on Western blot that the candidate proteins APP, RTN4, and LRP1 were present in METTL7B eluates but not in the controls (Figure 5.46D-E). RTN3 was not detected by Western blot in any of the samples, possibly because the pull-down amounts were below the detectability threshold. Using several published datasets, we found increased *METTL7B* expression in 4 out of 6 brain regions in AD brains compared to control (p value ≤ 0.05, Figure 5.48A). We surveyed an independent dataset of snRNA-seq of AD dlPFC (239) and MTG (Materials and methods) and found that the difference in cell populations stems from astrocytes (Figure 5.48B). In line with this observation, immunostaining for METTL7B in the hippocampal system of postmortem age matched control and AD brains, revealed numerous strongly METTL7B immunolabeled astrocytes in the HIP and EC of AD brains, compared to control brains (Figure 5.48C, Table 4.2). Taken together, these results suggest that METTL7B is potentially implicated in processes pertaining to glial cell reaction to the neuronal damage that typically occurs in Alzheimer's disease.

METTL7B has an annotated protein methyltransferase domain. However, its catalytic domain and specific activity has not been confirmed. To determine whether METTL7B possesses methyltransferase activity, we incubated purified recombinant proteins in a continuous enzyme-coupled S-adenosylmethionine (SAM) methyltransferase assay in which methyl group transfer results in fluorescence. We observed a significant increase in signal in all four cases where candidate proteins (RT3, RTN4, APP, and LRP1) were incubated with recombinant METTL7B, compared to candidate proteins incubated alone (Figure 5.46F). These results suggest that METTL7B uses SAM as a methyl donor and methylates the four candidate proteins.

To further build upon understanding the subcellular localization and mobility of METTL7B, we supplemented cell culture media with high levels of fatty acids, linoleic and

oleic acid complexes. This supplementation resulted in the expected, increased formation of LD, visualized by the accumulation of the LD marker ADFP (Figure 5.49A-B). On immunoblotting, we also observed increased METTL7B in the LD fraction with a matching depletion of METTL7B from the ER fraction (sedimented organelle, SO) (Figure 5.49A). However, METTL7B-interacting proteins largely retained their localization in the ER regardless of the fatty acid treatment. These differences in translocation suggest that METTL7B-mediated methylation on the putative target proteins may be limited in conditions with high levels of lipids.

Taken together, our cross-species transcriptomic analysis highlighted a putative primate-specific protein methylation mechanism, that may have previously unappreciated role in the hippocampal physiology.

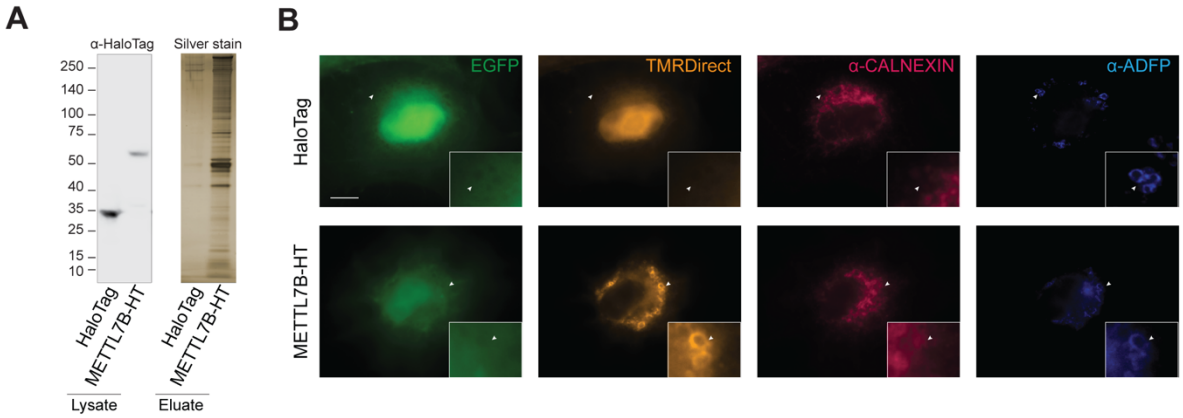

Figure 5.42 HaloTag pulldown

(A) Immunoblot validation of HT proteins and silver stain of pulldown eluates showing more proteins captured in METTL7B-HT sample.

(B) Immunofluorescence staining showing that METTL7B fusion protein (TMR-Direct) co- localizes with CALNEXIN and ADFP, markers of the ER and LD, respectively (271). ER = endoplasmic reticulum; LD = lipid droplet. Scale bars = 10 μm

Source: Adapted from (185).

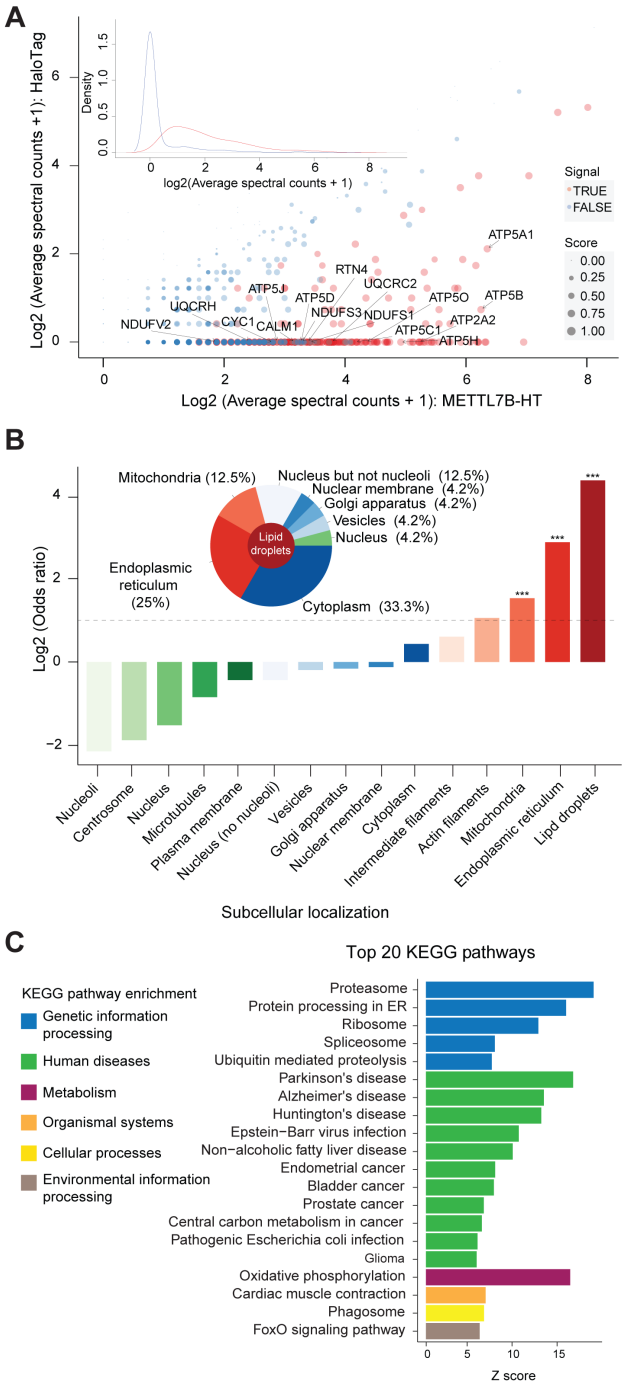

Figure 5.43 KEGG pathway enrichment of METTL7B interacting proteins identified in HaloTag pulldown. **(A)** SAINT analysis distinguishes true METTL7B interactors (red) from false ones (blue) based on MS spectral counts. The figure shows the average spectral counts in 3 test experiments (x axis) and 3 control experiments for all detected proteins. The inset clarifies separation between true METTL7B interactors (red curve) and the false ones (blue curve) in terms of spectral count distribution. **(B)** Fold-enrichment test for major subcellular compartments cataloged in Human Protein Atlas database (228) and mammalian cytoplasmic lipid droplet proteomes (229). The inset shows subcellular composition (%) of lipid droplet (LD) associated proteins. ***p <0.001. **(C)** KEGG pathway enrichment analysis showing molecular pathways involving true interactors are associated with three neurodegenerative diseases: Alzheimer's, Parkinson's, and Huntington's disease.
Source: Adapted from (185).

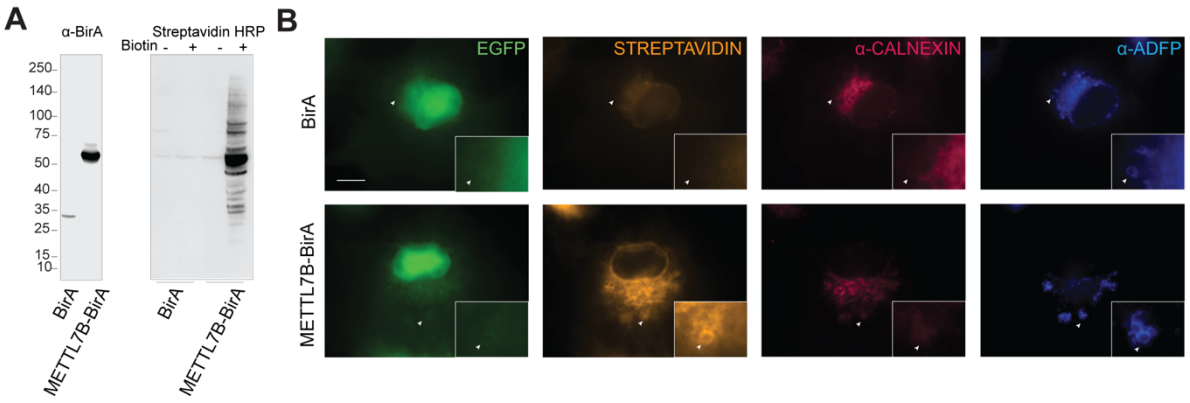

Figure 5.44 BioID pulldown
(A) Immunoblot validation of BioID proteins (a-BirA) and pulldown efficiency (STREPTAVIDIN-HRP) after supplementing cell culture media with 50 µM biotin for 24 hours. **(B)** METTL7B-expressing cells exhibit vast biotinylation of endogenous proteins (STREPTAVIDIN) which co-localize with CALNEXIN and ADFP, ER and LD markers, respectively. ER = endoplasmic reticulum; LD = lipid droplet. Scale bars = 10 µm
Source: Adapted from (185).

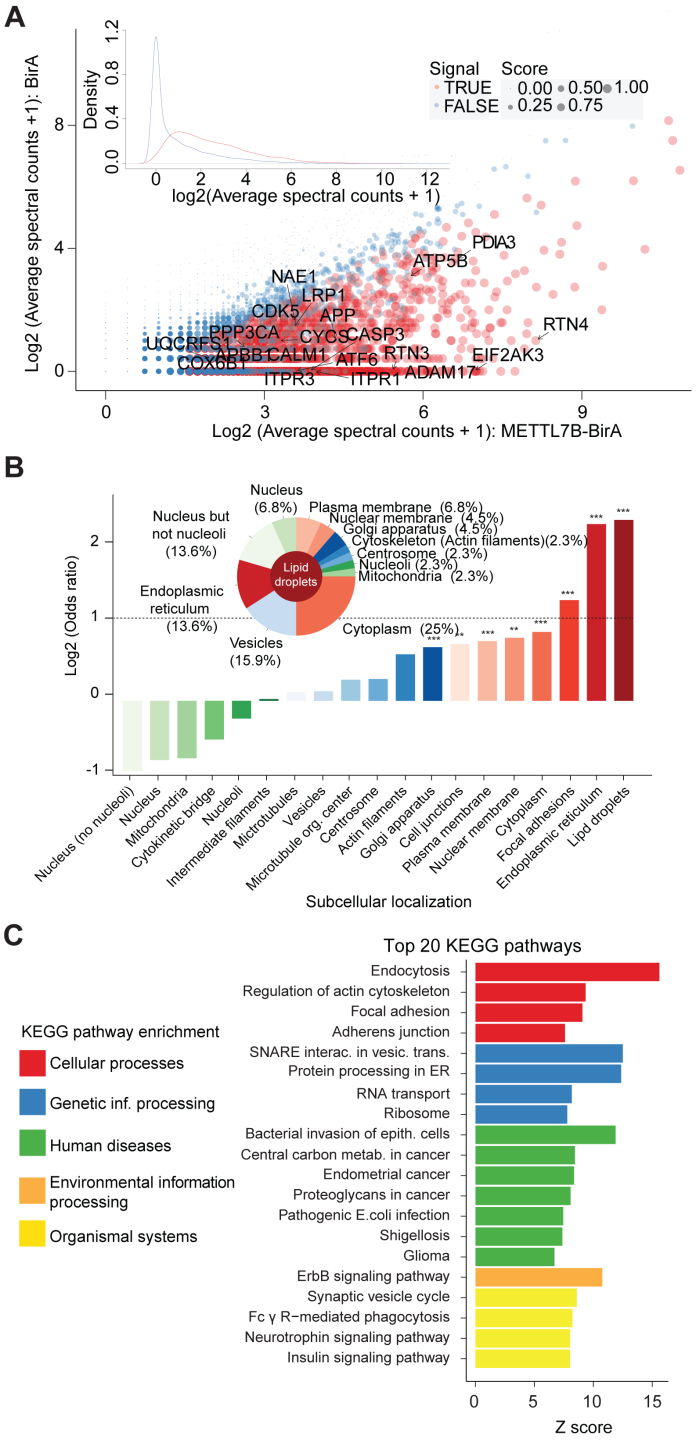

Figure 5.45 KEGG pathway enrichment of METTL7B interacting proteins identified in BioID pulldown. **(A)** SAINT analysis distinguishes true METTL7B interactors (red) from false ones (blue) based on MS spectral counts. The figure shows the average spectral counts in 3 test experiments (x axis) and 3 control experiments for all detected proteins. The inset clarifies separation between true METTL7B interactors (red curve) and the false ones (blue curve) in terms of spectral count distribution. **(B)** Fold-enrichment test for major subcellular compartments cataloged in Human Protein Atlas database (228) and mammalian cytoplasmic lipid droplet proteomes (Hodges and Wu, 2010). The inset shows subcellular composition (%) of lipid droplet (LD) associated proteins. ***p<0.001, **p<0.01. **(C)** KEGG pathway enrichment analysis.
Source: Adapted from (185).

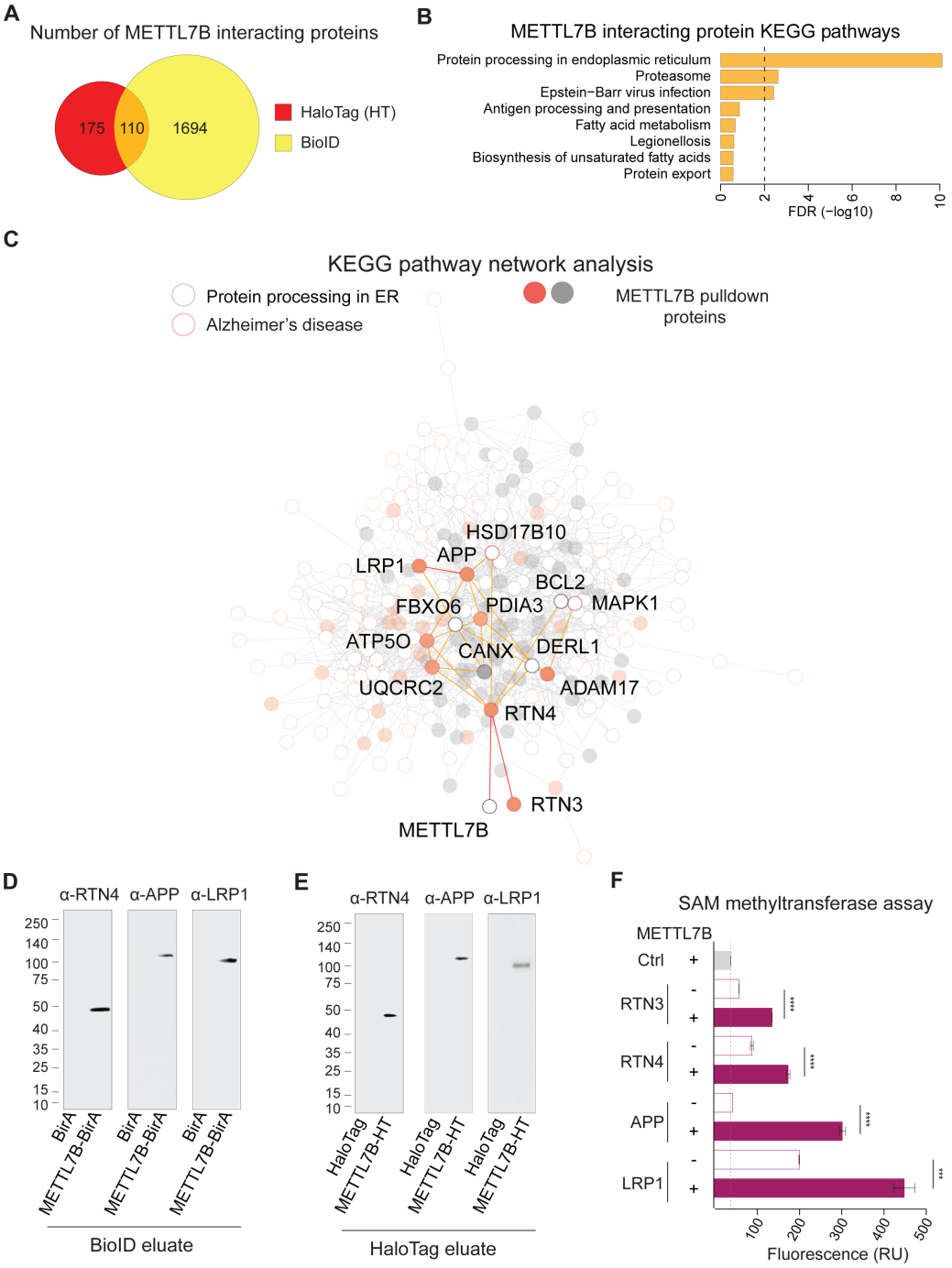

Figure 5.46 Overlap of HaloTag and BioID pulldowns

(A) Venn diagram of high-confidence METTL7B interacting proteins revealed by HaloTag and BioID. **(B)** KEGG enrichment of METTL7B interacting proteins from the intersection of HaloTag and BioID. **(C)** Interaction network with proteins in KEGG Protein Processing in the ER pathway (grey) and Alzheimer's disease pathway (orange). METTL7B interactors are shown as filled circles. **(D-E)** Immunoblot confirmation of top interacting candidates. The molecular weight of the RTN4-immunoreactive band is consistent with a known proteolytic fragment of RTN4A or RTN4B (277, 278). **(F)** SAM methyltransferase activity assay showing an increased reactivity in the presence of METTL7B. P-values calculated by unpaired two-tailed Student's t test, N=3. ER = endoplasmic reticulum

Source: Adapted from (185).

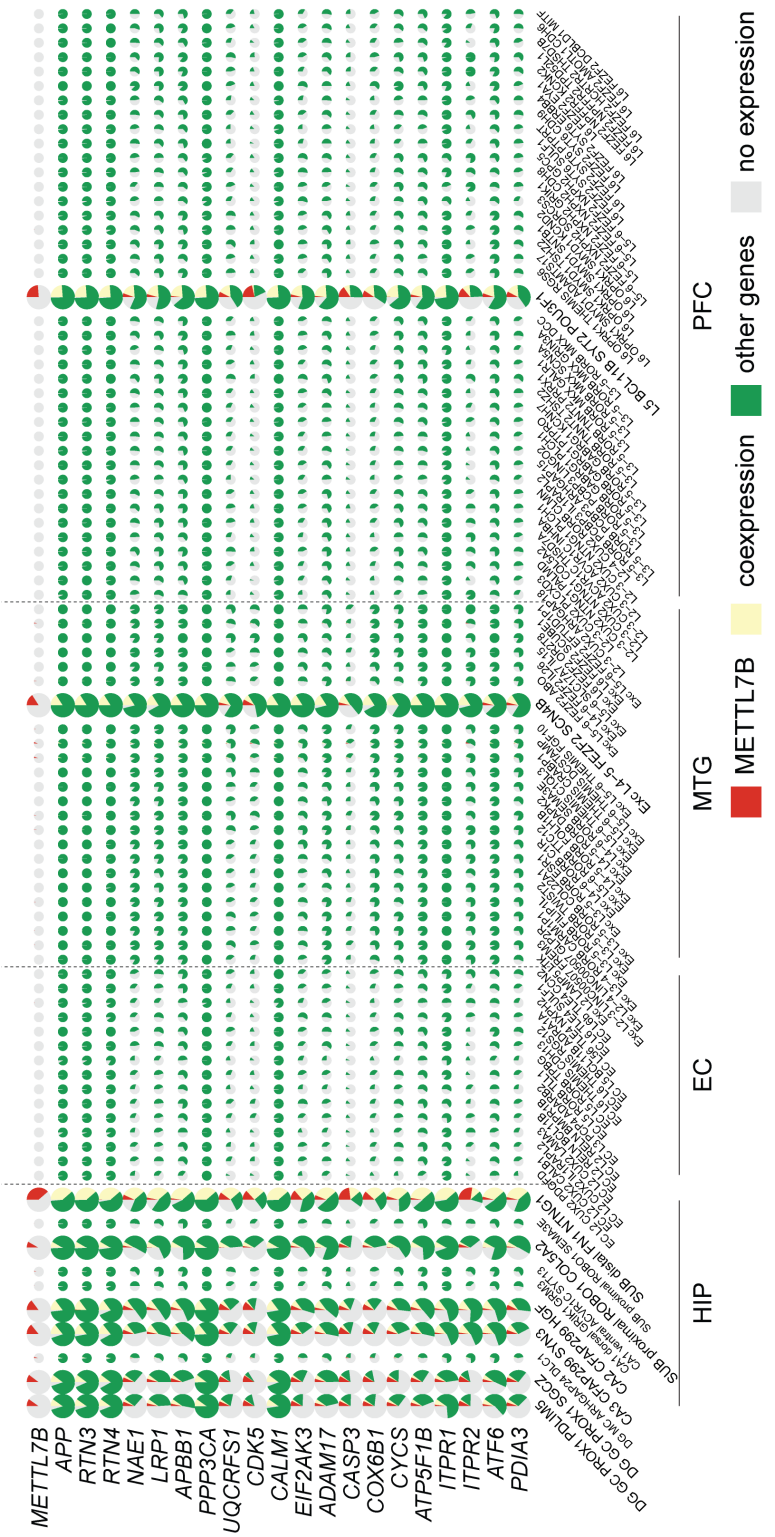

Figure 5.47 Pie charts showing the percent of cells expressing METTL7B but not certain METTL7B interactor (red), the percent of cells expressing each of the METTL7B interactors but not METTL7B (green), as well as the percent of cells co-expressing METTL7B and certain interactor (yellow) out of all cells within the subtypes of HIP, EC, MTG and PFC. Each row represents a gene, and each column denotes a subtype. HIP = hippocampal formation; EC = entorhinal cortex; MTG = middle temporal gyrus; PFC = prefrontal cortex
Source: Adapted from (185).

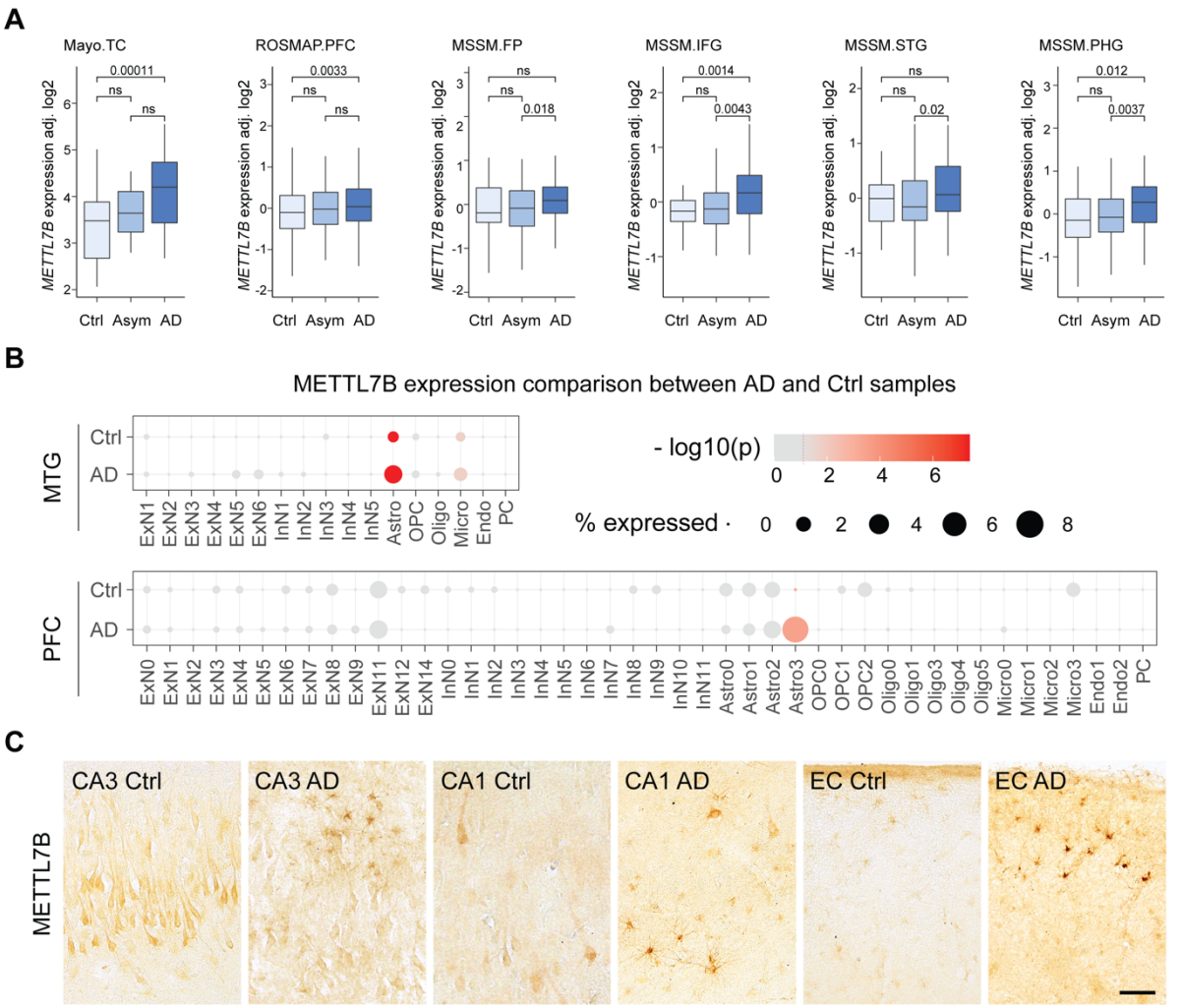

Figure 5.48 METTL7B expression in control and Alzheimer's disease brains.
(A) *METTL7B* expression from bulk tissue RNA-seq of control (Ctrl), asymptomatic AD (Asym), and AD from several brain regions. TC, temporal cortex; PFC, prefrontal cortex; FP, frontal pole; IFG, inferior frontal gyrus; STG, superior temporal gyrus; PHG, parahippocampal gyrus. Data analyzed from Swarup Lab (http://swaruplab.bio.uci.edu:3838/bulkRNA/).
(B) Expression of *METTL7B* across cell types from Ctrl and AD brains. The sizes of dots represent the expression ratio of *METTL7B* and the color gradients represent significance of METTL7B enriched in AD subtypes (measured by Fisher's exact test, two-sided). All dots with p value smaller than 0.05 are colored in red gradients. Top: prefrontal cortex (239). Bottom: middle temporal cortex (Materials and methods).
(C) Immunostaining of METTL7B in CA1, CA3 and EC in both control and AD brains.
Scale bar is 60 µm for all panels. AD = Alzheimer's disease; CA = Cornu Ammonis; EC = entorhinal cortex; MTG = middle temporal gyrus; PFC = prefrontal cortex
Source: Adapted from (185).

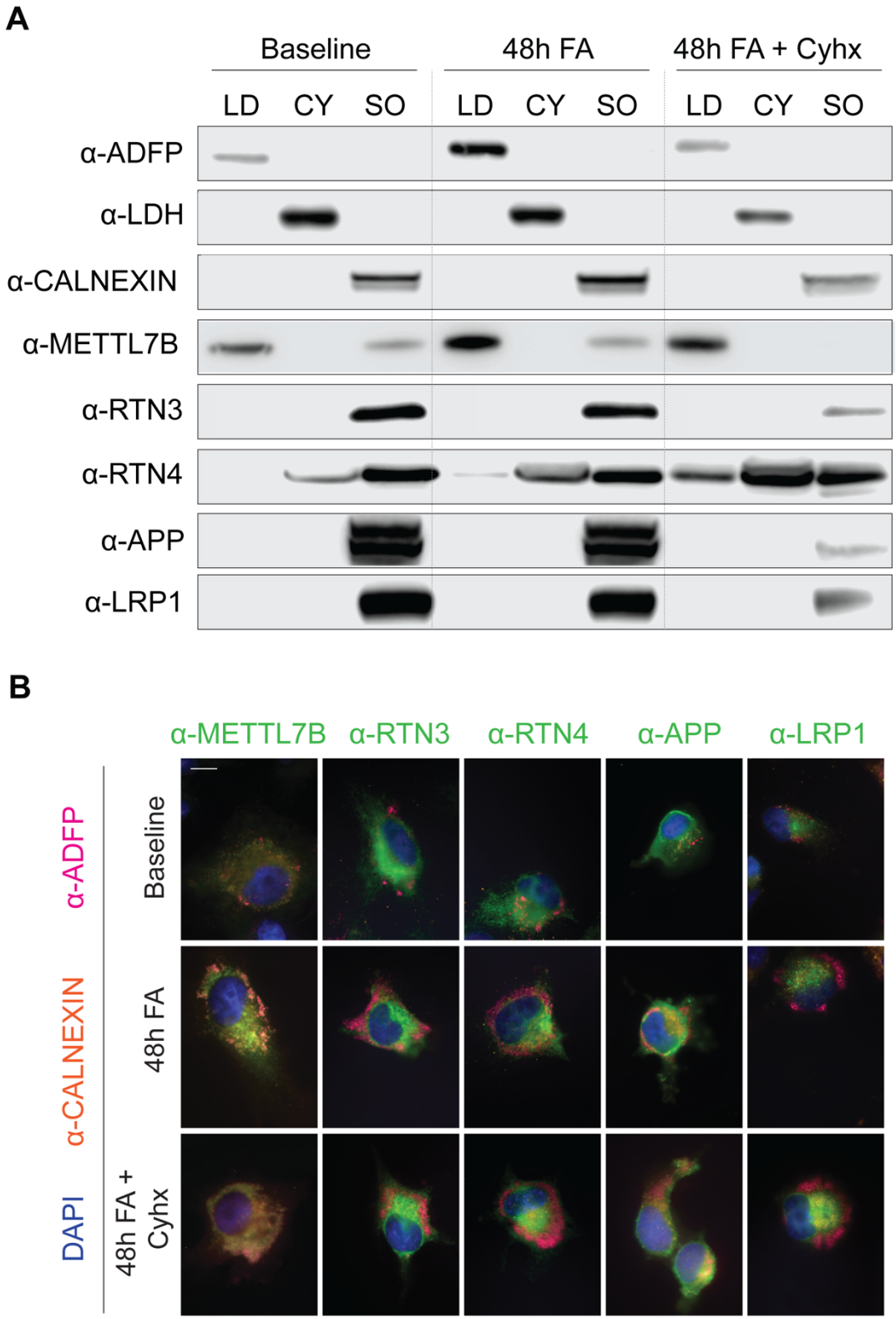

Figure 5.49 Immunoanalysis of METTL7B translocation. **(A-B)** Increased fatty acid (FA) load leads to a shift of METTL7B from ER to lipid droplets (LDs), while high confidence interactors remain unaffected. Blocking translation of new proteins with cycloheximide (Cyhx) suggests a complete shift of METTL7B. Scale bar = 10 μm. CY = cytosol; SO = sedimented organelle (containing the ER). All data are mean ± SEM. ****P< 0.0001, ***P< 0.001.
Source: Adapted from (185).

6. Discussion

We present a comprehensive single-cell transcriptomic analysis of several anatomically defined subregions of the adult human, rhesus macaque, and pig hippocampal system. This dataset allows us to provide unique, novel insights into adult neurogenesis in the hippocampus, contribute to our understanding of the transition from the allo- to meso- to neocortex at the molecular level, and reveal genes selectively expressed in certain cell types that might be involved in pathological processes uniquely associated with the human brain.

Current methods to study neurogenesis in the human hippocampus rely on the detection of specific cellular markers expressed by cells at various stages of the neurogenic lineage such as Nestin for progenitors (73) or DCX for neuroblasts and immature granule cells (75, 121). Single cell transcriptomic analysis is a more robust approach, as it uses combined gene expression to define specific cell populations instead of relying on a single marker (128). In addition, it allows integration of datasets for objective comparisons of cell populations between different species or structures, and dynamic interpretation of the data through splicing events to reveal differentiation trajectories of the cells under study. Moreover, it allows amplification of signals that may remain uncovered when analyzed separately.

Leveraging this potential, we integrated our datasets from human, pig, and rhesus macaque DG samples with a set of existing mouse data, providing dramatically increased analytic capacity. This allowed us to identify cells along the neurogenic lineage, including RGL cells, nIPCs and neuroblasts in mouse, pig, and macaque. However, these populations were scant or almost non-existent in the human. We only detected one cell with the characteristic features of nIPC and one with neuroblast profile out of 32,067 granule cells (0.003%) in the adult human DG. These numbers are considerably lower than the expected DCX neuroblasts in the range of 0.09% to 3.8% based on the recently published reports analyzing DCX protein expression in the DG (Table 5.1) (73, 75, 121). Also, using a mathematical model to explain incorporation of ^{14}C in the human hippocampus Spalding and colleagues (119) reported that 700 new granule cells are added daily to the human hippocampus. Data from rhesus macaque indicates that expression of *DCX*, and therefore maturation of newly generated cells in the macaque DG last for about 6 months or more (115). Assuming similar timing of maturation in the human DG, the number of neuroblasts and immature cells present at any timepoint would be 126,000 (700 × 180 days), or 0.84% of a 15 million DG cells (257), again further away from the scarce 0.003% detected in our study. Alternatively, it is possible that adult hippocampal neurogenesis is extremely variable in the human population and is rare in all our human

specimens. However, this possibility is unlikely, as studies showing evidence of adult neurogenesis (or lack of it) in humans do not show such variability (72, 73, 75, 119-121, 125, 127, 279, 280). Contrary to human findings, much higher proportions of neuroblasts were identified in the other species analyzed using the same analytic strategy and confirming its sensitivity to detect such cells (mouse – 6.6%, pig – 55.6%, rhesus macaque – 2.0%) (Figure 5.9B; Table 5.2). As a reference, one possible explanation is that the differentiation of human granule cells is defined by unique transcriptomic signatures distinct from that of mouse, pig, and macaque. However, those species all show a single domain of neuroblasts and nIPCs in the vicinity of the mature granule cell cluster, and the human UMAP layout does not include any alternative clustering of potential neuroblasts and nIPCs that could represent such divergent pathway in neither Seurat or Harmony algorithms (Figure 5.9B and 5.11). Alternatively, adult human neuroblasts can be different from mouse and macaque and resemble mature human granule cells with only a few genes differentially expressed. Although a small amount of human granule cells also expressed *DCX* (110 cells), they had transcriptomic characteristics of mature granule cells without showing any enrichment of neuroblast markers (Figure 5.19B). Overall, the lack of cell populations with progenitor profile, either RGL cells or nIPC in human, supports the interpretation that the adult human DG lacks a population of neuroblasts (Figure 5.9B; Table 5.2). Notably, the proportion of neuroblasts in the other species described above surpasses previous estimates based on cell proliferation and detection of neuroblasts expressing specific molecular markers, such as DCX (Tables 5.1). Overall, these high numbers of neuroblasts (Figure 5.9B) suggest that single cell profiling of neuroblasts might not be stringent enough, and more studies are required to refine the detection of those cell types. Nonetheless, this seemingly permissive protocol also suggests that we have not overlooked any significant neuroblast populations in human, even when their profile may be unclear.

Analysis of *DCX* expression and immunohistochemistry showed expression in mature neurons and glial cells in all species analyzed, showing that *DCX* expression is not exclusive of DG neuroblasts (Figures 5.18-19A). In fact, in humans, *DCX* was detected in the same cellular types as in the other species, mostly in InN, mossy cells and CA ExN, but surprisingly, it was more prevalent in InN than in granule cells. As mentioned above, a small amount of human granule cells that expressed *DCX* (110 cells) had transcriptomic characteristics of mature granule cells but did not show any enrichment of neuroblast markers (Figure 5.19B).

Recent reanalysis of the dataset of adult human hippocampus single-cell properties by the Alvarez-Buylla group (197) has shown similar results: most *DCX* expressing cells were

InN, CA ExN and OPCs, but few cells (3 cells) clustered as excitatory DG cells from 99 DCX expressing cells in the hippocampus, and from a total of 8903 hippocampal cells analyzed (126). In addition, Sorrells and coworkers showed that the cell cluster labeled as neural stem cells (NSC) in (197) was actually characteristic of ependymal cells, indicating the lack of a cluster of progenitor cells in the adult human DG, which is similar to our results. Also, a recent study analyzing the rostro-caudal transcriptome of the human hippocampus (198) revealed a granule cell cluster with potential features of neural progenitors, as it was enriched in *LPAR1* expression, a gene reported to be expressed in neural progenitors in the DG (128, 281). However, after reanalysis of their data, we showed that this cluster actually represented doublets composed of granule cells and oligodendrocytes, as *LPAR1* was also strongly expressed in oligodendrocytes (Figure 6.1). Therefore, our substantial RNA-seq dataset, demonstrate the potential of this method to detect and describe a neurogenic pathway in neurogenic species, but our data and the combined analysis of similar large datasets, all failed to show significant populations matching the putative progenitor and neuroblast cells that would define neurogenic potential in the adult human hippocampus.

Studies on DCX protein are typified by specific expression in DG neuroblasts in most mammalian species (6, 282). Contemporary reports also describe DCX immunolabeling in the pyriform cortex, amygdala, EC, parahippocampal and associative cortices in postmitotic neurons that retain immature cellular features (126, 260, 283-285). Currently, there is a strong ongoing debate surrounding DCX immunolabeling in the human dentate gyrus. While some studies have reported no presence of DCX-IL cells in the human DG (125, 126, 279, 280), other studies found DCX-IL cells in variable amounts from 0.09% to 3.8% of the total number of granule cells (72, 73, 75, 121, 286, 287). These proportions are larger than those reported in rhesus macaques (approximately 0.03-0.05%, Table 5.1) and the 3.8% reported by Moreno-Jimenez and colleagues (121) is even higher than in the granule cell layer of the two-month-old mouse (3.4%, Table 5.1) when the number of DCX-IL cells is about 9 times the steady adult level (0.4%) (253). The study by Moreno-Jimenez and colleagues (121) outlined a detailed antigen retrieval protocol as a critical step in unmasking the DCX signal in the adult human DG. Interestingly, they did not report any DCX-IL in the EC, which is in contrary to our (Figure 5.21A) and other studies (126) using standard citrate buffer antigen retrieval method. Our immunostaining against DCX showed clearly stained cells in the EC and amygdala but could not find reliable immunopositive cells resembling neuroblasts in the human DG in the same sections. It is unlikely that this was due to postmortem degradation of DCX protein since we were able to detect DCX-IL cells even in samples with prolonged PMIs

(Figure 5.21A-D and 5.21F-I). Since we were unable to identify neuroblasts in the human DG through transcriptomics or immunolabeling with different antigen retrieval protocols, it raises a question about the nature of the cells reported in prior studies. One possibility is that the DCX antibodies have so far unknown non-specific binding or that stringent antigen retrieval protocols revealed non-specific signals (126). Another hypothesis is that those studies were labeling GABAergic interneurons and granule cells containing low levels of DCX protein only detected after antigen retrieval. In fact, some of the lightly labeled cells we detected in the vicinity of the granule cells co-labeled with antibodies against GAD1, a marker of interneurons (Figure 5.20B and 5.22A-E). We also identified occasional cells immunopositive for GAD1 in the macaque hippocampus that co-labeled faintly with DCX immunostaining (Figure 5.5F). In addition, this light labeling significantly differs from pronounced staining and clearly defined morphology we observed in the EC and the amygdala (Figure 5.21A-B) and resembles more the subtle DCX immunolabeling previously documented (127). In summary, our findings suggest that DCX protein may be present in low quantities in interneurons or certain mature granule cells and exhibit faint staining under typical antigen retrieval conditions. However, under more rigorous antigen retrieval conditions, the staining may become more pervasive and less specific. Indeed, Moreno-Jimenez and colleagues (121) reported that over 70% of the DCX-IL cells they detected were also immunolabeled for NeuN, a marker of mature granule cells, supporting the possibility that most DCX-IL cells were actually mature neurons and not neuroblasts or immature neurons. They also reported that 91% of DCX-IL cells were also positive for Prospero homeobox1 (PROX1), a transcription factor highly enriched in later stages of the granule cell lineage (288). However, PROX1 is also expressed by GABAergic interneurons generated in the caudal ganglionic eminence (289, 290) suggesting that some of the cells identified as granule cells might actually be GABAergic interneurons in the analysis from Moreno-Jimenez and colleagues (121). The collective findings derived from both our transcriptomic analysis and DCX immunolabeling indicate that, unlike the other examined mammals, there is no continuous baseline neurogenesis in the adult human DG or it is exceedingly uncommon.

We found region-specific differences in gene expression patterns across the allo-, meso-, and neo-cortex and discovered that these differences primarily stem from the ExN population (Figures 5.23A-B, 5.29A-B, and 5.32A-B). Overall, we found that HIP ExN had little resemblance with ExN from EC or neocortical areas MTG and dlPFC. Conversely, EC ExN clustered together with corresponding layers of neocortical areas, as expected from cortical regions exhibiting similar lamination. Within the HIP, granule cells of the DG and pyramidal

cells of CA1 clustered separately from any other hippocampal ExN. While the major cytoarchitectonic difference of granule cells with any other cell type suggests a possible differential transcriptome, the singularity of CA1 pyramidal neurons is more unexpected. Mossy cells, another relatively distinct cell type, are closer to CA4-CA2 pyramidal cells, while the subiculum pyramidal cells cluster with subsets of deep layers 5 and 6 from the EC and neocortical areas MTG and dlPFC (Figure 5.23B). Overall, our analysis opens an opportunity for deeper exploration of these populations and to better understand their role in the biology of the hippocampal system. Furthermore, these results provide novel insights into the evolution of the mammalian hippocampal system and indicate similarities between the mammalian allocortex and deep layers of the meso- and neo-cortex.

We identified a previously uncharacterized *METTL7B* as a region- and cell-type-specific gene potentially implicated in aging and disease mechanisms affecting the human hippocampus. We found that METTL7B is enriched in ExN known to be less vulnerable to early neuropathological changes in the Alzheimer's disease in the hippocampal system and primary neocortical areas. We found that METTL7B interacts and promotes methylation of proteins implicated in the Alzheimer's disease (e.g., APP, RTN3, RTN4, and LRP1). More importantly, we further substantiated its relevance to AD by accessing its expression in bulk-tissue transcriptome data, single nuclei transcriptome data and immunochemistry and revealed elevated expression in multiple neocortical regions, EC and hippocampal formation in AD brains, which is mostly likely attributed to its expression increase in astrocytes (Figure 5.48). Our results also suggest that the subregional and cell type enrichment we observed could be specific to Old World monkeys and apes (parvorder Catarrhini), known to exhibit signs of Alzheimer's disease related pathology, such as amyloid plaques and tau-like lesions in the neocortex and hippocampus (180-183). Moreover, our findings could further substantiate implications of lipids and lipid droplets in the development of Alzheimer's disease. We found that high levels of lipids might diminish the availability of METTL7B in the ER as it translocates to lipid droplets and therefore restrict its interactions with candidate proteins implicated in Alzheimer's disease. Evidence suggests that dysregulation of lipid metabolism can directly affect proteolysis of APP and increase Aβ generation (291). Hypercholesterolemia is considered a risk factor for AD and *APOE4* gene variant, encoding a lipid transporter, is considered a strong risk for developing late onset familial AD (291, 292). Moreover, echoing Alois Alzheimer's report of lipid inclusions in an AD brain more than a century ago (162),

lipid droplet accumulations have recently been identified in postmortem AD brains and a transgenic AD mouse models (3xTg-AD) (293).

In summary, our analyses provided a detailed molecular map of the hippocampal system across multiple species, illuminating species-specific distinctions in the neurogenic trajectory, laminar elaboration, and potential candidate genes involved in hippocampal disease.

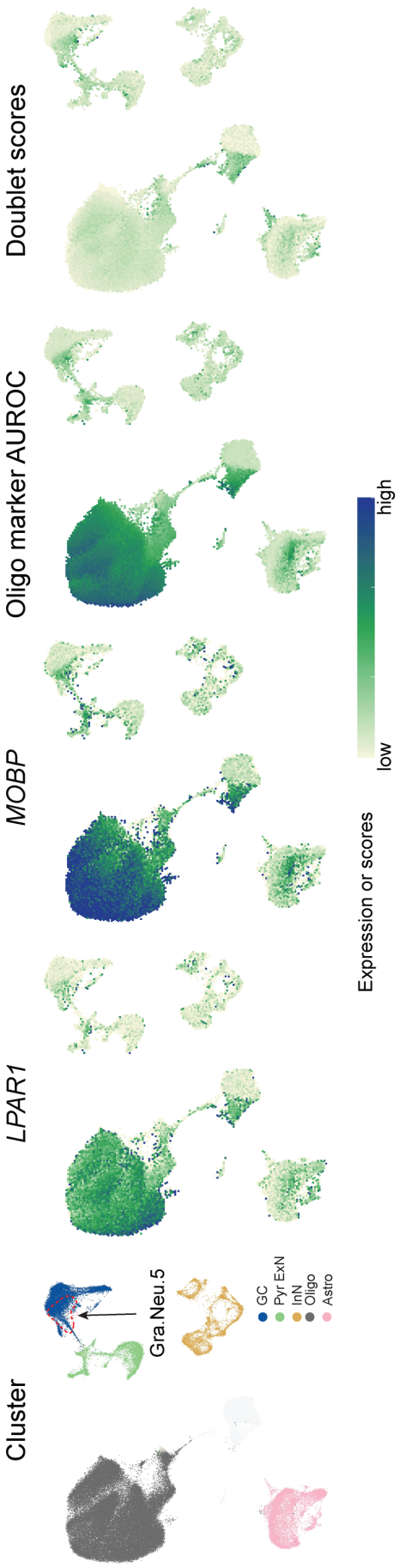

Figure 6.1 From left to right: UMAP visualizing the clusters identified in (198), expression of LPAR1 and MOBP (an oligodendrocyte marker), AUC scores of the top 50 oligodendrocyte markers and the doublet scores. The outlined cell populations represent the "Gra.Neu.5" cluster, which suggested to be a neural progenitor cluster by the original study. GC = granule cell; ExN = excitatory neuron; InN = inhibitory neuron; Oligo = oligodendrocyte; Astro = astrocyte
Source: Adapted from (185).

7. Conclusion

Our findings demonstrate that snRNA-seq technology is a powerful tool to study the neurogenic process in several species, and while it provides strong evidence of a conserved neurogenic pathway sustained by neural progenitors and neuroblasts and immature neurons in the DG of known neurogenic species such as mouse, pig and rhesus macaque, it also provides strong evidence suggesting that such neurogenic pathway is virtually absent in adult humans. Additionally, transcriptomic analysis of the human hippocampal system provides a detailed profile of the distinct cell populations beyond cytoarchitectonic divisions, that can be the source of comparative studies to assess hippocampal evolution and human specific features, and to understand the etiology and progress of neurological diseases, such as AD, in the hippocampal system. Novel, comprehensive single cell transcriptomic analysis now complements histological studies of adult neurogenesis to a level previously only available in certain animal models, and illuminates species specific mechanisms of cortical organization and disease susceptibility and progression.

8. Abstract in English

The hippocampal system is a critical component in cognition, adult neurogenesis, and selectively sensitive to aging and neurodegenerative processes. To gain insights into neurogenic potential and diversity of cell types in adult humans, we profiled single-nucleus transcriptomes in five hippocampal subregions. Integration of dentate gyrus data with mouse, pig and macaque, showed strong neurogenesis trajectories in these species that was absent in humans. Doublecortin (DCX), the common marker of neurogenesis in the dentate gyrus, showed widespread expression in the human hippocampal system, including some mature dentate granule cells, but did not define immature cell populations in humans. We further revealed prominent diversity among excitatory neurons across the hippocampal system that echoed the transition from three-layered archicortex to six-layered neocortex. Our results highlighted the uncharacterized METTL7B associated with Alzheimer's disease-related proteins and enriched in primates in neuronal subtypes and subregions more resilient to early neuropathological changes in the Alzheimer's disease. Overall, our findings unveiled cell type-specific molecular characteristics pertinent to hippocampal physiological function.

Keywords: Single-cell; RNA-seq; hippocampus; entorhinal cortex; evolution; adult neurogenesis; neocortex; aging

9. Sažetak na hrvatskom jeziku

Neuralni krugovi hipokampalne (HIP) i entorinalne moždane kore (EC) ključni su dijelovi široke neuronske mreže odgovorne za pamćenje te reprezentaciju prostora i vremena. U svrhu boljeg uvida u pojedinačne neuronske i ne-neuronske populacije tog sustava, provedeno je RNA sekvencioniranje pojedinačnih staničnih jezgara (snRNA-seq) uzoraka iz pet anatomski definiranih podregija hipokampalnog sustava. Integrirana analiza između vrsta pokazala je transkriptomske i histološke znakove neurogeneze u odraslim miševima, svinjama i makaki majmunima, ali ne i u ljudi. DCX, marker novonastalih zrnatih stanica, pronađen je u različitim neuronskim populacijama odraslog čovjeka, ali nije definirao populacije nezrelih neurona. Također, opisali smo specifične, subregionalno transkriptomski definirane tipove stanica i promjene u prijelazu iz troslojnog arhikorteksa u šestoslojni neokorteks. Naši rezultati istaknuli su da je METTL7B povezan s proteinima povezanim s Alzheimerovom bolešću i obogaćen u primata u podtipovima stanica i podregijama otpornijim na rane neuropatološke promjene u Alzheimerovoj bolesti. Ovo istraživanje je otkrilo molekularne karakteristike određenih vrsta i podtipova stanica koje potencijalno imaju važnu ulogu u fiziološkoj funkciji i/ili patološkim promjenama hipokampalnog sustava.

Ključne riječi: RNA-sekvenciranje pojedinačnih stanica; hipokampus; entorinalna moždana kora; evolucija; neurogeneza u odrasloj dobi; neokorteks; starenje

10. List of references

1. Andersen P. The Hippocampus Book. Andersen P, Morris R, Amaral D, Bliss T, O'Keefe J, editors: Oxford University Press; 2006 01 May 2009.
2. Buzsaki G, Moser EI. Memory, navigation and theta rhythm in the hippocampal-entorhinal system. Nat Neurosci. 2013;16(2):130-8.
3. Gloor P. The temporal lobe and limbic system. New York: Oxford University Press; 1997. xii, 865 p. p.
4. Freund TF. Changes in the views of neuronal connectivity and communication after Cajal: examples from the hippocampus. Prog Brain Res. 2002;136:203-13.
5. Klausberger T, Somogyi P. Neuronal diversity and temporal dynamics: the unity of hippocampal circuit operations. Science. 2008;321(5885):53-7.
6. Patzke N, Spocter MA, Karlsson KAE, Bertelsen MF, Haagensen M, Chawana R, et al. In contrast to many other mammals, cetaceans have relatively small hippocampi that appear to lack adult neurogenesis. Brain Struct Funct. 2015;220(1):361-83.
7. Rajmohan V, Mohandas E. The limbic system. Indian J Psychiatry. 2007;49(2):132-9.
8. Papez JW. A proposed mechanism of emotion. 1937. J Neuropsychiatry Clin Neurosci. 1995;7(1):103-12.
9. Broca P. Anatomie comparée des circonvolutions cérébrales: Le grand lobe limbique et la scissure limbique dans la série des mammifères1878.
10. Catani M, Dell'acqua F, Thiebaut de Schotten M. A revised limbic system model for memory, emotion and behaviour. Neurosci Biobehav Rev. 2013;37(8):1724-37.
11. Hendelman M.D. W. Atlas of Functional Neuroanatomy: CRC Press; 2005.
12. Destrieux C, Bourry D, Velut S. Surgical anatomy of the hippocampus. Neurochirurgie. 2013;59(4-5):149-58.
13. Cajal SRY, Azoulay DL, swanson N, Swanson lW. Histology Of The Nervous System: Of Man And Vertebrates: Oxford University Press; 1995 31 Oct 2023.
14. Chauhan P, Jethwa K, Rathawa A, Chauhan G, Mehra S. The Anatomy of the Hippocampus. In: Pluta R, editor. Cerebral Ischemia. Brisbane (AU)2021.
15. Tracey I, Leknes SG. Hippocampus and Entorhinal Complex: Functional Imaging. In: Gebhart GF, Schmidt RF, editors. Encyclopedia of Pain. Berlin, Heidelberg: Springer Berlin Heidelberg; 2013. p. 1476-81.
16. Nieuwenhuys R, Voogd J, Van Huijzen C. The human central nervous system: a synopsis and atlas: Springer Science & Business Media; 2007.

17. Johns P. Chapter 5 - Neurons and glial cells. In: Johns P, editor. Clinical Neuroscience: Churchill Livingstone; 2014. p. 61-9.
18. Augustinack JC, Huber KE, Stevens AA, Roy M, Frosch MP, van der Kouwe AJ, et al. Predicting the location of human perirhinal cortex, Brodmann's area 35, from MRI. Neuroimage. 2013;64:32-42.
19. Amaral DG, Scharfman HE, Lavenex P. The dentate gyrus: fundamental neuroanatomical organization (dentate gyrus for dummies). Prog Brain Res. 2007;163:3-22.
20. Han ZS, Buhl EH, Lorinczi Z, Somogyi P. A high degree of spatial selectivity in the axonal and dendritic domains of physiologically identified local-circuit neurons in the dentate gyrus of the rat hippocampus. Eur J Neurosci. 1993;5(5):395-410.
21. Soriano E, Frotscher M. A GABAergic axo-axonic cell in the fascia dentata controls the main excitatory hippocampal pathway. Brain Res. 1989;503(1):170-4.
22. Amaral DG. Introduction: what is where in the medial temporal lobe? Hippocampus. 1999;9(1):1-6.
23. Ribak CE, Seress L, Amaral DG. The development, ultrastructure and synaptic connections of the mossy cells of the dentate gyrus. J Neurocytol. 1985;14(5):835-57.
24. Acsady L, Kamondi A, Sik A, Freund T, Buzsaki G. GABAergic cells are the major postsynaptic targets of mossy fibers in the rat hippocampus. J Neurosci. 1998;18(9):3386-403.
25. Ribak CE, Vaughn JE, Saito K. Immunocytochemical localization of glutamic acid decarboxylase in neuronal somata following colchicine inhibition of axonal transport. Brain Res. 1978;140(2):315-32.
26. Ribak CE, Seress L. Five types of basket cell in the hippocampal dentate gyrus: a combined Golgi and electron microscopic study. J Neurocytol. 1983;12(4):577-97.
27. Scharfman HE. Electrophysiological evidence that dentate hilar mossy cells are excitatory and innervate both granule cells and interneurons. J Neurophysiol. 1995;74(1):179-94.
28. Amaral DG. A Golgi study of cell types in the hilar region of the hippocampus in the rat. J Comp Neurol. 1978;182(4 Pt 2):851-914.
29. Andersen P. The hippocampus book. Oxford ; New York: Oxford University Press; 2007. xx, 832 p. p.
30. Kubie JL, Muller RU, Bostock E. Spatial firing properties of hippocampal theta cells. J Neurosci. 1990;10(4):1110-23.

31. Ranck JB, Jr. Studies on single neurons in dorsal hippocampal formation and septum in unrestrained rats. I. Behavioral correlates and firing repertoires. Exp Neurol. 1973;41(2):461-531.
32. Pyapali GK, Sik A, Penttonen M, Buzsaki G, Turner DA. Dendritic properties of hippocampal CA1 pyramidal neurons in the rat: intracellular staining in vivo and in vitro. J Comp Neurol. 1998;391(3):335-52.
33. Amaral DG, Dolorfo C, Alvarez-Royo P. Organization of CA1 projections to the subiculum: a PHA-L analysis in the rat. Hippocampus. 1991;1(4):415-35.
34. Gaarskjaer FB. Organization of the mossy fiber system of the rat studied in extended hippocampi. II. Experimental analysis of fiber distribution with silver impregnation methods. J Comp Neurol. 1978;178(1):73-88.
35. Claiborne BJ, Amaral DG, Cowan WM. A light and electron microscopic analysis of the mossy fibers of the rat dentate gyrus. J Comp Neurol. 1986;246(4):435-58.
36. Blackstad TW, Brink K, Hem J, Jeune B. Distribution of hippocampal mossy fibers in the rat. An experimental study with silver impregnation methods. J Comp Neurol. 1970;138(4):433-49.
37. Greene JR, Totterdell S. Morphology and distribution of electrophysiologically defined classes of pyramidal and nonpyramidal neurons in rat ventral subiculum in vitro. J Comp Neurol. 1997;380(3):395-408.
38. O'Mara S. The subiculum: what it does, what it might do, and what neuroanatomy has yet to tell us. J Anat. 2005;207(3):271-82.
39. Stafstrom CE. The role of the subiculum in epilepsy and epileptogenesis. Epilepsy Curr. 2005;5(4):121-9.
40. Matsumoto N, Kitanishi T, Mizuseki K. The subiculum: Unique hippocampal hub and more. Neurosci Res. 2019;143:1-12.
41. Insausti R. Comparative anatomy of the entorhinal cortex and hippocampus in mammals. Hippocampus. 1993;3 Spec No:19-26.
42. Insausti R, Munoz-Lopez M, Insausti AM, Artacho-Perula E. The Human Periallocortex: Layer Pattern in Presubiculum, Parasubiculum and Entorhinal Cortex. A Review. Front Neuroanat. 2017;11:84.
43. Insausti R, Tunon T, Sobreviela T, Insausti AM, Gonzalo LM. The human entorhinal cortex: a cytoarchitectonic analysis. J Comp Neurol. 1995;355(2):171-98.
44. Solodkin A, Van Hoesen GW. Entorhinal cortex modules of the human brain. J Comp Neurol. 1996;365(4):610-7.

45. Witter MP, Doan TP, Jacobsen B, Nilssen ES, Ohara S. Architecture of the Entorhinal Cortex A Review of Entorhinal Anatomy in Rodents with Some Comparative Notes. Front Syst Neurosci. 2017;11:46.
46. Strange BA, Witter MP, Lein ES, Moser EI. Functional organization of the hippocampal longitudinal axis. Nat Rev Neurosci. 2014;15(10):655-69.
47. Amaral DG, Insausti R, Cowan WM. The entorhinal cortex of the monkey: I. Cytoarchitectonic organization. J Comp Neurol. 1987;264(3):326-55.
48. Simic G, Bexheti S, Kelovic Z, Kos M, Grbic K, Hof PR, et al. Hemispheric asymmetry, modular variability and age-related changes in the human entorhinal cortex. Neuroscience. 2005;130(4):911-25.
49. Augustinack JC, Huber KE, Postelnicu GM, Kakunoori S, Wang R, van der Kouwe AJ, et al. Entorhinal verrucae geometry is coincident and correlates with Alzheimer's lesions: a combined neuropathology and high-resolution ex vivo MRI analysis. Acta Neuropathol. 2012;123(1):85-96.
50. Witter MP. Organization of the entorhinal-hippocampal system: a review of current anatomical data. Hippocampus. 1993;3 Spec No:33-44.
51. Insausti R, Amaral DG, Cowan WM. The entorhinal cortex of the monkey: III. Subcortical afferents. J Comp Neurol. 1987;264(3):396-408.
52. Ramón S. Estructura del Asta de Ammon [Anales de la Sociedad Española de Historia Natural, 1892, vol. 22, pp. 53-114]. Memorias de la Real Sociedad Española de Historia Natural. 1999(2):2.
53. Witter MP, Amaral DG. Entorhinal cortex of the monkey: V. Projections to the dentate gyrus, hippocampus, and subicular complex. J Comp Neurol. 1991;307(3):437-59.
54. Felleman DJ, Van Essen DC. Distributed hierarchical processing in the primate cerebral cortex. Cereb Cortex. 1991;1(1):1-47.
55. Kohler C. Intrinsic projections of the retrohippocampal region in the rat brain. I. The subicular complex. J Comp Neurol. 1985;236(4):504-22.
56. Mosko S, Lynch G, Cotman CW. The distribution of septal projections to the hippocampus of the rat. J Comp Neurol. 1973;152(2):163-74.
57. Swanson LW, Sawchenko PE, Cowan WM. Evidence for collateral projections by neurons in Ammon's horn, the dentate gyrus, and the subiculum: a multiple retrograde labeling study in the rat. J Neurosci. 1981;1(5):548-59.
58. Swanson LW, Cowan WM. Hippocampo-hypothalamic connections: origin in subicular cortex, not ammon's horn. Science. 1975;189(4199):303-4.

59. Kostović I, Judas M, editors. Embryonic and Fetal Development of the Human Cerebral Cortex2015.
60. Tau GZ, Peterson BS. Normal development of brain circuits. Neuropsychopharmacology. 2010;35(1):147-68.
61. Molnar Z, Clowry GJ, Sestan N, Alzu'bi A, Bakken T, Hevner RF, et al. New insights into the development of the human cerebral cortex. J Anat. 2019;235(3):432-51.
62. Super H, Soriano E, Uylings HB. The functions of the preplate in development and evolution of the neocortex and hippocampus. Brain Res Brain Res Rev. 1998;27(1):40-64.
63. Rakic P. Specification of cerebral cortical areas. Science. 1988;241(4862):170-6.
64. Rakic P. A small step for the cell, a giant leap for mankind: a hypothesis of neocortical expansion during evolution. Trends Neurosci. 1995;18(9):383-8.
65. Bystron I, Blakemore C, Rakic P. Development of the human cerebral cortex: Boulder Committee revisited. Nat Rev Neurosci. 2008;9(2):110-22.
66. Rakic P. Principles of neural cell migration. Experientia. 1990;46(9):882-91.
67. Ge X, Shi Y, Li J, Zhang Z, Lin X, Zhan J, et al. Development of the human fetal hippocampal formation during early second trimester. Neuroimage. 2015;119:33-43.
68. Kier EL, Kim JH, Fulbright RK, Bronen RA. Embryology of the human fetal hippocampus: MR imaging, anatomy, and histology. AJNR Am J Neuroradiol. 1997;18(3):525-32.
69. Vannson JL, Duvernoy HM. The Human Hippocampus: An Atlas of Applied Anatomy: J.F. Bergmann-Verlag; 2013.
70. Merz K, Lie DC. Evidence that Doublecortin is dispensable for the development of adult born neurons in mice. PLoS One. 2013;8(5):e62693.
71. Corbo JC, Deuel TA, Long JM, LaPorte P, Tsai E, Wynshaw-Boris A, et al. Doublecortin is required in mice for lamination of the hippocampus but not the neocortex. J Neurosci. 2002;22(17):7548-57.
72. Knoth R, Singec I, Ditter M, Pantazis G, Capetian P, Meyer RP, et al. Murine features of neurogenesis in the human hippocampus across the lifespan from 0 to 100 years. PLoS One. 2010;5(1):e8809.
73. Boldrini M, Fulmore CA, Tartt AN, Simeon LR, Pavlova I, Poposka V, et al. Human Hippocampal Neurogenesis Persists throughout Aging. Cell Stem Cell. 2018;22(4):589-99 e5.

74. Moreno-Ajona D, Chan C, Villar-Martinez MD, Goadsby PJ. Targeting CGRP and 5-HT1F Receptors for the Acute Therapy of Migraine: A Literature Review. Headache. 2019;59 Suppl 2:3-19.
75. Tobin MK, Musaraca K, Disouky A, Shetti A, Bheri A, Honer WG, et al. Human Hippocampal Neurogenesis Persists in Aged Adults and Alzheimer's Disease Patients. Cell Stem Cell. 2019;24(6):974-82 e3.
76. Bingman VP, Muzio RN. Reflections on the Structural-Functional Evolution of the Hippocampus: What Is the Big Deal about a Dentate Gyrus? Brain Behav Evol. 2017;90(1):53-61.
77. Striedter GF. Principles of brain evolution. Sunderland, MA, US: Sinauer Associates; 2005. xii, 436-xii, p.
78. Hevner RF. Evolution of the mammalian dentate gyrus. J Comp Neurol. 2016;524(3):578-94.
79. Butler AB, Hodos W. Comparative vertebrate neuroanatomy: Evolution and adaptation. New York, NY, US: Wiley-Liss; 1996. xvii, 514-xvii, p.
80. Broglio C, Martín-Monzón I, Ocaña FM, Gómez A, Durán E, Salas C, et al. Hippocampal Pallium and Map-Like Memories through Vertebrate Evolution. Journal of Behavioral and Brain Science. 2015;5:109-20.
81. Rodriguez F, Lopez JC, Vargas JP, Broglio C, Gomez Y, Salas C. Spatial memory and hippocampal pallium through vertebrate evolution: insights from reptiles and teleost fish. Brain Res Bull. 2002;57(3-4):499-503.
82. Puelles L. Thoughts on the development, structure and evolution of the mammalian and avian telencephalic pallium. Philos Trans R Soc Lond B Biol Sci. 2001;356(1414):1583-98.
83. Bachy I, Berthon J, Retaux S. Defining pallial and subpallial divisions in the developing Xenopus forebrain. Mech Dev. 2002;117(1-2):163-72.
84. Wullimann MF, Mueller T. Teleostean and mammalian forebrains contrasted: Evidence from genes to behavior. J Comp Neurol. 2004;475(2):143-62.
85. Manns JR, Eichenbaum H. 3.33 - Evolution of the Hippocampus. In: Kaas JH, editor. Evolution of Nervous Systems. Oxford: Academic Press; 2007. p. 465-89.
86. Striedter GF. Evolution of the hippocampus in reptiles and birds. J Comp Neurol. 2016;524(3):496-517.

87. Bingman VP, Salas C, Rodriguez F. Evolution of the Hippocampus. In: Binder MD, Hirokawa N, Windhorst U, editors. Encyclopedia of Neuroscience. Berlin, Heidelberg: Springer Berlin Heidelberg; 2009. p. 1356-60.
88. Naumann RK, Ondracek JM, Reiter S, Shein-Idelson M, Tosches MA, Yamawaki TM, et al. The reptilian brain. Curr Biol. 2015;25(8):R317-21.
89. Northcutt RG. Variation in reptilian brains and cognition. Brain Behav Evol. 2013;82(1):45-54.
90. Bingman VP, Rodríguez F, Salas C. The Hippocampus of Nonmammalian Vertebrates. 2017. p. 479-89.
91. Schwerdtfeger WKaS, W.J.A.J. The Forebrain of Reptiles: Current Concepts of Structure and Function Meeting on Recent Advances in Understanding the Structure and Function of the Forebrain in Reptiles, Frankfurt a.M., August 1987. Schwerdtfeger WK, Smeets WJ, editors: S.Karger AG; 1988 10 Oct 1988.
92. Ulinski PS. The Cerebral Cortex of Reptiles. In: Jones EG, Peters A, editors. Comparative Structure and Evolution of Cerebral Cortex, Part I. Boston, MA: Springer US; 1990. p. 139-215.
93. Welker WI. The significance of foliation and fissuration of cerebellar cortex. The cerebellar folium as a fundamental unit of sensorimotor integration. Arch Ital Biol. 1990;128(2-4):87-109.
94. Krubitzer L, Kaas J. The evolution of the neocortex in mammals: how is phenotypic diversity generated? Curr Opin Neurobiol. 2005;15(4):444-53.
95. Rosene DL, Van Hoesen GW. The Hippocampal Formation of the Primate Brain. In: Jones EG, Peters A, editors. Cerebral Cortex: Further Aspects of Cortical Function, Including Hippocampus. Boston, MA: Springer US; 1987. p. 345-456.
96. Ishizuka N. Laminar organization of the pyramidal cell layer of the subiculum in the rat. J Comp Neurol. 2001;435(1):89-110.
97. Kriegstein AR, Connors BW. Cellular physiology of the turtle visual cortex: synaptic properties and intrinsic circuitry. J Neurosci. 1986;6(1):178-91.
98. Reiner A. A comparison of neurotransmitter-specific and neuropeptide-specific neuronal cell types present in the dorsal cortex in turtles with those present in the isocortex in mammals: implications for the evolution of isocortex. Brain Behav Evol. 1991;38(2-3):53-91.
99. Shepherd GM, Rowe TB. Neocortical Lamination: Insights from Neuron Types and Evolutionary Precursors. Front Neuroanat. 2017;11:100.
100. Stephan H. Allocortex Springer. 1975.

101. Demeter S, Rosene DL, Van Hoesen GW. Fields of origin and pathways of the interhemispheric commissures in the temporal lobe of macaques. J Comp Neurol. 1990;302(1):29-53.
102. Morrison JH, Hof PR. Life and death of neurons in the aging brain. Science. 1997;278(5337):412-9.
103. Sousa AMM, Zhu Y, Raghanti MA, Kitchen RR, Onorati M, Tebbenkamp ATN, et al. Molecular and cellular reorganization of neural circuits in the human lineage. Science. 2017;358(6366):1027-32.
104. Suzuki WA, Amaral DG. Functional neuroanatomy of the medial temporal lobe memory system. Cortex. 2004;40(1):220-2.
105. Burwell RD, Amaral DG. Cortical afferents of the perirhinal, postrhinal, and entorhinal cortices of the rat. J Comp Neurol. 1998;398(2):179-205.
106. Kempermann G. New neurons for 'survival of the fittest'. Nat Rev Neurosci. 2012;13(10):727-36.
107. Zhao C, Deng W, Gage FH. Mechanisms and functional implications of adult neurogenesis. Cell. 2008;132(4):645-60.
108. Imayoshi I, Sakamoto M, Ohtsuka T, Takao K, Miyakawa T, Yamaguchi M, et al. Roles of continuous neurogenesis in the structural and functional integrity of the adult forebrain. Nat Neurosci. 2008;11(10):1153-61.
109. Sahay A, Scobie KN, Hill AS, O'Carroll CM, Kheirbek MA, Burghardt NS, et al. Increasing adult hippocampal neurogenesis is sufficient to improve pattern separation. Nature. 2011;472(7344):466-70.
110. Clelland CD, Choi M, Romberg C, Clemenson GD, Jr., Fragniere A, Tyers P, et al. A functional role for adult hippocampal neurogenesis in spatial pattern separation. Science. 2009;325(5937):210-3.
111. Treves A, Tashiro A, Witter MP, Moser EI. What is the mammalian dentate gyrus good for? Neuroscience. 2008;154(4):1155-72.
112. Tronel S, Belnoue L, Grosjean N, Revest JM, Piazza PV, Koehl M, et al. Adult-born neurons are necessary for extended contextual discrimination. Hippocampus. 2012;22(2):292-8.
113. Gould E, Reeves AJ, Fallah M, Tanapat P, Gross CG, Fuchs E. Hippocampal neurogenesis in adult Old World primates. Proc Natl Acad Sci U S A. 1999;96(9):5263-7.

114. Jabes A, Lavenex PB, Amaral DG, Lavenex P. Quantitative analysis of postnatal neurogenesis and neuron number in the macaque monkey dentate gyrus. Eur J Neurosci. 2010;31(2):273-85.
115. Kohler SJ, Williams NI, Stanton GB, Cameron JL, Greenough WT. Maturation time of new granule cells in the dentate gyrus of adult macaque monkeys exceeds six months. Proc Natl Acad Sci U S A. 2011;108(25):10326-31.
116. Kornack DR, Rakic P. Continuation of neurogenesis in the hippocampus of the adult macaque monkey. Proc Natl Acad Sci U S A. 1999;96(10):5768-73.
117. Ngwenya LB, Peters A, Rosene DL. Maturational sequence of newly generated neurons in the dentate gyrus of the young adult rhesus monkey. J Comp Neurol. 2006;498(2):204-16.
118. Yuan TF, Li J, Ding F, Arias-Carrion O. Evidence of adult neurogenesis in non-human primates and human. Cell Tissue Res. 2014;358(1):17-23.
119. Spalding KL, Bergmann O, Alkass K, Bernard S, Salehpour M, Huttner HB, et al. Dynamics of hippocampal neurogenesis in adult humans. Cell. 2013;153(6):1219-27.
120. Eriksson PS, Perfilieva E, Bjork-Eriksson T, Alborn AM, Nordborg C, Peterson DA, et al. Neurogenesis in the adult human hippocampus. Nat Med. 1998;4(11):1313-7.
121. Moreno-Jiménez EP, Flor-García M, Terreros-Roncal J, Rábano A, Cafini F, Pallas-Bazarra N, et al. Adult hippocampal neurogenesis is abundant in neurologically healthy subjects and drops sharply in patients with Alzheimer’s disease. Nature Medicine. 2019;25(4):554-60.
122. Kang HJ, Kawasawa YI, Cheng F, Zhu Y, Xu X, Li M, et al. Spatio-temporal transcriptome of the human brain. Nature. 2011;478(7370):483-9.
123. Zhu Y, Sousa AMM, Gao T, Skarica M, Li M, Santpere G, et al. Spatiotemporal transcriptomic divergence across human and macaque brain development. Science. 2018;362(6420).
124. Cipriani S, Ferrer I, Aronica E, Kovacs GG, Verney C, Nardelli J, et al. Hippocampal Radial Glial Subtypes and Their Neurogenic Potential in Human Fetuses and Healthy and Alzheimer's Disease Adults. Cereb Cortex. 2018;28(7):2458-78.
125. Dennis CV, Suh LS, Rodriguez ML, Kril JJ, Sutherland GT. Human adult neurogenesis across the ages: An immunohistochemical study. Neuropathol Appl Neurobiol. 2016;42(7):621-38.

126. Sorrells SF, Paredes MF, Zhang Z, Kang G, Pastor-Alonso O, Biagiotti S, et al. Positive Controls in Adults and Children Support That Very Few, If Any, New Neurons Are Born in the Adult Human Hippocampus. J Neurosci. 2021;41(12):2554-65.
127. Seki T, Hori T, Miyata H, Maehara M, Namba T. Analysis of proliferating neuronal progenitors and immature neurons in the human hippocampus surgically removed from control and epileptic patients. Sci Rep. 2019;9(1):18194.
128. Hochgerner H, Zeisel A, Lonnerberg P, Linnarsson S. Conserved properties of dentate gyrus neurogenesis across postnatal development revealed by single-cell RNA sequencing. Nat Neurosci. 2018;21(2):290-9.
129. Kempermann G, Gage FH, Aigner L, Song H, Curtis MA, Thuret S, et al. Human Adult Neurogenesis: Evidence and Remaining Questions. Cell Stem Cell. 2018;23(1):25-30.
130. Kuhn HG, Toda T, Gage FH. Adult Hippocampal Neurogenesis: A Coming-of-Age Story. J Neurosci. 2018;38(49):10401-10.
131. Lee H, Thuret S. Adult Human Hippocampal Neurogenesis: Controversy and Evidence. Trends Mol Med. 2018;24(6):521-2.
132. Paredes MF, Sorrells SF, Cebrian-Silla A, Sandoval K, Qi D, Kelley KW, et al. Does Adult Neurogenesis Persist in the Human Hippocampus? Cell Stem Cell. 2018;23(6):780-1.
133. Abbott LC, Nigussie F. Adult neurogenesis in the mammalian dentate gyrus. Anat Histol Embryol. 2020;49(1):3-16.
134. Schacter DL, Tulving E. What are the memory systems of 1994? Memory systems 1994. Cambridge, MA, US: The MIT Press; 1994. p. 1-38.
135. Squire LR, Stark CE, Clark RE. The medial temporal lobe. Annu Rev Neurosci. 2004;27:279-306.
136. Squire LR. Declarative and nondeclarative memory: multiple brain systems supporting learning and memory. J Cogn Neurosci. 1992;4(3):232-43.
137. Squire LR, Zola-Morgan S. The medial temporal lobe memory system. Science. 1991;253(5026):1380-6.
138. Eichenbaum H, Cohen NJ. From conditioning to conscious recollection: Memory systems of the brain. New York, NY, US: Oxford University Press; 2001. x, 583-x, p.
139. Scoville WB. The limbic lobe in man. J Neurosurg. 1954;11(1):64-6.
140. Scoville WB, Milner B. Loss of recent memory after bilateral hippocampal lesions. J Neurol Neurosurg Psychiatry. 1957;20(1):11-21.

141. Zola-Morgan S, Squire LR, Amaral DG. Lesions of the amygdala that spare adjacent cortical regions do not impair memory or exacerbate the impairment following lesions of the hippocampal formation. J Neurosci. 1989;9(6):1922-36.
142. Milner B. Disorders of learning and memory after temporal lobe lesions in man. Clin Neurosurg. 1972;19:421-46.
143. Milner B, Corkin S, Teuber HL. Further analysis of the hippocampal amnesic syndrome: 14-year follow-up study of H.M. Neuropsychologia. 1968;6(3):215-34.
144. Tolman EC. Cognitive maps in rats and men. Psychol Rev. 1948;55(4):189-208.
145. O'Keefe J, Dostrovsky J. The hippocampus as a spatial map. Preliminary evidence from unit activity in the freely-moving rat. Brain Res. 1971;34(1):171-5.
146. O'Keefe J, Nadel L, editors. The Hippocampus as a Cognitive Map1978.
147. Epstein RA, Patai EZ, Julian JB, Spiers HJ. The cognitive map in humans: spatial navigation and beyond. Nat Neurosci. 2017;20(11):1504-13.
148. Knierim JJ. The hippocampus. Curr Biol. 2015;25(23):R1116-21.
149. Derdikman D, Moser EI. A manifold of spatial maps in the brain. Trends Cogn Sci. 2010;14(12):561-9.
150. O'Keefe J. Place units in the hippocampus of the freely moving rat. Exp Neurol. 1976;51(1):78-109.
151. Moser MB, Rowland DC, Moser EI. Place cells, grid cells, and memory. Cold Spring Harb Perspect Biol. 2015;7(2):a021808.
152. Kjelstrup KB, Solstad T, Brun VH, Hafting T, Leutgeb S, Witter MP, et al. Finite scale of spatial representation in the hippocampus. Science. 2008;321(5885):140-3.
153. Jung MW, Wiener SI, McNaughton BL. Comparison of spatial firing characteristics of units in dorsal and ventral hippocampus of the rat. J Neurosci. 1994;14(12):7347-56.
154. McNaughton BL, Battaglia FP, Jensen O, Moser EI, Moser MB. Path integration and the neural basis of the 'cognitive map'. Nat Rev Neurosci. 2006;7(8):663-78.
155. Taube JS. Head direction cells and the neurophysiological basis for a sense of direction. Prog Neurobiol. 1998;55(3):225-56.
156. Fortin NJ, editor 1.21 – Navigation and Episodic-Like Memory in Mammals2008.
157. Solstad T, Boccara CN, Kropff E, Moser MB, Moser EI. Representation of geometric borders in the entorhinal cortex. Science. 2008;322(5909):1865-8.
158. Savelli F, Yoganarasimha D, Knierim JJ. Influence of boundary removal on the spatial representations of the medial entorhinal cortex. Hippocampus. 2008;18(12):1270-82.

159. Eichenbaum H. Time cells in the hippocampus: a new dimension for mapping memories. Nat Rev Neurosci. 2014;15(11):732-44.
160. Schmidt-Kastner R, Freund TF. Selective vulnerability of the hippocampus in brain ischemia. Neuroscience. 1991;40(3):599-636.
161. Blumcke I, Pauli E, Clusmann H, Schramm J, Becker A, Elger C, et al. A new clinico-pathological classification system for mesial temporal sclerosis. Acta Neuropathol. 2007;113(3):235-44.
162. Alzheimer A. Über eine eigenartige Erkrankung der Hirnrinde. Allgemeine Zeitschrift für Psychiatrie und Psychisch-Gerichtliche Medicin. 1907;64:146-8.
163. Ballatore C, Lee VMY, Trojanowski JQ. Tau-mediated neurodegeneration in Alzheimer's disease and related disorders. Nature Reviews Neuroscience. 2007;8:663-.
164. Fischer O. Miliare Nekrosen mit drusigen Wucherungen der Neurofibrillen, eine regelmässige Veränderung der Hirnrinde bei seniler Demenz. Monatsschrift für Psychiatrie und Neurologie. 1907;22:361-72.
165. Glenner GG, Wong CW. Alzheimer's disease: initial report of the purification and characterization of a novel cerebrovascular amyloid protein. Biochem Biophys Res Commun. 1984;120(3):885-90.
166. Hardy J, Selkoe DJ. The amyloid hypothesis of Alzheimer's disease: progress and problems on the road to therapeutics. Science. 2002;297(5580):353-6.
167. Jonsson T, Atwal JK, Steinberg S, Snaedal J, Jonsson PV, Bjornsson S, et al. A mutation in APP protects against Alzheimer's disease and age-related cognitive decline. Nature. 2012;488(7409):96-9.
168. Tanzi RE, Bertram L. Twenty Years of the Alzheimer’s Disease Amyloid Hypothesis: A Genetic Perspective. Cell. 2005;120(4):545-55.
169. Karran E, De Strooper B. The amyloid cascade hypothesis: are we poised for success or failure? J Neurochem. 2016;139 Suppl 2:237-52.
170. Wilcock GK, Esiri MM. Plaques, tangles and dementia: A quantitative study. Journal of the Neurological Sciences. 1982;56(2):343-56.
171. Braak H, Del Trecidi K. Neuroanatomy and pathology of sporadic Alzheimer's disease. Advances in anatomy, embryology, and cell biology. 2015;215:1-162.
172. Hyman BT, Gomez-Isla T. Alzheimer's disease is a laminar, regional, and neural system specific disease, not a global brain disease. Neurobiol Aging. 1994;15(3):353-4; discussion 79-80.

173. Pearson RC, Esiri MM, Hiorns RW, Wilcock GK, Powell TP. Anatomical correlates of the distribution of the pathological changes in the neocortex in Alzheimer disease. Proc Natl Acad Sci U S A. 1985;82(13):4531-4.
174. Ohm TG. The dentate gyrus in Alzheimer's disease. Prog Brain Res. 2007;163:723-40.
175. West MJ, Kawas CH, Stewart WF, Rudow GL, Troncoso JC. Hippocampal neurons in pre-clinical Alzheimer's disease. Neurobiol Aging. 2004;25(9):1205-12.
176. Jin K, Peel AL, Mao XO, Xie L, Cottrell BA, Henshall DC, et al. Increased hippocampal neurogenesis in Alzheimer's disease. Proc Natl Acad Sci U S A. 2004;101(1):343-7.
177. Davies DC, Horwood N, Isaacs SL, Mann DM. The effect of age and Alzheimer's disease on pyramidal neuron density in the individual fields of the hippocampal formation. Acta Neuropathol. 1992;83(5):510-7.
178. Schonheit B, Zarski R, Ohm TG. Spatial and temporal relationships between plaques and tangles in Alzheimer-pathology. Neurobiol Aging. 2004;25(6):697-711.
179. Reid AT, Evans AC. Structural networks in Alzheimer's disease. European neuropsychopharmacology : the journal of the European College of Neuropsychopharmacology. 2013;23(1):63-77.
180. Edler MK, Sherwood CC, Meindl RS, Hopkins WD, Ely JJ, Erwin JM, et al. Aged chimpanzees exhibit pathologic hallmarks of Alzheimer's disease. Neurobiol Aging. 2017;59:107-20.
181. Finch CE, Austad SN. Commentary: is Alzheimer's disease uniquely human? Neurobiol Aging. 2015;36(2):553-5.
182. Paspalas CD, Carlyle BC, Leslie S, Preuss TM, Crimins JL, Huttner AJ, et al. The aged rhesus macaque manifests Braak stage III/IV Alzheimer's-like pathology. Alzheimers Dement. 2018;14(5):680-91.
183. Perez SE, Raghanti MA, Hof PR, Kramer L, Ikonomovic MD, Lacor PN, et al. Alzheimer's disease pathology in the neocortex and hippocampus of the western lowland gorilla (Gorilla gorilla gorilla). J Comp Neurol. 2013;521(18):4318-38.
184. Rapoport SI. Hypothesis: Alzheimer's disease is a phylogenetic disease. Medical hypotheses. 1989;29(3):147-50.
185. Franjic D, Skarica M, Ma S, Arellano JI, Tebbenkamp ATN, Choi J, et al. Transcriptomic taxonomy and neurogenic trajectories of adult human, macaque, and pig hippocampal and entorhinal cells. Neuron. 2022;110(3):452-69 e14.

186. Liu C, Chen N, Huang K, Jiang M, Liang H, Sun Z, et al. Identifying hub genes and potential mechanisms associated with senescence in human annulus cells by gene expression profiling and bioinformatics analysis. Mol Med Rep. 2018;17(3):3465-72.
187. Velmeshev D, Schirmer L, Jung D, Haeussler M, Perez Y, Mayer S, et al. Single-cell genomics identifies cell type-specific molecular changes in autism. Science. 2019;364(6441):685-9.
188. Matsuda T, Cepko CL. Electroporation and RNA interference in the rodent retina in vivo and in vitro. Proceedings of the National Academy of Sciences. 2004;101(1):16 LP-22.
189. Lois C, Hong EJ, Pease S, Brown EJ, Baltimore D. Germline Transmission and Tissue-Specific Expression of Transgenes Delivered by Lentiviral Vectors. Science. 2002;295(5556):868 LP-72.
190. Roux KJ, Kim DI, Raida M, Burke B. A promiscuous biotin ligase fusion protein identifies proximal and interacting proteins in mammalian cells. The Journal of cell biology. 2012;196(6):801-10.
191. Dull T, Zufferey R, Kelly M, Mandel RJ, Nguyen M, Trono D, et al. A Third-Generation Lentivirus Vector with a Conditional Packaging System. Journal of Virology. 1998;72(11):8463 LP-71.
192. Roux KJ, Kim DI, Burke B. BioID: A screen for protein-protein interactions. Current Protocols in Protein Science. 2013(SUPPL.74):1-14.
193. Kim DI, Kc B, Zhu W, Motamedchaboki K, Doye V, Roux KJ. Probing nuclear pore complex architecture with proximity-dependent biotinylation. Proceedings of the National Academy of Sciences. 2014;111(24):E2453 LP-E61.
194. Butler A, Hoffman P, Smibert P, Papalexi E, Satija R. Integrating single-cell transcriptomic data across different conditions, technologies, and species. Nat Biotechnol. 2018;36(5):411-20.
195. Becht E, McInnes L, Healy J, Dutertre CA, Kwok IWH, Ng LG, et al. Dimensionality reduction for visualizing single-cell data using UMAP. Nat Biotechnol. 2018.
196. Becht E, McInnes L, Healy J, Dutertre CA, Kwok IWH, Ng LG, et al. Dimensionality reduction for visualizing single-cell data using UMAP. Nature Biotechnology. 2019;37(1):38-+.
197. Habib N, Avraham-Davidi I, Basu A, Burks T, Shekhar K, Hofree M, et al. Massively parallel single-nucleus RNA-seq with DroNc-seq. Nat Methods. 2017;14(10):955-8.

198. Ayhan F, Kulkarni A, Berto S, Sivaprakasam K, Douglas C, Lega BC, et al. Resolving cellular and molecular diversity along the hippocampal anterior-to-posterior axis in humans. Neuron. 2021;109(13):2091-105 e6.
199. Cembrowski MS, Phillips MG, DiLisio SF, Shields BC, Winnubst J, Chandrashekar J, et al. Dissociable Structural and Functional Hippocampal Outputs via Distinct Subiculum Cell Classes. Cell. 2018;173(5):1280-92 e18.
200. Li M, Santpere G, Imamura Kawasawa Y, Evgrafov OV, Gulden FO, Pochareddy S, et al. Integrative functional genomic analysis of human brain development and neuropsychiatric risks. Science. 2018;362(6420):eaat7615.
201. Cembrowski MS, Bachman JL, Wang L, Sugino K, Shields BC, Spruston N. Spatial Gene-Expression Gradients Underlie Prominent Heterogeneity of CA1 Pyramidal Neurons. Neuron. 2016;89(2):351-68.
202. Cembrowski MS, Wang L, Sugino K, Shields BC, Spruston N. Hipposeq: a comprehensive RNA-seq database of gene expression in hippocampal principal neurons. Elife. 2016;5:e14997.
203. Ramsden HL, Surmeli G, McDonagh SG, Nolan MF. Laminar and dorsoventral molecular organization of the medial entorhinal cortex revealed by large-scale anatomical analysis of gene expression. PLoS Comput Biol. 2015;11(1):e1004032.
204. Tang Q, Ebbesen CL, Sanguinetti-Scheck JI, Preston-Ferrer P, Gundlfinger A, Winterer J, et al. Anatomical Organization and Spatiotemporal Firing Patterns of Layer 3 Neurons in the Rat Medial Entorhinal Cortex. J Neurosci. 2015;35(36):12346-54.
205. Ohara S, Onodera M, Simonsen OW, Yoshino R, Hioki H, Iijima T, et al. Intrinsic Projections of Layer Vb Neurons to Layers Va, III, and II in the Lateral and Medial Entorhinal Cortex of the Rat. Cell Rep. 2018;24(1):107-16.
206. Tasic B, Yao Z, Graybuck LT, Smith KA, Nguyen TN, Bertagnolli D, et al. Shared and distinct transcriptomic cell types across neocortical areas. Nature. 2018;563(7729):72-8.
207. Hodge RD, Bakken TE, Miller JA, Smith KA, Barkan ER, Graybuck LT, et al. Conserved cell types with divergent features in human versus mouse cortex. Nature. 2019;573(7772):61-8.
208. Frazer S, Prados J, Niquille M, Cadilhac C, Markopoulos F, Gomez L, et al. Transcriptomic and anatomic parcellation of 5-HT(3A)R expressing cortical interneuron subtypes revealed by single-cell RNA sequencing. Nat Commun. 2017;8:14219.

209. Lanjakornsiripan D, Pior BJ, Kawaguchi D, Furutachi S, Tahara T, Katsuyama Y, et al. Layer-specific morphological and molecular differences in neocortical astrocytes and their dependence on neuronal layers. Nat Commun. 2018;9(1):1623.
210. Vanlandewijck M, He L, Mae MA, Andrae J, Ando K, Del Gaudio F, et al. A molecular atlas of cell types and zonation in the brain vasculature. Nature. 2018;554(7693):475-80.
211. Zhong S, Ding W, Sun L, Lu Y, Dong H, Fan X, et al. Decoding the development of the human hippocampus. Nature. 2020;577(7791):531-6.
212. Stuart T, Butler A, Hoffman P, Hafemeister C, Papalexi E, Mauck WM, 3rd, et al. Comprehensive Integration of Single-Cell Data. Cell. 2019;177(7):1888-902 e21.
213. Korsunsky I, Millard N, Fan J, Slowikowski K, Zhang F, Wei K, et al. Fast, sensitive and accurate integration of single-cell data with Harmony. Nat Methods. 2019;16(12):1289-96.
214. La Manno G, Soldatov R, Zeisel A, Braun E, Hochgerner H, Petukhov V, et al. RNA velocity of single cells. Nature. 2018;560(7719):494-8.
215. Dobin A, Davis CA, Schlesinger F, Drenkow J, Zaleski C, Jha S, et al. STAR: ultrafast universal RNA-seq aligner. Bioinformatics. 2013;29(1):15-21.
216. Bergen V, Lange M, Peidli S, Wolf FA, Theis FJ. Generalizing RNA velocity to transient cell states through dynamical modeling. Nat Biotechnol. 2020;38(12):1408-14.
217. Aibar S, Gonzalez-Blas CB, Moerman T, Huynh-Thu VA, Imrichova H, Hulselmans G, et al. SCENIC: single-cell regulatory network inference and clustering. Nat Methods. 2017;14(11):1083-6.
218. Wolock SL, Lopez R, Klein AM. Scrublet: Computational Identification of Cell Doublets in Single-Cell Transcriptomic Data. Cell Syst. 2019;8(4):281-91 e9.
219. Smyth GK. Limma: linear models for microarray data BT - Bioinformatics and Computational Biology Solutions Using R and Bioconductor. Bioinformatics and Computational Biology Solutions Using R and Bioconductor. 2005:397-420.
220. Nesvizhskii AI, Keller A, Kolker E, Aebersold R. A statistical model for identifying proteins by tandem mass spectrometry. Anal Chem. 2003;75(17):4646-58.
221. Brill LM, Motamedchaboki K, Wu S, Wolf DA. Comprehensive proteomic analysis of Schizosaccharomyces pombe by two-dimensional HPLC-tandem mass spectrometry. Methods. 2009;48(3):311-9.

222. Xu T, Venable JD, Park SK, Cociorva D, Lu B, Liao L, et al. ProLuCID, a fast and sensitive tandem mass spectra-based protein identification program. Molecular & cellular proteomics. 2006;5(10).
223. Tabb DL, McDonald WH, Yates 3rd JR. DTASelect and Contrast: tools for assembling and comparing protein identifications from shotgun proteomics. Journal of proteome research. 2002;1(1):21-6.
224. Park SK, Venable JD, Xu T, Yates Iii JR. A quantitative analysis software tool for mass spectrometry–based proteomics. Nature Methods. 2008;5:319-.
225. Robinson PN, Wollstein A, Böhme U, Beattie B. Ontologizing gene-expression microarray data: characterizing clusters with Gene Ontology. Bioinformatics. 2004;20(6):979-81.
226. Choi H, Liu G, Mellacheruvu D, Tyers M, Gingras AC, Nesvizhskii AI. Analyzing protein-protein interactions from affinity purification-mass spectrometry data with SAINT. Current protocols in bioinformatics. 2012;Chapter 8:Unit8 15.
227. Teo G, Liu G, Zhang J, Nesvizhskii AI, Gingras A-C, Choi H. SAINTexpress: Improvements and additional features in Significance Analysis of INTeractome software. Journal of Proteomics. 2014;100:37-43.
228. Uhlén M, Fagerberg L, Hallström BM, Lindskog C, Oksvold P, Mardinoglu A, et al. Tissue-based map of the human proteome. Science. 2015;347(6220):1260419-.
229. Hodges BD, Wu CC. Proteomic insights into an expanded cellular role for cytoplasmic lipid droplets. J Lipid Res. 2010;51(2):262-73.
230. Stark C, Breitkreutz BJ, Reguly T, Boucher L, Breitkreutz A, Tyers M. BioGRID: a general repository for interaction datasets. Nucleic Acids Res. 2006;34(Database issue):D535-9.
231. Abul-Husn NS, Bushlin I, Morón JA, Jenkins SL, Dolios G, Wang R, et al. Systems approach to explore components and interactions in the presynapse. Proteomics. 2009;9(12):3303-15.
232. Huang da W, Sherman BT, Lempicki RA. Systematic and integrative analysis of large gene lists using DAVID bioinformatics resources. Nat Protoc. 2009;4(1):44-57.
233. Kostylev MA, Kaufman AC, Nygaard HB, Patel P, Haas LT, Gunther EC, et al. Prion-Protein-interacting Amyloid-beta Oligomers of High Molecular Weight Are Tightly Correlated with Memory Impairment in Multiple Alzheimer Mouse Models. J Biol Chem. 2015;290(28):17415-38.

234. Kostylev MA, Tuttle MD, Lee S, Klein LE, Takahashi H, Cox TO, et al. Liquid and Hydrogel Phases of PrP(C) Linked to Conformation Shifts and Triggered by Alzheimer's Amyloid-beta Oligomers. Mol Cell. 2018;72(3):426-43 e12.
235. Choi H, Larsen B, Lin Z-Y, Breitkreutz A, Mellacheruvu D, Fermin D, et al. SAINT: probabilistic scoring of affinity purification–mass spectrometry data. Nature Methods. 2010;8:70-.
236. Krishnaswami SR, Grindberg RV, Novotny M, Venepally P, Lacar B, Bhutani K, et al. Using single nuclei for RNA-seq to capture the transcriptome of postmortem neurons. Nat Protoc. 2016;11(3):499-524.
237. Lake BB, Ai R, Kaeser GE, Salathia NS, Yung YC, Liu R, et al. Neuronal subtypes and diversity revealed by single-nucleus RNA sequencing of the human brain. Science. 2016;352(6293):1586-90.
238. Lake BB, Chen S, Sos BC, Fan J, Kaeser GE, Yung YC, et al. Integrative single-cell analysis of transcriptional and epigenetic states in the human adult brain. Nat Biotechnol. 2018;36(1):70-80.
239. Mathys H, Davila-Velderrain J, Peng Z, Gao F, Mohammadi S, Young JZ, et al. Single-cell transcriptomic analysis of Alzheimer’s disease. Nature. 2019.
240. Schirmer L, Velmeshev D, Holmqvist S, Kaufmann M, Werneburg S, Jung D, et al. Neuronal vulnerability and multilineage diversity in multiple sclerosis. Nature. 2019;573(7772):75-82.
241. Grubman A, Chew G, Ouyang JF, Sun G, Choo XY, McLean C, et al. A single-cell atlas of entorhinal cortex from individuals with Alzheimer's disease reveals cell-type-specific gene expression regulation. Nat Neurosci. 2019;22(12):2087-97.
242. Leng K, Li E, Eser R, Piergies A, Sit R, Tan M, et al. Molecular characterization of selectively vulnerable neurons in Alzheimer's disease. Nat Neurosci. 2021;24(2):276-87.
243. DeFelipe J, Alonso-Nanclares L, Arellano JI. Microstructure of the neocortex: comparative aspects. J Neurocytol. 2002;31(3-5):299-316.
244. Arellano JI, Morozov YM, Micali N, Rakic P. Radial Glial Cells: New Views on Old Questions. Neurochem Res. 2021;46(10):2512-24.
245. Bonaguidi MA, Wheeler MA, Shapiro JS, Stadel RP, Sun GJ, Ming GL, et al. In vivo clonal analysis reveals self-renewing and multipotent adult neural stem cell characteristics. Cell. 2011;145(7):1142-55.
246. Marsh B, Blelloch R. Single nuclei RNA-seq of mouse placental labyrinth development. Elife. 2020;9.

247. Wolfien M, Galow AM, Muller P, Bartsch M, Brunner RM, Goldammer T, et al. Single-Nucleus Sequencing of an Entire Mammalian Heart: Cell Type Composition and Velocity. Cells. 2020;9(2).
248. Angata K, Suzuki M, Fukuda M. ST8Sia II and ST8Sia IV polysialyltransferases exhibit marked differences in utilizing various acceptors containing oligosialic acid and short polysialic acid. The basis for cooperative polysialylation by two enzymes. J Biol Chem. 2002;277(39):36808-17.
249. Liu ZZ, Zhu J, Wang CL, Wang X, Han YY, Liu LY, et al. CRMP2 and CRMP4 Are Differentially Required for Axon Guidance and Growth in Zebrafish Retinal Neurons. Neural Plast. 2018;2018:8791304.
250. Kim SY, Han YM, Oh M, Kim WK, Oh KJ, Lee SC, et al. DUSP4 regulates neuronal differentiation and calcium homeostasis by modulating ERK1/2 phosphorylation. Stem Cells Dev. 2015;24(6):686-700.
251. Dennis DJ, Han S, Schuurmans C. bHLH transcription factors in neural development, disease, and reprogramming. Brain Res. 2019;1705:48-65.
252. Berg DA, Su Y, Jimenez-Cyrus D, Patel A, Huang N, Morizet D, et al. A Common Embryonic Origin of Stem Cells Drives Developmental and Adult Neurogenesis. Cell. 2019;177(3):654-68 e15.
253. Ben Abdallah NM, Slomianka L, Vyssotski AL, Lipp HP. Early age-related changes in adult hippocampal neurogenesis in C57 mice. Neurobiol Aging. 2010;31(1):151-61.
254. Perera TD, Lu D, Thirumangalakudi L, Smith EL, Yaretskiy A, Rosenblum LA, et al. Correlations between hippocampal neurogenesis and metabolic indices in adult nonhuman primates. Neural Plast. 2011;2011:1-6.
255. Allen KM, Fung SJ, Rothmond DA, Noble PL, Weickert CS. Gonadectomy increases neurogenesis in the male adolescent rhesus macaque hippocampus. Hippocampus. 2014;24(2):225-38.
256. West MJ. Regionally specific loss of neurons in the aging human hippocampus. Neurobiol Aging. 1993;14(4):287-93.
257. West MJ, Gundersen HJ. Unbiased stereological estimation of the number of neurons in the human hippocampus. J Comp Neurol. 1990;296(1):1-22.
258. Sa MJ, Madeira MD, Ruela C, Volk B, Mota-Miranda A, Lecour H, et al. AIDS does not alter the total number of neurons in the hippocampal formation but induces cell atrophy: a stereological study. Acta Neuropathol. 2000;99(6):643-53.

259. Guidi S, Bianchi P, Alstrup AK, Henningsen K, Smith DF, Bartesaghi R. Postnatal neurogenesis in the hippocampal dentate gyrus and subventricular zone of the Gottingen minipig. Brain Res Bull. 2011;85(3-4):169-79.
260. Sorrells SF, Paredes MF, Velmeshev D, Herranz-Perez V, Sandoval K, Mayer S, et al. Immature excitatory neurons develop during adolescence in the human amygdala. Nat Commun. 2019;10(1):2748.
261. Flor-Garcia M, Terreros-Roncal J, Moreno-Jimenez EP, Avila J, Rabano A, Llorens-Martin M. Unraveling human adult hippocampal neurogenesis. Nat Protoc. 2020;15(2):668-93.
262. Seki T. Expression patterns of immature neuronal markers PSA-NCAM, CRMP-4 and NeuroD in the hippocampus of young adult and aged rodents. J Neurosci Res. 2002;70(3):327-34.
263. Cenquizca LA, Swanson LW. Spatial organization of direct hippocampal field CA1 axonal projections to the rest of the cerebral cortex. Brain Res Rev. 2007;56(1):1-26.
264. Yao Z, van Velthoven CTJ, Nguyen TN, Goldy J, Sedeno-Cortes AE, Baftizadeh F, et al. A taxonomy of transcriptomic cell types across the isocortex and hippocampal formation. Cell. 2021;184(12):3222-41 e26.
265. Breunig JJ, Sarkisian MR, Arellano JI, Morozov YM, Ayoub AE, Sojitra S, et al. Primary cilia regulate hippocampal neurogenesis by mediating sonic hedgehog signaling. Proc Natl Acad Sci U S A. 2008;105(35):13127-32.
266. Rhee S, Kirschen GW, Gu Y, Ge S. Depletion of primary cilia from mature dentate granule cells impairs hippocampus-dependent contextual memory. Sci Rep. 2016;6:34370.
267. Park SM, Jang HJ, Lee JH. Roles of Primary Cilia in the Developing Brain. Front Cell Neurosci. 2019;13:218.
268. Oberheim NA, Takano T, Han X, He W, Lin JH, Wang F, et al. Uniquely hominid features of adult human astrocytes. J Neurosci. 2009;29(10):3276-87.
269. Court J, Martin-Ruiz C, Piggott M, Spurden D, Griffiths M, Perry E. Nicotinic receptor abnormalities in Alzheimer's disease. Biol Psychiatry. 2001;49(3):175-84.
270. Lombardo S, Maskos U. Role of the nicotinic acetylcholine receptor in Alzheimer's disease pathology and treatment. Neuropharmacology. 2015;96(Pt B):255-62.
271. Turro S, Ingelmo-Torres M, Estanyol JM, Tebar F, Fernandez MA, Albor CV, et al. Identification and characterization of associated with lipid droplet protein 1: A novel membrane-associated protein that resides on hepatic lipid droplets. Traffic. 2006;7(9):1254-69.

272. Thomas A, Klein MS, Stevens AP, Reinders Y, Hellerbrand C, Dettmer K, et al. Changes in the hepatic mitochondrial and membrane proteome in mice fed a non-alcoholic steatohepatitis inducing diet. J Proteomics. 2013;80:107-22.
273. McMenemey WH. Alzheimer's Disease: A Report of Six Cases. J Neurol Psychiatry. 1940;3(3):211-40.
274. Hof PR, Morrison JH. Quantitative analysis of a vulnerable subset of pyramidal neurons in Alzheimer's disease: II. Primary and secondary visual cortex. J Comp Neurol. 1990;301(1):55-64.
275. Cardoso-Moreira M, Halbert J, Valloton D, Velten B, Chen C, Shao Y, et al. Gene expression across mammalian organ development. Nature. 2019;571(7766):505-9.
276. Hook B. Cleaner Protein with HaloTag Purification Resins Promega Corporation Web site.: Promega; 2014 [Available from: www.promega.com/resources/pubhub/tpub_153-cleaner-protein-with-halotag-purification-resins-article.
277. Kim JE, Li S, GrandPre T, Qiu D, Strittmatter SM. Axon regeneration in young adult mice lacking Nogo-A/B. Neuron. 2003;38(2):187-99.
278. Sekine Y, Lindborg JA, Strittmatter SM. A proteolytic C-terminal fragment of Nogo-A (reticulon-4A) is released in exosomes and potently inhibits axon regeneration. J Biol Chem. 2020;295(8):2175-83.
279. Cipriani S, Nardelli J, Verney C, Delezoide AL, Guimiot F, Gressens P, et al. Dynamic Expression Patterns of Progenitor and Pyramidal Neuron Layer Markers in the Developing Human Hippocampus. Cereb Cortex. 2016;26(3):1255-71.
280. Sorrells SF, Paredes MF, Cebrian-Silla A, Sandoval K, Qi D, Kelley KW, et al. Human hippocampal neurogenesis drops sharply in children to undetectable levels in adults. Nature. 2018;555(7696):377-81.
281. Walker TL, Overall RW, Vogler S, Sykes AM, Ruhwald S, Lasse D, et al. Lysophosphatidic Acid Receptor Is a Functional Marker of Adult Hippocampal Precursor Cells. Stem Cell Reports. 2016;6(4):552-65.
282. Amrein K, Hoffmann M, Lobmeyr E, Martucci G. Vitamin D in critical care: where are we now and what is next? Curr Opin Crit Care. 2021;27(4):378-84.
283. Nacher J, Crespo C, McEwen BS. Doublecortin expression in the adult rat telencephalon. Eur J Neurosci. 2001;14(4):629-44.
284. Gomez-Climent MA, Castillo-Gomez E, Varea E, Guirado R, Blasco-Ibanez JM, Crespo C, et al. A population of prenatally generated cells in the rat paleocortex maintains an immature neuronal phenotype into adulthood. Cereb Cortex. 2008;18(10):2229-40.

285. La Rosa C, Cavallo F, Pecora A, Chincarini M, Ala U, Faulkes CG, et al. Phylogenetic variation in cortical layer II immature neuron reservoir of mammals. Elife. 2020;9.
286. Epp JR, Beasley CL, Galea LA. Increased hippocampal neurogenesis and p21 expression in depression: dependent on antidepressants, sex, age, and antipsychotic exposure. Neuropsychopharmacology. 2013;38(11):2297-306.
287. Le Maitre TW, Dhanabalan G, Bogdanovic N, Alkass K, Druid H. Effects of Alcohol Abuse on Proliferating Cells, Stem/Progenitor Cells, and Immature Neurons in the Adult Human Hippocampus. Neuropsychopharmacology. 2018;43(4):690-9.
288. Kempermann G, Song H, Gage FH. Neurogenesis in the Adult Hippocampus. Cold Spring Harb Perspect Biol. 2015;7(9):a018812.
289. Ma T, Wang C, Wang L, Zhou X, Tian M, Zhang Q, et al. Subcortical origins of human and monkey neocortical interneurons. Nat Neurosci. 2013;16(11):1588-97.
290. Laclef C, Metin C. Conserved rules in embryonic development of cortical interneurons. Semin Cell Dev Biol. 2018;76:86-100.
291. Di Paolo G, Kim TW. Linking lipids to Alzheimer's disease: Cholesterol and beyond. Nature Reviews Neuroscience. 2011;12(5):284-96.
292. Strittmatter WJ, Saunders AM, Schmechel D, Pericak-Vance M, Enghild J, Salvesen GS, et al. Apolipoprotein E: high-avidity binding to beta-amyloid and increased frequency of type 4 allele in late-onset familial Alzheimer disease. Proc Natl Acad Sci U S A. 1993;90(5):1977-81.
293. Hamilton LK, Dufresne M, Joppe SE, Petryszyn S, Aumont A, Calon F, et al. Aberrant Lipid Metabolism in the Forebrain Niche Suppresses Adult Neural Stem Cell Proliferation in an Animal Model of Alzheimer's Disease. Cell Stem Cell. 2015;17(4):397-411.

11. Curriculum Vitae

Daniel Franjić graduated from the School of Medicine, Osijek in 2010 and obtained a Medical Doctor degree. Shortly after graduation, Daniel continued his education at Yale University (USA) as a Postdoctoral Associate in Neuroscience in Sestan Lab where his focus was functional characterization of genes potentially implicated in human diseases. Daniel also taught Neuroanatomy to first year medical students at Yale School of Medicine for one year. Following his postdoctoral education in 2016, Daniel continued his work in Sestan lab as an Associate Research Scientist. He started his PhD studies in 2019 at Croatian Institute for Brain Research (CIBR) with prof. Goran Sedmak (CIBR) and prof. Nenad Sestan (Yale University) as his mentors. As of recently, Daniel is working at Pfizer, Inc. (USA) as a Director of Clinical Development.

Daniel published 7 peer-reviewed papers and 1 abstract at an international meeting.